



Quaid Zaman

**Surface Plasmon Resonance Spectroscopy for the
Characterization of Nanoparticles, Organic Thin Film
and 2-D Materials**

Tese de Doutorado

Thesis presented to the Programa de Pós-graduação em Física of
PUC-Rio in partial fulfillment of the requirements for the degree of
Doutor em Ciências-Física

Advisor: Prof. Tommaso Del Rosso

Rio de Janeiro

May 2019



Quaid Zaman

**Surface Plasmon Resonance Spectroscopy for the
Characterization of Nanoparticles, Organic Thin Film
and 2-D Materials**

Thesis presented to the Programa de Pós-graduação em Física of PUC-Rio, in partial fulfillment of the requirements for the degree of Doutor em Ciências-Física. Approved by the undersigned Examination Committee.

Prof. Tommaso Del Rosso

Advisor

Departamento de Física - PUC-Rio

Prof. Marco Cremona

Departamento de Física - PUC-Rio

Prof. Karlo Queizor da Costa

UFPA

Prof. Alexandre de Resende Camara

UERJ

Prof. Jorge Ricardo Mejía Salazar

INATEL

Rio de Janeiro, May 24th, 2019

All right reserved.

Quaid Zaman

The author is graduated from University of Peshawar KPK, Pakistan in 2007, where he studied Physics and Mathematics. He obtained his Master's degree in Physics at the same university in 2010. After he did a two-year Master of Philosophy (M. Phil) in Physics from Quaid-i-Azam University Islamabad in 2013.

Bibliographic data

<p>Zaman, Quaid</p> <p>Surface Plasmon Resonance Spectroscopy for the Characterization of Nanoparticles, Organic Thin Film and 2-D Materials / Quaid Zaman; advisor: Tommaso Del Rosso -Rio de Janeiro: PUC- Rio, Departamento de Física, 2019.</p> <p>194 f.: il. color.; 30cm</p> <p>Tese (doutorado) - Pontifícia Universidade Católica do Rio de Janeiro, Departamento de Física.</p> <p>Inclui bibliográficas</p> <p>1. Física – Teses. 2. Espectroscopia de Ressonância de Plasmon de Superfície (SPR). 3. Sensores Óticos SPR. 4. Guias de Onda Carregadas por Dielétrico (DLWG). 5. Interfaces Metal-Dielétrico. 6. Nanopartículas de Ouro (AuNPs). 7. Grafeno. 8. Filmes Finos Orgânicos. I. Del Rosso Tommaso. II. Pontifícia Universidade Católica do Rio de Janeiro. Departamento de Física. III. Título.</p>

CDD: 530

Acknowledgments

Studying and carrying out high level scientific research was a great honor for me and I am very grateful to all of peoples who have helped me a lot with their guidance, knowledge, assistance and patience. I am deeply thankful to my supervisor Tommaso Del Rosso who is incredibly smart, good and very kind person. It is his trust and motivation from beginning to end that enables me to focus my mind and efforts on my research.

I would like to appreciate all generous help from Prof. Marco Cremona and Dr. Omar Pandoli. I want to thank to the teachers and staff of Department of Physics PUC-Rio.

Yet most importantly, my family gives me happiness, courage and perspective that always encourage me. I dedicate this thesis and all the hard work it presents, to all my brothers, sisters, my wife and parents (late).

Without the help from my colleagues, the research presented in this thesis could not have happened. I would like to thanks, Tahir, Harold Jose Camargo Avila, Rafael dos Santos Carvalho and Arthur Rodrigues Jardim Barreto for help in the laboratory. I would also like to thanks, Rafaqat Ali, Syed Adnan Raza, Hamza, Asmat, Saba, Dr. Raj wali khan, Rafi and Khalil for their nice friendship and company during my PhD.

This study was financed in part by the Coordenação de Aperfeiçoamento de Pessoal de Nível Superior - Brasil (CAPES) - Finance Code 001. I also thank to CNPq and FAPERJ for their financial support.

Abstract

Zaman, Quaid; Del Rosso, Tommaso (Advisor). **Surface Plasmon Resonance Spectroscopy for the Characterization of Nanoparticles, Organic Thin Film and 2-D Materials.** Rio de Janeiro, 2019. 194p. Tese de Doutorado- Departamento de Física, Pontifícia Universidade Católica do Rio de Janeiro

Surface Plasmon Resonance (SPR) Spectroscopy based sensors have emerged as a versatile and widely used optical tool for the label free ultrasensitive detection of gas and (bio) chemical analytes. The sensing mechanism is relying on the sensitivity of the evanescent field of the Surface Plasmon Polariton (SPP) wave propagating at metal dielectric interface, which acts as an efficient optical nanoprobe in the external medium. Despite the excellent results in the real-time sensing applications, SPR Spectroscopy has found limited applications in the accurate ellipsometric characterization of thin films with thickness higher than a few nm. The limitations are mainly associated with the long-time instability of the metal-dielectric interfaces of the SPR devices, which deteriorates the accuracy in the simultaneous determination of thickness and refractive index of the thin films under investigation.

For these reasons, the first part of the dissertation is dedicated to the study of the degradation and stabilization process of the metal-organic interfaces of different SPR sensing platforms, in both air and water environment. The sensing platforms were monitored by SPR spectroscopy and atomic force microscopy (AFM). Different metal-dielectric interfaces configurations were analyzed, in terms of both adhesion layers, type of metal supporting the plasma wave and super-layers, with the aim to optimize the stability and the sensitivity of both monomodal and multimodal SPR platforms. The best performances were obtained when a low damping metal-dielectric interface is created through the self-assembling of a monolayer of (3-Mercaptopropyl) trimethoxysilane (MPTS), and a single layer graphene (SLG) is transferred as a super-layer on the gold (Au) thin film.

The study of the process of stabilization of the SPR platforms was the base for the development of the second part of the dissertation, where we

demonstrate the potentialities of the SPR spectroscopy in the Kreschmann configuration for the accurate ellipsometric characterization of a class of three different materials: gold nanoparticles (AuNPs), organic luminescent materials, and graphene. To obtain the simultaneous determination of both the thickness and refractive index of the thin films, a two-color and/or two-mode approach was adopted, the latter performed by the use of dielectric loaded waveguides (DLWG) with symmetric Au/MPTS/SiO₂ interfaces.

Finally, the three class of materials have been used for the development of novel SPR optical sensors with environmental or biological interest. The proof of principle of an SPR based UVA dosimeter is demonstrated via the monitoring of the radiation induced modifications of the thickness and refractive index of luminescent thin film of tris(8-hydroxyquinoline) (Alq₃) and tris(dibenzoylmethane) mono(1,10-phenanthroline) europium (III) (Eu(dbm)₃Phen).

Sodium Citrate stabilized AuNPs with a nominal diameter of about 15 nm were used to show the principle work of a two-color SPR spectroscopy nanosizer and nanocounter. In the latter case, we demonstrate experimentally that DLWGs can be used as accurate nanocounters in the range of surface density between 20 and 200 NP/μm², with results important for both optical metrology and the emerging particle amplified PA-SPR spectroscopy.

Finally, we show the use of the Au/SLG interface for the ultrasensitive detection of heavy metal ions of environmental interest, with an unprecedented limit of detection (LoD) of the order of part per billion (ppb). The experimental results support the theoretical predictions about the affinity of particular sites of the infinite graphene to heavy metal ions, and the possibility to enhance the sensitivity of SPR devices by the plasmon assisted electron transfer between the metal film and the SLG.

Keywords

Surface Plasmon Resonance (SPR) Spectroscopy, SPR Optical Sensors, Dielectric Loaded Waveguide (DLWG), Metal-Dielectric Interface, Gold Nanoparticles (AuNPs), Graphene, Organic Thin Film.

Resumo

Zaman, Quaid; Del Rosso, Tommaso. **Espectroscopia de Ressonância de Plasmon de Superfície para a Caracterização de Nanopartículas, Filmes Finos Orgânicos e Materiais 2-D.** Rio de Janeiro, 2019. 194p. Tese de Doutorado -Departamento de Física, Pontifícia Universidade Católica do Rio de Janeiro

Sensores baseados na espectroscopia de ressonância de plásmons de superfície (SPR) são dispositivos fotônicos amplamente usados para a detecção ultra sensível de gases e analitos (bio) químicos sem marcadores. O mecanismo de sensoriamento baseia-se na sensibilidade do campo eletromagnético evanescente associado aos Polaritons de Plásmom de Superfície (SPP) propagando-se na interface metal-dielétrica, o qual age como uma eficiente nanosonda no meio exterior. Mesmo com resultados excelentes em aplicações de sensoriamento em tempo real, a espectroscopia SPR encontra severas limitações nas caracterizações elipsométricas de filmes finos com espessuras maiores que alguns nm. As limitações são principalmente associadas a instabilidade no longo prazo das propriedades físico-químicas das interfaces metal-dielétricas dos dispositivos SPR, a qual prejudica a acurácia na determinação simultânea da espessura e do índice de refração dos filmes finos que estão sendo investigados.

Por estas razões, a primeira parte da tese é dedicada ao estudo da degradação e do processo de estabilização das interfaces metal-dielétricas de diferentes plataformas de sensoriamento SPR, tanto no ar como em ambiente aquoso. As plataformas de sensoriamento foram monitoradas por espectroscopia SPR e microscopia de força atômica (AFM). Diferentes configurações de interfaces metal-dielétricas foram analisadas, tanto em termos de camadas de adesão, tipo de metal que suporta a onda de plasma, e supercamadas, com o objetivo de otimizar a estabilidade e a sensibilidade de plataformas SPR monomodais e multimodais. As melhores performances foram obtidas quando uma interface metal-dielétrica com baixo amortecimento eletromagnético é criada através da deposição de uma monocamada adesiva de (3-Mercaptopropyl) trimethoxysilane (MPTS), e quando uma monocamada de grafeno (SLG) é transferida como supercamada na cima de um filme fino metálico de ouro.

O estudo do processo de estabilização das plataformas SPR foi a base para o desenvolvimento da segunda parte da tese, onde nós mostramos as potencialidades da espectroscopia SPR na configuração Kretschmann para a acurada caracterização elipsométrica de três classes de materiais deferentes: nanopartículas de ouro (AuNPs), filmes finos de materiais orgânicos luminescentes, e grafeno. Para determinar simultaneamente a espessura e o índice de refração dos filmes finos, foram adoptados os métodos das duas cores e/ou dois modos, esse último realizado através do uso de guias de onda carregadas por dielétricos (DLWGs) com interfaces simétricas do tipo Au/MPTS/SiO₂.

Por fim, estas três classes de materiais foram usadas no desenvolvimento de novos sensores ópticos SPR de interesse biológico e ambiental. A prova de conceito de um dosímetro de raios UVA baseado em espectroscopia SPR é demonstrado através do monitoramento das modificações da espessura e índice de refração induzidas pela radiação em filmes finos de tris (8-hydroxyquinoline) (Alq₃) e tris (dibenzoylmethane) mono (1,10-phenanthroline) europium (III) (Eu (dbm)₃Phen).

AuNPs com um diâmetro nominal de 15nm estabilizadas por citrato de sódio, foram usadas para demonstrar o princípio de funcionamento de medidores de tamanho de partículas e contadores superficiais de AuNPs baseados na espectroscopia SPR de duas cores. Neste último caso, nós mostramos experimentalmente que as DLWG podem ser usadas como acurados nanocontadores para densidades superficiais entre 20 e 200 NP/μm², com importantes resultados para a metrologia óptica e a emergente espectroscopia SPR amplificada por nanopartículas (PA-SPR).

Por último, mostramos o utilizo da interface Au/SLG para a detecção ultrasensível de íons de metais pesados de interesse ambiental, com um limite de detecção (LoD) sem precedentes da ordem de uma parte por bilhão (ppb). Os resultados experimentais suportam as previsões teóricas sobre a afinidade de sítios particulares do grafeno infinito para íons de metais pesados, e a possibilidade de aumentar a sensibilidade dos dispositivos SPR através da transferência de elétrons assistida por plásmons entre o filme de metal e o SLG.

Palavres- chave

Espectroscopia de Ressonância de Plasmon de Superfície (SPR), Sensores Óticos SPR, Guias de Onda Carregadas por Dielétrico (DLWG), Interfaces Metal-Dielétrico, Nanopartículas de Ouro (AuNPs), Grafeno, Filmes Finos Orgânicos.

Table of contents

1 Introduction	28
1.1. Plasmonics	28
1.2. State of Art of SPR Spectroscopy	29
1.3. Objectives	32
1.4. Thesis layout	34
2 Theoretical background of plasmonics	36
2.1. Optical properties of metals	37
2.2. From Maxwell's equation to Surface Plasmon Polaritons	40
2.2.1. Dispersion relation of Surface Plasmon Polariton	40
2.3. Excitation of Surface Plasmon Polariton	46
2.3.1. Prism coupling	46
2.4. Surface Plasmon Resonance Sensors	49
2.4.1. Working principle of SPR sensors	49
2.4.2. SPR affinity biosensor	51
2.4.3. Performance Parameters of SPR sensors	51
2.5. Dielectric Loaded Waveguide (DLWGs)	55
2.6. SPR based Ellipsometry	57
2.6.1. Two Medium Method	59
2.6.2. Two color method	61
2.6.3. Two films thickness and Two metal deposition	62
2.6.4. Dual modes DLWGs Spectroscopy	63
2.7. Localized Surface Plasmon in metal nanostructures	65
2.7.1. Quasi Static Approximation	67
2.7.2. Mie Theory	68
2.8. Optical density, extinction coefficient and mass concentration	69
2.9. Maxwell Garnett theory	73
2.9.1. Theoretical model of two-color SPR nanosizer	75
2.9.2. Mean free path limitation	77
2.10. Particle Amplified SPR Spectroscopy	78
2.11. Numerical analysis of plasmonics structures	79

2.12. Sensitivity enhancement of SPR sensor via graphene	81
3 Experimental methods and techniques	83
3.1. Fabrication of Conventional SPR platform	83
3.1.1. Glass Substrate cleaning	83
3.1.2. Deposition of Self Assembled Monolayer (SAM) of organic adhesion layers	84
3.1.3. Electron beam gun assisted deposition	85
3.1.4. Thermal deposition in vacuum	87
3.2. Fabrication of Dielectric Loaded Waveguide (DLWGs)	88
3.3. Growth and transfer process of Graphene	89
3.3.1. Chemical Vapor Deposition (CVD)	89
3.3.2. Transfer of graphene on SPR chips	90
3.4. Structural Characterization	92
3.4.1. Two-color Surface Plasmon Resonance (SPR) spectrometer	92
4 Study of the degradation process of metal-dielectric interfaces in SPR sensing platforms	100
4.1. SPR sensing platforms in air and nitrogen	102
4.1.1. Monitoring of the reflectivity curves of single mode SPR sensing platforms	102
4.1.2. AFM measurement on single mode SPR sensing platforms	104
4.2. SPR sensing platforms in DI water	107
4.2.1. Monitoring of the reflectivity curves of single mode Au based SPR sensing platforms in DI water	107
4.2.2. Monitoring of the reflectivity curves of single mode Ag based SPR sensing platforms in DI water	109
4.2.3. AFM measurement on single mode SPR sensing platforms after immersion in DI water	111
4.2.4. Au based DLWGs in water	113
4.3. Refractive index (RI) Sensitivity analysis	114
4.4. Conclusion	117
5 Optical sensing by SPR Spectroscopy	119

5.1. SPR UVA dosimeter	120
5.1.1. Characterization techniques	121
5.1.2. Monitoring the degradation of Alq ₃ and Eu(dbm) ₃ (phen) thin films in an air environment	122
5.1.3. Degradation of Alq ₃ and Eu(dbm) ₃ (phen) thin films under UVA irradiation	126
5.1.4. Working principle of the SPR dosimeter in the SPCE configuration	128
5.2. SPR nanocounter	130
5.3. Hybrid Au/SLG interfaces for Hg ⁺² optical sensing	135
5.3.1. Adsorption isotherm model	140
5.3.2. Full Width Half Maximum (FWHM)	141
5.4. Hybrid Au/SLG interfaces for Pb ⁺² optical sensing	141
6 Ellipsometric Application of SPR spectroscopy	144
6.1. SPR two-color nanosizer	144
6.1.1. Experimental method	145
6.1.2. Results and discussion	146
6.2. Ellipsometric characterization of luminescent organic thin films by DLWGs	155
6.2.1. Characterization of Alq ₃ using two film thickness method	156
6.2.2. Dual mode analysis for characterization of Alq ₃ and Eu(dbm) ₃ phen	158
6.3. Investigation of the anisotropy of SLG by DLWGs	162
6.3.1. SPR and Raman spectroscopy on Au/SLG	162
6.3.2. Anisotropy characteristics of graphene by DLWGs	164
7 Conclusions and perspectives	167
7.1. Conclusions	167
7.2. Perspective and future work	172
8 Productions	173
8.1. List of publications	173
8.2. Conferences	174

AppendixA Matlab Codes developed	175
A.1 Calculation of the dielectric function of small NPs	175
A.2 Application of Mie Theory for the calculation of the mass concentration of metal NPs with statistical size distribution	176
A.3 XPS spectra of silver thin film	179
9 Bibliography	181

List of figures

Figure 1.1: The Roman Lycurgus cup made of mixture of silver and AuNPs embedded in ruby glass viewed (a) green in reflected light but (b) red in transmitted light Copyright of the British Museum.	29
Figure 1.2: Schematic illustration of the main objectives of the proposed research.	34
Figure 2.1: Comparison between the permittivity of gold calculated by Drude model (dash line) and the experimental data obtained by Johnson (solid line). The values of damping constant and plasma frequency are listed in table 2.1. The interband transition restrict the validity of Drude model in visible region [49].	39
Figure 2.2: Representation of the TE (a) and TM (b) polarized plane wave's incident on a metal dielectric interface. The electric and magnetic field components along x, y, z axis are (a) H_z, E_y, H_x and (b) E_z, H_y, E_x	41
Figure 2.3: Schematic picture of surface plasmon oscillations propagating along a metal-dielectric interface. The electric field in the dielectric medium and electrical charges moving in the plasma at metal surface. Right hand side show the SPPs field perpendicular to the interface decay exponentially and characterized by the penetration depths (δ_m, δ_d) in both side of the media.....	43
Figure 2.4: Dispersion relation of SPP propagating along interface between dielectric and Drude metal with no damping. Light line (orange) represents the dispersion of light wave in free space, while the red line shows the dispersion of SPP.....	45
Figure 2.5: (a) Excitation of SPP in Kretschmann -Reather configuration. (b) Dispersion relations for SPPs modes in Kretschmann -Reather configuration.....	47
Figure 2.6: Excitation of SPP in Kretschmann configuration. The TM reflectivity curves with variation of (a) silver thickness, (b) wavelength λ and	

(c) refractive index of external medium. The refractive index of prism is 1.5 and the optical constant of silver are taken from Johnson [50]. Simulation were obtained using Winspall free software [56]. 48

Figure 2.7: Reflectivity and phase for light wave exciting an SPPs in Krestchmann geometry (SF14 glass prism -50 nm thick gold layer-dielectric) versus (a) the angle of incidence for two different refractive indices of the dielectric (wavelength 682nm), and (b) wavelength for two different refractive indices of the dielectric (angle of incidence 54°) [57]. . 50

Figure 2.8. Conceptual illustration of SPR sensor operation. The interaction of selected analyte by bio-recognition element change the SPP propagation constant..... 51

Figure 2.9: Representation of SPR sensor in Krestchmann configuration (a) before analyte deposition (injection) and after analyte binding with sensor surface by changing the (b) bulk refractive index and the (c) surface refractive index near the interface. 53

Figure 2.10: Schematic of (a) Dielectric loaded waveguide configuration and (b) its ATR reflectivity curve for TM (in black solid line) and TE (red dash line) polarized light. Above the optical parameters and excitation wavelength are also shown. 55

Figure 2.11: The absolute values of the electric field for the resonant modes in the SPR platform. In colors for a cut plane parallel to the zx-plane: (a) Ez Field for TM_0 mode (b) Ez field for TM_1 mode and (c) E_y field for TE1 mode (d) Norm of E field for the resonant modes in a cut line parallel to the z-axis. Fixed parameters: $\lambda = 633$ nm, $d_{Au} = 46$ nm, and $d_{SiO_2} = 600$ nm [31]. 57

Figure 2.12: Scheme of the four layers SPR based ellipsometry. (a) The resonance angle of SPR curve shift by an amount $\Delta\theta$ after the deposition of metal composite thin film. (b) The trial curves of the different experimental methods in the (ϵ_d, t_d) plane. The intersection point gives the actual values of the parameters of metal composite layer..... 59

Figure 2.13: (a) TM experimental reflectivity SPR curves recorded on bare Au and Au/SiO₂ in air and water at a wavelength of 783nm. (b) Trial curves of two medium method obtained from a set of couples of values in plan $(\epsilon_{SiO_2}, t_{SiO_2})$. The intersection point gives the actual value of the SiO₂. 61

Figure 2.14: Example of SPR reflectivity data management for two-color method in the determination of the thickness and refractive index of a thin film of SiO ₂ deposited over gold by electron-beam deposition [73].....	62
Figure 2.15: Scheme of the encapsulated multilayer structures used to perform the TMD and TFT methods. All the samples presented a region with only bare metals that was used to characterize the metal deposition by SPR spectroscopy.	63
Figure 2.16: Calculated points representing the possible values of thickness (t_0) and dielectric constant (ϵ_0) of the organic layers over the TMD and TFT samples. In the latter, the ratio between the thicknesses t_1 and t_2 of the different organic layers is known, and the intersection point corresponding to the actual characteristic of the thin film is obtained by shifting one set of points. The points are generated using the mean value of refractive index of the metal depositions [34].....	63
Figure 2.17: (a) Simulated SPR reflectivity curves before and after graphene on the DLWGs. The insets show the change the resonance angle. (b) Curves of the set of coupled values of (t_{graphene} , $\epsilon_{\text{graphene}}$) in refractive index thickness plan.....	65
Figure: 2.18: Scheme of the light interaction with a metallic NP. The electric field of the light induces the movement of conduction electrons, which accumulate at the NP surface creating an electric dipole. This charge accumulation creates an electric field opposite to that of the light [78].	66
Figure 2.19: A sphere of radius R, in uniform static electric field under the study of quasi-static approximation.	67
Figure 2.20: Scattering and absorption of NPs illuminated with plan EM wave.	70
Figure 2.21: (a) TEM image of the Au@Carbynoid. The inset show the experimental statistical size distribution using Equation 2.67 (b) Extinction spectra of the synthesized NCs (black line with open circles) and Mie's theoretical fit (dashed grey line) obtained using the statistical distribution reported in (a). In the inset are reported the concentration of Au and C produced by CO ₂ recycling during PLA [80].	71
Figure 2.22: The optical geometry of the composite layer of AuNPs immersed in a medium ϵ_m with effective thickness $t_{\text{eff}} = 2h$. Where h is the	

effective radius of the AuNPs in composite layer. The optical properties of this inhomogeneous layer is estimated by effective dielectric constant ϵ_{eff} ... 73

Figure 2.23: The size corrected (a) real and (b) imaginary part of the refractive index of small AuNPs when only the effect of mean free is included in the imaginary part of the dielectric function. 77

Figure 2.24: (a) sandwich assay scheme for the N-AuNPs enhanced detection of CEA. (b) Sensor response obtained during a typical CEA assay using 33 nm N-AuNPs [40]. 79

Figure 2.25: a) Unit periodic cell considered in the numerical simulations by the COMSOL® software.(b) Mesh of the FEM model of the sensor. Colors indicate the size of the elements, which is defined by physical and geometrical factors; (c) Resultant planar structure of the PA-SPR sensor in the effective layer approximation to represent the AuNPs periodic [31]. .. 80

Figure 2.26: (a) metal-graphene based SPR spectroscopy (b) The scheme of the transfer process of electron from graphene to gold due to the difference in the work function and subsequent adjustment of the Fermi level..... 81

Figure 3.1: Fabrication of SPR platform (a) clean glass substrate (b) hydroxylation leads to hydroxyl group (c) silanization (d) thin film deposition. 84

Figure 3.2: Univex 450. (a) crucible with metal pellet, (b) tungsten filament, (c) sample holder, (d) quartz crystal balance, (e) pressure detector, (f) electron gun controller, (g) vacuum chamber. 85

Figure 3.3: (a) Intensity curve of the Univex 450 system (b) the list of working parameters to control the deposition of target materials..... 86

Figure 3.4: (a) Different parts of vacuum chamber: 1-5 are possible places for crucibles, 6-7 are quartz crystal controlling the thickness, 8 is shutter, 9 is a door mask and 10 is the sample holder. (b) Crucible structure and (c) glove box. *Laboratorio de Espectroscopia Óptica e Optoeletrônica Molecular (LOEM) at the Physics department in PUC-Rio.* 88

Figure 3.5: Schematic diagram showing the fabrication of the DLWGs. (a) 49 nm gold thin film deposited on clean SF4 glass. (b) Silanization with MPTS. (c) Hydrolysis process: methoxy groups are converted to Si-OH

group. (d) Condensation leads to Si-O-Si network. (e) Deposition of SiO₂.
.....89

Figure 3.6: Photograph of the graphene growth using CVD technique (a) CVD system, (b) copper foil inside the quartz tube and (c) graphene on Cu ready for transfer. 90

Figure 3.7: (a) and (c) represent etching of copper film using Ferro III chloride (FeCl₃), (d) partial disappearance of copper and (b) total disappearance of copper.91

Figure 3.8: Scheme of the etching of copper (a) to (c), (d)-(e) transfer of graphene/PU on the SPR sensor and (f) the removal of PU using THF. ...92

Figure 3.9: Scheme of the optical configuration of our two-color homemade SPR spectrometer in the Kretschmann configuration. It consists of two independent laser sources (λ_1, λ_2), (b) an attenuator, (c) mirror (d) two pinholes, (P) a linear polarizer, (BS) a beam splitter, (D_R) a reference detector, (D_S) a signal detector, a PC linked to a data acquisition system (DAQ), and a covering black box. Inside the black-box is visible the multilayer metal-dielectric SPR device and the flow-cell used for analyte injection and sensing (gas or liquid). 93

Figure 3.10: Photograph of the two-color SPR spectrometer in the Kretschmann configuration installed in *NanoLaser Lab* at the Department of Physics PUC-Rio. Optical table equipped with two laser sources (λ_1, λ_2), and different optical instruments, (a) isolator (b) attenuator, (c) mirror (d) pinholes, (e) oscilloscope, (f) stage controller, (BS) beam splitter, (P) a linear polarizer, (D_R) reference detector, and a PC connected to data acquisition system (DAQ). Inside the black box there is a signal detector (D_S), prism and the flow cell.94

Figure 3.11: Experimental setup of the SPR fluidic channel in PEEK, used to flow the desired analyte and detect in real time.(b) The typical SPP wave on the Au/graphene chip. 95

Figure 3.12: The isosceles prism used for SPR coupling, θ_{in} is the angle of incidence that we measure directly with the goniometer, and θ_x is the angle of incidence related with θ_{in} , used by the elaboration data program (Winspill free software). 96

Figure 3.13: The Labview program window for the measurement of the reflectivity SPR curve.	98
Figure 3.14: Experimental SPR reflectivity spectrum (black dots) fitted using Winspall, and the simulated SPR curve (continuous line) for a three-layer system: BK7 prism, Au (-10.83+i1.433) and air at $\lambda = 633\text{nm}$	99
Figure 4.1: Structure of the most general SPR multilayer platform, consisting of metal, adhesions and dielectric layers. The dielectric layer can be protected with a thin film of different nature.....	101
Figure 4.2: (a) Time dependence of the SPR curve of bare gold devices without MPTS adhesion layer. (b) Comparison between the time dependence of the SPR curve of bare gold samples with MPTS adhesion layer and gold devices protected by graphene. (c, d) Variation in time of the FWHM and resonance angle θ of the SPR spectra of samples with different architectures and MPTS as adhesion layer: bare metals, samples with OLED encapsulation and graphene protected devices [100]......	103
Figure 4.3: Peak Force Tapping™ AFM images of silver layer on glass slide silanized with MPTS (A–B) and without MPTS (C–D). The surface roughness average on $1 \times 1 \mu\text{m}$ images was measured with a fresh substrate ($t = 0$) and after 6 h. For all the images, we used a scan rate of 0.95 Hz and scan size of $1 \mu\text{m}^2$ [100]......	105
Figure 4.4: Peak force Tapping™ AFM images of gold layer on glass slide silanized with MPTS (A–B) and without MPTS (C–D). The surface roughness average on $1 \times 1 \mu\text{m}$ images was measured with a fresh substrate ($t= 0$) and after 24 h. For all the images, we used a scan rate of 0.95 Hz and scan size of $1 \mu\text{m}^2$ [100].	105
Figure 4.5: Simulation of the effect that the metal delamination process has during its first phase on the SPR spectra of a gold plasmonic device. An angular shift of about 0.0150° is obtained introducing an air gap up to 40 nm between the gold and SiO_2 [100]......	106
Figure 4.6: Influence of graphene transfer and Au/SF4 interface adhesion layer on the temporal stability of (a) the SPR angle ($\Delta\theta_{\text{SPR}}$) and (b) FWHM. The continuous and dashed lines are relatives to water and air environments, respectively.	108
Figure 4.7: Comparison of low damping and high damping SPR curve.	108

Figure 4.8: Influence of adhesion, without adhesion layer and graphene-protected layer on (a) the variation of SPR angle, and (b) FWHM for Ag thin film as a function of time in air and DI water.....	110
Figure 4.9: AFM images of 49nm gold thin films deposited over SF4 substrates with MPTS as adhesion layer. Morphology (left side) and phase (right side) images were taken before (A, B) and after (C, D) immersion in water for 44 hours.	112
Figure 4.10: AFM images of 49nm silver thin films deposited over SF4 substrates with MPTS as adhesion layer. Morphology (left side) and phase (right side) images were taken before (A, B) and after (C, D) immersion in water for 44 hours.	112
Figure 4.11: The simulated SPR curves for different gap thicknesses induced by the delamination of the Ag thin film from the SiO ₂ substrate. For a water gap thickness of about 30nm, we obtained an angular shift equal to 0.03°. (b) The change in resonance angle and FWHM as a function of gap thickness.	113
Figure 4.12 (a) SPR reflectivity curve collected for the stability of DLWG in water at excitation wavelength of 633nm for different time. (b) The waveguide was stable up to 5 hours with almost no changes in the FWHM.	114
Figure 4.13: (a) Experimentally calculated RI sensitivity for various concentration of glycerin in deionized water using Cr/Au, MPTS/Au and monolayer graphene coated Au thin film sensors.....	115
Figure 4.14: The E field distribution for the resonant modes parallel to the z-axis.....	116
Figure 5.1: Chemical structure of Alq ₃ (C ₂₇ H ₁₈ AlN ₃ O ₃) and (Eu(dbm) ₃ phen) (C ₅₇ H ₄₁ EuN ₂ O ₆).....	121
Figure 5.2: (A) Time dependence of the FWHM of Au/Alq ₃ , Au/Eu(dbm) ₃ (phen), Ag/Alq ₃ , Ag and Au SPR devices in air. (B) Time dependence of the refractive index variation Δn for Alq ₃ and Eu(dbm) ₃ (phen) thin films over an Au metal layer. The nominal thickness of the organic thin films was 30 nm. The temperature was maintained at approximately 23 °C with a humidity of 50% [46].....	122

Figure 5.3: AFM images of Alq₃ (A, B, C, and D) and Eu(dbm)₃(phen) (E, F, G, and H) thin films deposited over silicon substrates. Morphology (left side) and phase (right side) images were taken on fresh samples (A, C, E, and G) and samples aged for 24 hours (B, D, F, and H). The nominal thickness of the organic thin films was 30 nm. The temperature was maintained at approximately 23 °C with a humidity of 50%. [46]. 124

Figure 5.4: Time dependence of the photoluminescence intensity of Alq₃ (A) and Eu(dbm)₃(phen) (B) thin films deposited over silicon substrates under air exposure. The nominal thickness of the organic layer was approximately 30 nm. The temperature was maintained at approximately 23 °C with a humidity of 50% [46]. 125

Figure 5.5: Monitoring of the refractive index variation (Δn) and photoluminescence intensity (I/I_0) of the Alq₃ (A) and Eu(dbm)₃(phen) (B) thin films under UVA irradiation in nitrogen environment. The continuous lines represent the exponential fit on the experimental results [46]. 127

Figure 5.6: Scheme of the working principle of the proposed SPR dosimeter in the SPCE configuration [46]. 129

Figure 5.7: Comparison between the experimental SPR spectra $R_\lambda(\theta)$ at a wavelength of 610 nm (grey line) and theoretical curve $R^*(\theta)$ for an organic thin film of Eu(dbm)₃(phen) with a nominal thickness of 30 nm before (black continuous line) and after (black dotted line) an UVA dose of approximately 60 J/cm² [46]. 129

Figure 5.8: E_z field between two adjacent AuNPs with the diameter of 60 nm embedded in water. The centers of the AuNPs are separated by the distance d , as highlighted in the inset [31]. 131

Figure 5.9: The relative deviation $\delta\sigma$ between the real surface density σ_{FEM} and the density σ_{MG} calculated by MG formula to fit the resonance angle θ_{FEM} [31]. 132

Figure 5.10: (a) DLWGs fabricated by the deposition of thick dielectric layer of SiO₂. (b) Immobilization of AuNPs on APTS functionalizes SiO₂ surface. 133

Figure 5.11: SPR sensogram relative to the sensing of the interaction between the APTS functionalized external surface of the DLWGs and the

negatively charged AuNPs. The TM_1 mode of the DLWG has been used as evanescent optical probe. The excitation wavelength was 783 nm, and the sensogram was taken at a fixed incidence angle of 50.695° 134

Figure 5.12: Comparison of experimental SPR reflectivity curve of the TM_1 mode of the DLWGs in water before and after interaction of the AuNPs with the SiO_2 surface (left side), and AFM image of a $1 \mu m \times 1 \mu m$ region of the SiO_2 surface of the device, analyzed by SPR spectroscopy (right size), with a NPs surface density of $25 \text{ NP}/\mu m^2$. (c) $\sigma = 120 \text{ NP}/\mu m^2$. (d) $\sigma = 200 \text{ NP}/\mu m^2$ [31]. 134

Figure 5.13: The possible adsorption sites. Neutral atoms and charged ions of heavy metals are placed at the (a) on-top (T), (b) bridge (B), and (c) hollow (H) sites on the hexagonal cell, as well as, on a defect (D) site (d) of graphene sheet [87]. 136

Figure 5.14: (a) Reflectivity at half maximum of SPR curve versus time graph at wavelength of $\lambda = 783 \text{ nm}$. (b) The corresponding SPR reflectivity curve of the Au thin film (49 nm) in deionized water. 137

Figure 5.15: Experimental (a) SPR angle shift and (b) FWHM variation as a function of different concentration of Hg^{+2} ions using the low-damping SPR sensors in the bare Au, Au/ SiO_2 /SLG and Au/SLG architectures. The solid lines show the Langmuir fit on each experimental data. 138

Figure 5.16: (a) The SPR angle shift as a function of different concentration of Pb^{+2} ions for bare Au and hybrid Au/SLG sensors. (b) The corresponding change in the FWHM with different concentration of Pb^{+2} ions. 142

Figure 6.1: Two-color SPR nanosizer in the Kretschmann configuration. The thickness of the nanocomposite layer t_{eff} is considered equal to the statistical mean diameter of the AuNPs [143]. 146

Figure 6.2: (a) TEM image of the AuNPs and (b) AFM image on $1 \mu m \times 1 \mu m$ region. The inset of the images show the statistical AuNPs size distribution obtained using (a) TEM and (b) AFM microscopy over a set of 400 data points. (c) Comparison between the experimental (open grey circles) and theoretical (continuous black line) extinction spectra of the colloidal dispersion of AuNPs in water [143]. 147

Figure 6.3: (a) Experimental SPR minimum angle profiles at λ_1 (black) and λ_2 (grey) before (open circles) and after (fill circles) the AuNPs. The

observed SPR angle shift are $\Delta\theta_{\lambda_1} = 0.0471^\circ$ and $\Delta\theta_{\lambda_2} = 0.0186^\circ$. (b) Curves of the possible values in the plane $\epsilon_{\text{eff}} \text{ Vs } t_{\text{eff}}/2$ at the wavelengths λ_1 and λ_2 . The intersection point of the curves represents the real value, obtained by shifting the curves using the parameter $Q_{\lambda_1, \lambda_2} = 1.266$ calculated from Equation (2.88) [143]. 149

Figure 6.4: Curves in the plane $\epsilon_{\text{eff}} \text{ Vs } \langle r \rangle = t_{\text{eff}}/2$ corresponding to a variation $\delta\epsilon_r$ of the dielectric constant of the thin layer of gold supporting the plasma wave. (a) + 0.5%, (b) – 0.5%. The experimental accuracy in the determination of the main radius by SPR spectroscopy is $\pm 0.5 \text{ nm}$, corresponding to $\Delta r_{\text{experimental}} \approx 7\%$.) [143]. 150

Figure 6.5: (a) Percentage deviation $\Delta r_{\text{density}}$ between the value $\langle r \rangle_{\text{TEM}}$ and the value of the average radius $\langle r \rangle_{\text{SPR}}$ obtained by the application of the two-color method depending on σ . (b) Percentage deviation $\Delta r_{\text{dispersion}}$ between $\langle r \rangle_{\text{log-normal}}$ and $\langle r \rangle_{\text{SPR}}$ obtained by the application of the two-color method depending on the relative radius standard deviation $\delta_{\text{rel}} = (\delta_{\text{log-normal}}/\langle r \rangle_{\text{log-normal}})$ [143]. 151

Figure 6.6: Theoretical behavior of SAM of monodisperse AuNPs with same optical density $\tau \approx \tau_{\lambda_1}$. (a) Surface density $\sigma(r)$ (black points, left Y-axes) and mass surface density of gold $\sigma_{\text{mass}(r)}$ expressed in $\text{ng}/\mu\text{m}^2$ (grey circles, right Y-axes) in function of the radius r of the AuNPs. (b) Shift of the angle of resonance $\Delta\theta(r)$ at both the excitation wavelengths λ_1 (black points) and λ_2 (grey circles) after the deposition of the associated mass surface density of gold $\sigma_{\text{mass}(r)}$. The dashed horizontal red-line is set in correspondence of $\Delta\theta_{\text{SPR}} = 0.01^\circ$ [143]. 155

Figure 6.7: (a) Theoretical and experimental monomodal SPR curves of TFT method at wavelength of 633nm. The gray closed and open circles corresponds to the experimental SPR curve of nominal thickness of $t_1 = 16\text{nm}$ and $t_2 = 32\text{nm}$ respectively. (b) The set of possible values of ϵ_{Alq_3} and t_{Alq_3} of Alq_3 collected over the TFT sample. With the knowing values of the ratio between the thickness t_1 and t_2 , the intersection point gives the actual value of the Organic thin film. 157

Figure 6.8: Theoretical and experimental monomodal SPR curves at wavelength of 783nm. 157

Figure 6.9: (a) Theoretical and experimental SPR curves of dual mode method. The closed and open circles correspond to the experimental SPR curve of at wavelength of 633nm and 783nm respectively. (b) The set of possible values of ϵ_{Alq_3} and t_{Alq_3} of Alq_3 collected over the sample at the wavelength of 633 nm. The intersection point gives the actual value of the organic thin film. 159

Figure 6.10: (a) Theoretical and experimental SPR curves of dual mode method for $\text{Eu}(\text{dbm})_3\text{phen}$ characterization. The closed and open circles correspond to the experimental SPR curve of at wavelength of 633nm and 783nm respectively. (b) The set of possible values of $\epsilon_{\text{Eu}(\text{dbm})_3\text{phen}}$ and $t_{\text{Eu}(\text{dbm})_3\text{phen}}$ of $\text{Eu}(\text{dbm})_3\text{phen}$ collected over the sample near to the resonance of each mode. 160

Figure 6.11: (a) The experimental SPR curves of the DLWGs structure with $\text{Eu}(\text{dbm})_3\text{phen}$ as organic thin film, before and after UVA radiation at wavelength of 633nm. The inset show the observable shift in the resonance angles after the organic thin film modification. (b) Application of dual mode analysis method before and after UVA treatment. 162

Figure 6.12: (a) Raman spectra of graphene on copper (black) and after transfer on gold (red) and silver (blue) thin films via PU route [92]. (b) SPR curve of bare gold and typical graphene protected gold device. The inset shows the values of the thickness and optical constants of gold and graphene used for the calculus of the theoretical fit [100]. 163

Figure 6.13: The experimental SPR curves collected on DLWGs structure for TM polarization mode with and without graphene layers at (a) $\lambda_1 = 633\text{nm}$ and (b) $\lambda_2 = 783\text{nm}$ 166

Figure 6.14: The experimental SPR curves collected on DLWGs structure for TE polarization mode with and without graphene layers at (a) $\lambda_1 = 633\text{nm}$ and (b) $\lambda_2 = 783\text{nm}$ 166

List of tables

Table 2.1 Calculated values of plasma frequency ω_p , damping constant Γ and Fermi velocity V_F of nobles metals.	38
Table 2.2: The optical parameter of prism, Au and bulk layer collected at wavelength of 783nm using Winspall software through best curve fitting.	60
Table 2.3: Optical parameters of each layer used in dual mode DLWG method.	64
Table 4.1: Average Roughness (RA) of freshly and aged metal layers (Ag, Au) deposited on glass slide surface, with and without MPTS adhesive layer. Similar results have been obtained analyzing different regions of the samples.	104
Table 4.2: Optical parameters of DLWGs structure obtained at 633nm.	114
Table 4.3: Optical parameters of different layers used to calculate the electric field distribution of MPTS/Au and Cr/Au SPR sensors.	116
Table 5.1: Exponential functions and values of the parameters used to fit the dependence of the variation of the refractive index (Δn) and PL (I/I_0) on the UVA dose for both organic materials.	127
Table 5.2: The dielectric constant and thickness of gold and SiO_2 obtained from the fitting of SPR curves before the injection of AuNPs.	133
Table 5.3: The calculated interaction parameters of neutral and charged Hg specie on infinite graphene [87].	136
Table 5.4: Experimentally calculated values of sensitivity and LoD. The SD and $\Delta\theta_{\text{HM}}$ were measured from figure 5.14.	138
Table 5.5: Comparison of some of the reported graphene-based sensors for Hg^{+2} ions detection.	139
Table 5.6: The Langmuir parameters obtained from the fitting of different sensors used for the detection of Hg^{+2}	140
Table 5.7: Experimentally calculated values of sensitivity and LoD. The SD and $\Delta\theta_{\text{HM}}$ were measured from figure 5.14.	142

Table 6.1: Mean value $\langle r \rangle$ and standard deviation δ of the statistical distribution of radius of the citrate stabilized AuNPs measured using different experimental techniques.....	147
Table 6.2: Experimental values of the optical parameters of the SPR sensing platform obtained using section 2.6.2. The refractive index of water and SF4 were taken from [144].	148
Table 6.3: Thickness and dielectric constant of Au thin before the deposition of Alq ₃	156
Table 6.4: Comparison of the real part of refractive index of Alq ₃ calculated at 633nm and 783nm using in this work and other characterization techniques.....	158
Table 6.5: The thickness and dielectric constant of Au and SiO ₂ obtained using Winspall free software.....	159
Table 6.6: The thickness and dielectric constants of Au and SiO ₂ determine by Winspall at two wavelengths before the deposition of organic materials	160
Table 6.7: The calculated optical parameters of each layer in the BK7/Au/SiO ₂ /Eu(dbm) ₃ phen structure before and after irradiation with UVA light.....	161

List of Abbreviation

Alq ₃	Tris(8-hydroxyquinoline)
APTS	3- Aminopropyltriethoxysilane
Au	Gold
Ag	Silver
AuNPs	Gold nanoparticle
DLWGs	Dielectric Loaded Waveguides
EM	Electromagnetic field
Eu(dbm) ₃ Phen)	tris(dibenzoylmethane)mono(1,10-phenanthroline)
europium(III)	
FWHM	Full Width Half Maximum
HM	Half Maximum
Hg ⁺²	Mercuric ion
LoD	Limit of detection
MPTS	3-Mercaptopropyltrimethoxysilane
OLED	Organic Light Emitting Diode
Pb ⁺²	Lead (II) ion
RIU	Refractive Index Unit
SLG	Single Layer Graphene
SPP	Surface Plasmon Polariton
SPR	Surface Plasmon Resonance
TE	Transverse Electric
TM	Transverse Magnetic

1 Introduction

1.1. Plasmonics

The ideas and concepts behind nanotechnology traced back to a classical talk given by quantum physicist Richard Feynman in 1959 entitled “There is a plenty of room at the bottom” [1] where he acknowledged the possibility of manipulating the materials down to the level of individual atoms for technological purposes. He invited his listeners to open a new field of physics. Over a decade later, the term nanotechnology was coined by Professor Norio Taniguchi [2] and soon after the remarkable progress in nanotechnology it became a reality with the development of Scanning Tunneling Microscope (STM) in 1981[3], which visualize and manipulate particles at the atomic scale. Owing to the fundamental law of diffraction of light, dielectric media cannot localize the Electromagnetic Waves into nanoscale regions smaller than the wavelength of light [4]. However, the unprecedented ability of nanometallic structures to squeeze light into deep subwavelength volumes break the diffraction limit and led to a new branch of photonics known as plasmonic [5, 6].

One of the first application of plasmonic date back to the Roman Empire (4th century AD), who empirically developed methods to add a small inclusion of metal nanostructures in stain glass for vibrant colors without a full understanding of the physics behind it. The Lycurgus cup in the British Museum is the famous example of the first known metamaterial consists of a mixture of silver and gold nanoparticles (AuNP) embedded in ruby glass. The plasmonic resonance induced in the metal nanoparticle offered the cup vibrant colors, appearing red with light transmitted through glass but give green color when viewed in reflected light as shown in the Figure 1.1.

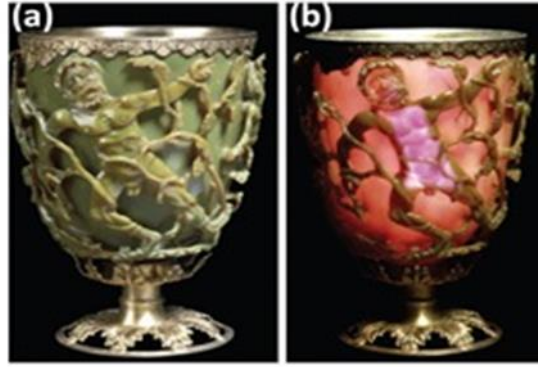


Figure 1.1: The Roman Lycurgus cup made of mixture of silver and AuNPs embedded in ruby glass viewed (a) green in reflected light but (b) red in transmitted light Copyright of the British Museum.

Nowadays, plasmonic is an emerging science and hot research area of nanophotonic that aims to exploit the nanoscale interaction between electromagnetic fields and free electrons in metal nanostructure, thus providing a way to manipulate the light below the diffraction limit with a remarkable enhancement of the local electromagnetic field (EM) [6]. This nanometer scale coupling between a photon energy (light) and a free electron gas (matter) creating a subwavelength oscillating mode, is known as Surface Plasmon Resonance (SPR) which can either propagate along a planar interface (surface plasmon polaritons, SPP) or be confined on a subwavelength metallic nanostructure (localized surface plasmon resonance, LSPR). These SPP modes with a penetration depth of more than 100nm (depending on wavelength) into the dielectric are highly sensitive to the physical and chemical changes occurring near to the interface. Such a unique feature lead to the basis of a label free and nondestructive optical technique called, SPR spectroscopy, which has found its use in a broad range of disciplines, including biophysics [7, 8] chemistry [9], energy [10, 11], photonics [12], and life sciences [13,14].

1.2. State of Art of SPR Spectroscopy

The origin of surface plasmon dates back to 1902, when R.M. Wood observed an unusual light and dark bands in the spectrum of light reflected from the metallic diffraction grating, which he termed as Wood anomalies [15]. In 1907 Lord Rayleigh theoretically predicted that the Wood's anomalies correspond to a

wavelength (Rayleigh wavelength) at which a new propagating diffraction order appears from the grating at the grazing angle [16]. However, the Rayleigh approach did not yield the shape of the bands associated with the anomaly due to singularity at the Rayleigh wavelength. In 1938 U. Fano showed that these anomalies are due to the excitation of SPP supported by corrugated dielectric metal interfaces [17]. The existence of surface plasmons was experimentally verified by Ritchie in 1957 [18], considering the diffraction of electrons by thin metals films. In the late 1960's, a major advance was made when Kretschmann, Reather [19] and Otto [20] demonstrated methods for the optical excitation of surface plasmon by visible light using metal thin films via prism-based attenuated total reflection (ATR) configurations, making experiments on surface plasmon accessible to many researchers. In 1977, Pockrand and Swalen [21] used for the first time ATR phenomena for the characterization of organic monolayer on metal films in the visible wavelength, in 1982 Nylander and Liederg [22] applied the surface plasma wave for gas detection and biosensing. SPR sensor technology received a great attention in the early 1990, when Biacore industry launched the first commercial SPR biosensor to determine the specificity, affinity and kinetics parameters during the molecular interactions [23].

Due to its versatility and multidisciplinary nature, the application in optical sensing of SPR spectroscopy became a quite common tool in the last decades, and nowadays SPR biosensors are widely used in pharmaceutical research, food safety, drug screening and environment monitoring [24]. Exploiting different excitation and detection schemes in SPR spectroscopy [25, 26] an outstanding ultimate resolution of the SPR sensors of the order of 10^{-7} RIU has been experimentally demonstrated [27]. In order to further enhance the resolution of the SPR sensors, the attention has been recently focused on the use of alternative sensor surfaces, like hybrid metal-SLG plasmonic layers [28, 29], or gold thin films functionalized with ligands for metal nanoparticles, giving origin to the so called Particle Amplified (PA) – SPR spectroscopy [30]. In the first case, the enhancement of the sensitivity of the optical sensors is attributed to the equilibrium between the work functions of the metal and the SLG (not oxidized), which induces an electron transfer between the two structures, changing the polarizability of the hybrid thin film supporting the plasma wave [28]. In the case of PA-SPR spectroscopy, the enhancement in the sensitivity is due to the big mass that any metal nanoparticle

has in comparison with small molecular analites, and its range of applicability is limited only by difficulties associated to the accurate counting the number of nanoparticles deposited over the external surface of the sensor [31].

Interestingly, SPR spectroscopy has been rarely used for the ellipsometric characterization of thin films, and its use has been limited to the simultaneous measurements of the thickness and refractive index of transparent organic ultra-thin films deposited by self-assembling techniques [21]. The determination of these parameters using classical SPR metal substrate requires two independent sets of measurement on the same thin film sample. The methods reported in literature to achieve this goal are referred as two colors [32], two medium [33] and two-thickness methods [34]. In the first one two measurements are performed using different wavelengths of the electromagnetic radiation incident on the sample for a fixed external medium, while the second one is based on a fixed excitation wavelength and the change of the refractive index of the external medium (gas, liquid).

The calculus of the parameter of the thin film proposed in literature is performed by a simple analytical model, and is mathematically valid only for ultrathin film with a maximum thickness of the order of a few nm [32, 35] Moreover, these techniques can be applied only if the dispersion function of the thin film under investigation is known or the external fluid doesn't induce the degradation of the material like, for example, in the case of the characterization of luminescent organic thin films, for which a new approach called "two film thickness" method has been recently proposed [34]. Thin films of luminescent organic materials are generally analyzed by variable-angle spectroscopic ellipsometry (VASE) both in terms of the accurate measurements of the refractive index and for the investigations of their degradation processes in different environmental conditions [36]. Although the mean accuracy of VASE is about 0.5% but it still has some drawbacks, including the use of complicated model for data analysis, low spatial resolution (spot size: several mm) and the elevated costs [36, 37].

Concerning 2D-materials, S Cheon et al. [38] demonstrated a way to determine the complex refractive index of SLG using two independent measurements based on the detection of SPR angle of a thin gold layer coated with graphene and the detection of the reflection ratio R_p/R_s at critical angle using graphene without gold

layer. In other approach H Jussila et al. [39] studied the SPR based measurement for the simultaneous characterization of thickness and complex refractive index of graphene using multiple wavelength analysis. Both the approaches suffer of a basic assumption, yet not verified experimentally until now, about the isotropy of graphene for polarization parallel and perpendicular to its plane. Moreover, in some of the measurements proposed in literature, the SLG is transferred directly onto the gold thin films, provoking a transfer of electron between the SLG and the metal [28]. This transfer, provokes an alteration of the dielectric constant of the gold thin film, which has not been considered in the analysis of the experimental results reported in [38, 39].

The detection of nanostructured material by SPR spectroscopy in the Kretschmann configuration was boosted in the last years due the utility of PA-SPR spectroscopy in optical sensors [31,40,41]. Anyway, excluding the results presented in this dissertation, there are no reports in literature about the use of SPR spectroscopy in the accurate characterization of nanomaterials, commonly conducted by expensive techniques such as Dynamic Light Scattering (DLS) [42], Transmission Electron Microscopy (TEM) and Atomic Force Microscopy (AFM) [43].

1.3. Objectives

The research proposed in the present dissertation aim to study the potentialities in optical sensing of hybrid metal-graphene SPR devices, to define the limits of application of the PA-SPR spectroscopy, and extend the use of SPR spectroscopy as accurate ellipsometric tool for organic thin films, SLG and nanostructured metal films.

The first objective of the research consists in the fabrication of SPR sensing platforms characterized by low damping of the SPP and a high angular stability in time, comparable with the order of the systematic error introduced in SPR spectroscopy by the determination of the angle of reference [34]. The realization of this objective is based on the understanding of the chemical-physical processes governing the degradation and stabilization of different metal-dielectric interfaces of SPR devices, in different geometrical configurations, and different environmental conditions. The low-damping SPR interfaces guarantee a better

resolution of the optical sensors in terms of refractive index (RI) sensitivity, while an optimal temporal stability of the sensing platform is of absolute importance for the SPR based ellipsometric characterization of the different thin films, which, depending on the application of the sensor, may be time consuming.

The second objective concern with the development of innovative SPR sensors using different kind of nanomaterials as sensing layers, such as SLG, AuNPs and organic thin films, with the possibility to enhance the sensitivity of the sensors by the use of hybrid devices of the type Au/SLG and Au/SiO₂/AuNPs (PA-SPR spectroscopy).

In particular, using the Au/SLG sensing platforms, we want to explore the potentialities of pure infinite graphene in the sensing of metal ions in water solutions, with a specific attention to the Hg²⁺ heavy metal, and the possibility of electron transfer between all the SLG, the Au thin film and the metal ions, with possible reduction process of the latter [44].

Concerning PA-SPR spectroscopy, we want to understand what are the characteristics of the Au/SiO₂/AuNPs SPR devices, which allow the accurate counting of the surface density σ_{AuNPs} of the metal NPs deposited over the glass external surface of the sensor. The accuracy in the determination of σ_{AuNPs} depends on their linear dimension, their actual surface density, the thicknesses of the metal and dielectric thin films constituting the sensing platform, and the correct modeling of the complex dielectric function of the AuNPs, for which the free mean-path electron limitation has to be taken in consideration [31, 45].

We also want to explore the potentialities of SPR spectroscopy in the monitoring of the degradation processes of organic luminescent thin films, with the aim to develop organic material based SPR-UVA dosimeter in the Surface Plasmon Coupled Emission configuration [46].

The second main objective of the thesis is the use of monomodal and multimodal dielectric loaded waveguides (DLWGs) for the accurate ellipsometric characterization (simultaneous measurement of thickness and refractive index) of organic luminescent thin films in nitrogen-protected environment, composite metal-dielectric films with AuNPs and SLG. The objectives of our research are schematized in Figure 1.2.

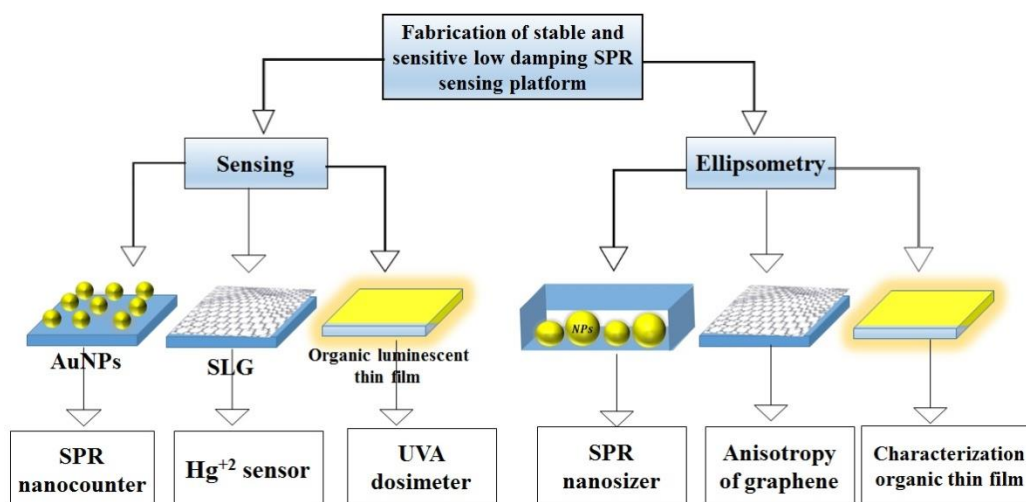


Figure 1.2: Schematic illustration of the main objectives of the proposed research.

1.4. Thesis layout

The thesis is divided into nine chapters. The present chapter deals with the review of the state of art of SPR spectroscopy, its current use, and the main objectives of the presented research.

Chapter 2 presents a brief and comprehensive theoretical background of the fundamental concepts of surface plasmon, where the focus is on the aspects necessary to understand and interpret the experimental results.

Chapter 3 is dedicated to the description of the fabrication process of the monomodal and multimodal (DLWGs) SPR sensing platforms, and the different characterization techniques used for organic luminescent thin films, the AuNPs and the SLGs.

Chapter 4 reports the experimental results on the degradation and stabilization processes of the different metal-dielectric interfaces of the SPR sensing platforms. It also describes the sensitivity and the limit of detection (LoD) of the proposed sensors, before and after the transfer of SLG.

Chapter 5 shows new potentialities of SPR spectroscopy in optical sensing. Herein is shown the experimental proof of principle of an SPR based UVA dosimeter using luminescent organic thin films, the applicability of SPR

nanocounters for AuNPs, and the demonstration of high sensitivity Au/SLG hybrid interfaces for the detection of mercuric ion (Hg^{+2}) in water.

Chapter 6 reports the ellipsometric application of SPR spectroscopy for the characterization of luminescent organic thin film by DLWGs, the application of a two-color SPR nanosizer for AuNPs, and the investigation of the anisotropy of SLG by the use of multimodal DLWGs.

Chapter 7 report the conclusions about the presented research, the experimental work missing in order to complete the research on the Au/SLG sensors, and the future direction of the research in the development of new and functional SPR optical sensors.

Chapter 8 reports a list of the published articles and the conferences attended during the years of my PhD studies.

In the final **Chapter 9**, a comprehensive bibliography is cited to support the conclusions on the research activity performed in the thesis.

2 Theoretical background of plasmonics

In this chapter a short overview of the theoretical basics of surface plasmons is given, where the focus is on the aspects necessary to understand and interpret the experimental results. We will open with a section to discuss the fundamental optical properties of metals using Drude Lorentz model and Maxwell's equations. We will rapidly derive the dispersion relation of SPP on flat metal-dielectric interfaces, and describe the different experimental methods for the simultaneous determination of refractive index and thickness of dielectric thin film.

We will also explore the physics of localized surface plasmon resonance (LSPR), due to the interaction of metal nanoparticles with electromagnetic radiation. We will introduce the quasi-static approximation (QSA), and the well-known Mie theory, used to model the optical cross section of spherical NPs with statistical size distributions, and show how to derive the density and the mass concentration of the NPs by the fit of the experimental UV-Vis extinction spectra.

We introduce the concept of mean free-path electron limitation in the modelling of the dielectric constant of metal NPs, and describe the modified Maxwell-Garnet effective medium theory used for the development of SPR based nanocounters and nanosizers, with their respective limits of applications. We conclude the description of the theory used for the modelling of metal-dielectric nanostructures by introducing the basic concepts about the COMSOL software, which make use of the Finite Element Method (FEM) in order to retrieve the distribution of the EM evanescent fields in the plasmonic devices.

We introduce the concepts and mathematical definition of resolution, sensitivity and limit of detection of SPR sensors, and finally propose a brief introduction about the concepts of PA-SPR spectroscopy and hybrid metal/SLG plasmonic devices. The codes developed in MATLAB language and used to model the extinction cross-section of the NPs are reported in the Appendix A.

2.1. Optical properties of metals

In the optical frequency range, the physical properties of metals can be explained by the Drude model [47, 48] in term of dielectric constant of metals. In this model, the free charge carriers in metals are considered as a free electron gas moving through a fixed frame of positive ion core. The applicability domain of this model depends on the frequency range of electromagnetic radiation that interact with metals. For example, in the case of alkali metals, the validity domain is extending up to ultraviolet region whereas for noble metals interband electron transition takes place in the visible range, and restrict the applicability domain of this model. Furthermore, the effects of inhomogeneous lattice potential and electron-electron interaction are ignored. The electronic band structure and lattice potential are included in effective mass of electron instead of free electron mass. Under an applied external EM field, the electron oscillates and dissipative forces due to collision influence its motion with a characteristic collision frequency $\Gamma = 1/\tau$. The time constant τ is called the relaxation time of electrons and equals 10^{-14} sec by order of magnitude. The equation of motion of electron subjected to uniform EM field can be written as [48]:

$$m_e^* \frac{d^2 \vec{x}}{dt^2} + m_e^* \Gamma \frac{d\vec{x}}{dt} = -e \vec{E}_0 e^{-i\omega t}, \quad (2.1)$$

where m_e^* and e are the effective mass and charge of electron. On right side of the equation, the term $e \vec{E}_0 e^{-i\omega t}$ represent the driving EM force in metal, E_0 and ω are the amplitude and frequency of EM fields. Solving differential Equation (2.1) by using the oscillation of electron $x(t) = x_0 e^{-i\omega t}$ we get

$$\vec{x}_0 = \frac{e \vec{E}_0}{m_e^* (\omega^2 + i\Gamma\omega)}, \quad (2.2)$$

This displacement of electron leads to the density of dipole moments; whose accumulative effects gives rise to macroscopic polarization $P_x = -N_e e x_0$ given by

$$\vec{P}_x = -\frac{N_e e^2 \vec{E}_0}{m_e^* (\omega^2 + i\Gamma\omega)}, \quad (2.3)$$

from definition of displacement field \vec{D} , and its relation with \vec{E} we have

$$\vec{D} = \epsilon_0 \vec{E} + \vec{P}_x, \quad (2.4)$$

$$\vec{D} = \epsilon_0 \epsilon \vec{E}. \quad (2.5)$$

And now the dielectric permittivity of free electron (ϵ_f) plasma is expressed as

$$\epsilon_f(\omega) = 1 - \frac{N_e e^2}{\epsilon_0 m_e^* (\omega^2 + i\Gamma\omega)} = 1 - \frac{\omega_p^2}{\omega^2 + i\Gamma\omega}, \quad (2.6)$$

where $\omega_p = \sqrt{N_e e^2 / \epsilon_0 m_e^*}$ is the plasma frequency of the free electron gas and N_e is the total number of electrons. Separating the real and imaginary part, we get

$$\epsilon_f(\omega) = 1 - \frac{\omega_p^2}{\omega^2 + \Gamma^2} + i \frac{\Gamma\omega_p^2}{\omega(\omega^2 + \Gamma^2)} = \epsilon'(\omega) + i\epsilon''(\omega), \quad (2.7)$$

This expression shows the insightful features about the response of metal to EM field in different frequency regimes. For $\omega > \omega_p$, the $\omega > \Gamma$, resulting to negligible damping ($\Gamma \rightarrow 0$) and equation (2.7) becomes

$$\epsilon_f(\omega) = 1 - \frac{\omega_p^2}{\omega^2}. \quad (2.8)$$

For higher frequencies the ratio $\omega_p^2 / \omega^2 < 1 \Rightarrow \epsilon_f(\omega) > 0$. Here $\epsilon_f(\omega)$ is real and positive, therefore the refractive index $\sqrt{\epsilon}$ is purely real represents the propagation of light wave into metal and behave like a transparent material. For $\omega < \omega_p$, on other hand $\epsilon_f(\omega)$ is real and negative number. Therefore, the complex refractive index $\tilde{n} = \sqrt{\epsilon} = n + i\kappa$ contains only the imaginary component $i\kappa$, which indicates that the light cannot be transmitted through metal and will be strongly reflected. From these results, one can conclude that metals are reflecting low frequency light, but they become transparent at high frequency light. Table 2.1 shows the summary of the Drude model parameters of some common metals used in plasmonic.

Table 2.1 Calculated values of plasma frequency ω_p , damping constant Γ and Fermi velocity V_F of nobles metals.

Metal	ω_p (10^{15}s^{-1})	Γ (10^{15}s^{-1})	V_F (10^6ms^{-1})
Gold	13.8	0.11	1.4
Silver	14.0	0.03	1.4
Aluminium	22.9	0.92	2.0

Although the Drude model is an elegant and concise treatment for the optical properties of metals at higher wavelength (infrared regime), at shorter wavelength

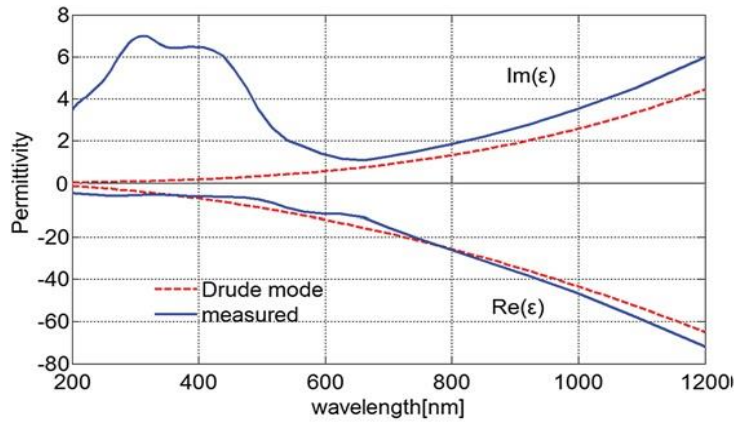


Figure 2.1: Comparison between the permittivity of gold calculated by Drude model (dash line) and the experimental data obtained by Johnson (solid line). The values of damping constant and plasma frequency are listed in table 2.1. The interband transition restrict the validity of Drude model in visible region [49].

(visible range) the assumption of free electron gas is no longer valid due to contribution of bound electrons or interband transition. Figure 2.1 show the calculated dielectric function of gold using the Drude model compared to the widely accepted experimental data obtained by Johnson and Chirsty [50]. It can be seen that the experimental data agree well with Drude theory in infrared wavelengths longer than 650nm, however there is substantial deviation of the measured imaginary part of dielectric function in the visible wavelengths shorter than 650nm. The measured imaginary part increases suddenly than that predicated by the Drude theory. This difference is attributed to the fact that higher energies photons can excite the electrons of lower lying band (d band) into conduction band which have not been taken into account in Drude Model.

To address this, the so-called model of Lorentz can model the contribution of bound electron to the dielectric permittivity of metal, where the electrons are connected to its nuclei by Hooke's law restoring force. Under the action of applied EM field, the equation of motion for bound electrons is given by

$$m_b^* \frac{d^2 \vec{x}}{dt^2} + m_b^* \Gamma \frac{d \vec{x}}{dt} + K \vec{x} = -e \vec{E}_0 e^{-i\omega t} , \quad (2.9)$$

where m_b^* is the effective mass of bound electron and K is the spring constant of a potential that keep the binding. Following the same procedure before, we find the contribution of bound electron to dielectric permittivity of metal:

$$\varepsilon_b(\omega) = 1 - \frac{\tilde{\omega}_p^2}{\omega_0^2 - \omega^2 - i\Gamma_b\omega^2}. \quad (2.10)$$

Here $\tilde{\omega}_p = \sqrt{\tilde{N}e^2/m_b^*\varepsilon_0}$ defines along similar lines to the plasma frequency, \tilde{N} being the density of bound electrons and $\omega_0 = \sqrt{K/m_b^*}$. The composite dielectric permittivity of metals that includes both the free ($\varepsilon_f(\omega)$) and bound electrons ($\varepsilon_b(\omega)$) contributions yields a model known as Drude-Lorentz model which has [51]:

$$\varepsilon(\omega) = 1 - \frac{\omega_p^2}{\omega^2 + i\Gamma\omega} + \sum_j \frac{\tilde{\omega}_{pj}^2}{\omega_{0j}^2 - \omega^2 - i\Gamma_{bj}\omega^2}. \quad (2.11)$$

Here the summation represents the contribution of different interband transitions of electrons.

2.2. From Maxwell's equation to Surface Plasmon Polaritons

Plasmon are quantized collective oscillations of quasi-free electrons in a metal. When these coherent electrons oscillations couple to EM radiation it creates a bound electromagnetic mode that propagate along the metal/dielectric interface, which is called, Surface Plasmon Polariton (SPP). The excitation of SPP by incident light strongly depends on the choice of light polarization and the geometry of the metal surface. Thin films of noble metals such as gold and silver with a thickness of about 50 nm, are widely used to support these SPP modes that have their strong enhancement in the electric field within a few nanometers at surface, and exponentially decaying fields perpendicular to the metal-dielectric interface. The wave vector of SPP strongly depends on the dielectric constants of thin metal film and the adjacent dielectric medium, which resulted in its extensively use for sensing applications. In the following subsections, we summarize the fundamental characteristics of SPP.

2.2.1. Dispersion relation of Surface Plasmon Polariton

The coupling mechanism between EM fields and SPP can be better understood from the dispersion relation, which correlates the space wave vector and permittivity of both the metal and dielectric. The SPP dispersion equation was

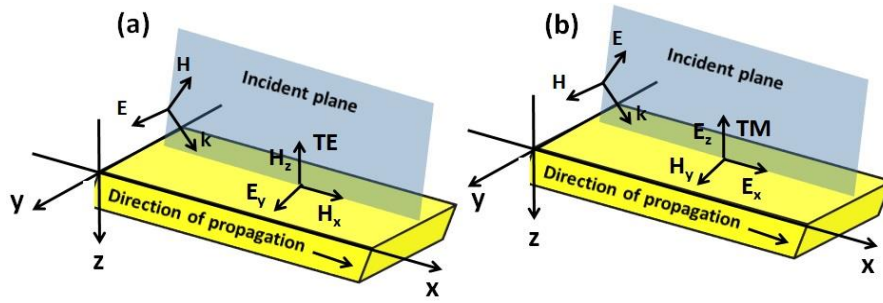


Figure 2.2: Representation of the TE (a) and TM (b) polarized plane wave's incident on a metal dielectric interface. The electric and magnetic field components along x, y, z axis are (a) H_z , E_y , H_x and (b) E_z , H_y , E_x .

derived from the solution of the Maxwell's equations within proper boundary conditions by Reather [25]. Let us consider a single flat interface between dielectric ($z > 0$) with dielectric constant $\epsilon_d(\omega)$ and metal ($z < 0$) described by dielectric constant $\epsilon_m(\omega)$ as shown in Figure 2.2. The interface coincides at $z = 0$, while, $x - z$ plane define the plane of incident where an electromagnetic wave with wave vector k falls onto metal surface. When the magnetic field vector \vec{H} of light is perpendicular to the plane of incidence (right panel), the polarization is called transverse magnetic (TM), whose field components are restricted to \vec{E}_x , \vec{E}_z , \vec{H}_y . On other hand an electromagnetic wave is said to be TE (transverse electric) polarized, when the electric field \vec{E} vector is perpendicular to the plane of incident with field components \vec{E}_y , \vec{H}_z , \vec{H}_x . The interaction of electromagnetic wave with non-magnetic and source free media ($\rho = j = 0$) can be described by Maxwell's equations:

$$\vec{\nabla} \times \vec{E} = -\mu_0 \frac{\partial \vec{H}}{\partial t}, \quad (2.12)$$

$$\mu_0 \vec{\nabla} \cdot \vec{H} = 0, \quad (2.13)$$

$$\vec{\nabla} \times \vec{H} = \epsilon_0 \epsilon \frac{\partial \vec{E}}{\partial t}, \quad (2.14)$$

$$\epsilon_0 \epsilon \vec{\nabla} \cdot \vec{E} = 0, \quad (2.15)$$

where ϵ_0 and μ_0 are the permittivity and permeability of the free space respectively. Here we will derive the dispersion relation for TM polarized (Fig. 2.2(b)) wave, because it only fulfilled the requirement of the normal E field to create a surface charges and hence induced polarization changes at interface [52]. The oscillating

electric field \vec{E} and magnetic field \vec{H} characterized by wave vector k can be expressed as

$$\vec{E}(r, t) = \vec{H}_0(r) e^{i(\vec{k} \cdot \vec{r} - \omega t)}, \quad (2.16)$$

$$\vec{H}(r, t) = \vec{H}_0(r) e^{i(\vec{k} \cdot \vec{r} - \omega t)}, \quad (2.17)$$

applying curl operator to Equations (2.12) and (2.14), we get the following differential equation for TM wave ($\vec{E}_x, \vec{E}_z, \vec{H}_y$)

$$\frac{\partial H_y}{\partial z} = i\omega \varepsilon \varepsilon_0 E_x, \quad (2.18)$$

$$\frac{\partial E_x}{\partial z} - \frac{\partial E_z}{\partial x} = i\omega \mu_0 H_y, \quad (2.19)$$

$$\frac{\partial H_y}{\partial x} = -i\omega \varepsilon \varepsilon_0 E_z, \quad (2.20)$$

the value of wave vector \vec{k} within any dielectric medium is proportional to the refractive index and can be expressed as

$$k_d(\omega) = k_0 n(\omega), \quad (2.21)$$

The refractive index n and dielectric constant ε are related by $\varepsilon = n^2$. Since the incident wave vector k_i is lying in the $x - z$ plane, so it can be written as

$$k_d^2 = (k_x^d)^2 + (k_z^d)^2 = \varepsilon_d k_0^2, \quad (2.22)$$

$$k_m^2 = (k_x^m)^2 + (k_z^m)^2 = \varepsilon_m k_0^2, \quad (2.23)$$

where \vec{k}_m is the transmitted wave vector on the metal side of the interface. The boundary conditions of the electromagnetic fields at $z = 0$ implies that the parallel component of E and H and the perpendicular component of electric flux density D should be continuous at interface, that is $E_x^m(x, 0) = E_x^d(x, 0)$, $H_y^m(x, 0) = H_y^d(x, 0)$ and $\varepsilon_m E_z^m(x, 0) = \varepsilon_d E_z^d(x, 0)$. The three field components $\vec{E}_x, \vec{E}_z, \vec{H}_y$ for TM wave on both sides of the interface can be calculated by substituting the electric field (Eq. 2.16) and magnetic field (Eq. 2.17) expressions into differential Equations (2.18) and (2.20). Now applying the boundary conditions, we find the relationship between the normal components of the wave vectors and dielectric constants in two media given by

$$k_x^d = k_x^m = k_x = k_{SPP}, \quad (2.24)$$

$$\frac{k_z^d}{\varepsilon_d} = \frac{k_z^m}{\varepsilon_m}, \quad (2.25)$$

from Equations (2.22) and (2.23) we can write:

$$\frac{(k_z^m)^2}{(k_z^d)^2} = \frac{\varepsilon_m k_0^2 - (k_x^m)^2}{\varepsilon_d k_0^2 - (k_x^d)^2}. \quad (2.26)$$

In terms of equations (2.24), (2.25) and (2.26) we can express the dispersion equation of SPP as

$$k_{SPP} = k_x = k_0 \sqrt{\frac{\varepsilon_d \varepsilon_m}{\varepsilon_d + \varepsilon_m}} = k'_{SPP} + ik''_{SPP}. \quad (2.27)$$

where k'_{SPP} and k''_{SPP} are the real and imaginary parts of the wave vector of SPP. The expression for the normal component of wave vector can also be obtained by replacing (2.27) in (2.22), we get

$$k_z^j = k_0 \sqrt{\frac{\varepsilon_j^2}{\varepsilon_m + \varepsilon_d}}, \quad j = m, d \quad (2.28)$$

To obtain a bound propagating SPP mode, the normal component of the \vec{k}_z should be purely imaginary, giving rise to an evanescent wave which decays exponentially on both sides of the interface. This condition is satisfied only if $\varepsilon_m + \varepsilon_d < 0$ and if the real part of the dielectric constant ε'_m (Eq.2.7) in the metal is negative [53]. In Figure 2.3, it is shown that evanescent fields associated with SPP decaying in the direction perpendicular to the metal-dielectric interface is related to the confinement factors,

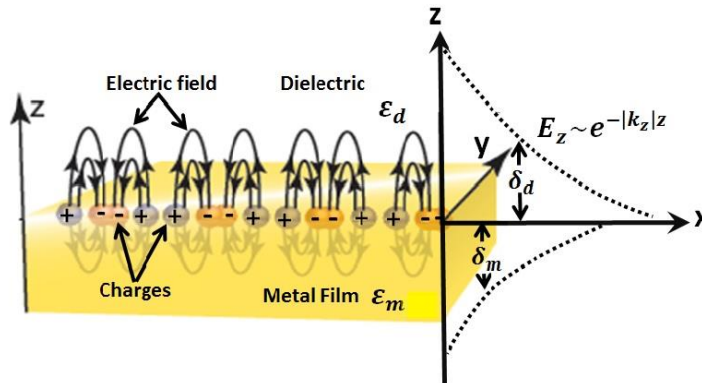


Figure 2.3: Schematic picture of surface plasmon oscillations propagating along a metal-dielectric interface. The electric field in the dielectric medium and electrical charges moving in the plasma at metal surface. Right hand side show the SPPs field perpendicular to the interface decay exponentially and characterized by the penetration depths (δ_m, δ_d) in both side of the media.

defines as the distance from the interface at which the amplitude of the field falls to $1/e$ [52]:

$$\delta_m = 1/k_z^m = \frac{\lambda}{2\pi} \left| \frac{\epsilon_m + \epsilon_d}{\epsilon_d^2} \right|^{\frac{1}{2}}, \quad (2.29)$$

$$\delta_d = 1/k_z^d = \frac{\lambda}{2\pi} \left| \frac{\epsilon_m + \epsilon_d}{\epsilon_m^2} \right|^{\frac{1}{2}}. \quad (2.30)$$

Moreover, if $|\epsilon'_m| > \epsilon''_m$, the complex propagation wave vector of surface plasmon can be expressed in term of real and imaginary part

$$\begin{aligned} k_{\text{SPP}} &= k'_{\text{SPP}} + ik''_{\text{SPP}} \\ &= \frac{\omega}{c} \sqrt{\frac{\epsilon'_m \epsilon_d}{\epsilon'_m + \epsilon_d}} + i \frac{\epsilon''_m}{2(\epsilon'_m)^2} \frac{\omega}{c} \left(\frac{\epsilon'_m \epsilon_d}{\epsilon'_m + \epsilon_d} \right)^{\frac{3}{2}}. \end{aligned} \quad (2.31)$$

The real part \vec{k}'_{SPP} determines the wavelength of the SPPs via $\lambda = 2\pi/\vec{k}'_{\text{SPP}}$, whereas the imaginary \vec{k}''_{SPP} is associated with the damping or attenuation of surface plasmon. This damping of SPP is characterized by the propagation length (L), which is define as the distance after which the energy of SPP decreases by a factor of $1/e$ [54]:

$$L = 1/2[i\vec{k}''_{\text{SPP}}]. \quad (2.32)$$

In table 2.1, the values of the propagation length and penetration depth are listed for different metal/air interface.

Table 2-1: Comparison of the skin depth of SPP between gold and silver on both side of the metal dielectric (air) interface at two different wavelengths .The value of propagation length are also given.

Metal layer	Silver		Gold	
Wavelength (nm)	630	850	630	850
Propagation Length (μm)	19	57	3	24
Skin depth in metal(nm)	24	23	29	25
Skin depth in dielectric(nm)	219	443	162	400
Concentration of field in dielectric (%)	90	95	85	94

Assuming the free electron gas model of metals with negligible damping with lossless metal permittivity given by

$$\varepsilon_f(\omega) = 1 - \frac{\omega_p^2}{\omega^2}, \quad (2.33)$$

It can be seen that the metal dielectric constant become negative, when the light frequency is smaller than SPP frequency ($\omega < \omega_p$). This condition confirms that a metallic surface is necessary for the propagation of SPP. Figure (2.4) show the graphical representation of the dispersion relation (2.27) which is obtained by putting Eq. (2.33) in Eq. (2.27). For small frequency (small value of wave vector) the dispersion of SPP closely follow the light line and at these frequencies the SPP has minimal longitudinal character, and weakly bound to the interface. Nevertheless, when the frequency increases the dispersion relation of SPP moves away from the light line and at a certain frequency (ω_{SP}), the wave vector of SPP approach to infinity $\vec{k}_{SPP} \rightarrow \infty$. This frequency is called the characteristic surface plasmon frequency:

$$\omega_{SP} = \frac{\omega_p}{\sqrt{1 + \varepsilon_d}}. \quad (2.34)$$

At this particular frequency, the mode becomes tightly bound to the surface and more closely resemble a pure surface plasmon. It is clear that the dispersion curve lies right of the light line, which indicate that the surface plasmon have longer wave vector than light waves, therefore the incident light cannot provide the correct wave vector to excite the SPP due to wave vector difference as shown in Figure 2.4. In other word the momentum of free space photon ($\hbar\vec{k}_0$) is smaller than that of SPP ($\hbar\vec{k}_{SPP}$), which results a momentum mismatch between the light and SPP.

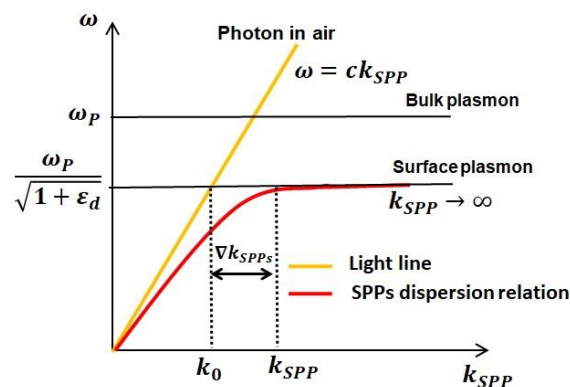


Figure 2.4: Dispersion relation of SPP propagating along interface between dielectric and Drude metal with no damping. Light line (orange) represents the dispersion of light wave in free space, while the red line shows the dispersion of SPP.

2.3. Excitation of Surface Plasmon Polariton

According to the dispersion relation discussed in previous section, the coupling between EM field and electrons results an increase in the SPP momentum as compared to free space due to which it is difficult to directly excite the SPP. However, for a given frequency the SPP can be efficiently excited if the both the energy and momentum conservation are fulfilled:

$$\vec{E}_{exc} = \vec{E}_{SPP} \Leftrightarrow \omega_{exc} = \omega_{SP} , \quad (2.35)$$

$$\hbar\vec{k}_{exc} = \hbar\vec{k}_{SPP} . \quad (2.36)$$

where \vec{E}_{exc} , ω_{exc} and \vec{k}_{exc} are the excitation energy, frequency and wave vector of the light in free space. The momentum mismatch can be achieved via different techniques such as prism coupling, grating coupling and charged particle impact [47]. Among these, the prism coupling is the most common used technique for SPR excitation, which will be discussed here in detail.

2.3.1. Prism coupling

The first experimental technique to provide an additional momentum by using a high index prism for SPP excitation were developed by Otto [20], Raether and Kretschmann in 1968 [19]. In literature two types of prism coupling have been proposed referred as Otto and Kretschmann configuration [55]. In Otto configuration, the evanescent wave tunneling occurs through the air gap (few hundred nm) between the prism/air and metal/air interfaces. In Kretschmann configuration the momentum matching to SPP can be achieved in a three-layer system consisting of a thin metal (ϵ_m) sandwiched between high index prism (ϵ_p) and dielectric medium (ϵ_d) as sketched in Figure 2.5(a). In this geometry a TM polarized electromagnetic wave is illuminated on thin metal film through an optically dense prism at an angle of incidence θ_{inc} . At certain incidence angle larger than the critical angle, the in-plane wave vector (k_x) of light in the prism match with the wave vector of SPP (k_{SPP}) which give rise to the excitation of SPP.

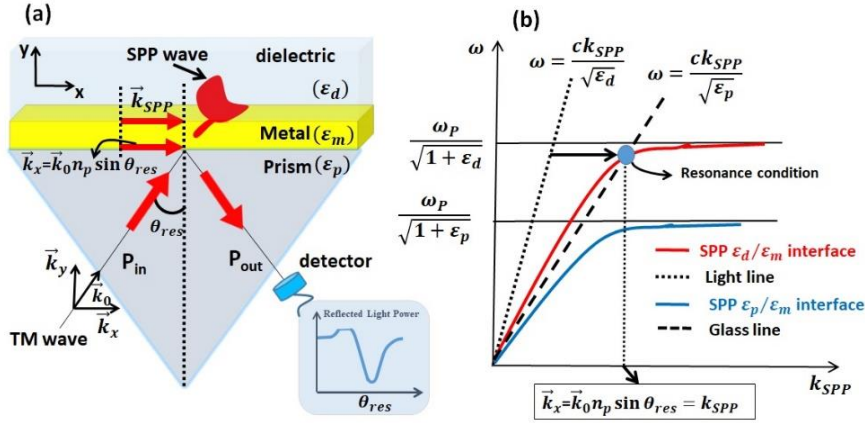


Figure 2.5: (a) Excitation of SPP in Kretschmann -Raether configuration. (b) Dispersion relations for SPPs modes in Kretschmann - Raether configuration.

Figure 2.5 (b) rather presents a simple interpretation, where the dispersion curve for the parallel component of light in glass prism (black dashed line) have a maximum wave vector greater than in dielectric region and, hence able to intersects the SPP dispersion curve (red line) of metal dielectric interface. The physical meaning of this intersection is the strong coupling between light and SPP, which according to Kretschmann configuration occurs at a certain incident angle called the resonance angle for which, the following relation takes hold:

$$\vec{k}_x = \vec{k}_{SPP} , \quad (2.37)$$

$$\vec{k}_0 n_p \sin \theta_{res} = \vec{k}_0 \sqrt{\frac{\epsilon_m n_d^2}{\epsilon_m + n_d^2}} , \quad (2.38)$$

where n_p and n_d are the refractive index of the prism and the dielectric medium respectively, \vec{k}_0 is the free space vector. The excitation of SPP show up a dip in the reflectivity ($R = P_{out}/P_{in}$) curve corresponding to the so called attenuated total reflection (ATR). The Kretschmann-Raether geometry will be widely used throughout this work, so it is important to discuss the parameters that influence the reflectivity curve.

Figure 2.6 summarize the dependence of the TM polarized reflectivity of SPR curve on metal film thickness, wavelength and the refractive index of external medium. The thickness of the metal is the most sensitive parameter as can be clearly seen in Figure 2.6 (a). The depth of the reflectivity curve is decreasing by increasing the thickness of metal and reach to a value of zero for a certain thickness. Moreover,

the full width half maximum (FWHM) of the SPR curve becomes narrow as the thickness is increasing. For small metal thickness the wave vector of SPP suffer a perturbation due to sensing the high refractive index of the prism and shifted by an amount Δk [21, 44]:

$$\vec{k}_r = \vec{k}_{spp} + \Delta\vec{k}. \quad (2.39)$$

This additional term $\Delta\vec{k}$ can accounts both the internal damping as well as the radiation damping. In internal damping, the electric field intensity of the evanescent wave is attenuated by the metal film via Joule heating. Therefore, the metal film is so thin enough such that the evanescent wave is able to excite the SPP at metal dielectric interface. The radiation damping can be thought as the transformation of SPP to light, which is possible only when the metal is thin enough so that the

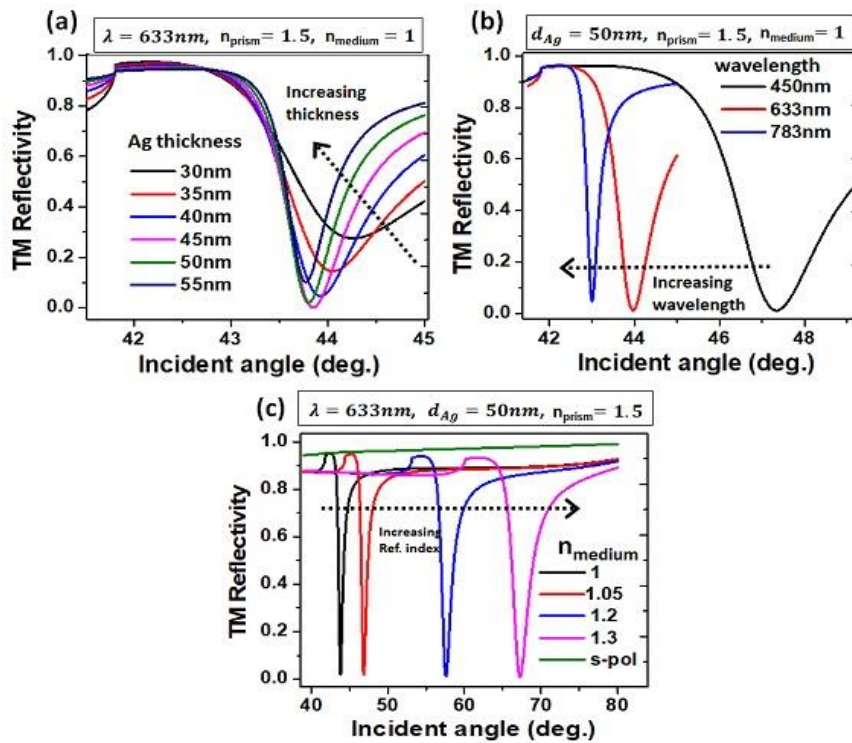


Figure 2.6: Excitation of SPP in Kretschmann configuration. The TM reflectivity curves with variation of (a) silver thickness, (b) wavelength λ and (c) refractive index of external medium. The refractive index of prism is 1.5 and the optical constant of silver are taken from Johnson [50].

Simulation were obtained using Winspall free software [56].

electromagnetic field of the SPP contact the prism medium. Moreover, the imaginary part of Δk is related to the thickness of the metal and the presence of

prism, while the real part causes the displacement of the resonance position. The analytical expression of reflected intensity for the three layer media close to the angle of resonance can be written as [55]:

$$R = 1 - \frac{4\text{Im}(k_{spp})\text{Im}(\Delta k)}{n_p^2 k_0^2 (\sin \theta_{inc} - \sin \theta_{res})^2 + \text{Im}(k_r)^2}, \quad (2.40)$$

in case of minimum reflectivity $\theta_{inc} = \theta_{res}$, Equation (2.40) can be written as

$$R_{min} = 1 - \frac{4 \text{Im}(k_{spp})/\text{Im}(\Delta k)}{(1 + \text{Im}(k_{spp})/\text{Im}(\Delta k))^2}. \quad (2.41)$$

It is clear from above equation that on resonance, the reflected intensity is zero when the inner (Ohmic) and radiation damping have the same value. The ratio $\text{Im}(k_{spp})/\text{Im}(\Delta k)$ depends on the thickness and the optical constant of the metal.

Figure 2.6(b) show the dependence of the wavelength on the SPR reflectivity curve for a fixed Ag thickness (50nm), prism (BK7) and external medium (air). It can be seen that a smaller wavelength excites the SPP at larger resonance angle. In addition, the SPR curve are also broader for small wavelength due to larger internal damping. The influence of the refractive index of the external medium is displaced in Figure 2.6 (c). It is clear to see that for a small change in the refractive index of external medium a significant shift in the SPR angle can be observed, which promise the development of a sensor. For comparison, it is shown that the s-polarized wave cannot excite the SPP and has a large reflectivity over the completely angular range.

2.4. Surface Plasmon Resonance Sensors

2.4.1. Working principle of SPR sensors

Surface plasmon polariton, propagating at metal-dielectric interface is extremely sensitive to probe variation in the refractive index of the dielectric medium because its vast portion of field is penetrating into the dielectric region. A small refractive index variation of the dielectric layer give rise to a change in the propagation constant of the SPP (k_{spp}) wave and hence alters the coupling condition between SPP and light. This property of SPP propagation constant is the fundamental principle of SPR based optical sensors which can be measured by changing some characteristics of light interacting with SPP wave [57]. The

variation in k_{SPP} can be related to the change in the optical properties of dielectric layer using the perturbation theory [26, 57]. According to this theory, any refractive index change (Δn) within the penetration depth of SPP field produce a change in the real part of k_{SPP} through the relation: $Re\{k_{SPP}\} \cong k_0 \Delta n$, where k_0 is the free space wave number.

Depending on which light characteristic is modulated by the change in the propagation constant, SPR sensors can be classified as sensors with angular, wavelength, intensity or phase modulation [26]. In angular modulation based SPR sensors, the SPP are excited with a monochromatic light wave at different angles of incidence [58]. The coupling strength between the tangential component of incident light and SPP wave vector is observed as a dip in the reflected light that can also determine the resonance angle, which yields the strongest coupling. This resonance angle is used as a sensor output as shown in Fig. 2.7(a) [upper plot]. In wavelength modulation, a surface plasmon is excited by a collimated light containing different wavelength at fixed angle of incidence. Among this broadband spectrum, only one wavelength will couple to SPP and the reflected light will therefore show an absorption dip at this wavelength, called resonance wavelength. The resonance wavelength gives the strongest coupling and used as a sensor output as shown in Figure 2.7 (b). In phase modulation, the shift in phase of the light interacting with SPP is measured at fixed wavelength and angle of incidence as shown in Fig. 2.7(a) [lower plot].

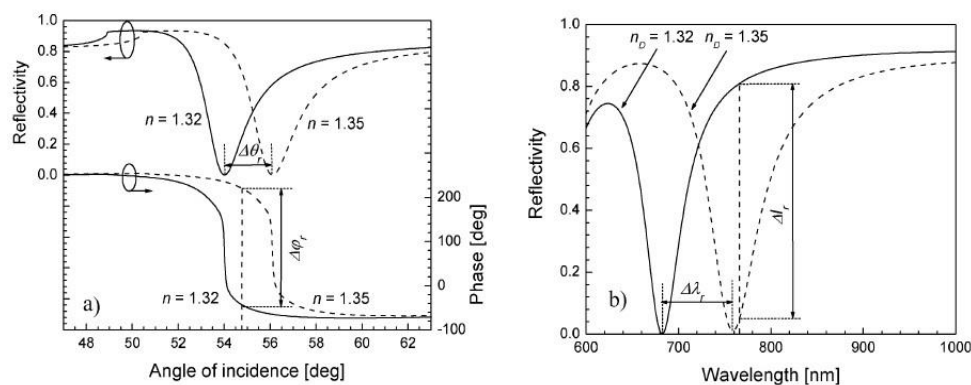


Figure 2.7: Reflectivity and phase for light wave exciting an SPPs in Krestchmann geometry (SF14 glass prism -50 nm thick gold layer-dielectric) versus (a) the angle of incidence for two different refractive indices of the dielectric (wavelength 682nm), and (b) wavelength for two different refractive indices of the dielectric (angle of incidence 54°) [57].

2.4.2. SPR affinity biosensor

Figure 2.8 sketched the basic components of SPR affinity biosensor which consist of bio recognition elements (i.e. antibodies or ligand) which are immobilized on the metal surface that can recognize and interact with selected analyte. Due to the binding between ligand and analyte a change in the refractive index (Δn) of the sensing layer is induced which consequently modify the propagation constant of SPP wave. This binding event on the recognition layer can be observed in real time by continuously monitoring the shift in SPR angle or wavelength as illustrated in Figure 2.7. The main advantage of SPR biosensor is its label free optical detection without using any labeling such as fluorescent molecules. The first SPR sensor was demonstrated for the gas sensing [22] and then its application has been found in various fields of health and biological sciences [59, 60] as well as for the measurement of optical constant [61].

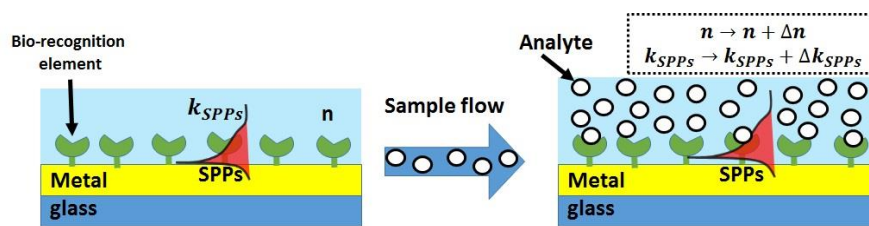


Figure 2.8. Conceptual illustration of SPR sensor operation. The interaction of selected analyte by bio-recognition element change the SPP propagation constant.

2.4.3. Performance Parameters of SPR sensors

There are several different parameters to describe the performance of the SPR sensors during the measurement and detection. The most frequently used parameters for the qualitative analysis of SPR sensors are the sensitivity and the limit of detection (LoD), which will be discussed in this section.

2.4.3.1. Sensitivity

The sensor sensitivity is the main characterizing parameter of a SPR sensor that determines the extent of detectable minute changes in the sensing layer. It is defined as the ratio of the change in sensor output (angle of incidence, wavelength, phase, intensity, polarization) to the change in the quantity to be measured (measurand). The sensitivity of SPR biosensor can be written into two components- refractive index (RI) sensitivity (S_{RI}) produced by the sensor output (shift in angle or wavelength) with the change in the refractive index profile (n_a) of the analyte and the Efficiency E, derived from the refractive index change caused by the binding of target moiety at concentration c [26];

$$S = \frac{\partial Y}{\partial c} = \frac{\partial Y}{\partial n_a} \frac{\partial n_a}{\partial c} = S_{RI} E , \quad (2.42)$$

here Y is the sensor output which could be the angular modulation ($\partial\theta_{SPR}$), wavelength modulation ($\partial\lambda_{SPR}$), intensity (∂R_{SPR}) and phase modulation ($\partial\varphi_{SPR}$). Furthermore, the RI sensitivity can also be decomposed into two contributions [26]:

$$S_{RI} = \frac{\partial Y}{\partial n_{ef}} \frac{\partial n_{ef}}{\partial n_a} = S_{RI1} S_{RI2} . \quad (2.43)$$

Where n_{ef} is the effective refractive index of surface plasmon. The first term represents the instrumental contribution to sensitivity and principally depends on modulation approach and the excitation method of surface plasmon. While the second term refers to the sensitivity of the effective index of SPP with the change in the refractive index. In order to calculate the sensitivity of the effective index with change of the refractive index (∂n_a), here we will discussed the two limiting cases: (i) the variation in the refractive index of dielectric medium (∂n_a) is uniform all along the extension of EM field of SPP as shown in Fig. 2.9(b). (ii) The ∂n_a occurs within a short distance h from the sensor surface as shown in Fig. 2.9(c). The first case is called the bulk refractive index sensitivity (S_B) of the effective index of SPP, which is always larger than the sensitivity of the free space wave in infinite dielectric medium due to the fact that $n_{ef} > n_a$.

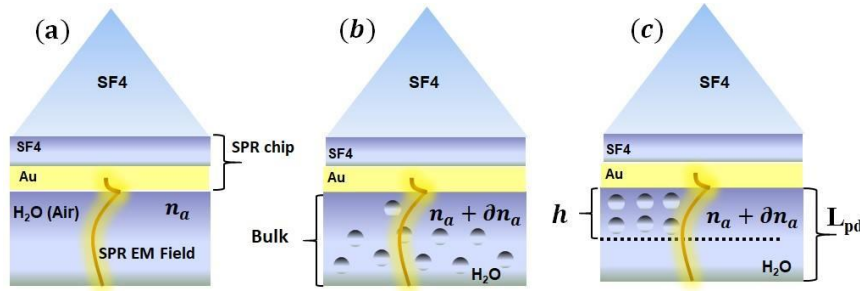


Figure 2.9: Representation of SPR sensor in Kretschmann configuration (a) before analyte deposition (injection) and after analyte binding with sensor surface by changing the (b) bulk refractive index and the (c) surface refractive index near the interface.

Mathematically the sensitivity of the perturbed SPP at metal dielectric interface can be expressed as [26]:

$$S_B = \left(\frac{\partial n_{ef}}{\partial n_a} \right)_B = \left(\frac{\epsilon'_m}{\epsilon'_m + n_a^2} \right)^{\frac{3}{2}}. \quad (2.44)$$

As we can see that, the sensitivity depends upon the real part of the metal dielectric constant (ϵ'_m). For the second case, the sensitivity of effective index of surface plasmon to the variation of surface refractive index happens near to the interface at a distance h from the surface and can be written as:

$$S_S = \left(\frac{\partial n_{ef}}{\partial n_a} \right)_S = \left(\frac{\partial n_{ef}}{\partial n_a} \right)_B \frac{2h}{L_{pd}}, \quad (2.45)$$

here S_S represents the surface sensitivity. With the assumption that h is much smaller than the penetration depth of SPPs (L_{pd}). By substituting Eq. (2.44) into Eq. (2.45) we get:

$$S_S = \left(\frac{\partial n_{ef}}{\partial n_a} \right)_S = \left(\frac{\epsilon'_m}{\epsilon'_m + n_a^2} \right)^{\frac{3}{2}} \frac{2h}{L_{pd}}. \quad (2.46)$$

Equation (2.46) suggest that the surface refractive index sensitivity is proportional the thickness h and is inversely related to the penetration depth of SPP. The sensitivity of an SP sensor is usually measured in refractive index units (RIU). The expression for the angular sensitivity in the Kretschmann configuration can be obtained by differentiating the dispersion relation of SPP (Eq.2.38) in θ and n_a [62]:

$$S_{\theta} = \frac{d\theta}{dn_d} = \frac{\varepsilon'_m \cdot \sqrt{-\varepsilon'_m}}{(\varepsilon'_m + n_d^2) \cdot \sqrt{\varepsilon'_m(n_d^2 - n_p^2) - n_d^2 \cdot n_p^2}} \quad (2.47)$$

Here n_p is the refractive index of prism. From Eq. (2.47), it is clear that the sensitivity mainly depends on the type of metal layer, prism index and the analyte refractive index.

2.4.3.2. Resolution

The SPR sensor resolution, also known as the refractive index uncertainty is the ratio of the standard deviation of noise of the sensor output (σ_{SO}) to the bulk refractive index sensitivity (S_B) and can be written as [26]:

$$\sigma_{RI} = \frac{\sigma_{SO}}{S_B} \quad (2.48)$$

In other words, it defines the smallest change in the bulk refractive index that produced a detectable change in the sensor output and is expressed as refractive index unit (RIU).

2.4.3.3. Limit of detection

Limit of detection is another key factor that described the ability of SPR sensors to detect the smallest quantity of change in the analyte refractive index (or translated into concentration) with a reasonable certainty. The magnitude of the sensor output due to small change in the analyte concentration is constrained by the standard deviation (σ_{SO}) of the noise at the sensor output. Usually the LoD is expressed as the ratio of 3 times standard deviations of sensor output measured for blank sample to the sensor sensitivity of analyte concentration according [26]:

$$LoD = \frac{3\sigma_{SO}}{S} \quad (2.49)$$

the standard deviation of sensor output noise in angular based SPR sensor can be calculated from the reflectivity curve as [26]

$$\sigma_{SO} = K \frac{\sigma_{th}}{R_{max} - R_{min}} \frac{FWHM}{\sqrt{N}} \quad (2.50)$$

Where σ_{th} is the intensity noise at the threshold, K is a constant which depends on the type of noise (additive, shot noise etc.), N is the number of the detector over which the noise is averaged, $R_{max} - R_{min}$ is the difference between maximum and

minimum reflection and FWHM is the width of the SPR curve. Equation (2.49) suggest that the sensor will operate accurately if the value of LoD is low as possible, or in other words the enhancement in LoD can be achieved by increasing the sensitivity or reducing the noise level. For SPR based sensor, there exist three ways to compute the LoD [63]. The first way is to use the RI change in the bulk solution in unit of RIU (refractive index unit), which is naturally apply for the sensor performance. In the second way the LoD is quantify in unit of pg/mm^2 from the surface mass density, however, experimentally it is very difficult to measure it accurately. The third way is to use sample concentration in units of ng/mL or molarity, which is rather useful and easy to determine experimentally.

2.5. Dielectric Loaded Waveguide (DLWGs)

The Dielectric loaded waveguide (DLWGs) is the extension of conventional SPR sensor, when a thick dielectric layer such as silicon dioxide or some polymer like PMMA is deposited on the metal surface, this gives rise to the excitation of two additional guided modes that allow the measurement in both transverse magnetic (TM) and transverse electric (TE) polarization states.

Figure 2.10(a), illustrate the schematic structure of DLWGs, which can simultaneously support the SPR mode (short range) and the WG modes (long range) with different penetration depths in the analyte region. Figure 2.10(b) show the

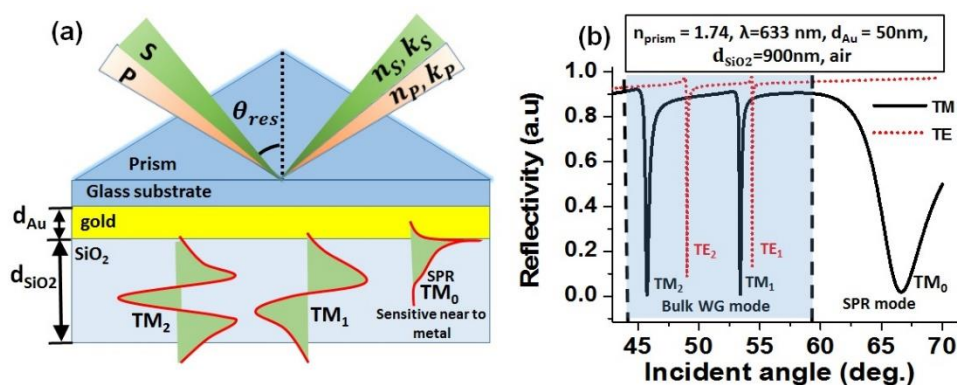


Figure 2.10: Schematic of (a) Dielectric loaded waveguide configuration and (b) its ATR reflectivity curve for TM (in black solid line) and TE (red dash line) polarized light. Above the optical parameters and excitation wavelength are also shown.

calculated DLWGs reflectivity curves at a wavelength of 633 nm for TM and TE polarized light of 900 nm thick layer of SiO₂ over gold (50 nm) in air.

The presence of the WG modes excited by both TM and TE polarized light, make the DLWG spectroscopy particularly useful to probe the birefringence and optical dichroism of anisotropic materials such as lipid bilayer membranes, self-assembled monolayers and thin film [64, 65]. The desired results were achieved from the four optical parameters $\left((n_p, k_p) \text{ and } (n_s, k_s) \right)$ rather than two in the conventional SPR platform. Moreover, the SPR mode (TM₀) explore the region near to the substrate and its evanescent field decays completely within the waveguide layer. On other hand the TE polarized mode with small probing depth is ideal for surface sensing [66].

For some specific applications, the demand of a higher sensitive SPR sensor need to optimize the optical and geometrical properties of the sensing structure by considering the interaction between analyte and the EM field of the SPP. For example, the sensitivity of SPR sensors can be enhanced by using a nanometric spacer over the surface of 30 nm of SiO₂ deposited on the Au thin film [67]. Owing to longer extension tail of the EM field of the guided modes, the DLWGs has been used to obtain the best sensitivity for the detection of bio-molecules with system mimicking the physiological cell membrane [64]. The sensitivity enhancement depends on the fraction of the total EM energy associated to the portion of SPP in the external interface.

Figure 2.11 present the distribution of the electric field intensity as a function of distance from the glass metal interface for the TM₀, TM₁ and TE₁ resonant modes when the SiO₂ thickness is 600nm at excitation wavelength $\lambda = 633\text{nm}$ [31]. The comparison reveals a small low peak intensity of plasmonic mode (TM₀) which is perturbed by the dielectric layer and mainly bound to Au/SiO₂ interface as shown in figure 2.11(d). While the guided modes (TM₁ and TE₁) show relatively higher intensity [shown in Fig. 2.8 (b)-(c)] and are concentrated at SiO₂ analyte layer interface with a significant tail inside the analyte. Among them, the TM₁ mode appears to have a high evanescent field profile extended to analyte region which can be used as the electromagnetic sensing nanoprobles.

Taking advantages of these guided modes, in this work, we proposed and fabricated the DLWGs for the simultaneous determination of refractive index and

thickness of organic thin luminescent films, counting the metal nanoparticle as well characterizing the anisotropic properties of graphene. Since the anisotropic films depends on all three indices (n_x , n_y , n_z) as well as the layer thickness which can be determined simultaneously by the waveguide modes of DLWGs.

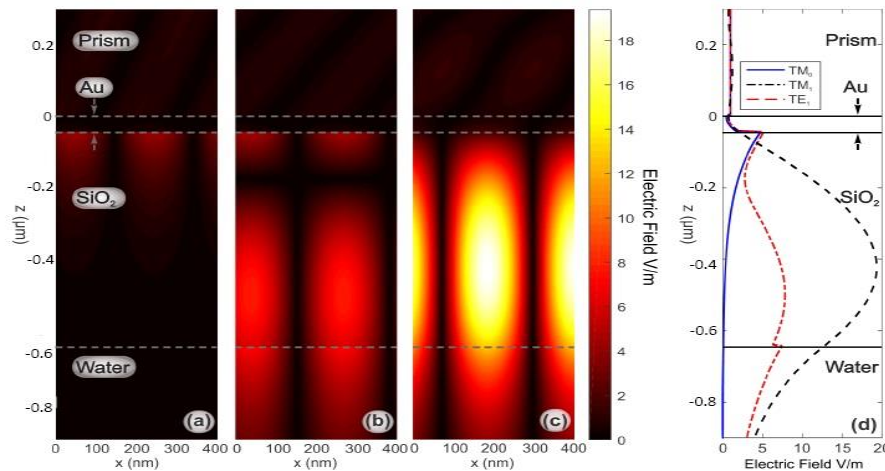


Figure 2.11: The absolute values of the electric field for the resonant modes in the SPR platform. In colors for a cut plane parallel to the zx -plane: (a) E_z Field for TM_0 mode (b) E_z field for TM_1 mode and (c) E_y field for TE_1 mode (d) Norm of E field for the resonant modes in a cut line parallel to the z -axis. Fixed parameters: $\lambda = 633$ nm, $d_{Au} = 46$ nm, and $d_{SiO_2} = 600$ nm [31].

2.6. SPR based Ellipsometry

Spectroscopic ellipsometry is an optical measurement technique in which a p- or s- polarized light is incident onto a sample at the Brewster angle to determine the optical constant and film thickness of the sample from the change in the polarization state upon light reflection or transmission [36]. In literature, the variable-angle spectroscopic ellipsometry (VASE) is a widely used experimental approach for the characterization of thin film in vacuum or inert environment. It is used in a wide range of wavelength (250nm to 2000nm) with an accuracy of about 0.5%. However, the ellipsometry technique still has some drawbacks, including the use of complicated model for data analysis, low spatial resolution (spot size: several mm) and the elevated costs [36, 37].

Concerning thin film characterization, the challenging task of the SPR spectroscopy is the simultaneous determination of the thickness and refractive index of the organic or inorganic thin films deposited on the metal layer. The determination of these parameters using classical SPR metal substrate requires at least two independent sets of measurement on the same thin film sample. In the last decades a significant efforts have been made in the development of experimental methods, fast algorithms and iteration processes to extract both the thickness and optical constants of metal and dielectric layer from the SPR reflectivity curve [33, 68].

The reflectivity curve can be described by three main parameters: the minimum value of reflectivity R_{min} , the full width half maximum Δk_{FWHM} , and the propagation wave vector at minimum k_{SPR} . All these three parameters are linked to the two unknown physical parameters ($\varepsilon = \varepsilon_r + i\varepsilon_i, d$) through approximated analytic relations which give SPR reflectivity curve by using the transfer matrix method [69]. In fact, the information contained in the reflectivity curve gives a single set of data, which is insufficient to determine the two unknown parameters, creating an ambiguity in the optical characterization of thin film and thus forcing a second independent measurement on the same thin film. To eliminate this ambiguity, the second remaining data can be obtained by either taking the SPR curve at several incident wavelengths [32], or, the variation of the refractive index of the external medium [33] as well as the deposition of different metals in different regions of the sample [34].

In SPR based four layered systems (prism, metal, dielectric layer of finite thickness, external medium (bulk)), the determination of the thickness (t_d) and optical constant (ε_d) of the dielectric layer over the metal is bit complex. However, when the dielectric layer is ultra-thin ($< 2nm$) the shift in the SPPs wave vector ΔK_{min} can be written as [32,33, 68].

$$\Delta K_{min} = \frac{t_d}{\varepsilon_d} \left(\frac{2\pi}{\lambda} \right)^2 \frac{(\varepsilon_r \varepsilon_{bulk})^{\frac{3}{2}}}{\varepsilon_r - \varepsilon_{bulk}} (\varepsilon_d - \varepsilon_{bulk}) . \quad (2.51)$$

where ε_r is the real part of the dielectric constant of metal. Once fixed the parameters in Eq. (2.51), there exist an infinite number of couples of values of (ε_d, t_d) associated to the experimentally observed ΔK_{min} . In order to determine the

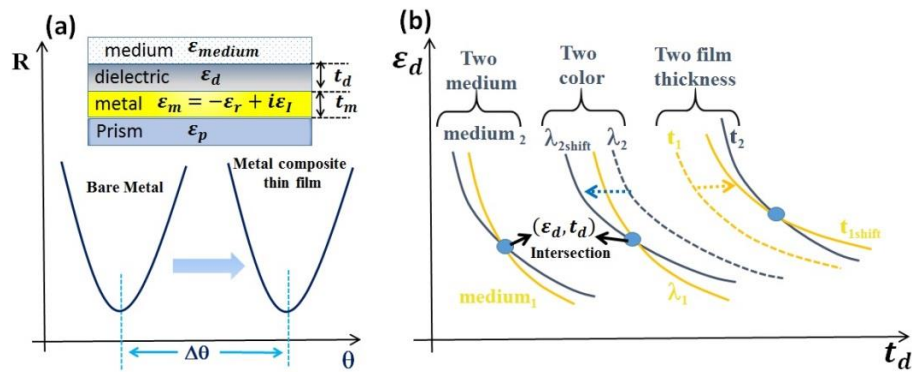


Figure 2.12: Scheme of the four layers SPR based ellipsometry. (a) The resonance angle of SPR curve shift by an amount $\Delta\theta$ after the deposition of metal composite thin film. (b) The trial curves of the different experimental methods in the (ϵ_d, t_d) plane. The intersection point gives the actual values of the parameters of metal composite layer.

thickness and refractive index of thin dielectric layer, it is necessary to change at least one of the parameters in the equation and performed a new measurement of ΔK_{min} . This equation strongly suggests the simultaneous determination of the optical indices and thickness of the dielectric thin layer by giving the two independent data measurement of the same sample.

Figure 2.12(a) show a four-layered SPR platform, where a change in the resonance angle is occurred by the deposition of an unknown dielectric layer. In order to find the unknown parameters (ϵ_d, t_d) , two independent measurement of ΔK_{min} may be performed using the two medium, two color or two film thickness methods, as shown in the Figure 2.12(b). Each measurement method yields an intersection point corresponding to the desired value of the deposited unknown dielectric layer.

The procedures used to retrieve the parameters of the dielectric thin film using the different methods described above, will be discussed in the following sections.

2.6.1. Two Medium Method

In the two-medium approach, the reflectivity curve of the same SPR platform is measured in two independent experiments by changing the refractive index of the external medium (gas or liquid), thus obtaining two curves in the plane (ϵ_d, t_d) , each one associated with a particular environmental situation [33]. The intersection point

between the multiple curves represents the real values of the parameters of the dielectric deposition.

Figure 2.13 shows the example of two medium methods for the simultaneous determination of thickness and dielectric constant of the SiO₂. Prior to the deposition of 30nm dielectric layer of SiO₂, we characterized the bare thin Au film in both air and water at a wavelength of 783nm by using Winspall free software [56]. The values of optical parameters for each layer are summarized in table 2.2. Figure 2.13(a) show the experimental reflectivity curves of the bare Au and Au/SiO₂ in both air and water with an apparent change of resonance angle of 1.91° and 1.29° respectively. After knowing the optical parameters of the bare gold, the SiO₂ layer is characterized by varying its thickness (t_{SiO_2}) from 25nm to 34nm. The Winspall free software is used to obtained a best fit on the experimental SPR curve for each value of t_{SiO_2} , that results into a set of couple of values ($\epsilon_{SiO_2}, t_{SiO_2}$). These set of data are plots in the plane ($\epsilon_{SiO_2}, t_{SiO_2}$), thus obtaining two curves associated with air and water as external medium. The intersection points between two curves represent the real values of the thickness and the dielectric constant of SiO₂ as shown in Figure 2.13(b).

Even though this is the most suitable method from a practical and economical point of view, it may lead to imprecise results or inconsistencies. This uncertainty has origin in the physical and chemical changes of the unknown dielectric layer, when passing from gaseous to liquid environments, or different liquid environments, with alteration of the propagation constant of the SPP [70, 71].

Table 2.2: The optical parameter of prism, Au and bulk layer collected at wavelength of 783nm using Winspall software through best curve fitting.

Medium	SF4	Gold		bulk
	ϵ_r	t(nm)	$\epsilon = \epsilon_r + i\epsilon_i$	ϵ
Air	3.02	47.68	-22.75+i1.63	1
Water	3.02	47.68	-22.75+i1.63	1.768

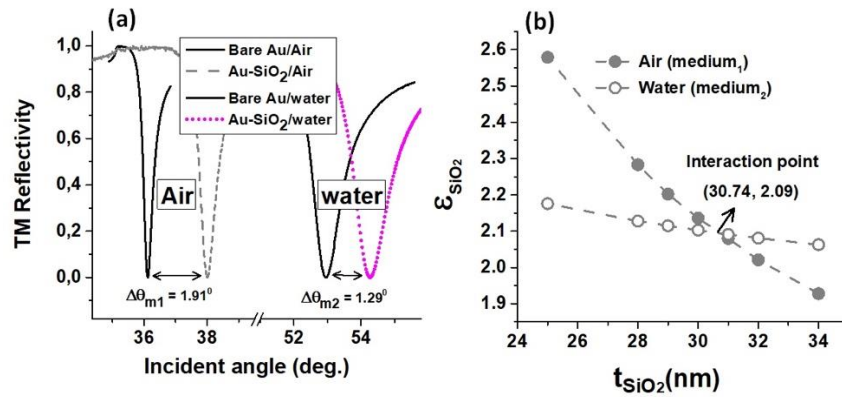


Figure 2.13: (a) TM experimental reflectivity SPR curves recorded on bare Au and Au/SiO₂ in air and water at a wavelength of 783nm. (b) Trial curves of two medium method obtained from a set of couples of values in plan (ϵ_{SiO_2} , t_{SiO_2}). The intersection point gives the actual value of the SiO₂.

2.6.2. Two color method

Two-color approach is the most robust and consistence method for the characterization of unknown thin films. It is based on the use of at least two laser sources at different wavelengths λ_1 and λ_2 and on the knowledge of the refractive index of the material at the different optical frequencies. This theoretical dispersion relation at two wavelength can expressed by the temperature-dependent Sell Meier equation, $n(\lambda_1) = f[n(\lambda_2)]$ [72]. Figure 2.14 show the data management process of two-color method used for the determination of optical parameters of amorphous silica. The SPR reflectivity curves measured at the two different wavelengths $\lambda_1 = 633nm$ and $\lambda_2 = 783nm$ give as result two curves in the thickness-refractive index plane, namely, $(t_{SiO_2}, n_{SiO_2})_{\lambda_1}$ and $(t_{SiO_2}, n_{SiO_2})_{\lambda_2}$. Using the Sellmeier equation the ratio between the refractive index of SiO₂ at the wavelengths λ_1 and λ_2 is $n(\lambda_1)/n(\lambda_2) = 1.005$. In order to obtained the intersection point the values of the refractive index of the curve $(t_{SiO_2}, n_{SiO_2})_{\lambda_1}$ in the thickness-refractive index plane have to be divided by the factor 1.005. The intersection point obtained from the two curves represent the actual value of thickness and dielectric constant of SiO₂. In this work, we use the two-color method for the simultaneous determination of the size and surface density of citrate stabilized AuNPs.

λ (nm)	SF4 prism	Gold		SiO ₂		Water
		thickness	$\epsilon = \epsilon_r + i\epsilon_i$	thickness	ϵ	
633nm	3.0614	48.1nm	-11.43+i1.56	31.7nm	2.132	1.77
783nm	3.0206	48.1nm	-22.45+i1.63	31.7nm	2.122	1.76

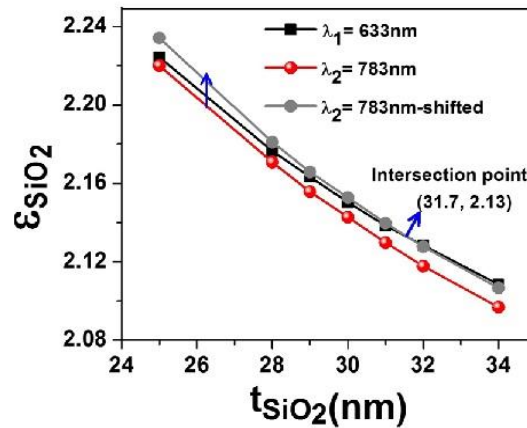


Figure 2.14: Example of SPR reflectivity data management for two-color method in the determination of the thickness and refractive index of a thin film of SiO₂ deposited over gold by electron-beam deposition [73].

2.6.3. Two films thickness and Two metal deposition

The two film thickness (TFT) and two metal deposition (TMD) are the two SPR based optical methods that have been recently proposed for the simultaneous determination of thickness and refractive index of thin organic films of tris(8-hydroxyquinoline) (Alq₃) [34]. Figure 2.15 display the fabricated two types of multilayer structures used for the application of TFT and TMD methods. In TFT sample two thin films of Alq₃ with nominal thickness of t_1 and t_2 are deposited over a single thin gold layer, while a TMD sample was fabricated by using two thin adjacent films of gold and silver covered by a thin film of Alq₃. Both the samples have been characterized in protected environment using OLED encapsulation technique. The experimental data required for the simultaneous determination of thickness t_0 and dielectric constant ϵ_0 collected from both methods are presented in Fig. 2.16. It is observed that the TMD is not an appropriate method for the precise characterization due to the errors associated to the dielectric function of both silver and gold layers, which induce a high dispersion of the possible values of thickness (t_0) and dielectric constant (ϵ_0) of the organic layer as shown in Fig. 2.16(a).

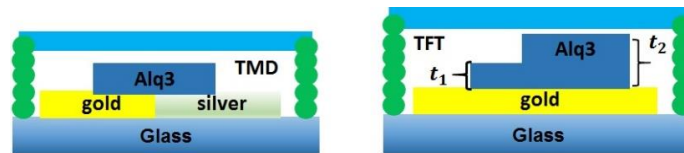


Figure 2.15: Scheme of the encapsulated multilayer structures used to perform the TMD and TFT methods. All the samples presented a region with only bare metals that was used to characterize the metal deposition by SPR spectroscopy.

On the other hand the TFT method which show an accuracy of 1% has a known thickness ratio (t_1/t_2) and therefore one of the two curves in the (ϵ_0, t_0) plane has to be shifted in the thickness axes of the factor t_1/t_2 , which gives an intersection point corresponding to the actual characteristic of the organic layer. The result is plotted in the Fig. 2.16(b).

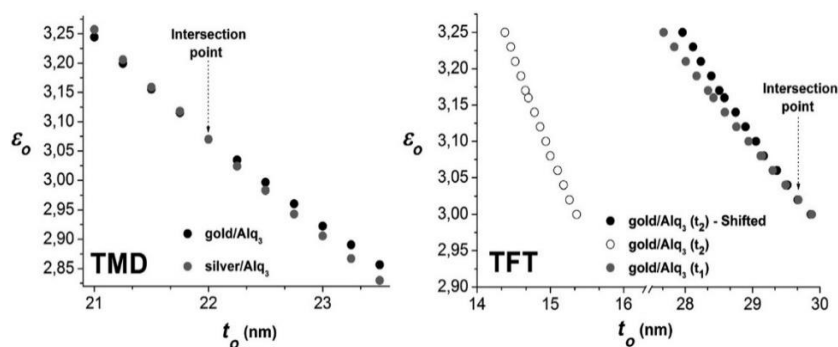


Figure 2.16: Calculated points representing the possible values of thickness (t_0) and dielectric constant (ϵ_0) of the organic layers over the TMD and TFT samples. In the latter, the ratio between the thicknesses t_1 and t_2 of the different organic layers is known, and the intersection point corresponding to the actual characteristic of the thin film is obtained by shifting one set of points. The points are generated using the mean value of refractive index of the metal depositions [34].

2.6.4. Dual modes DLWGs Spectroscopy

In section 2.4, we discussed the unique characteristic of DLWGs as a SPR platform with both TM and TE traveling modes. The excitation of these two independent TM and TE modes is possible when a dielectric thick layer of SiO_2 is

deposited over the gold thin film, and guarantees sufficient information (multiple resonant wave vectors k_{SPR} , multiple minimum of reflectivity R_{min} , and multiple full width half-maximum Δk_{FWHM}) to precisely determine physical properties of the unknown dielectric thin film.

Figure 2.17, show a simple example of dual modes DLWGs spectroscopy for the characterization of SLG. The *Winspall* free software is used to simulate the reflectivity curves of the multilayer structure with the optical parameters of each layer as listed in table 2.3. The real (n_G) and imaginary (K_G) parts of the refractive index of graphene in visible range are related by [74]:

$$K_G(\lambda) \approx C \frac{\lambda}{n_G(\lambda)}. \quad (2.52)$$

Where $C = 5.446 \mu m^{-1}$ and λ is the wavelength of the EM wave in visible region. In the framework of Fresnel equation the experimental calculated value of $n_G(\lambda) = 3.0$ in the range between 0.5 and 3.0 eV [75].

Table 2.3: Optical parameters of each layer used in dual mode DLWG method.

$\lambda(nm)$	SF4	Gold		SiO ₂		Air
	ϵ_r	t(nm)	$\epsilon = \epsilon_r + i\epsilon_i$	t(nm)	ϵ_r	ϵ
633	3.06	49	-11.75+i1.25	650	2.12	1

The SPR reflectivity curve of the DLWGs supporting TM_0 and TM_1 modes is shown in the Figure 2.17(a). These two distinct and independent modes yields a set of possible solutions $(t_{graphene}, \epsilon_{graphene})_{TM_1}$ and $(t_{graphene}, \epsilon_{graphene})_{TM_2}$ in the plane of $t_{graphene}$ and $\epsilon_{graphene}$. Thus, for each mode a single curve is constructed by making variation of the $t_{organic}$ axes in a certain range. As a result, the intersection point between the curves gives us the correct value of the thickness and the dielectric constant of graphene as shown in Figure 2.17(b). Apart from TM_1 and TM_2 we can also calculate the thickness and dielectric constant of graphene from the set of possible solutions of $(t_{graphene}, \epsilon_{graphene})_{TE_1}$ and $(t_{graphene}, \epsilon_{graphene})_{TE_2}$ by using TE polarizations modes in a similar way.

In the present work we simultaneously determine both the thickness ($t_{organic}$) and dielectric constant ($\epsilon_{organic}$) of thin film of organic luminescent materials (Alq₃ and Eu(dbm)₃Phen) through the characterization of dual modes DLWGs SPR

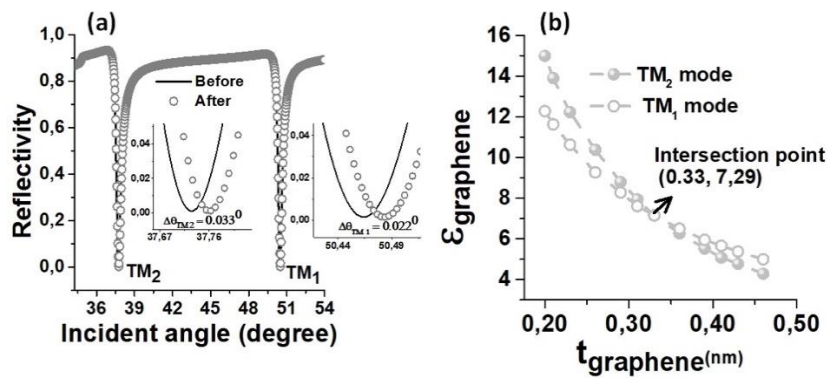


Figure 2.17: (a) Simulated SPR reflectivity curves before and after graphene on the DLWGs. The insets show the change the resonance angle. (b) Curves of the set of coupled values of $(t_{\text{graphene}}, \epsilon_{\text{graphene}})$ in refractive index thickness plan.

spectroscopy at wavelength of 633nm and 783nm. Moreover, we will also present the mixed dual mode/two-color DLWG method for the investigation of the anisotropic properties of graphene.

2.7.

Localized Surface Plasmon in metal nanostructures

We discussed in the previous sections that the surface plasmon polariton (SPP) are propagating, dispersive electromagnetic waves coupled to the conduction electrons of continuous thin metal surface at dielectric interface. However, there is another kind of plasmon mode excitation: Localized Surface Plasmon (LSPs). Unlike SPP, LSPs are the non-propagating excitation of conduction electrons in the metallic nanostructures of finite nanoscale volume. These confined excitations are associated to the coherent oscillation of the charge density of NPs with the incident electromagnetic field [47, 51, 76]. When the size of the NPs is significantly smaller than the wavelength of excitation light, the incident electromagnetic field exerts a force on the conduction electrons and drive them relative to the positive charge of static core towards the NPs surface. As a result of the displacement of charges an electric dipole is induced which creates an electric field inside the NPs opposite to that of the light that will pull back the electrons to the equilibrium position as shown in Figure. (2.18). With the removal of external field leads to oscillate the electrons with a natural frequency called plasmonic frequency and, when the frequency of

the incident light matches with plasmonic frequency, energy is coupled into Localized Surface Plasmon Resonance (LSPR) mode.

The resonant frequency of this coherent LSPR mode in transition metals fall in the ultraviolet-visible (UV-Vis) region and therefore, the surface plasmon absorption bands lies in this region of the spectrum. Noble atoms such as gold and silver are the most commonly used materials for the NPs production, which exhibit LSPR mode in the visible range of the spectrum [77]. Classically, the absorption efficiency of NPs can be expressed in term of absorption cross section σ_{abs} , which is the geometrical section of an ideal opaque particle absorbing the same number of photons as the studied particle. Along with absorption the NPs also scattered the

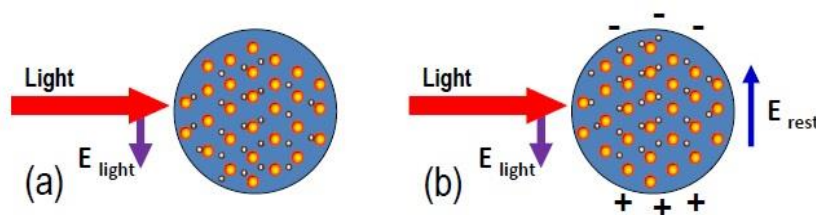


Figure: 2.18: Scheme of the light interaction with a metallic NP. The electric field of the light induces the movement of conduction electrons, which accumulate at the NP surface creating an electric dipole. This charge accumulation creates an electric field opposite to that of the light [78].

incident light that can be defines as a scattering cross section σ_{sca} . The sum of absorption and scattering cross section is called the extinction cross section σ_{ext} , that estimated the fraction of photons that are absorbed and scattered from the incident beam when it passes through the NPs.

The extremely localized electromagnetic (EM) fields induced by LSPR make NPs highly sensitive transducers of small changes in the local refractive index. These changes are exhibited in spectral shifts of extinction (absorption plus scattering) spectra. Moreover, the LSPR mode strongly depends on the composition, size, geometry, dielectric environment and particle–particle separation distance of NPs.

To deeply study the LSPR, one need to solve the Maxwell's equation of electromagnetism (beyond the scope of this thesis) for the metallic NPs under proper boundary conditions and approximation. The next section is dedicated to give a short review about the quasi-static approximations that results the extinction cross section coefficient by using Mie theory.

2.7.1. Quasi Static Approximation

The main contribution to the light absorption by metallic NPs comes from the dipolar mode if the NPs size is smaller than the light wavelength ($D \ll \lambda$). In this case, the harmonically oscillating electric field of the incident wave is approximately uniform within the NPs volume, so that it couples essentially to the dipolar mode. This leads to Quasi Static Approximation (QSA) in which the external field is spatially uniform but varies with time. As the plasmon resonance band falls at the visible part of the spectrum ($\sim 360\text{--}720\text{ nm}$), the condition of small NPs can be set by $D \ll \lambda/10 \sim 40\text{nm}$ [77]. Thus the spatial homogeneity of the

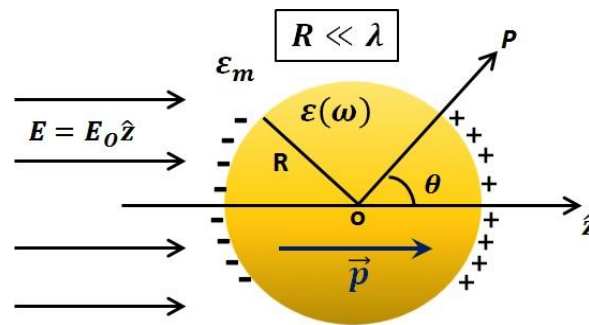


Figure 2.19: A sphere of radius R , in uniform static electric field under the study of quasi-static approximation.

electric field will be no longer valid if the NPs exceed this size. The quasi-static approximation is simpler approach to deduce the electric polarizability of the NPs subject to an external electric field. Let us consider a homogenous, isotropic spherical particle of radius R and complex dielectric function $\epsilon(\omega)$ is located at origin in a uniform static electric field $E = E_0 \hat{z}$ as shown in Fig 2.19. The particle is placed in isotropic and nonabsorbent medium of dielectric constant ϵ_m . Under QSA the solution of Laplace equation in spherical symmetry under the appropriate boundary conditions leads to the expression of dipole moment of the particle as

$$\vec{p} = 4\pi\epsilon_0\epsilon_m(\omega)R^3 \frac{\epsilon(\omega) - \epsilon_m(\omega)}{\epsilon(\omega) + 2\epsilon_m(\omega)} E_0, \quad (2.53)$$

it gives the frequency dependent polarizability $\alpha(\omega)$

$$\alpha(\omega) = 4\pi R^3 \frac{\epsilon(\omega) - \epsilon_m(\omega)}{\epsilon(\omega) + 2\epsilon_m(\omega)}. \quad (2.54)$$

Equation (2.54) represent the complex polarizability of a small metal sphere under electrostatic approximation. It is apparent that a resonance enhancement in the polarizability is obtained under the condition that $|\varepsilon(\omega) + 2\varepsilon_m(\omega)|$ is minimum at plasmon resonance frequency. At the resonant frequency, the optical response of the NPs is enhanced. Assuming that the $Im\varepsilon(\omega)$ is weakly dependent on the frequency, then the condition for resonance is

$$Re[\varepsilon(\omega)] = -2\varepsilon_m(\omega) . \quad (2.55)$$

This expression is known as Frölich condition, which implies that $Re[\varepsilon(\omega)] < 0$ at resonance. At this resonance frequency, Eq. (2.55) show a strong dependence on the dielectric constant of the external medium, suggesting the metal NPs as an ideal platform for the optical sensing. The corresponding scattering and absorption cross sections in the QSA are given by [47, 51]:

$$\sigma_{scat} = \frac{k^4}{6\pi} |\alpha(\omega)|^2 = \frac{8\pi}{3} k^4 R^6 \left| \frac{\varepsilon(\omega) - \varepsilon_m(\omega)}{\varepsilon(\omega) + 2\varepsilon_m(\omega)} \right|^2 \quad (2.56)$$

$$\sigma_{abs} = kIm[\alpha(\omega)] = 4\pi k R^3 Im \left[\frac{\varepsilon(\omega) - \varepsilon_m(\omega)}{\varepsilon(\omega) + 2\varepsilon_m(\omega)} \right] \quad (2.57)$$

Where k being the wave vector. It is evident that σ_{abs} scales with R^3 whereas σ_{scat} scales with R^6 . It means that for large particles extinction is dominated by scattering whereas for small particles it is associated with absorption.

2.7.2. Mie Theory

In 1908, Gustav Mie proposed an exact analytical solution of the Maxwell equations in the theory of absorption and scattering of light by spherical, isotropic, homogeneous and non-magnetic particles of arbitrary radius in a non-absorbing medium. His objective was to understand the colors of gold nanoparticles in a solution and to calculate the spectra of gold nanoparticles of different sizes. Under proper boundary condition the Maxwell equations can be solved analytically and the extinction cross section is given by [47, 76]

$$\sigma_{ext} = \frac{2\pi}{|k|^2} \sum_{L=1}^{\infty} (2L + 1) [Re(a_L + b_L)] , \quad (2.58)$$

where k is the light wave vector in the dielectric medium and L are the integers representing the dipole, quadrupole, and higher multipoles of the scattering. In the

above equation a_L and b_L representing the following expressions consists of Riccati Bessel functions ψ_L and χ_L :

$$a_L = \frac{m\psi_L(mx) \cdot \psi'_L(x) - \psi'_L(mx) \cdot \psi_L(x)}{m\psi_L(mx) \cdot \chi'_L(x) - \psi'_L(mx) \cdot \chi_L(x)}, \quad (2.59)$$

$$b_L = \frac{\psi_L(mx) \cdot \psi'_L(x) - m\psi'_L(mx) \cdot \psi_L(x)}{\psi_L(mx) \cdot \chi'_L(x) - m\psi'_L(mx) \cdot \chi_L(x)}, \quad (2.60)$$

Here $x = |k| \cdot R$, R is the radius of the NPs, $m = \tilde{n}/n_m$, where $\tilde{n} = n_R + in_I$ is the refractive index of metal, and n_m is the refractive index of surrounding medium. These equations are not easy to handle, to carry the calculation of these equations; we developed a code in the Matlab® R2017a given in appendix A2. However, if the nanoparticle is assumed very small as compared to the wavelength then mathematically this approximation is achieved when $x \ll 1$. Taking only the dipole ($L = 1$) term, Eq. (2.58) can be written as:

$$\sigma_{ext} = \frac{24\pi^2 R^3 \varepsilon_m^{3/2}}{\lambda} \frac{\varepsilon_I}{(\varepsilon_R + 2\varepsilon_m)^2 + \varepsilon_I^2}. \quad (2.61)$$

where $\varepsilon_R + i\varepsilon_I$ is the complex dielectric constant of the metal and ε_m is the real dielectric constant of the medium. When the size of the NPs increases then the electric field inside the NPs is no longer uniform and more multipoles terms must be considering in Eq. (2.58).

2.8.

Optical density, extinction coefficient and mass concentration

Generally, the optical density (often also called extinction) is the spectrophotometric measurement of light scattered and absorbed by a colloidal suspension of particles or thin films, at different wavelengths. In case of colloidal solutions of NPs, the optical density is used to determine the mass or molar concentration of NPs in solution. The characteristic optical properties of NPs strongly depend on the sizes, shapes, and distance between. Differently from thin films, NPs do not reflect but scatter the incident light. Let us consider an assembly of NPs confined in a transparent cell and illuminated by a plane EM radiation, as shown in Figure 2.20. Neglecting the multiple reflection at the cell wall, the internal transmittance $T(\lambda)$ at wavelength λ can be defined as the ratio of the transmitted to incident intensity of EM light [79]:

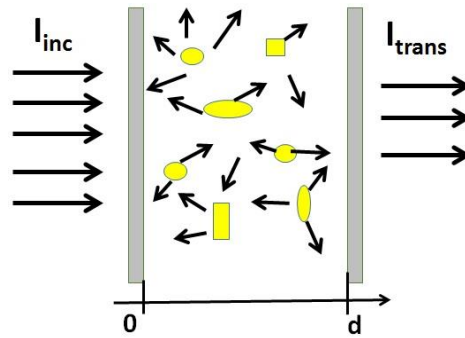


Figure 2.20: Scattering and absorption of NPs illuminated with planar EM wave.

$$T(\lambda) = \frac{I_{tran}(\lambda)}{I_{inc}(\lambda)} = A(\lambda), \quad (2.62)$$

the transmittance is linked with the optical density $\tau(\lambda)$ via the following equation

$$\tau(\lambda) = -\log_{10}[T(\lambda)]. \quad (2.63)$$

Equations (2.62) and (2.63) are applicable for all particle assemblies and can be extended to determine the optical properties, the topologies and the concentration of the nanoparticle composite. The optical response of an isotropic and statistically disordered composite sample can calculate by relating $T(\lambda)$ to $\tau(\lambda)$ using Lambert – Beer law. The Lambert – Beer law states that the irradiance of a beam of light is exponentially attenuated from I_{inc} ; to I_{trans} in traversing a distance d through a particular medium

$$T(\lambda) = \frac{I_{tran}(\lambda)}{I_{inc}(\lambda)} = e^{-e(\lambda)d}, \quad (2.64)$$

where $e(\lambda)$ defines the extinction coefficient and can be written as

$$e(\lambda) = \sigma_{ext}(\lambda) \frac{N}{V}, \quad (2.65)$$

here $\sigma_{ext}(\lambda)$ is the extinction cross section (m^2) and N/V is the particle number concentration. Using Equation (2.64) and (2.65) in equation (2.63) the optical density can express as:

$$\tau(\lambda) = \sigma_{ext}(\lambda) \frac{N}{V} \log(e)d, \quad (2.66)$$

the above equation is a theoretical model used to calculate the dielectric constant of the material of NPs and is used for uniformly sized particles. However, for particle size that is statistically distributed, the optical density can be written as sum over all different contributions:

$$\tau(\lambda) = \sum_k \sigma_{ext}(\lambda, r_k) \frac{n_k(r_k)}{V} \log(e) d. \quad (2.67)$$

where R_k denote the particle size and $n_k(R_k)/V$ is the concentration of particles in volume V . Considering the normalized statistical size distribution defined by

$$n_{norm}(r) = \frac{n(r)}{\sum_k n_k(R_k)} = \frac{n(r)}{N_{total}}, \quad (2.68)$$

and using the normalization condition $\int_0^{\infty} n(r) = 1$, a normalized Log-normal statistical distribution $n_{norm}(r)$, can be written as [79]

$$n_{norm}(r) = \frac{1}{\sqrt{2\pi}wr} e^{-\frac{[\ln r - \ln r_c]^2}{2w^2}}, \quad (2.69)$$

In the latter equation, w defines the width of the distribution and r_c is the central value of the distribution. Figure 2.21 represent the experimental statistical size distribution of a colloidal dispersion of Au@Carbynoid NCs [80] measured by TEM, and the relative *fit* using the normalized log-normal function. From the obtained experimental size distributions, we can calculate the statistical mean value $\langle r \rangle$ and standard deviation δ using the following approach

$$\langle r \rangle = e^{\ln r_c + \frac{w^2}{2}}, \quad (2.70)$$

$$\delta = \sqrt{e^{w^2 + 2\ln r_c} (e^{w^2} - 1)}, \quad (2.71)$$

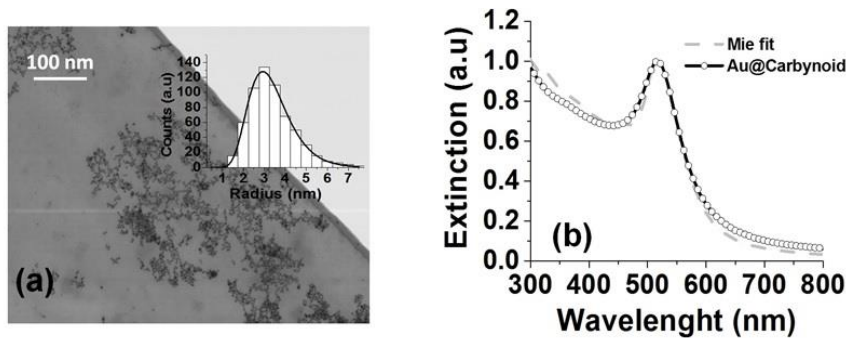


Figure 2.21: (a) TEM image of the Au@Carbynoid. The inset show the experimental statistical size distribution using Equation 2.67 (b) Extinction spectra of the synthesized NCs (black line with open circles) and Mie's theoretical fit (dashed grey line) obtained using the statistical distribution reported in (a). In the inset are reported the concentration of Au and C produced by CO₂ recycling during PLA [80].

Moreover, the statistical extinction coefficient at wavelength λ can be written as [79]:

$$e(\lambda) = \int_0^{\infty} \sigma_{ext}(\lambda, r_k) \frac{N_{total}}{V} n_{norm}(r) dr . \quad (2.72)$$

For each value of λ and r , $\sigma_{ext}(\lambda, r_k)$ is calculated using the Mie theory, and $e(\lambda)$ is calculated considering the experimental statistical distribution $n_{norm}(r)$. In Figure 2.21(b) show the theoretical Mie fit, calculated considering the statistical distribution obtained in 2.21 (a) and size dependent dielectric function of small AuNps [45]. The theoretical plot was handled by using code developed in the *Matlab® R2017a*, given in appendix A. A perfectly overlap between the Mie fit with the experimental UV-Vis spectra was observed.

The mass concentration of a monodispersed colloidal solution of nanoparticles can be written as:

$$C_{mass} = N_{total} \times V_{NPs} \times \rho_{NPs} , \quad (2.73)$$

where V_{NPs} is the volume and ρ_{NPs} the volume density of the NPs. The N_{total}/V can be calculated from the optical density and Mie fitting

$$\tau_{exp}(\lambda) = d_{exp} \log(e) e_{exp}(\lambda) , \quad (2.74)$$

Using equation (2.72), the optical density can be written as:

$$\tau_{exp}(\lambda) = d_{exp} \log(e) \frac{N_{total}}{V} \left[\int_0^{\infty} \sigma_{ext}(\lambda, r_k) n_{norm}(r) dr \right]_{Mie\ fit} \quad (2.75)$$

$$\frac{N_{total}}{V} = \frac{\tau_{exp}(\lambda) / d_{exp} \log(e)}{\left[\int_0^{\infty} \sigma_{ext}(\lambda, r_k) n_{norm}(r) dr \right]_{Mie\ fit}} \quad (2.76)$$

Here is $d_{exp} = 1cm$, the path length of the cuvette containing the nanomaterial. The value of $\tau_{exp}(\lambda)$ can be measured experimentally, while the value of the denominator can be calculated from Mie fitting. For statistical size distribution of NPs the mass concentration is given by

$$C_{mass} = \rho_{NPs} \frac{N_{total}}{V} \int_{r_{min}}^{r_{max}} n_{norm}(r) V_{NPs}(r) dr \quad (2.77)$$

For spherical gold nanoparticle $V_{NPs} = 4\pi r^3/3$ and $\rho_{NPs} = 19.32 gm/cm^3$. The theoretical calculated mass concentration can be compared with experimental measured by inductively coupled plasma mass spectrometry (ICPMS). For the theoretical calculation of mass concentration, we developed a code in the *Matlab®*

R2017a given in appendix A. The theoretical calculated value of the mass concentration of Au and C is 46 ± 4 ppm produced by the CO₂ recycling during pulsed laser ablation.

2.9. Maxwell Garnett theory

In 1904 Maxwell Garnett developed one of the most widely used theory with the aim to approximate a composite thin film to an homogeneous and isotropic thin layer, with thickness t_{eff} and complex dielectric constant ϵ_{eff} [81]. The composite film, is generally constituted by nano-objects included in a dielectric matrix. The fundamental limitation of Maxwell Garnett (MG) model reside in the fact that the inclusions particles should be isotropic, and its radius should be much smaller than the spacing between them, as well as smaller than the wavelength of the incident radiation.

Let us consider a composite layer of polydispersity spherical AuNPs having a dielectric constant $\epsilon_{AuNPs} = \epsilon_r + i\epsilon_i$, embedded in non-absorbing medium ϵ_m as shown in the Figure 2.22. MG approximation is only valid when there is no interaction between the NPs. Assuming that the thickness of the effective layer is equal to the average diameter of the AuNPs, and then the effective dielectric constant ϵ_{eff} of the inhomogeneous composite layer can be approximated as a homogenous layer by using Modified Maxwell's Garnett theory:

$$\epsilon_{eff} = \epsilon'_{eff} + i\epsilon''_{eff} = \epsilon_m \left(\frac{\epsilon_{AuNPs}(1 + 2f) + 2\epsilon_m(1 - f)}{\epsilon_{AuNPs}(1 - f) + \epsilon_m(2 + f)} \right) \quad (2.78)$$

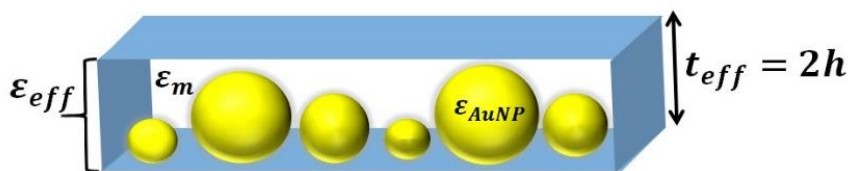


Figure 2.22: The optical geometry of the composite layer of AuNPs immersed in a medium ϵ_m with effective thickness $t_{eff} = 2h$. Where h is the effective radius of the AuNPs in composite layer. The optical properties of this inhomogeneous layer is estimated by effective dielectric constant ϵ_{eff} .

where $f = 2\pi R^2/3\langle d \rangle^2$ is the metallic volume fraction in the matrix that depend on the radius r and the distance d between the nanoparticles. The real ε'_{eff} and imaginary ε''_{eff} parts can be written separately as [41, 67]

$$\varepsilon'_{eff} = \varepsilon_m + \frac{AC + BD}{C^2 + D^2} \text{ and } \varepsilon''_{eff} = \frac{BC - AD}{C^2 + D^2} \quad (2.79)$$

Here $A = f(\varepsilon_r - \varepsilon_m)$, $B = f\varepsilon_i$, $C = \varepsilon_m + \beta(\varepsilon_r - \varepsilon_m) - f\gamma(\varepsilon_r - \varepsilon_m)$ and $D = (\beta - f)\varepsilon_i$. The term γ is related to the collective electric field created by NPs and can be described as:

$$\gamma \equiv \frac{1}{3\varepsilon_i} + \frac{K}{4\pi\varepsilon_m} , \quad (2.80)$$

where K represents the electric field at particle position created by the adjacent particles. If the particles are isolated from each other so that the dipolar interactions are negligible then $K = 0$. The parameter β depends on nanoparticle geometry and is equal to 1/3 for spherical gold nanoparticles.

In order to take into account, the statistical distributions of spherical AuNP's one need to effectively characterize the composite layer by deriving a new equation for the volume filling factor of AuNP's. To this aim, we consider a composite layer of different size of spherical AuNP's embedded in water having thickness equal to $2\langle r \rangle$ as shown in figure 2.22. The filling factor is the ratio of the volume occupied by individual nanoparticle to the volume of the total structure

$$f_{stat} = \frac{N\langle V_P \rangle}{V_S} = \frac{\sigma\langle V_P \rangle}{2h} = \frac{2\pi\sigma}{3h} \int_0^{2h} r^3 n(r) dr , \quad (2.81)$$

where $n(r)$ is given by Eq. (2.69), V is the volume of the thin composite layer of height $2h$, $\langle V_P \rangle$ is the statistical mean volume of a single nanoparticle, and N is the total number of AuNPs on the surface ($\sigma = N/A$). Inserting equation (2.69) in equation (2.81)

$$f_{stat} = \frac{\sqrt{2\pi}\sigma}{3wh} \int_0^h r^2 e^{-\frac{[\ln r - \ln r_c]}{2w^2}} dr , \quad (2.82)$$

From Equation (2.69), the ratio of the population of AuNPs with radius r_c and radius equal to h is given by

$$\frac{n(h)}{n(r_c)} = e^{-\left[\ln\left(\frac{h}{r_c}\right)\right]^2} = e^{-n} , \quad (2.83)$$

Defining, $y = \ln(h/r_c)$, Eq. (2.83) reduces to the equation of second order $y^2 + 2w^2 y - 2w^2 n = 0$, which leads to the solution

$$\frac{n(h)}{n(r_c)} = e^{-\left[\ln\left(\frac{h}{r_c}\right)\right]^2} = e^{-n} , \quad (2.84)$$

$$h = r_c e^{-w^2 + \sqrt{2nw^2 + w^4}} . \quad (2.85)$$

The choice of the thickness $2h$ of the composite layer, defines the maximum dimension of the NPs that we are taking in account to calculate the statistical filling factor.

2.9.1. Theoretical model of two-color SPR nanosizer

Recently, the MG theory described in the previous section, has been extensively applied in the interpretation of experimental data on the optical properties of composite system containing small metallic nanoparticles near metal surfaces. For example, M. Golden et al. used a multiwavelength angle-resolved surface plasmon resonance imaging (SPRi) along modified MG model for the determination of optical properties of gold nanoparticle immobilized on Au thin film coated with various thickness of SiO₂ [67]. In other study, Xinheng et al. estimated the dielectric function of biotin capped gold nanoparticles adsorbed on gold thin film by using SPR and atomic force microscopy (AFM) based on modified Maxwell Garnett theory [41]. They calculated the volume fraction of particles in nanocomposite layer with AFM and then accurately obtained the effective dielectric function of composite layer by SPR scan at three different wavelengths in vis-near IR region. The MG approximation is only valid when there is no inter AuNPs dipole-dipole interaction and the dipole interaction between the AuNPs and Au thin films.

In this work, we developed a new theory to show how SPR spectroscopy can be used as a two-color SPR nanosizer, that able to determine simultaneously both the statistical mean radius $\langle r \rangle$ and the surface density σ of citrate stabilized AuNPs deposited over 30 nm SiO₂ surfaces.

As we already discussed, in the SPR spectroscopy there exist three main techniques which can be used to determine both the thickness and refractive index of a thin film, namely the two-thickness, two-media and two-color methods [28, 32,

33]. The first method is not applicable in the present case, since SAMs of AuNPs with different thicknesses $\langle 2r \rangle$ could be realized only by the deposition of nanoparticles with different diameter. The second method consists in the measurement of the SPR reflectivity spectra of the sample after the deposition of the AuNPs using two different external media. This technique is also not appropriate for our application, since the change of the external liquid medium after the deposition of the metal nanoparticles might influence the strength of electrostatic interaction between the amino group of APTS and the negative charges of the AuNPs. The third technique is effective when the ratio of the refractive indices of the thin film at two different wavelengths is known. From Equation (2.77), it would appear that in our case the application of the third method is not possible because the parameter f is not known. Anyway, when considering the condition of very low the surface density ($f \ll \varepsilon'_m, \sigma \ll \varepsilon'_m/\langle r \rangle^2$), Equation (2.79) can be simplified as

$$\varepsilon'_{eff} - \varepsilon'_m = f \left[\frac{(\varepsilon' - \varepsilon'_m)C + \varepsilon''D}{C^2 + D^2} \right], \quad \varepsilon''_{eff} = 0, \quad (2.86)$$

where $C = \{\varepsilon'_m + (\varepsilon' - \varepsilon'_m)\}$ and $D = \varepsilon''_m/3$. Hence, in the low surface density regime, when $\varepsilon''_{eff} \approx 0$, it is possible to find an analytical relation for the ratio between the real part ε'_{eff} of at two different wavelengths, which is now independent from metal filling factor f . In these conditions, two-color spectroscopy may be applied for the characterization of the AuNPs/water composite layer using the following dispersion relation:

$$Q_{\lambda_1, \lambda_2} = \frac{(\varepsilon'_{eff} - \varepsilon'_m)_{\lambda_1}}{(\varepsilon'_{eff} - \varepsilon'_m)_{\lambda_2}} \quad (2.87)$$

$$Q_{\lambda_1, \lambda_2} = \frac{(\varepsilon' - \varepsilon'_m)_{\lambda_1} \times C_{\lambda_1} + (\varepsilon''D)_{\lambda_1}}{(\varepsilon' - \varepsilon'_m)_{\lambda_2} \times C_{\lambda_2} + (\varepsilon''D)_{\lambda_2}} \times \frac{C_{\lambda_1}^2 + D_{\lambda_1}^2}{C_{\lambda_2}^2 + D_{\lambda_2}^2} \quad (2.88)$$

It is to be noted that the theoretical model described above and the final Equation (2.88), is not restricted to a particular dimension of the AuNPs and are completely independent from the electron mean free path limitation assumption, discussed in the following Section.

2.9.2. Mean free path limitation

For very small metallic nanoparticles (below $\approx 20\text{nm}$), whose sizes are comparable to the electrons mean free path, the additional scattering of electrons at the particles surface modifies the bulk dielectric constant. This effect is called mean free path limitation. Therefore, in the Drude model for metals [5] the damping constant is increased due to this effect and can be written as [45]:

$$\Gamma(R) = \Gamma_{bulk} + C \frac{v_F}{R} \quad (2.89)$$

Where v_F the electron Fermi velocity for Au NPs and C is a constant, describing the scattering of electrons with the boundary of the particles safely assumed close to unity. After applying the mean free path limitation to the dielectric function of small AuNPs, only the imaginary part (ε''_{size}) gets modified in terms of size and the final expression of the refractive index corrected by size are given by [45]:

$$n_{size}(\lambda, r) = \left\{ \frac{1}{2} \left[\left(\varepsilon'_{size}(\lambda) + \varepsilon''_{size}(\lambda) \right)^{\frac{1}{2}} + \varepsilon'_{size}(\lambda) \right] \right\}^{\frac{1}{2}}, \quad (2.90)$$

$$k_{size}(\lambda, r) = \left\{ \frac{1}{2} \left[\left(\varepsilon'_{size}(\lambda) + \varepsilon''_{size}(\lambda) \right)^{\frac{1}{2}} - \varepsilon'_{size}(\lambda) \right] \right\}^{\frac{1}{2}}. \quad (2.91)$$

Here n_{size} and k_{size} are the real and imaginary parts of AuNPs corrected by size. Figure 2.23, plot both n_{size} and k_{size} as a function of wavelength. As can be seen that both the size corrected refractive index are higher than the bulk values and increases as the size of the nanoparticles decreases. The effect of modifying the imaginary part of the metals by including the mean free path limitation, improves the theoretical fitting on the experimental spectrum.

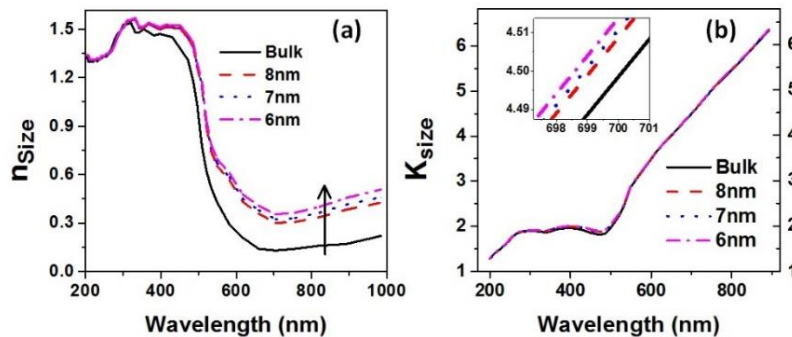


Figure 2.23: The size corrected (a) real and (b) imaginary part of the refractive index of small AuNPs when only the effect of mean free is included in the imaginary part of the dielectric function.

2.10. Particle Amplified SPR Spectroscopy

PA- SPR spectroscopy has gained much attention from the last 15 years due to the enhancement of the sensitivity in chemical and biochemical optical sensors [40, 81]. It found for example application in the ultrasensitive detection of DNA hybridization [83], prostate-specific antigen [84] and carcinoembryonic antigen, between the most [40]. Similarly to surface enhanced Raman scattering (SERS) spectroscopy based on two-dimensional arrays of AuNPs , it is important to know both the surface density and dimension of the nanoparticles in order to calculate the mass resolution of the sensor [40] or SERS gain [85], respectively.

In Figure (2.24) is depicted the particular detection scheme generally used in PA-SPR spectroscopy to enhance the sensitivity in presence of very small molecular analyte. In this sandwich assay scheme the neutravidin functionalized gold nanoparticles (N-AuNPs) are used to enhance the response of an SPR biosensor in the detection of a cancer biomarker called carcinoembryonic antigen (CEA)[40]. Essentially, the small size, mass and concentration of a molecule such as CEA, does not induce a significant change in the SPR signal.

To amplify the response or sensitivity, a sandwich detection structure is proposed, in which the surface of the sensor is functionalized with a specific bio-ligand of CEA (antibody Ab1). When CEA is fluxed, the response of the sensor with Ab1 is very low towards CEA molecule, as shown in the left panel of Figure 2.24(b). Subsequently, the analyte is again functionalized with another specific bio-ligand (biotinylated Ab2) which acts as a molecular bridge between CEA and the neutravidin functionalized AuNPs. If an analyte molecule binds on the sensor surface functionalized with Ab1, when the N-AuNPs are fluxed, they link to the CEA molecules, provoking a big shift of the resonance angle, as shown in the right panel of figure 2.24 (b). It is now clear how, in order to evaluate the analyte mass coverage on the sensor surface, it is fundamental to be able to measure the surface density σ_{AuNPs} of metal NPs.

For this reason, part of the presented research was dedicated to the development of an SPR based nanocounter.

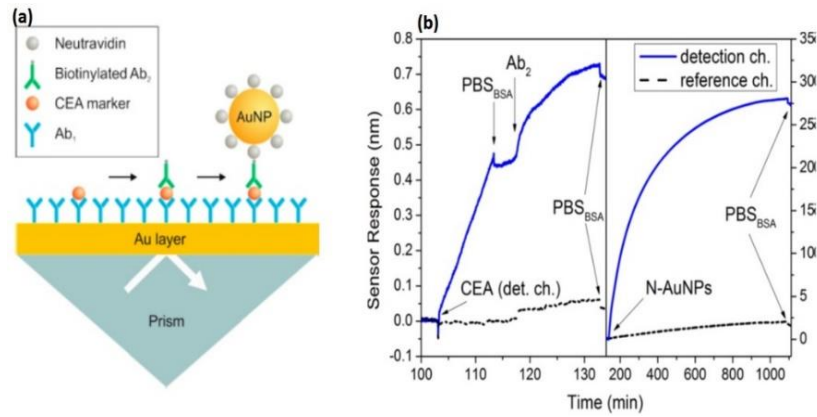


Figure 2.24: (a) sandwich assay scheme for the N-AuNPs enhanced detection of CEA. (b) Sensor response obtained during a typical CEA assay using 33 nm N-AuNPs [40].

2.11. Numerical analysis of plasmonics structures

The classical Fresnel equations are generally used to calculate the reflection coefficients and the reflectivity of a multilayered structure, where the layers are considered homogeneous and planar. This approach is fundamental for a fast data processing of the experimental results of SPR spectroscopy in the Kretschmann configuration, in order to get a real-time information about the surface coverage of the SPR sensors. Although this method can be effectively applied for the most of the devices fabricated in this work, this is not a trivial case when characterizing a thin composite film of metal NPs in dielectric environment, as we propose in the thesis.

An example of the general multilayered structure used for the sensing of NPs is depicted in figure 2.25(b). Here the thin composite NPs film is schematized as a planar homogeneous layer and characterized by an effective dielectric constant ϵ_{eff} by the use of the modified MG theory. In this case, the generalized reflection coefficient in terms of Fresnel's reflection coefficient for TM polarized light is written as [31]:

$$\tilde{R}_{n, n+1} = \frac{(R_{n, n+1} + \tilde{R}_{n+1, n+2}) e^{i2k_{n,z}(d_{n+1}-d_n)}}{1 + (R_{n, n+1} + \tilde{R}_{n+1, n+2}) e^{i2k_{n,z}(d_{n+1}-d_n)}}, \quad (2.92)$$

In case of TM polarization, the transverse magnetic field in the n-th layer is given by

$$H_{n, y} = A_n [e^{-ik_{n,z}z} + \tilde{R}_{n, n+1} e^{-ik_{n,z}(z+2d_n)}] e^{ik_x x}, \quad (2.93)$$

where

$$A_n = \frac{T_{n-1, n} A_{n-1} e^{i(k_{n-1, z} - k_{n, z}) d_{n-1}}}{1 - R_{n, n-1} \tilde{R}_{n, n+1} e^{[2ik_{n+1, z}(d_{n+1} - d_n)]}} \quad (2.94)$$

In equations (2.92)-(2.94), the amplitude of the incident field $A_1 = 1$, the propagation constant is $k_n^2 = k_0^2 n$, the angular frequency is $\omega = 2\pi c/\lambda$ and $k_x = k_1 \sin \theta$ is the wave vector in x –direction. The angular reflectivity in the prism gold interface is given by equation (2.92) $\Gamma(\theta) = |\tilde{R}_{1, 2}|^2$.

The approach based on the MG theory and Fresnel reflection coefficient is valid only under the hypothesis that dipolar interaction between the metal NPs and the metal substrate, and the interparticle interaction are negligible. Hence, in order to define a precise limit of application of the optical modeling proposed, it was necessary to model the near EM field surrounding the nanostructured devices proposed in this work. This task has been performed in collaboration with the group of Professors Victor Dmitriev and Karlo Costa of the Department of Electrical Engineering of Federal University of Pará (Brazil), by the use of the COMSOL Multiphysics® software, based on the Finite Element Method (FEM), a numerical method generally applied to compute the solution of space-time dependent EM equations under different types of space discretization.

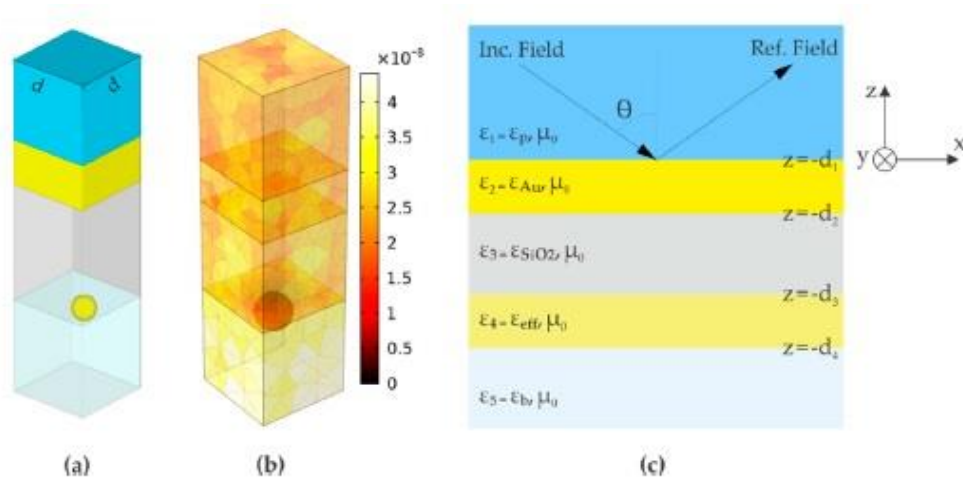


Figure 2.25: a) Unit periodic cell considered in the numerical simulations by the COMSOL® software. (b) Mesh of the FEM model of the sensor. Colors indicate the size of the elements, which is defined by physical and geometrical factors; (c) Resultant planar structure of the PA-SPR sensor in the effective layer approximation to represent the AuNPs periodic [31].

2.12. Sensitivity enhancement of SPR sensor via graphene

In this section, we will present a short overview about the role of graphene transfer on the plasmonics metal in terms of enhancement of sensitivity and the detection mechanism in the proposed heavy metal ion sensor.

The enhanced RI sensitivity of Au/graphene sensor originates from the shift of Fermi level in graphene by the adjustment of work function of Au and graphene, resulting in the formation of surface dipole at interface due to charge transfer between Au film and graphene [28] as shown in the figure 2.26. These intensified dipoles lead to increase the number density of electrons (N) transferred to gold and hence increasing the plasma frequency ($\omega_p = \sqrt{Ne^2/\epsilon_0 m_e}$) of free electrons in the metal and allowing the change in the real part of dielectric constant of Au by using the Drude Lorentz model ($\epsilon'_m = 1 - (\omega_p/\omega)^2$) [47].

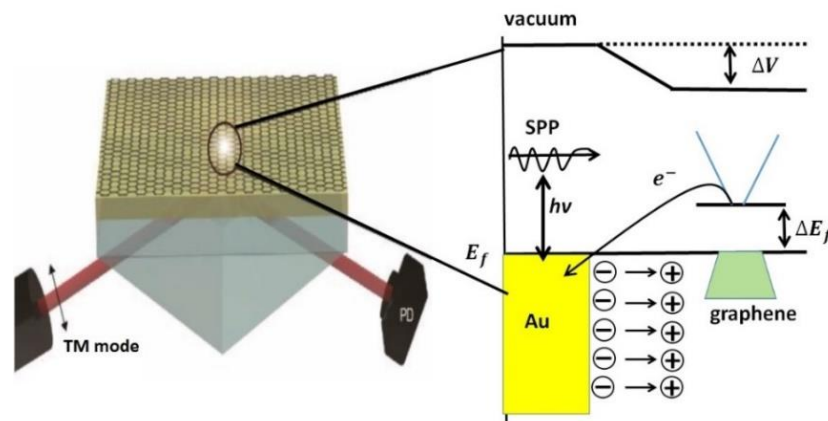


Figure 2.26: (a) metal-graphene based SPR spectroscopy (b) The scheme of the transfer process of electron from graphene to gold due to the difference in the work function and subsequent adjustment of the Fermi level.

Khomyakov and his co-workers studied analytically the interaction between graphene and metals (Al, Cu, Au and Ag) by Density Functional Theory (DFT) and concluded that the interaction is although very weak but lead to charge transfer that shift the Fermi level due to a smaller value of graphene work function (4.5 eV) relative to metal (5.4 eV) [86]. They observed that the hybridization between d states of metals with p_z states of graphene induced the band gap opening in graphene and the reduction of work function. Therefore, these changes not only modulate the plasmonics properties of metals but also the electronic properties of graphene as well as the transport phenomena at the interface of graphene.

We propose to use this sensitive Au/graphene sensing platform to detect the heavy metal ion of environmental interest such as Hg^{+2} , since it is known that the oxidized graphene has the possibility to detect the mercury ions and reduce them [44]. Although we aim to use a pure infinite SLG, we want to investigate the possibility of electron transfer from SLG also to the analytes, with a further enhancement of the SPR sensors. Nevertheless, a recent theoretical report showed that some specific binding sites of infinite graphene may provide the surface absorption of heavy metal ions [87]. In this work, we want to understand the reduction of Hg^{+2} using SPR spectroscopy.

3 Experimental methods and techniques

In this chapter, we present the fabrication methods of our samples and the experimental techniques and equipment used for their characterization. First, we describe the methods used for the fabrication of SPR monomodal sensing platforms and DLWGs. Subsequently, we will describe the processes for the deposition of organic luminescent thin films and SLG over the SPR sensors. We finish the chapter showing the experimental techniques used for the characterization of the AuNPs and of the metal-dielectric interfaces of the SPR devices.

3.1. Fabrication of Conventional SPR platform

The fabrication procedure of the SPR sensor consists of four main steps. It starts with the cleaning of the glass substrate by different organic solvents and ultrasonication, followed by the deep coating method for the formation of self-assembled monolayer of (3-mercaptopropyltrimethoxysilane) (MPTS), commonly used as an adhesion layer between clean glass and thin metal film. In the third step a thin metal film is deposited over the MPTS functionalized substrate. The process is completed with either the thermal deposition of organic thin film or the deposition of the SiO₂ for the further application.

3.1.1. Glass Substrate cleaning

Clean glass substrate is the most important parameter that affects the determination of the thickness and dielectric function of the different layers of the samples. It provides a good flat surface for the thin film deposition. In the ultrasonication process the substrate are shaken at ultrasonic frequency in order to remove the contamination and particles larger than 3-5 microns. The basic cleaning steps we used for glass substrate are the following:

- A natural detergent solution is prepared in deionized water and the glass substrates are gently rubbed with the help of a soft cloth. Washed the soapy substrate first with distilled water and then H₂O-MilliQ.

- The substrates are vertically suspended in Teflon box containing deionized water and put in ultrasound for 10 minutes. Replace the distilled water with MillQ water and leave again in ultrasound for 10 minutes. Dry with Nitrogen.
- Transfer the glasses into another clean Teflon box and put 20ml of trichloroethylene solution for 10 min in ultrasound.
- After trichloroethylene change the substrates to a new Teflon box and put 20ml of acetone solution for 10 minutes in an ultrasound
- Next, the substrates are immersed in 20 ml of ethanol solution for 10 minutes in ultrasound.
- Finally, Dry with N_2 and then in an oven for $100^\circ C$ for 10 minutes.
- After cleaning the substrate, it was treated with an O_2 Plasma at 200 W, 1.4 mbar for 3 min in a plasma cleaner. The purpose of the plasma treatment was not only the surface activation of the SiO_2 surface by adding (-OH) hydroxyl groups, but also removing traces of organic contamination left after acetone and ethanol. The whole process is called hydroxylation as shown in Fig. 3.1(b).

3.1.2.

Deposition of Self Assembled Monolayer (SAM) of organic adhesion layers

After the formation of hydroxyl (-OH) group on the clean substrates, a siloxane bond (-Si-O-Si-) is achieved by deep coating method through the silanization of (3-mercaptopropyl) trimethoxysilane (MPTMS). MPTMS is used as adhesion layer for metal nanostructures due to functional groups at both terminals of the molecules [87, 88]. At one terminal, the silanol group (Si-OCH₃) of MPTMS reacts with Si-OH groups of the modified substrate surface to form siloxane Si-O-Si bond with the removal of H₂O and CH₃OH as shown in Fig. 3.1(c). At the other terminal the thiol group (-SH) of the MPTMS attach strongly to the evaporated gold thin film through the well-known Au-S binding [90]. To achieve the silanization process we immersed the hydroxylated glass into a teflon box containing 2.5% MPTMS in ethanol solution at room temperature for 2 h, followed by rinsing with ethanol and drying under nitrogen flow and placed at $100^\circ C$ for 5 minutes.

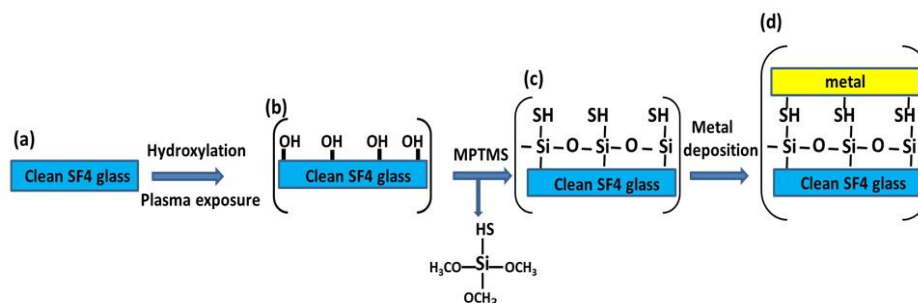


Figure 3.1: Fabrication of SPR platform (a) clean glass substrate (b) hydroxylation leads to hydroxyl group (c) silanization (d) thin film deposition.

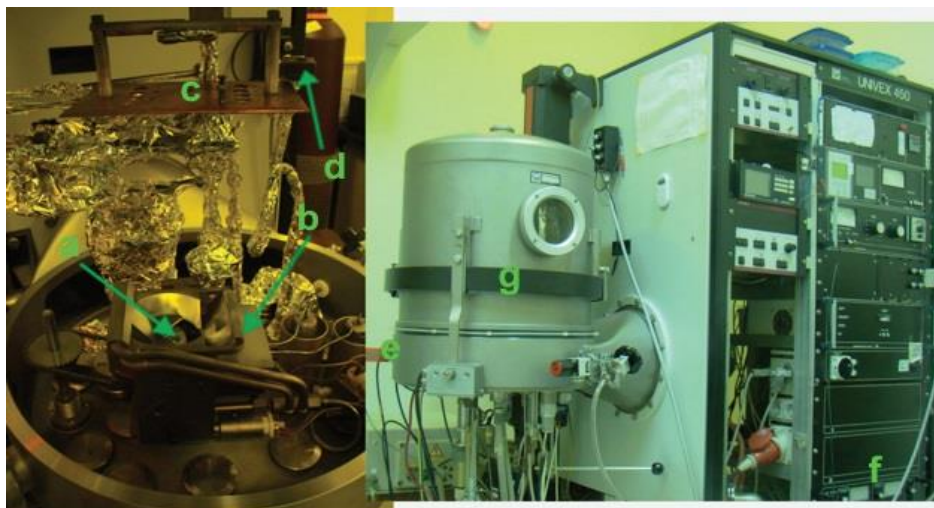


Figure 3.2: Univex 450. (a) crucible with metal pellet, (b) tungsten filament, (c) sample holder, (d) quartz crystal balance, (e) pressure detector, (f) electron gun controller, (g) vacuum chamber.

3.1.3. Electron beam gun assisted deposition

In this technique, electrons are generated by heating a tungsten filament through an external current. This type of emission of electrons is called thermionic emission. These electrons are accelerated by high voltage and focused to hit the target material using a magnetic field. In this work the thin metal films and dielectric SiO_2 layers are deposited by an e-Beam gun apparatus (model Univex 450) in high vacuum (10^{-6} Torr) environment in the clean room of Laboratório de Espectroscopia Óptica e Optoeletrônica Molecular (LOEM) at the Physics department in PUC-Rio. A high vacuum up to 10^{-7} Torr inside the chamber is made by a mechanical pump in series with a turbo molecular. The system is equipped with Pirani and Penning type sensors to measure the low as well as high pressure, respectively.

The copper made rotating stage with multiple crucibles having different target materials enable the e-beam system to evaporate more than one material without breaking the vacuum. The thickness of the deposited layer is measured with Quartz Crystal Microbalance (QCM) with a resolution of 0.01^0 \AA . A tooling factor (TF) is defined in order to make a correction factor of the rate at which the material is deposited on the QCM with the one at which it is deposited on the glass substrate. The exact formula for the TF is given by

$$TF(\%) = TF_i \left(\frac{t_A}{t_{QCM}} \right) \quad (3.1)$$

where t_A is the actual thickness deposit on the substrate, t_{QCM} is the thickness recorded by QCM and TF_i is the initial tooling factor. The new tooling factor is calculated by introducing an arbitrary value of TF equal to 100 in the control panel, and then the actual thickness is measured by profilometer.

All the parameters such as deposition rate, tooling factor, final thickness and the maximum current of the electron beam can be controlled from the control panel of the Univex 450 system. Figure 3.3 illustrate the intensity curve, which is programmed in the control panel. Initially at $t = 0$, there is no current supplied to the filament. The current is turn on during “rise time 1” (RT1), and the power is gradually increased which heat up the target. The power is held constant during “soak time 1” (ST1) to allow the degassing of the target material. In “rise time2” (RT2) the power is again increased to “soak power 2” (SP2) and remain constant over “soak time 2” (ST2). At a stage the system reached to the desired deposition rate and after gaining the stability in deposition rate, we open the shelter to allow the deposition of materials on the glass substrates. The power during the deposition should never exceed the maximum value. Table 3.3(b) demonstrate the list of different parameters used to fully characterize the deposition of metals (Au, Ag and Cr) and dielectric materials (silicon dioxide).

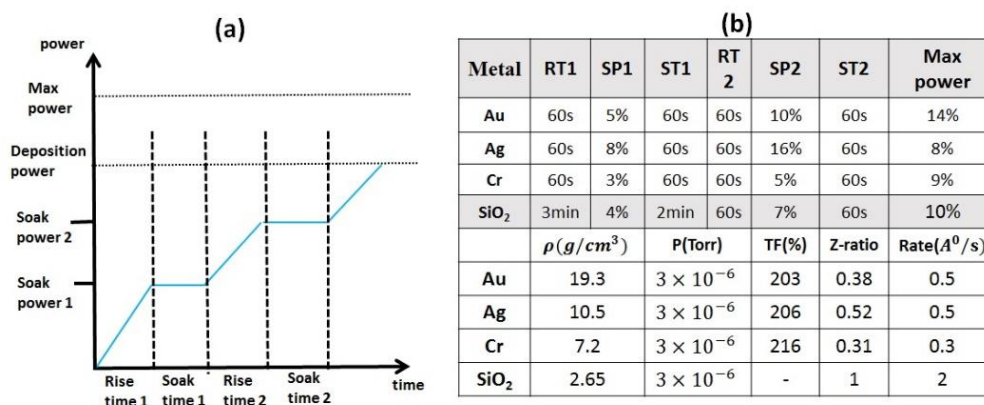


Figure 3.3: (a) Intensity curve of the Univex 450 system (b) the list of working parameters to control the deposition of target materials.

3.1.4. Thermal deposition in vacuum

The working principle of this technique is based on the Joule's effect in which the atoms are removed from the target source by heating under a high vacuum. It is mostly used for deposition of the thin luminescent organic film. The target material to be heated is placed in a crucible generally a boat or a baffle source made of Tungsten, carbon or Molybdenum. The crucible is connected to the metals electrodes and under the low AC voltage the current is slowly increased until the sublimation or evaporation of the materials is reached [91].

The deposition of the thin luminescent organic thin film was performed using a high vacuum equipment LEYBOLD brand Univex 300 located in the clean room of LOEM Laboratory at PUC-Rio. The vacuum chamber of the Univex 300 is inside a glove box MBraun brand that controls O₂ oxygen level and H₂O less than 0.1ppm. The determination of the deposited film thickness is performed through a sensor with a resolution of 0.0001Å / s. The system also has two stabilized voltage sources that supply the current to the crucibles so that the material evaporates. Univex 300 is equipped with two types of pumps, the first correspond to mechanical pump, which allow a pre-vacuum of the order of 10⁻³ mbar and the second one is the turbomolecular pump reach to a final vacuum of the order 10⁻⁶mbar.

We used the Univex for the deposition of two type of organic materials Alq₃ (tris(8-hydroxyquinoline)) and tris(dibenzoylmethane) mono(1,10-phenanthroline) europium (III) (Eu(dbm)₃Phen). Both of them are purchased from Luminescence Technology Corp. (LumTec) with a purity of 99%. Figure 3.4 show the (a) different parts of the vacuum chamber used to control the deposition, the internal structure of the crucible and the glove box.

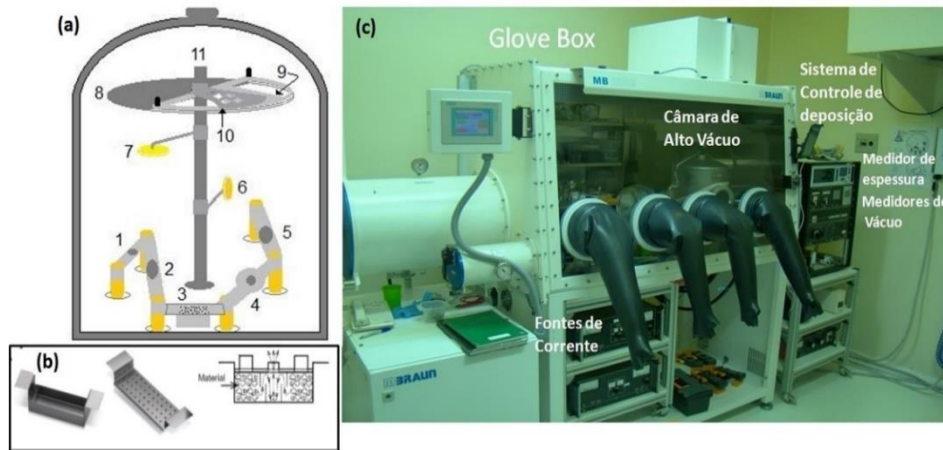


Figure 3.4: (a) Different parts of vacuum chamber: 1-5 are possible places for crucibles, 6-7 are quartz crystal controlling the thickness, 8 is shutter, 9 is a door mask and 10 is the sample holder. (b) Crucible structure and (c) glove box. *Laboratorio de Espectroscopia Óptica e Optoeletrônica Molecular (LOEM) at the Physics department in PUC-Rio.*

3.2. Fabrication of Dielectric Loaded Waveguide (DLWGs)

In section 3.1, we discussed the fabrication of the conventional SPR sensors. In this work, we successfully fabricated the DLWG structure by depositing a thick dielectric layer of SiO_2 over the thin metal surface of the conventional SPR sensors. The fabrication process completes in two step: (i) the hydrolysis and condensation of (3-mercaptopropyl) trimethoxysilane (MPTS) were carried out on the thin gold surface, which leads to the formation of amorphous 2D silica like surface [88]

. After that (ii) a thick dielectric layer of SiO_2 is deposited on the Au/2D silica surface by an electron beam assisted vacuum deposition system.

Prior to the deposition of SiO_2 , a self-assembled MPTS layer on the gold coated substrates was prepared at 0.5 % MPTS concentration in ethanol (for example 30 ml ethanol in 150 μl MPTS) for 90 min at room temperature. In this reaction the thiol group (-SH) of MPTS linked covalently with gold surface while the methoxy group (Si-OCH₃) remain on the top of gold film as shown in Fig. 3.5 (b). To carry out the hydrolysis process, the silanized gold film is immersed in a 0.1 M HCl water solution (0.85 ml of Hcl in 100 ml of MilliQ water) for 6 hours in room temperature. The methoxy groups undergo hydrolysis to silanols (Si-OH) groups as shown in Fig. 3.5(c). Finally, the condensation reaction is carried out at

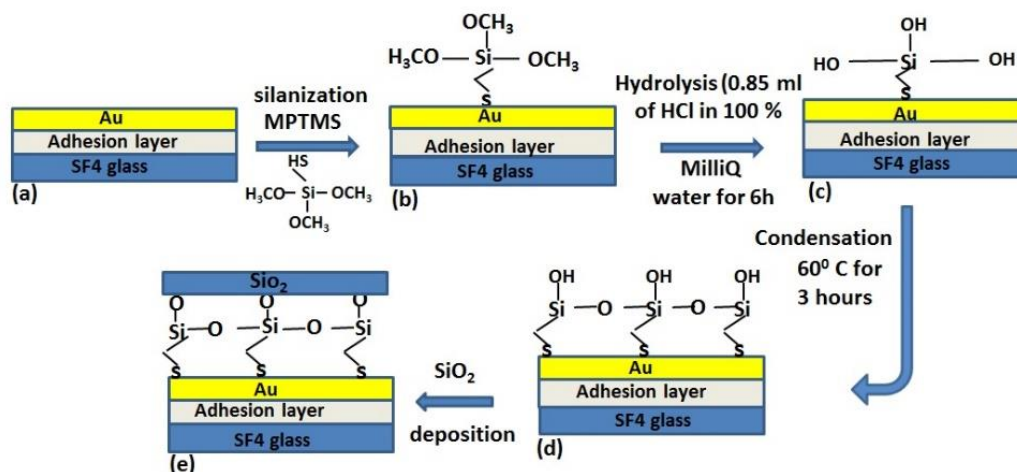


Figure 3.5: Schematic diagram showing the fabrication of the DLWGs. (a) 49 nm gold thin film deposited on clean SF₄ glass. (b) Silanization with MPTS. (c) Hydrolysis process: methoxy groups are converted to Si-OH group. (d) Condensation leads to Si-O-Si network. (e) Deposition of SiO₂.

60° C for 3 hours in oven. During condensation the silanols groups are converted into siloxy (Si-O-Si) network and created an amorphous 2D silica surface called glass monolayer as shown in Fig. 3.5(d). The Univex 450 deposits a thick layer of SiO₂ immediately after the MPTS treated gold thin film. These DLWGs are further used for the characterization of the organic thin film, counting of AuNPs and the determination of the anisotropic properties of graphene.

3.3. Growth and transfer process of Graphene

The Graphene films were grown by the group of Prof. Lazaro in the Department of Physics of PUC-Rio on Cu foils using the chemical vapor deposition method CVD [92].

3.3.1. Chemical Vapor Deposition (CVD)

In this work, the graphene samples were synthesized via chemical vapor deposition (CVD) technique using Copper (Cu) foils (Alpha Aesar, order number 46986, 99.8% purity) as a substrate and methane or ethanol vapor as carbon precursors in a quartz tube furnace as shown in Fig. (3.6). The experimental procedure for graphene growth starts with the cleaning of copper foils. Twenty-five

micrometer thick Cu foils were cut to the desired size and washed in ultrasonic bath with acetone for 5min followed by an immersion in isopropanol alcohol for 5min. The sample were dried by high purity N₂. The cleaned Cu foils were then inserted into a 25 mm (inner diameter) quartz tube, where it is heated at 30 °C/min rate up to 1050 °C under the folw of 2sccm of H₂ at 70m Torr environment. Prior to the growth, Cu foils were annealed for one hour at this temperature in order to remove any generated oxide layer on the Cu. After annealing the Cu films, the methane (CH₄) gas was allowed to enter the chamber with constant flow of 2 sccm for 20min, maintaining a growth pressure of 330 m torr. After the required growth time the system was cooled down at a rate of 300 C/min under H₂ and CH₄ flux at room temperature.

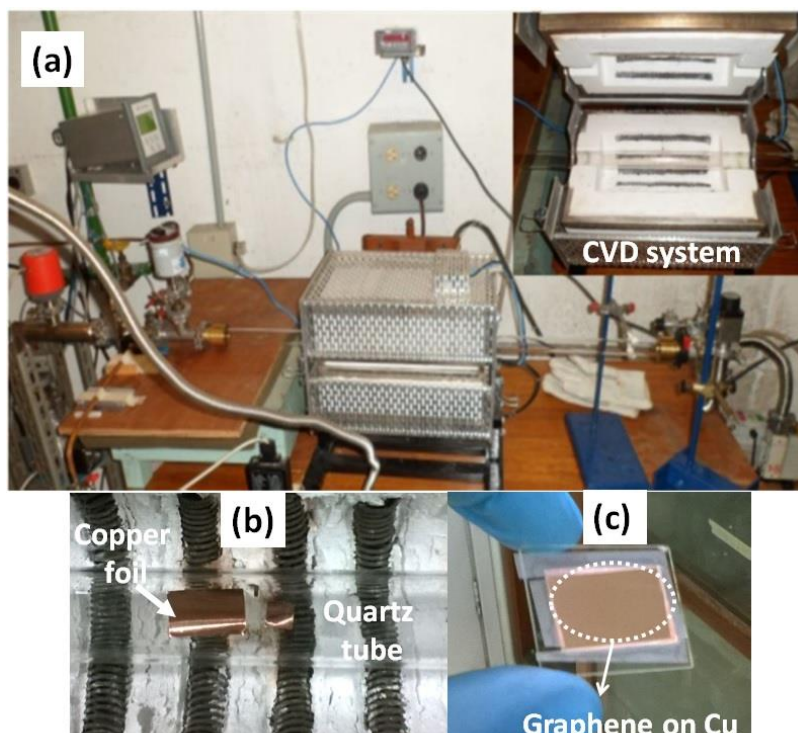


Figure 3.6: Photograph of the graphene growth using CVD technique
 (a) CVD system, (b) copper foil inside the quartz tube and (c) graphene on Cu ready for transfer.

3.3.2. Transfer of graphene on SPR chips

For the transfer on metal thin film a polymeric solution was prepared by dissolving polyurethane (PU) commercial pellets in tetrahydrofuran (THF) solvent

(1% wt). Next, the PU/THF solution was drop casted on the Cu/graphene, following a spin coating at 2500 rpm for 1 min. The Cu/graphene/PU/THF sample was placed inside a chamber for 10 min at room temperature for complete evaporation of THF solvent. Next, the PU/graphene/Cu was heated at 60 °C for 15 min. Chemical attack by iron (III) chloride (1 mol L⁻¹) on hot plate was used to remove completely of copper foil. Figure 3.7 show the photograph of the etching process of copper in FeCl₃. After etching, the graphene/PU film was washed several times in deionized water and transferred to gold/glass and silver/glass substrates. To finalize the transfer process, the sample was dried with nitrogen gas and heated to 60° for 30 min. In the final step, the sample was immersed in THF for 8 h to remove PU as shown in Fig. 3.8(f).

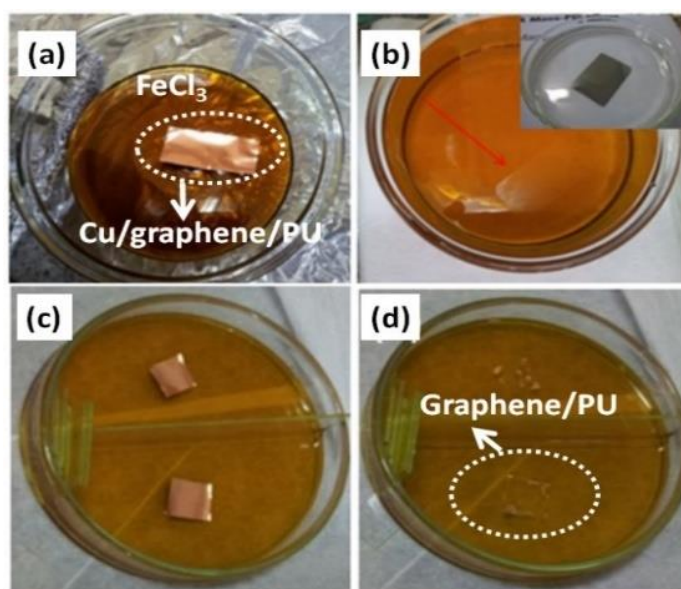


Figure 3.7: (a) and (c) represent etching of copper film using Ferro III chloride (FeCl₃), (d) partial disappearance of copper and (b) total disappearance of copper.

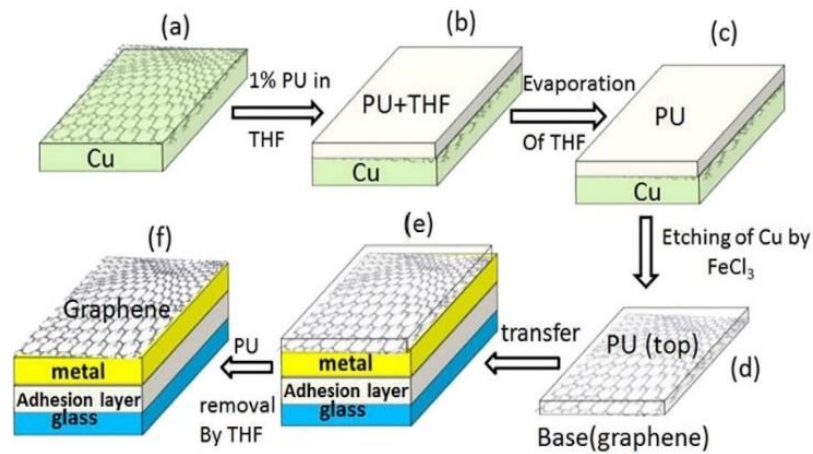


Figure 3.8: Scheme of the etching of copper (a) to (c), (d)-(e) transfer of graphene/PU on the SPR sensor and (f) the removal of PU using THF.

3.4. Structural Characterization

The main aim of this section is to discuss the basic principles of all the characterization techniques used to probe and measure the structure and properties of the fabricated SPR sensors, DLWG and the CVD grown graphene.

3.4.1. Two-color Surface Plasmon Resonance (SPR) spectrometer

This section is dedicated to present a brief description of the experimental setup and procedure used to perform SPR measurement. We begin with a description of the two-color SPR spectrometer in the Kretschmann configuration, and explain in the following the measurements procedures and the working principle of the software used to collect the experimental data.

3.4.1.1. Kretschmann Configuration

The Kretschmann configuration is the most widely used optical system for the excitation of surface plasmons (SP) in thin films. Figure 3.9 show the schematic optical configuration of the SPR system based on angular interrogation scheme. Figure 3.10 display a photograph of a homemade SPR optical device, showing different elements of the experimental setup. In this setup the SPP are excited in attenuated total internal reflection mode using a He-Ne laser (Thorlabs U.S.A, 5 mW) at wavelength of 632.8nm and laser diode of a wavelength of 783nm (Ondax

U.S.A, model LM-783-PLR-75-1, 75 mW). The beam coming from the laser source passes through power attenuators used to adjust the incident intensity of the beam. The pinholes are used for the measurements of the zero-reference angle, and to align on the same optical line the two different laser beams. Subsequently, the beam splitter deflects the incident beam intensity to a photodetector (Model DET36A) which is connected to the oscilloscope to measure the input intensity of the beam. Beyond the beam splitter, a polarizer is used to convert a light beam of undefined polarization into well-defined polarized light. In this setup, a ThorLabs linear polarizer is used to get both p- and s- polarized light.

After passing through the polarizer the light beam reaches to the sample, which is coupled to a triangular prism by using an index matching liquid (Cargille Laboratories, USA). Both the prism and sample are mounted over a motorized rotating stage (Sigma Koki, model SGSP-80Y AW, with controller Shot-202) with a minimum angular step of 0.0025° that allows changing the laser incident angle. A ThorLab detector moving along with the rotating base collects the reflected light coming from the sample. The rotating base, the sample along with prism and the detector are all placed inside a black box made of polypropylene. The output reflected and the input incident signals are finally sent to a personal computer and elaborated by a homemade software in LabView language, which allows real-time monitoring of the SPR response.

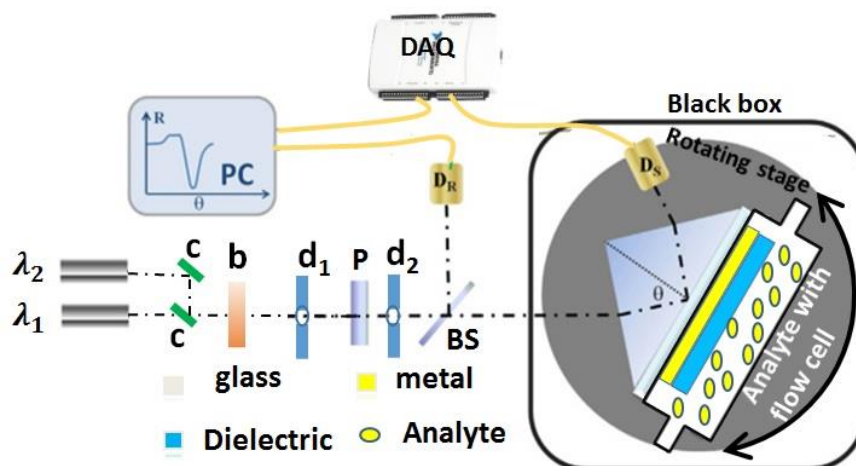


Figure 3.9: Scheme of the optical configuration of our two-color homemade SPR spectrometer in the Kretschmann configuration. It consists of two independent laser sources (λ_1 , λ_2), (b) an attenuator, (c) mirror (d)

two pinholes, (P) a linear polarizer, (BS) a beam splitter, (D_R) a reference detector, (D_S) a signal detector, a PC linked to a data acquisition system (DAQ), and a covering black box. Inside the black-box is visible the multilayer metal-dielectric SPR device and the flow-cell used for analyte injection and sensing (gas or liquid).

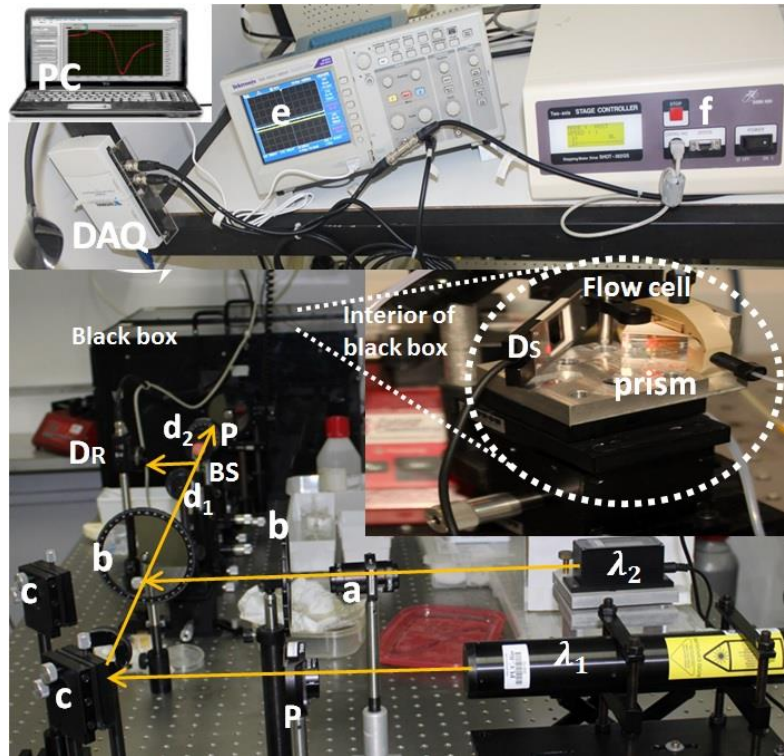


Figure 3.10: Photograph of the two-color SPR spectrometer in the Kretschmann configuration installed in *NanoLaser Lab* at the Department of Physics PUC-Rio. Optical table equipped with two laser sources (λ_1 , λ_2), and different optical instruments, (a) isolator (b) attenuator, (c) mirror (d) pinholes, (e) oscilloscope, (f) stage controller, (BS) beam splitter, (P) a linear polarizer, (D_R) reference detector, and a PC connected to data acquisition system (DAQ). Inside the black box there is a signal detector (D_S), prism and the flow cell.

3.4.1.2. SPR Fluidic channel

The homemade angle interrogation based SPR setup is equipped with a fluidic channel as shown in figure 3.11(a). In this setup, the prism is index matched with the SPR sensor chip and fixed in front of a flow cell in Polyetheretherketone, more commonly known as PEEK, with a volume of 900 mm^3 . All the fluidic connections

are prepared and connected to the flow cell and the flux pump (FutureChemistry, Nijmegen, The Netherland), used for the sensor rinsing and nanomaterials injection. The syringe is filled with the desired analyte and flux with a control rate over the functionalized SPR chip. The prism, SPR chip, flow cell and the detector are mounted on the motorized rotating stage employed for wide range angle scanning. The real time interaction of analyte with the chip surface is monitored at resonance angle, where the SPP wave is excited and propagate at metal dielectric interface. Figure 3.11(b) show the SPP wave excited on the Au/graphene SPR sensor chip.

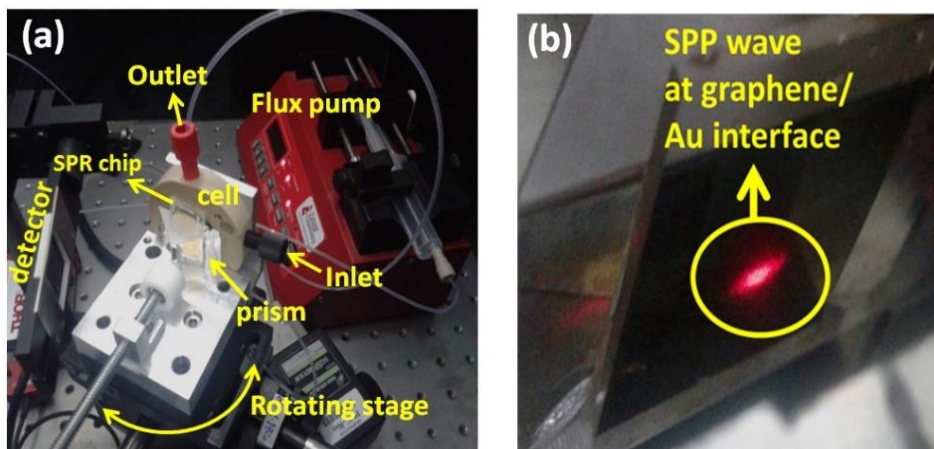


Figure 3.11: Experimental setup of the SPR fluidic channel in PEEK, used to flow the desired analyte and detect in real time.(b) The typical SPP wave on the Au/graphene chip.

3.4.1.3. Internal Reflectivity and angle of incidence

Figure 3.12 represent an isosceles prism with a base angle α . A light beam is incident on the external surface of the prism that make an angle θ_{in} with the line perpendicular to the interface. This angle, which can be directly measured, is called the angle of incidence. Due to the rotation of the platform, the angle θ_{in} changes according to the equation $\theta_{inc} = 0.0025^\circ \times N_s$, where N_s is the number of the step from 0-position to this angle with 1 step = 0.0025° . The sets of angles $(\alpha, \theta_x, \theta_{in}, \theta_{pt})$ defined in the Fig. 3.12 are related with each other by the following equations:

$$\theta_x = \alpha - \theta_{in} , \quad (3.2)$$

$$\alpha = \sin^{-1}\left(\frac{1}{n_p}\right) + \sin^{-1}\left(\frac{1}{n_p}\right) \sin \theta_{in}, \quad (3.3)$$

$$\theta_{pt} = \alpha - \sin^{-1}\left(\frac{1}{n_p} \sin(\alpha - \theta_x)\right), \quad (3.4)$$

$$\theta_x = \alpha - \sin^{-1}(n_p \sin(\alpha - \theta_{pt})). \quad (3.5)$$

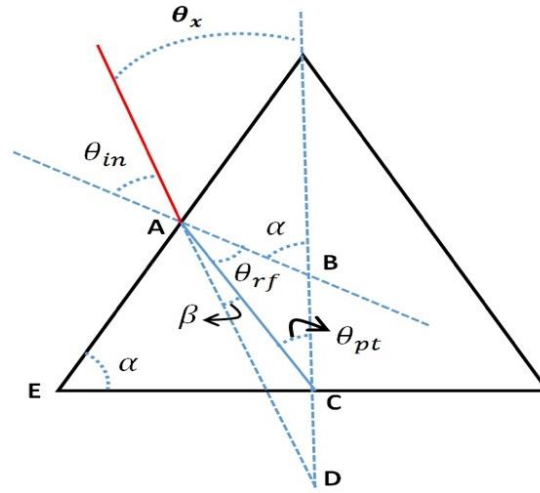


Figure 3.12: The isosceles prism used for SPR coupling, θ_{in} is the angle of incidence that we measure directly with the goniometer, and θ_x is the angle of incidence related with θ_{in} , used by the elaboration data program (Winspall free software).

Where n_p being the refractive index of the prism. The angle θ_x is the angle of incidence that is consider by our software designed for data analysis. The internal reflectivity $R_{in}(\theta_x)$ of the prism strongly depends on θ_x and can be expressed as the product of angle dependent correction factor $C(\theta_x)$ and the masured refelectivity $R_M(\theta_x)$:

$$R_{in}(\theta_x) = C(\theta_x)R_M(\theta_x), \quad (3.6)$$

Here the correction factor account for the reflection of light when it passing the legs of the isosceles prism and is given by the relation [92, 93]

$$C(\theta_x) = \frac{\sin^4(\theta_{ref} + (\alpha - \theta_x)) \cos^4(\theta_{ref} - (\alpha - \theta_x))}{\sin^2(2(\alpha - \theta_x)) \sin^2(2\theta_{ref})} \quad (3.7)$$

where

$$\theta_{ref} = \sin^{-1} \left(\frac{1}{n_p} \sin(\alpha - \theta_x) \right). \quad (3.8)$$

3.4.1.4.

Data extraction software and measurement procedure

A computer running LabView programming language was developed to handle the goniometer motion and the experimental data collected by the detector acquisition board. The written program is capable of measuring on real time the internal reflectivity ($R_{in}(\theta_x)$) as a function of incident angle (θ_x) and also measure the variation in reflected intensity over time at fixed angle. Each experiment first starts with the alignment of the laser beam in which the beam spot should impinge at the sample on the rotation axis of the goniometer. The rotation axis is chosen as a reference because during the angular scan only the points along the axis of rotation remain at the same position. Next step is to search manually the reference angle $\theta_{in} = 0$, where the beam reflected by the external face of the prism should exactly in the center of the pin hole located in the front of the black box. After this condition is satisfied, the goniometer is rest to 0 step.

Besides this, the software allows to control different measurement parameters such as the range of the initial and final steps of the scanning, angular step, mode of polarization (both p and s polarization) and the intensity of reflected and incident laser beam. Figure 3.13 shows the image of the typical SPR spectra collected on the control panel of the software. The SPR spectrum is obtained by measuring the reflectivity ($R_M(\theta_x)$) as a function of N_s , where we can differentiate the resonance angle (θ_R) at which the reflectivity shows a minimum and the critical angle (θ_C) above which the total internal reflection take place. The position of the θ_C depends on the refractive index of the prism n_p , base angle α and the external medium such as air or water. To find the exact position (N_s) of θ_C and hence the base angle, the LabView software first gives a scan of $R_M(\theta_x)$ versus N_s and then the position is manually searched on the screen. In this moment the PC ask the value of N_s at θ_C , the refractive index of the prism and the external medium. When inserted these values, the software automatically calculates the base angle α of the prism and the value of θ_x . At this point, the software generates a file with the values of $R_{in}(\theta_x)$ versus θ_x in the ASCII code for the data processing.

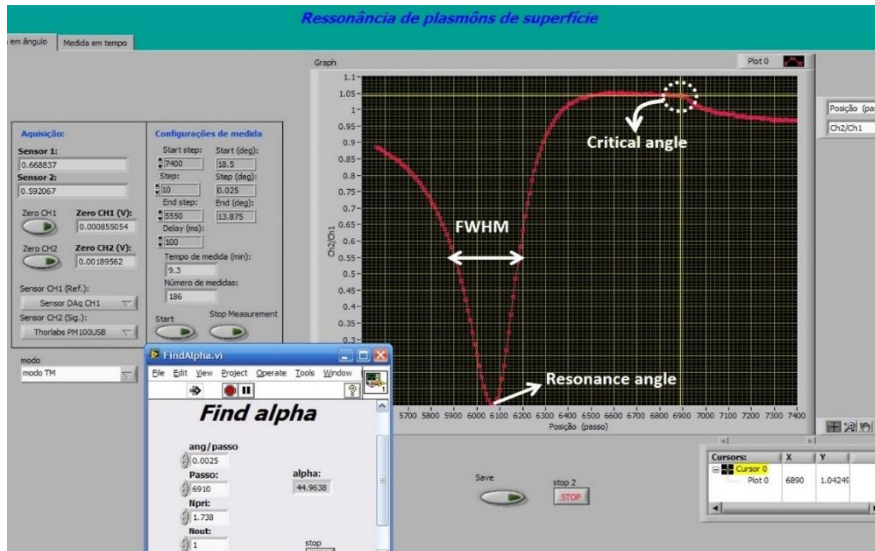


Figure 3.13: The Labview program window for the measurement of the reflectivity SPR curve.

3.4.1.5. Software for Simulation of SPR data

The experimental data obtained from our LabView program was compared with the simulated SPR spectra by using a freeware software Winspall 3.02 [56]. The code written by the group of Prof. Knoll at Max Plank institute for polymer Research, calculate the reflection as well as the transmission of multilayer system using Fresnel equations. Based on the desired experiment, the software allows to consider different parameters such as the type of prism (i.e., triangular, semicircular, cylindrical), the excitation wavelength, light polarization and the number of iterations points. It also has the ability to perform both the manual and iterative simulation. Figure 3.14 display the image of the simulated SPR spectra (continuous line) using the Winspall software and the experimental data (dotted points) for a three-layer system: prism, gold thin film (49nm) and air at a wavelength of 633nm with TM polarization mode. The inset table show the thickness and the complex dielectric constant of each layer. An iterative simulation that minimize the divergence between the simulated and measured data obtains these values.

The Winspall software is very easy to handle the multilayer structures due to control on the different parameters of each layers. Therefore, in the present work, the experimental SPR spectra of different proposed structures were fitted by using the Winspall software, which gives the thickness and the complex dielectric

constant of each layer. If the system shows some variation, then the simulation of SPR spectra determine the new parameters of the modified layer.

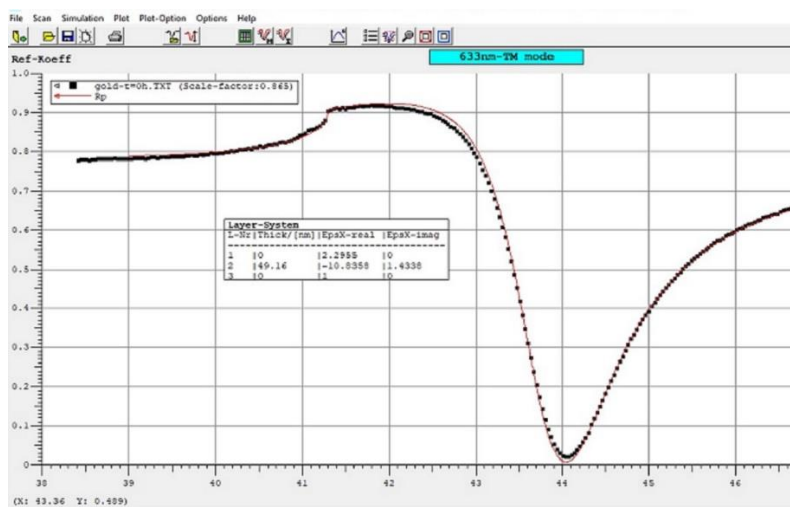


Figure 3.14: Experimental SPR reflectivity spectrum (black dots) fitted using WinSpall, and the simulated SPR curve (continuous line) for a three-layer system: BK7 prism, Au (-10.83+i1.433) and air at $\lambda = 633\text{nm}$.

4 Study of the degradation process of metal-dielectric interfaces in SPR sensing platforms

The plasmonic Nobel metals, such as gold and silver thin films are known to be the most important metals for SPR application and are used to excite the surface plasmons in the visible range. Gold is most widely applied as it has highly stable optical and chemical properties but it is not the best selection to achieve high sensitivity SPR signal. In contrast silver yields the sharpest SPR signal but suffer of poor chemical stability in air, with formation of silver sulphides and oxides [95].

One of the main problems to practical application of plasmonic devices is the chemical instability of the metal dielectric interfaces, which easily oxidize and degrade in time, influencing the performances of the optical devices. Either these problems are arising due to the use of metallic adhesion layer between metal thin film and glass substrates, or it could be the direct exposure of metal thin film to open environment where it can degrade due to interaction with gases and humidity. The use of chromium as metallic adhesion layer enhances the contact between the gold and the substrate but it diffuses to the metal surface and oxidizes, which causes angular shifts and broadening in the SPR curve, with a sever damping of the plasma wave by means of extra absorption and scattering of the SPPs. The surface defects [96] and the lack of phase detection [97] are the two main drawbacks of chromium as an intermediate layer which strongly alter the light properties, reduce the interaction of SPPs with sensing medium, and actually prevent the possibility to perform an accurate determination of the thickness and optical constants of the metal thin film.

Concerning the choice of the metal layer supporting the plasma wave, gold is still considered to be the most widely used metal for plasmonic applications due to chemical inertness and easy fabrication. On another hand, silver is an ideal plasmonic metal in a visible regime with lower damping and having sharp SPR full width half maximum (FWHM) than gold, but presenting a poor chemical stability due to quick oxidation in air. The situation becomes even worse when silver is

subjected to liquids, promoting undesired chemical reactions leading to metal corrosion [97].

To overcome the disrupting effects on the first SiO₂/metal interface (see Figure 4.1) of the SPR devices we propose here the replacement of the metallic adhesion layer with a self-assembled monolayer (SAM) [88] of (3-mercaptopropyl) trimethoxysilane(MPTS). MPTS is a good choice due to its chemical affinity with both SiO₂ and noble metals, low refractive index and small absorption coefficient at visible frequencies.

To inhibit the degradation processes at the outer hybrid interface we investigate two different methods: the encapsulation process of the device, which passivates the external surface of the sensor in a nitrogen atmosphere, and the transfer of a SLG on the outer surface of the sensing platform. Graphene, a two-dimensional (2D) one-atom thick carbon sheet, offers in fact the prospect of preserving the optical properties of the SPR devices, due to its extremely low permeability to all gases and liquids, thus providing a chemically inert protection barrier [97, 98].

Along the chapter, we investigate in details the degradation process of the metal-dielectric interfaces constituting the SPR sensing platforms both in air, nitrogen and water environment along 24 hours, by using SPR spectroscopy in the angle interrogation scheme together with AFM microscopy. We monitored the changes occurring in time with the SPR reflectivity curves for different device configurations, and associated the changes to the modifications of the external surface of the SPR device as observed by AFM microscopy. A scheme describing the general configuration of the SPR sensing platform is represented in Figure 4.1.



Figure 4.1: Structure of the most general SPR multilayer platform, consisting of metal, adhesions and dielectric layers. The dielectric layer can be protected with a thin film of different nature.

For the present study, we used MPTS or Cr as first adhesion layers, Ag or Au thin film as plasma supporting layers, MPTS as second adhesion layer, and SLG as protecting external layer. We tested both DLWGs and single mode SPR platforms, and investigated their behavior in air, nitrogen and water environment.

The first part of the chapter is related to the operation of the SPR devices in air and nitrogen. In the second part, we investigate the degradation and stabilization processes of the different sensing platforms in deionized (DI), and analyze the performances of the MPTS/Au, Cr/Au and MPTS/Au/graphene devices as refractive index (RI) sensors, using different concentration of glycerin in DI water as external medium.

4.1. SPR sensing platforms in air and nitrogen

4.1.1. Monitoring of the reflectivity curves of single mode SPR sensing platforms

The stability of silver or gold plasmonic thin film devices with MPTS as adhesion layer was investigated for the bare metal samples without any protection, typical OLED encapsulation (nitrogen environment) and graphene protected sample. The study was carried by monitoring the shift in resonance angle and FWHM of the SPR curves along a period of 24 h. The temperature was maintained at a value of 23 °C with a humidity of 50%. The measurements have been repeated on 5 different batches of samples, and the results have been averaged and represented in Figures 4.2(c) and (d). The behavior in time of the SPR curve of the bare gold surface without the MPTS adhesion layer is shown in Figure 4.3(a). In this case both the resonance angle and the FWHM of the SPR curve are rapidly increase in time together with an increase in the minimum level of reflectivity. In Fig. 4.2 (b) it can be seen that the SPR angle show strong shift on bare gold surface when compared to the gold/graphene bilayer.

The variation in the FWHM of the SPR curves for proposed devices is shown in Figure 4.2(c), where a small change of about 1.65% is observed for the Au/encapsulated sample. The bare Ag and the Cr/Au show the rapid increases in the FWHM, which show the poor chemical stability of both the sensors and thus limit its use for the application in SPR spectroscopy. For the devices with OLED

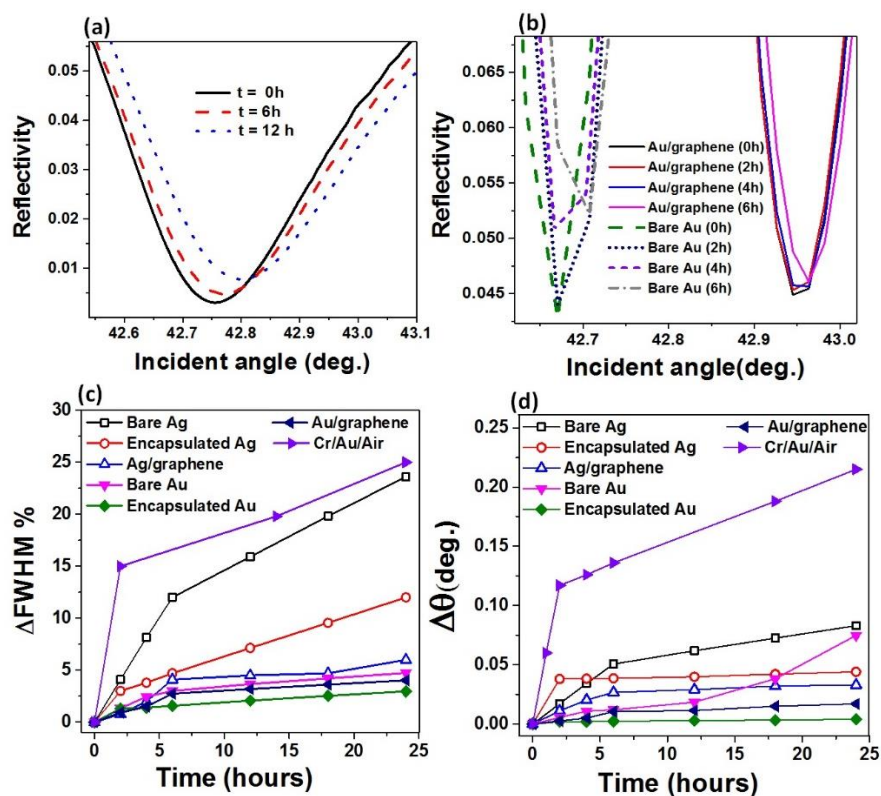


Figure 4.2: (a) Time dependence of the SPR curve of bare gold devices without MPTS adhesion layer. (b) Comparison between the time dependence of the SPR curve of bare gold samples with MPTS adhesion layer and gold devices protected by graphene. (c, d) Variation in time of the FWHM and resonance angle θ of the SPR spectra of samples with different architectures and MPTS as adhesion layer: bare metals, samples with OLED encapsulation and graphene protected devices [100].

encapsulation, we observed a shift smaller than 0.005° up to 4 h, in consistence with the zero-angle determination in SPR spectroscopy, as highlighted in Fig. 4.2(d). The worst scenario is again represented by the use of unprotected silver films, where degradation of the $\text{SiO}_2/\text{MPTS}/\text{Ag}$ interface might be accompanied also by chemical reactions with oxygen and Sulphur atoms happening at the Ag/Air interface, although the protection with graphene layer is known to prevent these surface modifications [99].

Essentially, the entire SPR platform consists of two main interfaces that may degrade with time. The first one is the MPTS/metal lower interface and the other one is the external metal/air interface that is exposed directly to the surrounding environment. In external metal/air interface, the metal surface may modify due to chemical reactions and the rearrangement of the nanostructured thin film, which

degrade the SPR signal. Another possible reason of the degradation of SPR curve is the delamination of the lower MPTS/metal interface. The undesired reactions might form defects into the metal/SiO₂ interface and inducing a partial delamination of the metal.

4.1.2. AFM measurement on single mode SPR sensing platforms

To clarify the role of the Metal/Air interface in the degradation of the SPR response of the devices, we monitored the bare metal surface of silver and gold thin film with and without the MPTS layer along 6 and 24 h by AFM microscopy, respectively. Particular attention was paid to the measurement of the average roughness R_A of the metal surfaces, a parameter that is proportional to the losses of the surface plasmon polariton (SPP) [25] and influences the FWHM of the SPR curve. In Table 4.1 are reported the values of the parameter R_A measured in the same region on fresh and aged metal thin film. The corresponding AFM images, taken in frames of $1.0 \mu\text{m} \times 1.00 \mu\text{m}$, are represented in Figures (4.3) and (4.4), respectively for silver and gold thin film with (A, B) and without (C, D) the MPTS layer.

Table 4.1: Average Roughness (RA) of freshly and aged metal layers (Ag, Au) deposited on glass slide surface, with and without MPTS adhesive layer. Similar results have been obtained analyzing different regions of the samples.

Ag Samples	$R_A(\text{nm})$ $t = 0$	$R_A(\text{nm})$ $t = 6\text{h}$	Gold Samples	$R_A(\text{nm})$ $t = 0$	$R_A(\text{nm})$ $t = 24\text{h}$
Ag-with MPTS	1.53	1.43	Au-with MPTS	3.43	3.48
Ag-without MPTS	1.83	1.91	Au-without MPTS	3.36	3.31

The values of the R_A parameter for both the silver and gold films are in good agreement with the literature [100, 101] and is surprising the reproducibility of the images both for Au and Ag, respectively after 6 h and 24 h. The AFM images confirm that the upper interface of the plasmonic devices is not responsible for the changes of the resonance angle and FWHM of the SPR spectra in time, since no significant variation of R_A was observed with aged samples.

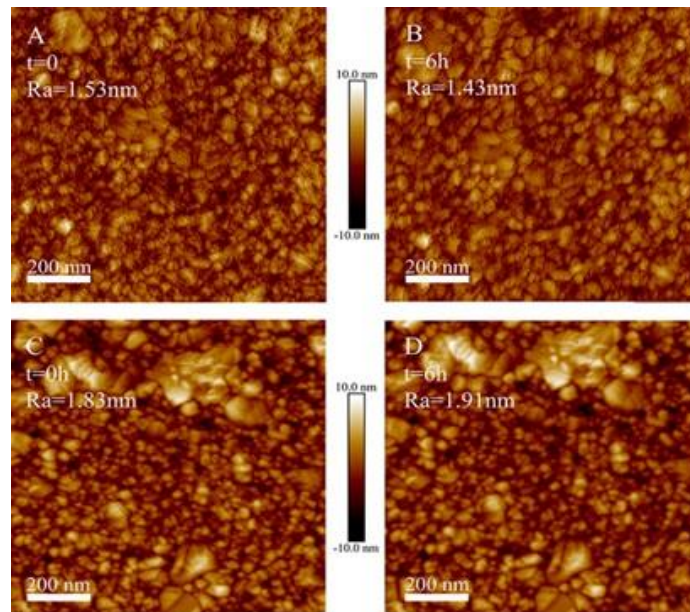


Figure 4.3: Peak Force Tapping™ AFM images of silver layer on glass slide silanized with MPTS (A–B) and without MPTS (C–D). The surface roughness average on $1 \times 1 \mu\text{m}$ images was measured with a fresh substrate ($t = 0$) and after 6 h. For all the images, we used a scan rate of 0.95 Hz and scan size of $1 \mu\text{m}^2$ [100].

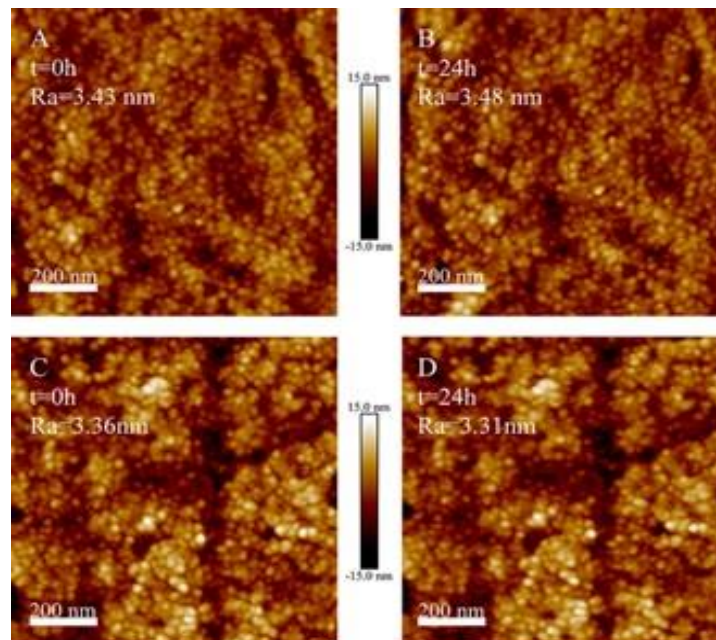


Figure 4.4: Peak force Tapping™ AFM images of gold layer on glass slide silanized with MPTS (A–B) and without MPTS (C–D). The surface roughness average on $1 \times 1 \mu\text{m}$ images was measured with a fresh substrate ($t = 0$) and after 24 h. For all the images, we used a scan rate of 0.95 Hz and scan size of $1 \mu\text{m}^2$ [100].

The shift of the SPR angle in time represented in Figure 4.2(d) can be hardly attributed to metal surface chemical reaction with air due to the inertness of gold, and is more probably associated to the progressive detachment of the metal at the glass interface. The delamination may arise due to either the partial oxidation of sulfhydryl (-SH) group, which may be cause the formation of disulfides bridge (RS-SR), or to the water humidity which can progressively break the siloxane (Si-O-Si) groups [103]. These undesired reactions might be responsible for the growth of defects into the metal/SiO₂ interface and final detachment of the metal thin film. The detachment would result in the creation of an air/metal nanocomposite layer, with degradation of the optical coupling between the laser and the plasmonic device and broadening of the SPR curve. Using Fresnel's reflection equations and transfer matrix method [104], we simulated the angle dependent SPR curves of the devices, and verified that effectively the propagation constant of the SPP would be increased by the creation of an air or air/metal gap between SiO₂ and the metal. The result of the simulation for a gold thin film is shown in Fig. 4.5, where an angular shift of about 0.015⁰ degrees is obtained introducing an air gap up to 40 nm between the gold and SiO₂. Although these results represent only a simplified and rough modeling of the detachment process, it takes in account the variation of the SPR curves observed experimentally.

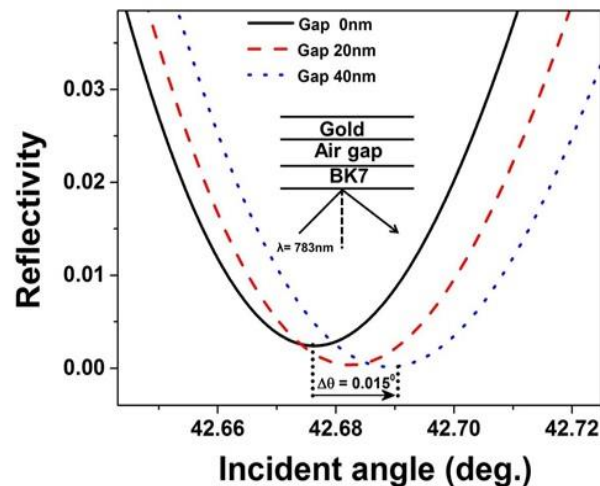


Figure 4.5: Simulation of the effect that the metal delamination process has during its first phase on the SPR spectra of a gold plasmonic device. An angular shift of about 0.015⁰ is obtained introducing an air gap up to 40 nm between the gold and SiO₂ [100].

4.2. SPR sensing platforms in DI water

In previous section, we demonstrated that the stability of the SPR sensors operating in air can be enhanced by taking protection against the environment through typical OLEDs encapsulation technique or graphene layer and confirm that the instability was occurred due the partial delamination of the metal thin film. In this section, the effect of organic and metallic adhesion layers in the stabilization process of different kind of metal-dielectric interfaces supporting surface plasmon polaritons (SPP) is studied upon interaction with water by surface plasmon resonance (SPR) spectroscopy and AFM.

The main objective is the stabilization of the metallic-dielectric interfaces in water environment, in order to use the SPR platform for both optical sensing and accurate ellipsometric characterization of transparent dielectric thin film.

4.2.1. Monitoring of the reflectivity curves of single mode Au based SPR sensing platforms in DI water

Figure 4.6 represents the behavior of the Au based devices. The measurements performed with and without MPTS in air environment are also shown for comparison. When no adhesion layer is used, both $\Delta\theta_{\text{SPR}}$ and ΔFWHM increase continuously with a divergent behavior before 24 hours. This result is obviously due to a progressive delamination of the Au film from the SF4 substrate [100]. In contrast, an approximate angle shift of about 0.004° is observed along 5 hours for both the high (Cr/Au/H₂O) and low (MPTS/Au/H₂O) SPP damping interfaces, which is comparable to the zero-angle indetermination in SPR spectroscopy. In the low damping case, a better stability was observed in water environment as compared to air, where fast oxidation of the thiol group (-HS) and formation of disulfides (R-S-S-R) [103] may occur. Interestingly, a smaller FWHM is obtained with the use of MPTS, which theoretically leads to a sharper Lorentzian profile of the SPR reflectivity curve and decreased SPP damping, resulting in a higher sensitivity of the sensor [89].

Figure 4.7 show the details of the SPR reflectivity curve relative to the fresh SF4/Cr/Au and fresh and aged SF4/MPTS/Au interfaces. In the inset is reported a table containing the value of the imaginary part of the dielectric constant of gold as measured by SPR spectroscopy. It can be seen clearly that the presence of the

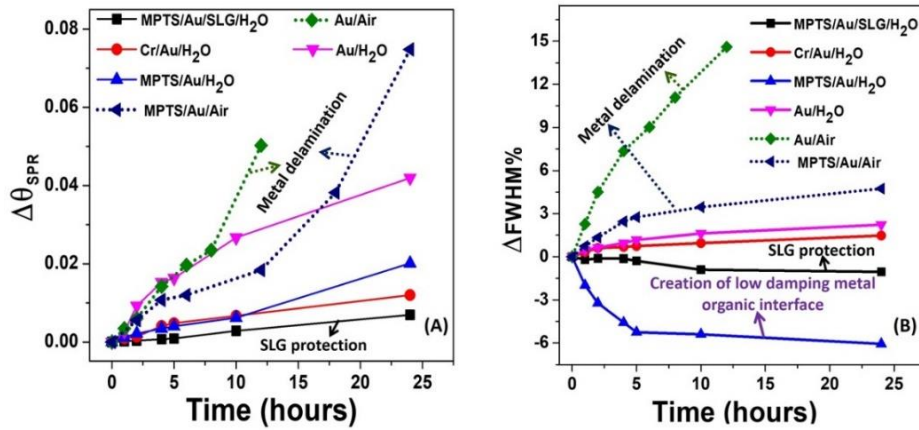


Figure 4.6: Influence of graphene transfer and Au/SF4 interface adhesion layer on the temporal stability of (a) the SPR angle ($\Delta\theta_{\text{SPR}}$) and (b) FWHM. The continuous and dashed lines are relatives to water and air environments, respectively.

metallic Cr adhesive layer broadens and distorts the SPR curve [73] due to enhanced absorption of plasmon resonance energy at the glass/Au interface. The enhanced absorption is related to the intrinsic higher imaginary part of the dielectric constant of Cr, and intermetallic diffusion of Cr into Au thin film during e-beam deposition, leading to a nanostructured metal-dielectric interface [105].

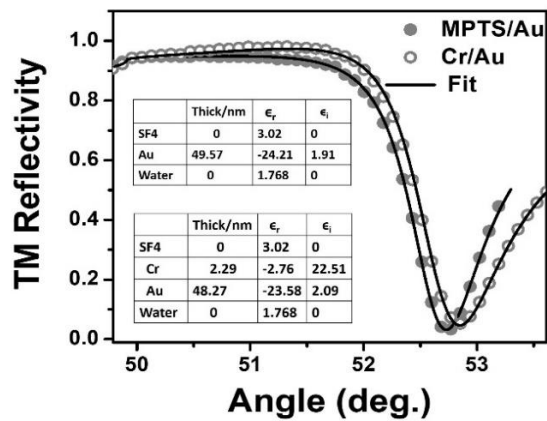


Figure 4.7: Comparison of low damping and high damping SPR curve.

The reduction of SPP interface damping when organic molecular layers are used is consistent with the observations reported by H. Shen and co-workers [106], where a narrower LSPR line width was observed for gold nanocylinders fabricated on glass using MPTS as adhesion layer. Our results suggest that MPTS not only acts as efficient organic ligand at the SF4/Au interface, but it reacts in water

environment promoting a reorganization of the Au nanostructure which leads to diminished SPP damping and enhanced plasmonics properties of the Au thin film. This interaction between water and the metal-dielectric interfaces is quenched after graphene transfer printing over the gold surface, as demonstrated by the stability curves in Figure 4.6(b). In this case, we observed a change in SPR angle of about 0.0007° along 5 hours, highlighting and confirming the high impermeability property of graphene to gases and liquids [98]. The results suggest that proper engineering and fabrication of stable SPR sensors with high sensitivity and low SPPs interface damping should include an initial dip coating of the MPTS/Au device in water environment along 24 hours, followed by transfer of graphene over the dried metal surface.

4.2.2. Monitoring of the reflectivity curves of single mode Ag based SPR sensing platforms in DI water

We also conducted a series of similar measurements replacing Au by Ag thin film. Figure 4.8(a-b) represents $\Delta\theta_{\text{SPR}}$ and ΔFWHM for Ag in three different situations: (i) without adhesion and protection layer, (ii) with Cr or MPTS as adhesion layer, and (iii) graphene protected layer. As in the case gold thin film, the measurements performed with MPTS in air environment are also shown for comparison as dashed lines.

When the adhesion layer is not present, both the parameters of the reflectivity curve rise up in a few hours, indicating a fast delamination of the silver film in DI water. Different from the results obtained for gold, the silver sensors present a better angular stability in air than DI water. When the latter is used as external medium, the temporal shift in the SPR resonance angle is one order of magnitude bigger than the gold-based sensor, indicating a rapid degradation of the plasmonic devices, due to chemical surface reactions and morphological changes occurring at the metal/H₂O interface supporting the plasma wave. Two main chemical reactions happening on the external surface of the silver thin film involve solubilization of preexisting surface Ag₂O [107] in water as silver hydroxide and sulfidation of Ag⁺ ions solubilized in water, with the formation of Ag₂S.

In the first mechanism the solid oxidized silver surface is in equilibrium with hydroxyl groups and Ag⁺ ions dissolved in water according to the reaction [108]:

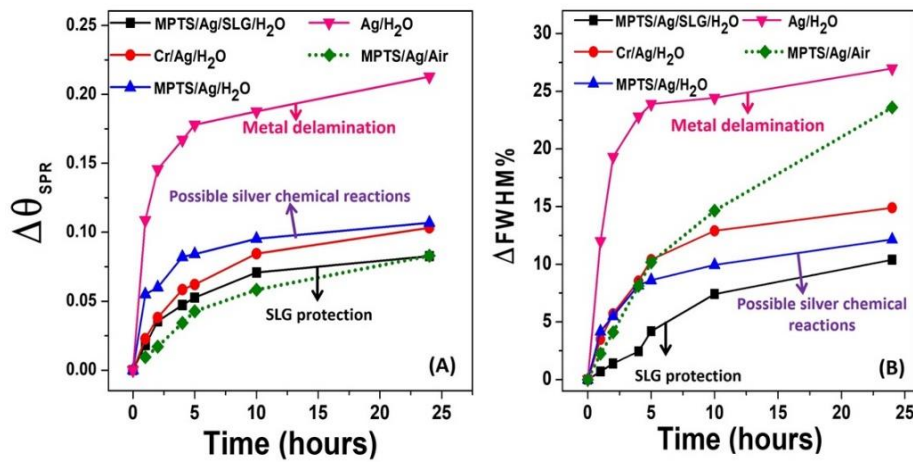
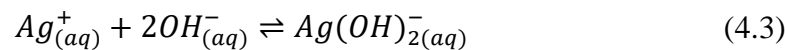
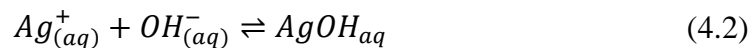
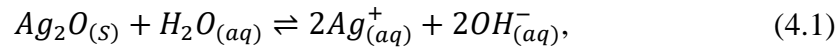
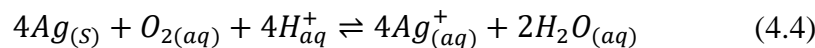


Figure 4.8: Influence of adhesion, without adhesion layer and graphene-protected layer on (a) the variation of SPR angle, and (b) FWHM for Ag thin film as a function of time in air and DI water.



Anyway, when metallic silver is in a water environment in contact with atmosphere, the absorption of ambient CO_2 gradually acidifies by decreasing the pH of the solution and promoting the formation of CO_3^{2-} (carbonate) with the additional Ag^+ ions release from the dissolution of metallic Ag, following the reaction [108]:



All the previous reactions contribute significantly to the solubilization of silver ions in the solution. The presence of the Ag^+ ions was confirmed by inductively coupled plasma mass spectrometry (ICPMS) measurements before and after immersion of the thin silver film in the deionized water solution. The observed concentration of Ag^+ ion after immersion of Ag thin film in 5 ml DI for 30h was 0.015ppm.

Also X-ray photoelectron spectroscopy (XPS), was carried out to investigate the potential oxidation of silver thin film before and after the immersion in DI water. Although we did not observe any oxidation of silver, but the concentration of the carbon increases after treatment of water, indicating the absorption of CO_2 from atmosphere. The XPS spectra is shown in Appendix A.3. This kind of corrosion process might be accompanied by an enhancement in the roughness of the metal surface, and be responsible for the progressive increase of FWHM.

4.2.3. AFM measurement on single mode SPR sensing platforms after immersion in DI water

To support the SPR results, the AFM characterization was performed to examine the physical appearance of gold surface in MPTS/Au structure. Figure 4.9 displays the morphology (A, C) and phase (B, D) images scanned over $2\ \mu\text{m} \times 2\ \mu\text{m}$ surface of 49nm thick Au before and after 44 hours' immersion in DI water. From these images the difference in surface morphologies are clearly observed, the fresh gold thin film deposited over MPTS SAM [Fig 4.9 (A)] shows a root mean square (rms) surface roughness of 1.94nm, while the same sample after DI water treatment over 44 hours indicates a surface roughness of 1.38nm [Fig 4.9 (C)]. All the AFM measurements were performed in the *MicroFlow ChemLab* in a collaboration with Prof. Omar Pandoli at Department of Chemistry of PUC-Rio. This decrease in RMS roughness of gold surface shows consistency with SPR results, where we observed the decrease in FWHM of SPR curve, which could be attributed to a smooth gold surface. This peculiar behavior may be attributed to the rupture of the strained siloxane (Si-O-Si) chains of the SAM of MPTS, in which the electronegative oxygen of water (OH^-) binds to the bound Si^+ and the water H^+ saturates the siloxane O, thus increasing the bond length and eventually breaking the siloxane backbone [103]. The created open linkage (Si-O), may then react with the water molecule to form silanol group (Si-OH), with final rearrangement of the SF4/MPTS/Au interface. Moreover, the AFM phase images before [Fig. 4.9(B)] and after [Fig. 4.9 (D)] immersion in DI water are uniform and did not reveal any variation in the chemical composition of gold.

Figure 4.10 shows the AFM morphology (A, C) and phase (B, D) images of 49nm Ag thin film deposited over MPTS salinized substrates. As can be seen the root mean square roughness of fresh sample is 3.71nm (Fig.4.10 (A)), while the one treated with DI water is 3.79 nm in $2\ \mu\text{m}^2$ area (Fig.4.10(C)). These results show that there is no pronounced effect on the surface roughness after water treatment. AFM phase images were recorded at room temperature on fresh 49nm Ag films deposited on MPTS salinized substrates as well as the same films treated with DI water for 44 hours. Figures 4.10 (B) and (D) shows the phase images of as deposited

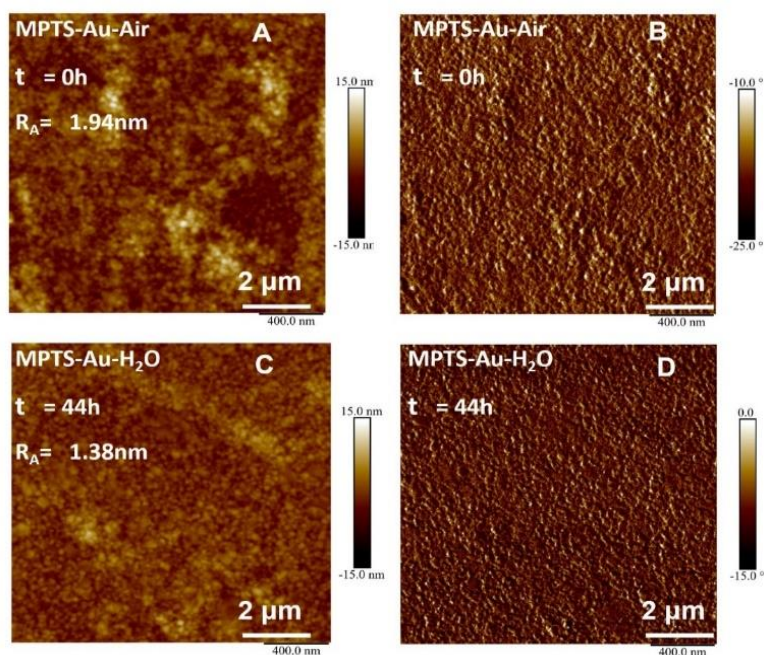


Figure 4.9: AFM images of 49nm gold thin films deposited over SF4 substrates with MPTS as adhesion layer. Morphology (left side) and phase (right side) images were taken before (A, B) and after (C, D) immersion in water for 44 hours.

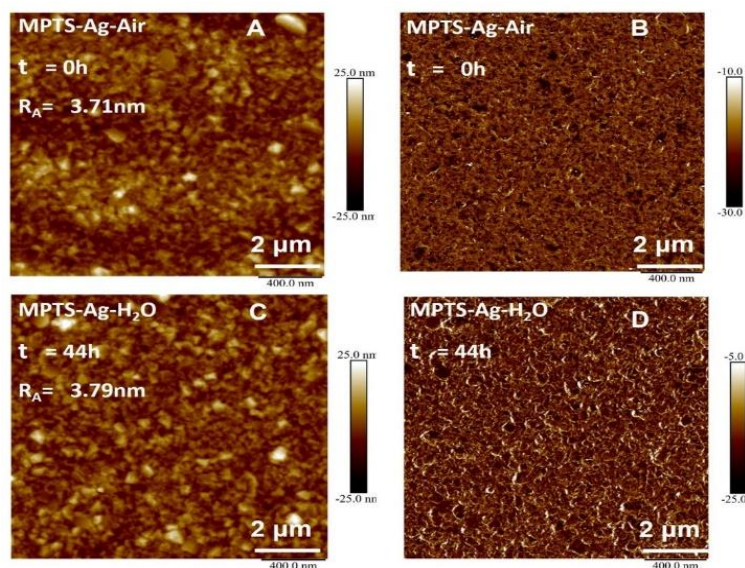


Figure 4.10: AFM images of 49nm silver thin films deposited over SF4 substrates with MPTS as adhesion layer. Morphology (left side) and phase (right side) images were taken before (A, B) and after (C, D) immersion in water for 44 hours.

and treated film in water respectively. We did not observe any contrast in the phase image of as deposited film and DI treated film, which doesn't shows the presence

of a new phase. The AFM results hence confirm that the Ag/water interface is not responsible for the degradation of SPR characteristics in time, so that the most probable reason for the degradation could be detachment of the thin silver film, with the insertion of water molecules at the SiO₂/MPTS interface.

In order to give a complete picture of the delamination behavior on the SPR curve, we performed simulation of the five-layer model using Fresnel's reflection equations and transfer matrix method [104]. Figure 4.11 (a) shows the simulated SPR curves of the five-layer structure by considering water as an intermediate layer between glass and silver. The real and imaginary parts of the dielectric function of silver were taken from [50] at a wavelength of 783nm, while the gap thickness was changing from 0nm to 30nm with an increment of 5nm. The results demonstrated that the surface plasmon resonance angle and FWHM of the SPR curves increases with the gap thickness as shown in Figure 4.11 (b). For instance, an SPR angle shift of about 0.03° is obtained for a gap thickness of 30nm. Based on these results, we conclude that the delamination process significantly contributed to the variation of plasmonic characteristics of the Ag based devices as observed experimentally.

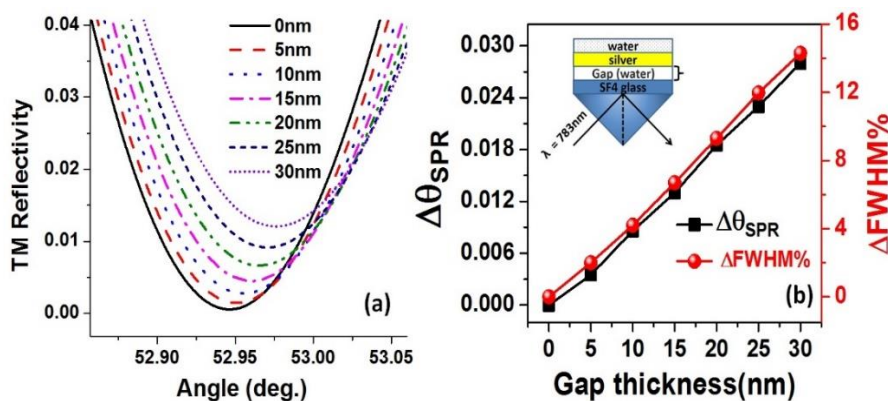


Figure 4.11: The simulated SPR curves for different gap thicknesses induced by the delamination of the Ag thin film from the SiO₂ substrate. For a water gap thickness of about 30nm, we obtained an angular shift equal to 0.03°. (b) The change in resonance angle and FWHM as a function of gap thickness.

4.2.4. Au based DLWGs in water

We extended the stability study to the DLWG structure studied in section 2.4. We fabricated DLWGs by depositing a thick dielectric layer of SiO₂ over the

silanized Au thin film through the procedure explained in section 3.2. Before the deposition of SiO₂ we immersed the sample into DI water for 24hours in order to stabilize the SF₄/MPTS/Au interface. Figure 4.12 (a) show the TM SPR reflectivity curves of the DLWG in DI water. Table 4.2 represent the optical parameters of each layer involving in the DLWG. We observed a maximum shift in the SPR angle of about 0.005° after almost 5 hours as shown in Figure 4.12(b).

Table 4.2: Optical parameters of DLWGs structure obtained at 633nm.

Layer	Thickness (nm)	ϵ_{real}	ϵ_{imag}
SF4 prism	0	3.06	0
Gold	45.47	-11.35	1.47
SiO ₂	611	2.12	0
Water	0	1.77	0

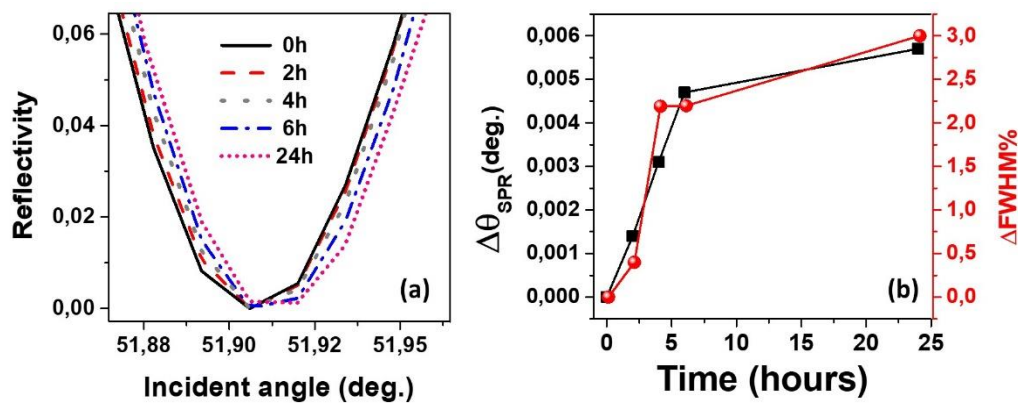


Figure 4.12 (a) SPR reflectivity curve collected for the stability of DLWG in water at excitation wavelength of 633nm for different time. (b)

The waveguide was stable up to 5 hours with almost no changes in the FWHM.

This resonance shift is comparable to the zero-angle indetermination of the SPR spectroscopy, signifying that the presented fabrication and stabilization process is effective, and results in low-damping, highly stable SPR sensing platforms.

4.3. Refractive index (RI) Sensitivity analysis

In order to assess the influence of the adhesion layers and SLG on the performance of the SPR sensors, we measured the sensitivity of the SPR sensing

platforms in different configurations. The sensitivity measurement of Cr/Au, MPTS/Au and MPTS/Au/SLG interfaces was performed in DI water and glycerol solution. (DI: glycerin = 6: 1). For all the samples with different interfaces, first we measured the reference TM reflectivity at the wavelength of 783nm in DI water. The parameters of the thin films constituting the sensing platforms were fitted with the *Winspall* software, considering a refractive index equal to 1.329. After, this the glycerol solution was injected with the fluidic cell at 0.3min/sec (as shown in section 3.4), and the SPR curve was recorded again. The refractive index of the glycerol solution, equal to 1.351, was calculated from the fit of the experimental SPR curve using the *Winspall* software.

Figures 4.13 (a-c) shows the shift of SPR angle with the change of the refractive index of the bulk from 1.329 (solid black) to 1.351 (dashed grey) collected at wavelength of 783nm, for the bare Cr/Au and MPTS/Au and MPTS/Au/SLG sensing interfaces. The RI change in the sensing medium induces the resonant angular shift of 1.212° , 1.318° and 1.352° for Cr/Au, MPTS/Au and MPTS/Au/SLG, respectively. In the case of Cr/Au interface, the RI sensitivity ($S_{RI} = \partial\theta/\partial n$) was $56.9 \text{ deg. RIU}^{-1}$, while for the MPTS/Au and MPTS/Au/SLG interfaces was $61.8 \text{ deg. RIU}^{-1}$ and as $63.5 \text{ deg. RIU}^{-1}$, respectively.

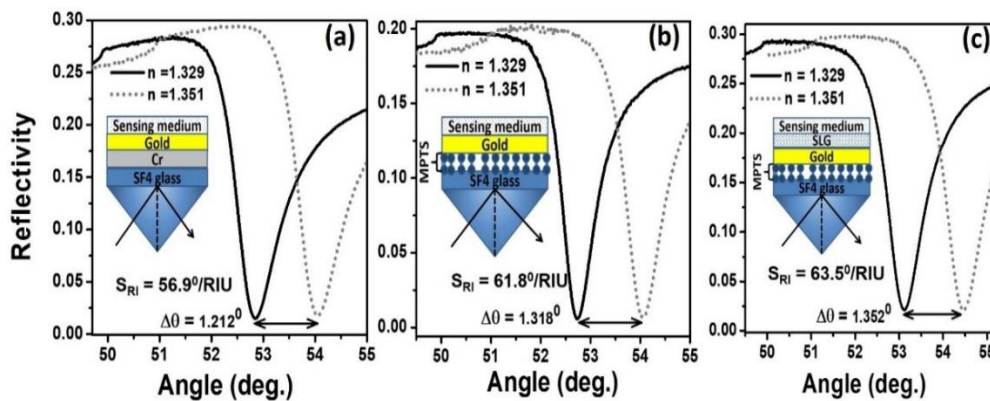


Figure 4.13: (a) Experimentally calculated RI sensitivity for various concentration of glycerin in deionized water using Cr/Au, MPTS/Au and monolayer graphene coated Au thin film sensors.

An interesting observation is that the MPTS/Au structure showed 8% increase in RI sensitivity than Cr/Au, which is attributed to the low plasmon damping effects of the MPTS due its smaller imaginary part of dielectric constant. The perturbation of the SPPs emerges from the imaginary part of the dielectric function of the

metallic adhesion materials, which introduces the damping by both scattering and absorption processes, leading to red shift, broadening of the curve and decrease of the sensitivity.

Figure 4.14 compares the electric field strengths and propagation lengths into water for the SF4/Cr/Au and SF4/MPTS/Au SPR sensors, near the resonance condition excited at 783nm. In the case of SF4/MPTS/Au sensor, the field strength at the sensor surface is not only higher in magnitude, but extend largely into water as compared to SF4/Cr/Au sensors. As evidenced from the above comparison, the structure with MPTS as adhesion layer exhibits the best sensor performances in terms of narrowest curve, intensity and extension of the SPR modes into analytes. To perform the modelling of the near electromagnetic field we considered the refractive index values reported in Table 4.3 of Section 4.2.1, and used the MATLAB written program to calculate the magnitude of the electric field in the z-axis for the resonance mode of 52.8°

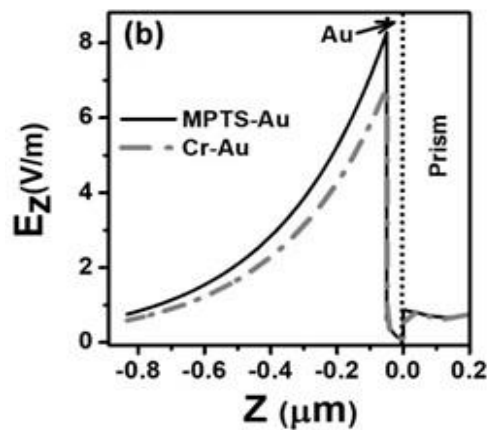


Figure 4.14: The E field distribution for the resonant modes parallel to the z-axis.

Table 4.3: Optical parameters of different layers used to calculate the electric field distribution of MPTS/Au and Cr/Au SPR sensors.

Cr as adhesion layer				MPTS as adhesion			
Layer	t(nm)	ϵ_{real}	ϵ_{imag}	Layer	t (nm)	ϵ_{real}	ϵ_{imag}
prism	0	3.02	0	prism	0	3.02	0
Cr	1.57	-1.58	24.28	MPTS	1	1	0
Au	48.56	-23.56	2.19	Au	49.75	-24.15	1.79
Water	0	1.77	0	water	0	1.77	0

Among the three types of sensors, hybrid Au/SLG devices exhibited the highest RI sensitivity, which is 12% and 3% higher than that of Cr/Au and MPTS/Au respectively. As reported in [28] enhanced RI sensitivity of the Au/SLG sensors originates from the shift of Fermi level in graphene by the adjustment of work function of Au and SLG, resulting in the formation of a surface dipole at the interface due to the charge transfer between Au film and graphene [28, 85]. These intensified dipoles lead to increase in the number density of electrons (N) participating in the plasma oscillations, increasing the effective plasma frequency ($\omega_p = Ne^2/\epsilon_0 m_e$) of free electrons in the metal, and allowing the change in the real part of dielectric constant of Au by using the Drude Lorentz model ($\epsilon_m = 1 - (\omega_p/\omega)^2$) [47]. This modification in the real part of the dielectric constant of metal is directly related to the sensitivity via equation (2.46), hence contribute to the enhancement of the sensitive. The new opportunities in optical sensing offered by the Au/SLG hybrid devices will be further discussed in Section 5.3.

4.4. Conclusion

We investigated the degradation and stabilization process affecting the metal-dielectric interfaces of SPR sensing devices in different experimental configurations. The experimental results suggest that degradation in air is mainly due to the progressive delamination of the metal deposition on the BK7 substrate, and that graphene protected Au and Ag thin films exhibit a stability similar to the samples protected by the encapsulation process. In particular, we observed a shift in the SPR angle of about 0.005° for Ag/graphene and Au/graphene samples after 4 h of observation, comparable to the zero-angle indetermination in SPR spectroscopy.

In water environment, we studied the effect of organic and metallic adhesion layers in the stabilization process of different kind of metal-dielectric interfaces supporting surface plasmon polaritons (SPP). While metallic adhesion layer such as chromium are responsible for enhanced interface damping, when (3-mercaptopropyl) trimethoxysilane (MPTS) is used a molecular link between SiO₂ and gold, the hydration of the siloxane group of MPTS leads along 7 hours to a progressive smoothing of the metal organic interface, as demonstrated by SPR and

AFM monitoring. In case of gold a reduction in the roughness from 1.94 nm to 1.38 nm has been measured which revealed a smooth gold surface and hence suppress the broadening of the SPR curves as observed experimentally. These low-damping SPR sensing platforms are characterized by an 8 % higher sensitivity to analyte detection, which is further increased by the transfer of chemical vapour deposition (CVD) grown infinite graphene, which acts as efficient shield against the chemical reaction occurring at metal dielectric interfaces of the plasmonic devices in water.

The stabilization process of the DLWG in water was investigated in order to use these SPR devices for both sensing of metal nanoparticles and UVA radiation, and the accurate ellipsometric characterization of AuNPs, organic thin films and SLG.

5 Optical sensing by SPR Spectroscopy

In the previous chapter, we studied the stabilization of different SPR platforms with the aim to understand the optimized physical and environmental condition suitable for sensing and characterization purposes. Knowing these parameters, this chapter will explore the sensing capability of SPR spectroscopy in the Kretschmann configuration using luminescent organic materials, AuNPs and SLG.

In the first part of this chapter, we will investigate the degradation process of tris(8-hydroxyquinoline) (Alq₃) and tris(dibenzoylmethane)mono(1,10-phenanthroline) europium (III) (Eu(dbm)₃(phen)) thin films both in air and nitrogen environment by the use of AFM, photoluminescence (PL) and SPR spectroscopy. Taking the advantages of a simple encapsulation technique, the degradation of the organic luminescent thin film was also analyzed under the controlled doses of UVA irradiation, in term of PL intensity change and refractive index changes observed by SPR spectroscopy. The experimental results obtained on (Eu(dbm)₃phen) complex thin films are finally used to theoretically demonstrate the proof of principle of an SPR UV dosimeter in the plasmon coupled emission (SPCE) configuration.

In the second part, we study the performance of the DLWGs in the accurate counting of citrate stabilized AuNPs deposited on the external surface of the sensor, and verify the SPR results by AFM measurements in a range of surface density between 20 and 200 NP/ μm^2 .

Finally, we explore the performance of optical sensors constituted by bare Au surface or hybrid Au/SLG interface, based on the detection of heavy metal Hg⁺² ions. The performance parameters such as sensitivity, LoD and the FWHM are calculated from the SPR reflectivity curves. In order to quantify the binding affinity of Hg⁺² ions towards the sensor layer, the calibration curve was computed from the SPR angle shift, using an Langmuir Isotherm model [109].

5.1. SPR UVA dosimeter

The study of the degradation process of organic luminescent materials in air or under UV irradiation is a critical subject for the merging of emerging energy and optical technologies based on organic materials [110]. The main cause of failure of the organic opto-electronic device such as organic field effect transistors (OFET), organic solar cells (OPV) and organic light emitting diodes (OLEDs), may be inherently linked to the cathode delamination or chemical reactions induced by light [111], the current density and heat [112]. Moreover, the low quality of encapsulation may lead to physico-chemical and morphological changes of the organic layers [113]. Tris(8-hydroxyquinoline) (Alq_3), is mostly used as a reference molecule to explore the degradation processes of molecular organic luminescent materials [114]. In literature, its exposure to an open air with a high humidity (~100 %) quenched the photoluminescence (PL) and formed crystallized clusters [115]. On other hand, the irradiation by UV EM radiation induced chemical changes of the organic molecules [116]. Ellipsometric techniques have been used to investigate the optical properties of Alq_3 long exposure time to an atmospheric environment or UV irradiation. The results show a decrease in the refractive index on exposure to the atmosphere [117], and an increase under exposure to UV irradiation [71].

The lanthanide β -diketonate complexes such as $(\text{Eu}(\text{dbm})_3(\text{phen}))$ is another class of molecular luminescent materials with promising potential in OLED technology due to high quantum yield, narrow emission band and high up-conversion efficiency [118]. In spite their widespread use, studies related to the degradation of β -diketonate complex thin films are rare, and there is no report available in the literature about the ellipsometric monitoring of their degradation.

In this section the degradation process of Alq_3 and $\text{Eu}(\text{dbm})_3(\text{phen})$ thin films are investigated in air by monitoring the change in FWHM and refractive index variation Δn using the SPR spectroscopy. The quenching of PL intensity of the organic thin films upon atmospheric exposure will also be presented in details, while the morphology and phase images of fresh and aged samples are examined by AFM measurement. The degradation of these encapsulated organic thin films is also investigated under UVA irradiation, by monitoring the variations in the PL intensity and changes observed in the refractive index of the organic optical

materials. The sensing platforms used in the present investigation are single mode, so that the hypothesis of a constant thickness of the organic thin film has been taken in consideration during the analysis of the experimental data, and the shift of the SPR reflectivity curves is attributed only to variation in the refractive index of the thin film. Finally, the experimental results obtained on $\text{Eu}(\text{dbm})_3(\text{phen})$ complex thin films are used to theoretically demonstrate the possibility of a SPR UV dosimeter in the surface plasmon coupled emission (SPCE) configuration. The chemical configuration of the organic luminescent material Alq_3 and $\text{Eu}(\text{dbm})_3\text{phen}$ are shown in Figure 5.1.

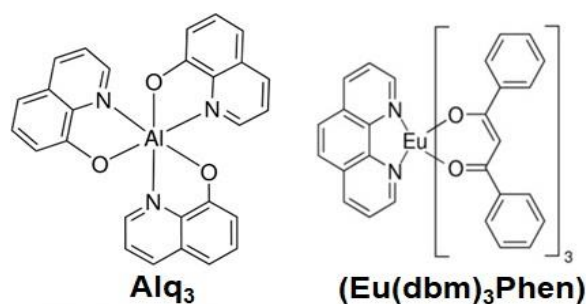


Figure 5.1: Chemical structure of Alq_3 ($\text{C}_{27}\text{H}_{18}\text{AlN}_3\text{O}_3$) and $(\text{Eu}(\text{dbm})_3\text{phen})$ ($\text{C}_{57}\text{H}_{41}\text{EuN}_2\text{O}_6$).

5.1.1. Characterization techniques

In the present work, the experimental set-up used to perform the SPR spectroscopy is described in section 3.4.1. The temperature was maintained at a value of 23 °C, with a humidity of 50%. The metal-organic devices were irradiated in situ using an UV lamp, followed by a band-pass optical filter with 70 % transmission in the spectral window between 300 nm and 400 nm. The optical irradiance reaching the sample was adjusted to be between 2 mW/cm^2 and 20 mW/cm^2 , by the use of neutral filters. The UV irradiance was measured by an UV enhanced silicon photodetector from Newport (U.S.A, model 818-UV/DB UV). When irradiated with UVA, the SPR sensors were encapsulated using a simple encapsulation process as reported in [34].

The PL spectra of both $\text{Eu}(\text{dbm})_3\text{phen}$ and Alq_3 were obtained by direct excitation at $\lambda = 360$ nm and $\lambda = 380$ nm, respectively. Atomic force microscope images on the organic thin film surfaces were taken using a Bruker AFM (model

Multimode 8) operated in the tapping mode with ScanAsyst-Air tips (spring constant ≈ 0.4 N/m).

5.1.2.

Monitoring the degradation of Alq_3 and $\text{Eu}(\text{dbm})_3(\text{phen})$ thin films in an air environment

Figure 5.2(A) shows behaviors of the FWHM of the Au/Alq_3 , Ag/Alq_3 , and $\text{Au}/\text{Eu}(\text{dbm})_3(\text{phen})$ device under air exposure. The nominal thickness of both organic thin films was 30 nm. The refractive indices of Alq_3 and $\text{Eu}(\text{dbm})_3(\text{phen})$ at a wavelength of 783 nm were considered as 1.69 [119] and 1.50 [120], respectively. The results on the bare metals layers are also shown for comparison. It can be seen that the organic luminescent thin films seem to act as a protective layer for the $\text{SiO}_2/\text{MPTS}/\text{metal}$ interface for both silver and gold, whose degradation is generally followed by a broadening of the SPR curve [100].

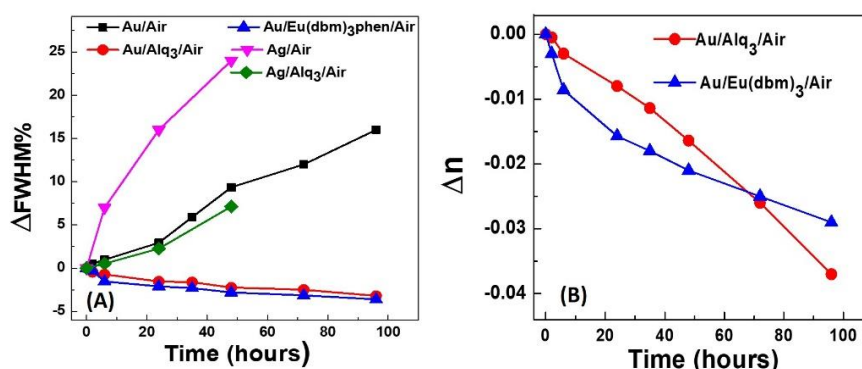


Figure 5.2: (A) Time dependence of the FWHM of Au/Alq_3 , $\text{Au}/\text{Eu}(\text{dbm})_3(\text{phen})$, Ag/Alq_3 , Ag and Au SPR devices in air. (B) Time dependence of the refractive index variation Δn for Alq_3 and $\text{Eu}(\text{dbm})_3(\text{phen})$ thin films over an Au metal layer. The nominal thickness of the organic thin films was 30 nm. The temperature was maintained at approximately 23 °C with a humidity of 50% [46].

It is observed that the FWHM of the Au based samples shows the small negative variation for both organic materials. Owing to its great stability, the SPR platforms with a gold metallic layer were selected to monitor the refractive index changes of the organic thin films under air exposure. It is evident that the organic thin films demonstrate efficient protection against the degradation induced by the oxidation processes at the $\text{SiO}_2/\text{MPTS}/\text{metal}$ interface of the plasmonic devices.

Comparing to the Au/air, the FWHMs of the SPR curves are constant throughout 4 days in the presence of the organic depositions. This can be explained from the observation that when Alq₃ is exposed to an atmospheric environment, molecular water is incorporated [115] in the organic thin film with the formation of 8-hydroxyquinoline and non-emissive polymer (III) [121], which actually acts like a molecular barrier for the diffusion of O₂ at the MPTS/metal interface. In the literature, the presence of water in Alq₃ thin films has been associated with a partial crystallization of the amorphous material [115].

Figure 5.2(B), demonstrate an almost linear decrease of the refractive index for Alq₃ throughout 100 hours, with no signals of saturation. The refractive index of Alq₃ is subject to a variation of approximately 0.035 RIU in 4 days, while the β -diketonate complexes start to show signals of saturation after approximately 50 hours of exposure. The results of the atmospheric exposure of both of the organic thin films induces a negative variation in their refractive index, which is consistent with the few results reported in the literature for Alq₃ [117].

Figure 5.3 represents the morphology and phase images of fresh and aged samples obtained from AFM measurement over an 8 μ m x 8 μ m surface of 30 nm thick Alq₃ (A, B, C, and D) and Eu(dbm)₃(phen) (E, F, G, and H) thin films deposited over silicon substrates. The scans were repeated after 24 hours without moving the samples (C, D, G, and H). The height images show quite uniform surfaces for both the Alq₃ and Eu(dbm)₃(phen) thin films. Anyway, some brighter spots are present for both materials, especially in the case of the β -diketonate complex. However, the morphology and the average roughness (R_A) of the surface of the organic deposition don't change significantly with time (A, C, E, and G), showing the impressive stability of the thin films under air exposure. The phase images relative to the fresh and aged Alq₃ (B and D) appear perfectly uniform, indicating that the bright spots might be associated with an amorphous material with a different density.

It is to be noted that the AFM phase images of the surfaces of the organic thin films reported in Figure 5.3 do not show any modifications throughout 24 hours. These results suggest that the crystallization process observed in other reports is more likely to be induced by intense white light illumination [122], Alq₃ hydration

in environments with a humidity higher than 50% [115], or defect points on the organic surfaces where the nucleation of microcrystals might happen.

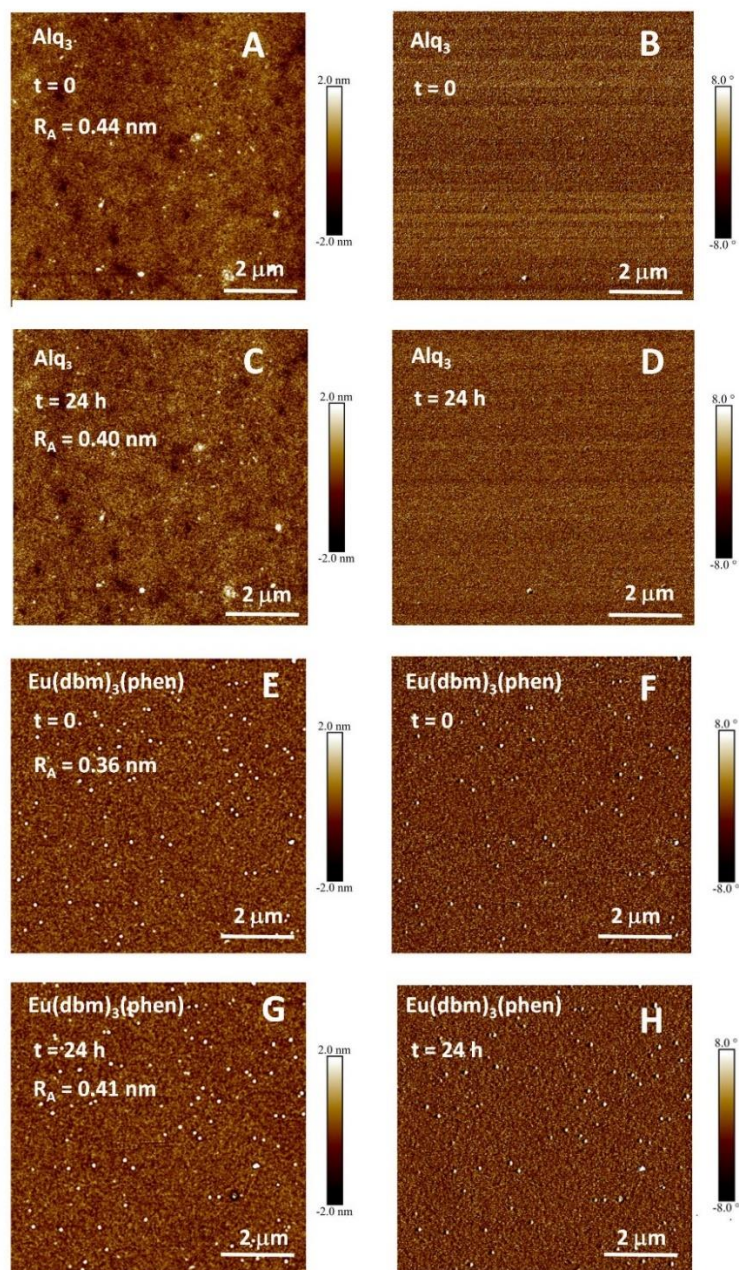


Figure 5.3: AFM images of Alq_3 (A, B, C, and D) and $\text{Eu}(\text{dbm})_3(\text{phen})$ (E, F, G, and H) thin films deposited over silicon substrates. Morphology (left side) and phase (right side) images were taken on fresh samples (A, C, E, and G) and samples aged for 24 hours (B, D, F, and H). The nominal thickness of the organic thin films was 30 nm. The temperature was maintained at approximately 23 °C with a humidity of 50%. [46].

The PL intensities of 30 nm-thick organic films were monitored over 24 hours. The results, reported in Figure 5.4, show that the minimum level luminescence intensity is reached for both Alq₃ (A) and Eu(dbm)₃(phen) (B) after 10 h of atmospheric exposure. The exposure does not completely quench the PL of the organic thin films, and there are residual PL intensities of 22 % and 31 % for the Alq₃ and β-diketonate complexes, respectively. Moreover, no changes are observed in both the spectral position corresponding to the maximum of the PL intensity and the full width half maximum (FWHM) of the spectra. The latter is approximately 140 nm for Alq₃ and as small as 5 nm for Eu(dbm)₃(phen) thin films.

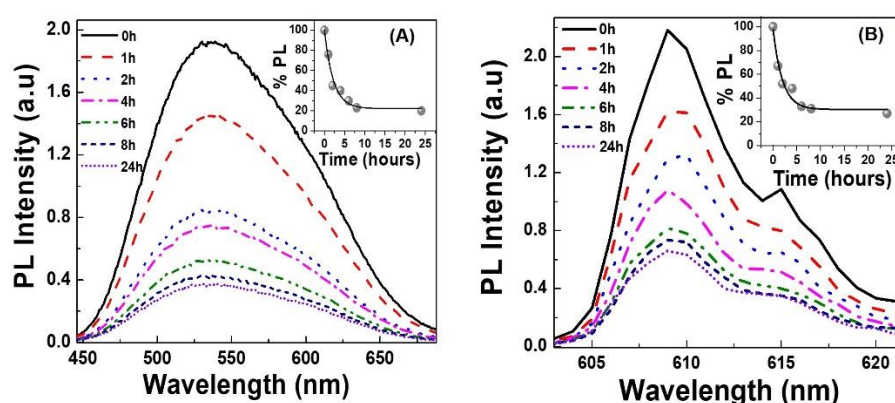


Figure 5.4: Time dependence of the photoluminescence intensity of Alq₃ (A) and Eu(dbm)₃(phen) (B) thin films deposited over silicon substrates under air exposure. The nominal thickness of the organic layer was approximately 30 nm. The temperature was maintained at approximately 23 °C with a humidity of 50% [46].

The quenching of the PL observed in Figure 5.4 is coherent with the results reported in the literature for Alq₃ depositions [122], and it seems to not be correlated in any manner with the refractive index variations observed in both of the organic materials. In fact, while the PL intensity reaches stability in approximately 10 hours of atmospheric exposure, the refractive index of the thin film is still decreasing after 4 days. In conclusion, the results suggest that the degradation of Alq₃ in the atmosphere is a multistep process, which starts with hydration, followed by the formation of polymer III with the quenching of the PL and further chemical reactions, which cause a continuous decrease of the refractive index of the organic moiety. The formation of crystalline regions seems instead to be associated with

irradiation with intense white light or exposure to an atmosphere with a high humidity (i.e., $\geq 50\%$).

5.1.3. Degradation of Alq_3 and $\text{Eu}(\text{dbm})_3(\text{phen})$ thin films under UVA irradiation

The degradation of the organic materials under UVA irradiation was studied using optical irradiances of 2 mW/cm^2 and 20 mW/cm^2 along with sample film thicknesses of approximately 15 nm and 30 nm for both of the organic species. For each material, four independent samples were analyzed, the experimental results were finally averaged and the error bar was calculated accordingly. Figure 5.5 represents the variations in the photoluminescence intensity (I/I_0) and refractive index (Δn) of Alq_3 (A) and $\text{Eu}(\text{dbm})_3(\text{phen})$ (B) thin films under irradiation with controlled UVA doses in a nitrogen environment. Independent from the thickness of the sample, both the photoluminescence intensity and refractive index of the organic thin films present a saturated behavior after a total UVA dose of approximately 60 J/cm^2 . Again, the exposure to UVA radiation doesn't completely quench the PL of the organic thin films, and there are residual PL intensities of approximately 50 % and 20 % for the Alq_3 and β -diketonate complexes, respectively. With UVA doses higher than $\sim 60 \text{ J/cm}^2$, there is almost no variation in the values of the refractive index of the organic moieties. The photodegradation of both materials is proven to be correlated with photochemical reactions. Meanwhile, for Alq_3 , the photodegradation leads to the formation of carboxylate groups bound to Al [123], but the precise mechanism leading to the quenching of the β -diketonate complex is not still understood [124].

The dependence of both PL and refractive index on the UVA dose can be expressed and fit by classical exponential functions, represented in Figure 5.5 by the continuous lines. The details of the function and results of the parameters used for the fit on both organic materials are resumed in Table 5.1.

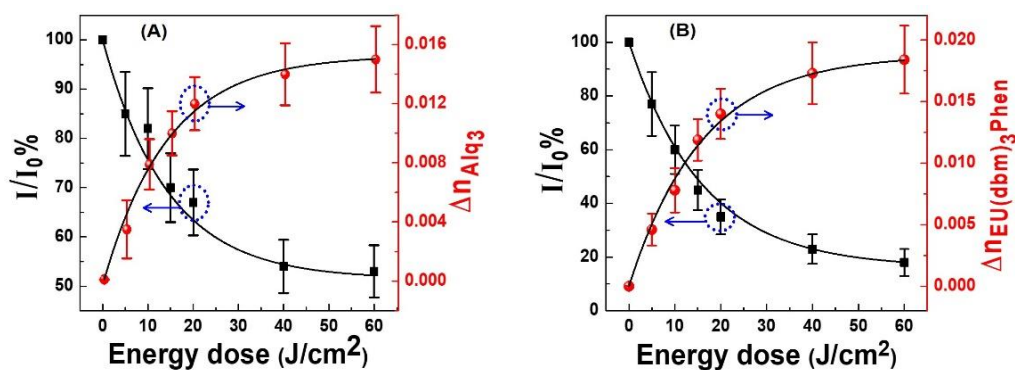


Figure 5.5: Monitoring of the refractive index variation (Δn) and photoluminescence intensity (I/I_0) of the Alq_3 (A) and $Eu(dbm)_3(phen)$ (B) thin films under UVA irradiation in nitrogen environment. The continuous lines represent the exponential fit on the experimental results [46].

Table 5.1: Exponential functions and values of the parameters used to fit the dependence of the variation of the refractive index (Δn) and PL (I/I_0) on the UVA dose for both organic materials.

Physical Quantity	$I/I_0\%$			Δn		
Equation	$y = y_0 + A_1(e^{-E/E_0})$			$y = y_0 + A_1(1 - e^{-E/E_0})$		
Parameters	y_0	A_1	E_0	y_0	A_1	E_0
Alq_3	51	48	14	0	0.015	14
$Eu(dbm)_3Phen$	16	83	16	0	0.018	16

The result shows a clear correlation between the quenching of the PL and the refractive index variation of the organic thin films, both for Alq_3 and $Eu(dbm)_3(phen)$ materials. In fact, the energy constant (E_0) values in the mathematical models used to fit the PL decay and refractive index enhancement of the organic thin films are the same independent of the material, as reported in Table 5.1. The results described above can be interestingly exploited for the development of a SPR-UVA dosimeter in the SPCE configuration.

5.1.4. Working principle of the SPR dosimeter in the SPCE configuration

The behavior of the refractive index of the organic luminescent materials when exposed to UVA radiation can be exploited for the development of SPR dosimeters. Although the sensors might be developed in the Kretschmann configuration used in our measurements, a more compact and less expensive UVA sensor can be designed in the SPCE configuration. In this particular reversed configuration, the luminescence of the organic material is excited by a LED source and is coupled to the surface plasmon polariton (SPP) of the metal-organic bilayer. The SPP is finally decoupled in free space on the side of the high index prism, and each wavelength composing the photoluminescence spectra of the organic thin film ($PL(\lambda)$) is emitted with an angular distribution of intensity, which depends on the FWHM of the SPR reflectivity spectra ($R_\lambda(\theta)$) of the device. The final angular distribution of the SPCE intensity, which we define as $PL(\lambda)_{norm}$, will depend on the mathematical convolution between the normalized photoluminescence spectra of the organic material $PL(\lambda)_{norm}$ and $R_\lambda(\theta)$. The convolution can be expressed as [46]:

$$R^*(\theta) = \int_{\lambda_1}^{\lambda_2} PL(\lambda)_{norm} \cdot R_\lambda(\theta) d\lambda, \quad (5.1)$$

where λ_1 and λ_2 are defined as the FWHM of the photoluminescence spectra, and the relation $\int_{\lambda_1}^{\lambda_2} PL(\lambda)_{norm} = 1$ holds. When the UV radiation alters the refractive index of the organic material, the angle of emission of the SPP changes accordingly. As shown in Figure 5.6 if the resonant angle is shifted by a quantity $\Delta\theta_{UVA}$, the variation in the refractive index can be in principle detected by monitoring the shift of the angular distribution $I(\theta)_{SPCE}$.

Alq_3 is not a good candidate material for the development of a sensor in the SPCE configuration. First, it emits in the green region so that the less stable silver metal substrate should be used to decouple the SPP efficiently. Second, its PL is characterized by a wide FWHM, leading to a broadening of the $R^*(\theta)$, which might hide the shift of the $\Delta\theta_{UVA}$ induced by UVA irradiation.

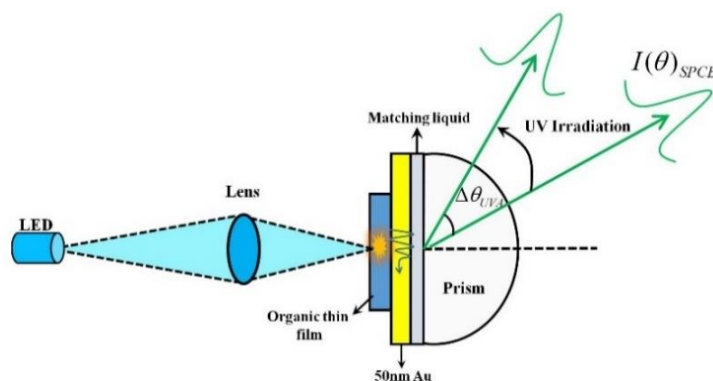


Figure 5.6: Scheme of the working principle of the proposed SPR dosimeter in the SPCE configuration [46].

This is not the case for the β -diketonate complex materials. Figure 5.7 shows, for example, the comparison between the theoretical curve $R_\lambda(\theta)$ at a wavelength of 610 nm and theoretical curve $R^*(\theta)$ for an organic thin film of $\text{Eu}(\text{dbm})_3(\text{phen})$ with a nominal thickness of 30 nm before and after irradiation with an UVA dose of 60 J/cm^2 . The maximum angular shift $\Delta\theta_{\text{UVA}}$ is approximately 0.35° , which can easily be detected by a proper alignment of the system depicted in Figure 5.6 and an optical detector such as a CCD camera with sufficient spatial resolution.

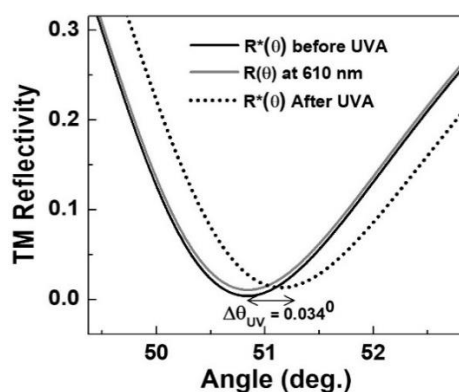


Figure 5.7: Comparison between the experimental SPR spectra $R_\lambda(\theta)$ at a wavelength of 610 nm (grey line) and theoretical curve $R^*(\theta)$ for an organic thin film of $\text{Eu}(\text{dbm})_3(\text{phen})$ with a nominal thickness of 30 nm before (black continuous line) and after (black dotted line) an UVA dose of approximately 60 J/cm^2 [46].

Most of the UV dosimeters based on organic materials presented in the literature exploit the changes in the PL intensity [125], imaginary part of the refractive index of the materials [126] or the current-voltage characteristics of

electro-organic devices [127]. The results reported here are highly encouraging for the development of innovative UVA SPR dosimeters in the SPCE configuration, exploiting, for the first time, the changes in the real part of the refractive index of the luminescent organic material. Nevertheless, in order to obtain the best performance, other organic materials should be investigated, with special attention to the class of lanthanide β -diketonate complexes with sharp emission spectra.

5.2. SPR nanocounter

In this section, we show the application of DLWGs as nanoparticle counters for AuNPs with a nominal diameter of 14.6nm. Experimentally we examine the functionality of the Maxwell-Garnett theory for the accurate counting of the AuNPs with a surface density in the range between 20 and 200 NP/ μm^2 . AFM measurements were performed as direct technique to count the AuNPs on the DLWG surface, and the results were compared with the ones obtained by SPR spectroscopy.

Before executing the experimental measurements, a theoretical study of the DLWG based nanocounter in the Kretschmann configuration has been performed by the group of Prof. Karlo Q. Costa (Faculty of Electric Engineering of the Technology Institute (ITEC) of the Federal University of Pará, Belem, Brazil), to determine the sensitivity response and the dependence of the dipole-dipole interactions on the dielectric spacer thickness, the dimension of the AuNPs, the surface density and the wavelength of the exciting electromagnetic wave [31]. We compare a semi-analytical approach based on the Maxwell's Garnett theory that neglects dipole-dipole interaction, with a numerical method developed by using Finite Element Method (FEM) in COMSOL Multiphysics® software [128]. Based on the theoretical results, three suitable conditions are obtained for quantitative, quick and accurate measurements of surface density: (i) the introduction of a SiO₂ spacing layer with a thickness higher than ~20 nm, (ii) the use of AuNPs with a diameter smaller than ~20 nm, (iii) the use of excitation wavelengths in the near infrared region, in order to have a reduced interparticle interaction for high values of surface density. The results also show that for the multimodal DLWGs, the evanescent field associated to the TM₁ mode has the best sensitivity to use as a nanoprobe for the detection of AuNPs [31].

The larger deviation between experimental and theoretical results with increasing surface density in the frame of the MG theory was associated to the onset of interparticle dipolar interaction. This discrepancy is the main cause to the failure of the effective medium theories in the determination of surface density. To show the effect of surface density on the dipole-dipole interparticle interaction, it is necessary to model the near EM field (E_z) in the center between the AuNPs. Figure 5.8 represent the E_z between two adjacent AuNPs with a diameter of 60nm, separated by the distance d , at the wavelength of 633nm.

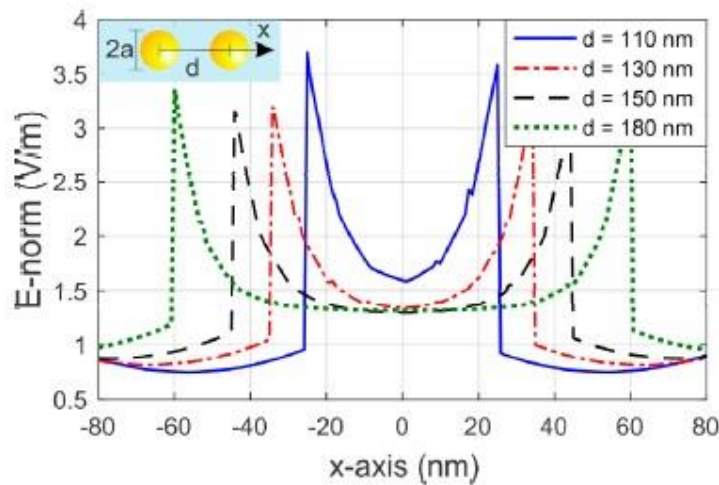


Figure 5.8: E_z field between two adjacent AuNPs with the diameter of 60 nm embedded in water. The centers of the AuNPs are separated by the distance d , as highlighted in the inset [31].

It is evident that when the AuNPs are close to each (value of d decreases), the E- field in the middle of AuNPs become enhanced. Remarkably, a sudden increase in the field intensity between adjacent AuNP is observed for distances smaller than 130 nm (equivalent to $\sigma = 44 \text{ NP}/\mu\text{m}^2$), due to onset of the dipole-dipole interparticle interaction regime [129].

A trade-off should be considered in the choice of both AuNPs dimensions and maximum surface density of the array, depending on the error that can be tolerated in the evaluation of the surface density and, in ultimate analysis, in the calibration of the PA-SPR sensor. In the way to define the error of the surface density $\delta\sigma$, we calculate the relative deviation between the real surface density σ_{FEM} , used in FEM simulations, and the density calculated using MG formula (σ_{MG}) to fit the TM_0 resonance angle θ_{FEM} as shown in Figure 5.9. The calculation was carried out for

AuNPs diameters of 20, 30, 40 and 60 nm, and surface densities σ between 26 and 83 NP/ μm^2 . It can be seen that the discrepancy increases for higher values of the surface density and for the bigger sized AuNPs. The best results are obtained for

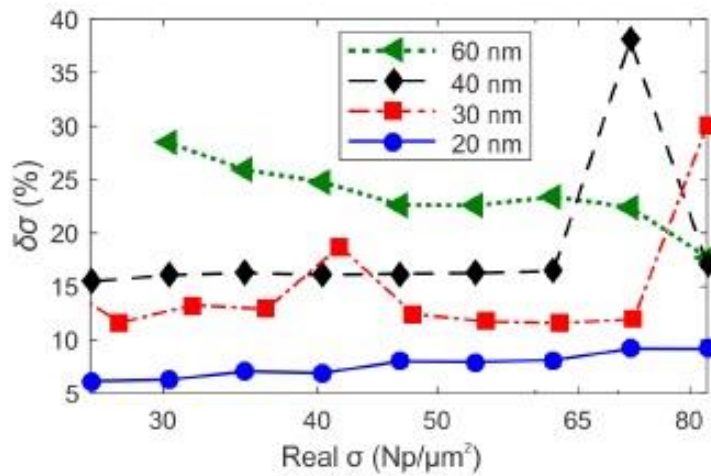


Figure 5.9: The relative deviation $\delta\sigma$ between the real surface density σ_{FEM} and the density σ_{MG} calculated by MG formula to fit the resonance angle θ_{FEM} [31].

AuNPs of 20 nm in diameter, for which the discrepancy remains lower than 10% for all the analyzed values of surface density. On the basis of above theoretical results, we tested the DLWGs fabricated in the present research as nanoparticle counter for AuNPs with the nominal diameter of 14.6 nm, a dimension for which the Maxwell-Garnett theory can be still applied under the assumption of inclusions with negligible value of the scattering-cross section.

The fabrication process of the DLWGs is explained in section 3.2. Here, the external surface of the DLWGs is further functionalized by immersing the samples in 3-aminopropyl trimethoxysilane (APTS)/ethanol solution for 2 h, followed by rinsing with ethanol and gentle drying with nitrogen. The amino functionalized SiO_2 surface serves as molecular link for the negative charged Citrate stabilized AuNPs. Figure 5.10 shows the immobilization process of the AuNPs on the surface of DLWGs.

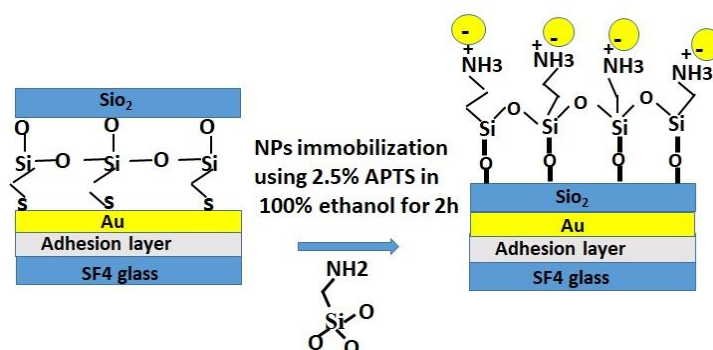


Figure 5.10: (a) DLWGs fabricated by the deposition of thick dielectric layer of SiO₂. (b) Immobilization of AuNPs on APTS functionalizes SiO₂ surface.

The citrate stabilized AuNPs are injected into the flow cell at a rate of 0.3 mL/min by using the continuous flux pump shown in Figure 3.11. The time interaction of AuNPs with the functionalized surface is varying from 1 to 5min to achieve different NPs surface densities. Before fluxing the AuNPs, the optical constants and thickness of the gold and SiO₂ layers forming the DLWGs are measured by two-color SPR spectroscopy, using the procedure explained in section 2.6.2. The values of the optical parameters of the DLWGs at the experimental wavelength of 783 nm are given in Table 5.2.

Table 5.2: The dielectric constant and thickness of gold and SiO₂ obtained from the fitting of SPR curves before the injection of AuNPs.

λ (nm)	Gold	SiO ₂	Water
783	$\epsilon = \epsilon_r + i\epsilon_i$	$\epsilon = \epsilon_r + i\epsilon_i$	ϵ_r
	t (nm)	t (nm)	
	44.57	644	1.76

Figure 5.11 shows the time-dependent SPR sensogram [31] relative to the different experimental phases involved in the sensing of the AuNPs. The different experimental phases involve in: base-line determination for TM₁ mode in a pure water environment, water removal with enhancement of the reflectivity, injection of the colloidal solution of AuNPs, monitoring of the interaction between the amino group of the SAM of APTS and the negative charge of the AuNPs, and final pure water rinsing and stabilization of the SPR signal. The raise of the reflectivity is due to a shift $\Delta\theta$ in the SPR angle after AuNPs detection and stabilization.

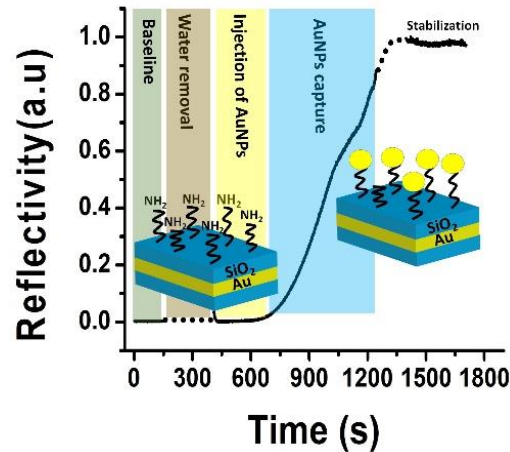


Figure 5.11: SPR sensogram relative to the sensing of the interaction between the APTS functionalized external surface of the DLWGs and the negatively charged AuNPs. The TM_1 mode of the DLWG has been used as evanescent optical probe. The excitation wavelength was 783 nm, and the sensogram was taken at a fixed incidence angle of 50.695° .

Figures 5.12 (a, b, c) are showing the shift of the SPR reflectivity curves and AFM image of the external surface of the DLWGs after nanoparticles sensing, with a final surface density of about 25, 120 and 200 $NP/\mu m^2$, respectively.

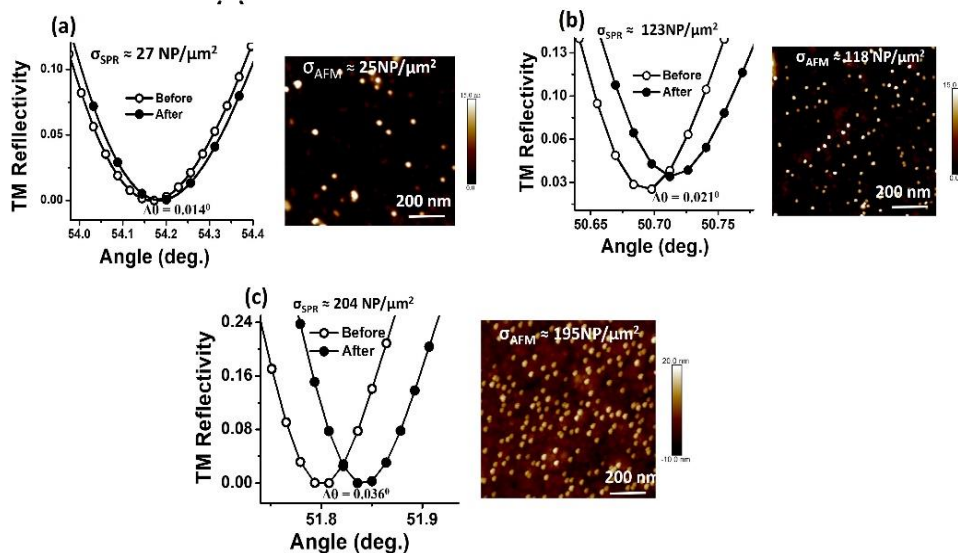


Figure 5.12: Comparison of experimental SPR reflectivity curve of the TM_1 mode of the DLWGs in water before and after interaction of the AuNPs with the SiO_2 surface (left side), and AFM image of a $1 \mu m \times 1 \mu m$ region of the SiO_2 surface of the device, analyzed by SPR spectroscopy (right size), with a NPs surface density of 25 $NP/\mu m^2$. (c) $\sigma = 120 \text{ NP}/\mu m^2$. (d) $\sigma = 200 \text{ NP}/\mu m^2$

[31].

Although, the AFM images reveal that the AuNPs are randomly distributed on the surface of SiO₂, which may not follow the simulation modeling of ordered bidimensional array of AuNPs. However, in the approximation of non-interacting NPs, the exact spatial distribution of the bidimensional array of AuNPs deposited over the SiO₂ thin film of the sensor does not influence the optical response of the device. This means that the shift in the angle of resonance of the DLWGs upon the interaction with the AuNPs depends only on the surface density, and not on their specific surface distribution. The excellent matching between the AFM and SPR experimental densities σ_{SPR} and σ_{AFM} during the nanoparticle counting supports this assumption.

5.3. Hybrid Au/SLG interfaces for Hg⁺² optical sensing

Monitoring of highly toxic heavy metal ions has received much attention because of it severs threats and adverse effects on the environment and on the human health. Among these the Mercury ion (Hg⁺²), which is widely spread in the air, water, and soil, is consider to be one of the most toxic metal pollutants because it can damage the nervous system, the brain and the immune system [130]. Therefore, a highly sensitive Hg⁺² sensor is in high demands for its detection. Graphene, a two dimensional and one atom thick carbon sheet has gained considerable interest in the sensing platform for the detection of heavy metals due to its unique physicochemical properties, edge termination (zig zag vs armchair) and specific highly symmetric adsorption sites [87]. The theoretical reports showed that these binding sites provide the possible mode of adsorption between infinite graphene and heavy metal ions [87].

Figure 5.12 show the possible four-adsorption sites of the adsorbed ions, namely Top site (T), bridge site (B), hollow site (H) and defect site (D). The binding sites, binding energies, the Mulliken charge transfer and the nature of interaction between neutral Hg⁰ atom and charged Hg⁺² (mercuric) with infinite graphene are illustrated in table 5.3. The most favorable binding site for the adsorption of Hg⁰ and Hg⁺² on graphene are the hollow and top with their corresponding binding energies of 0.161eV and 14.56 eV respectively.

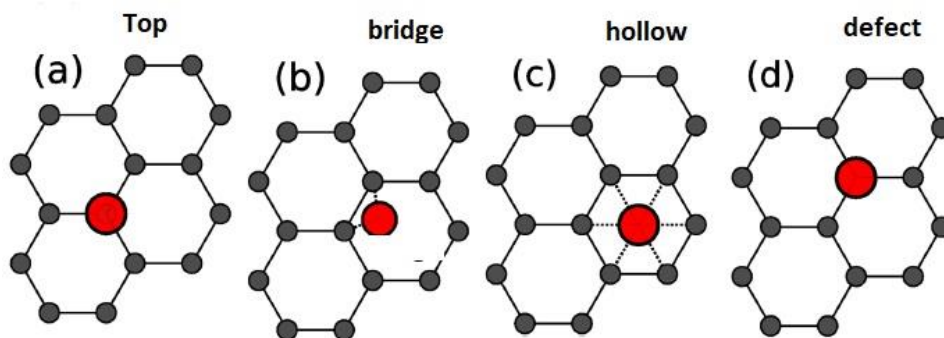


Figure 5.13: The possible adsorption sites. Neutral atoms and charged ions of heavy metals are placed at the (a) on-top (T), (b) bridge (B), and (c) hollow (H) sites on the hexagonal cell, as well as, on a defect (D) site (d) of graphene sheet [87].

Table 5.3: The calculated interaction parameters of neutral and charged Hg specie on infinite graphene [87].

Metal	Adsorption site	Binding energies (eV)	Mulliken charge transfer	Nature of interaction
Hg ⁰	Hollow	0.161	0.09	Physisorption
Hg ⁺²	Top	14.56	-1.94	Chemisorption

In this work, SPR spectroscopy was used for sensing of Hg⁺² ions on three different kinds of SPR platforms: bare gold, Au/SiO₂(30nm)/SLG and Au/SLG. By using the reflectivity SPR curves obtained from the binding of Hg⁺² on each sensor surface, the resonance angle, full width half maximum (FWHM), sensitivity and limit of detection (LoD) are calculated.

The SPR reflectivity curves were first recorded in deionized water as a blank measure (without Hg⁺² addition), and then in different concentration of Hg⁺² ranging from 0.01ppm to 1ppm. SPR fluidic channel equipped with syringe pump (Figure 3.11(a)) was used to inject the deionized water and analyte (Hg⁺²) solutions at a flow rate of 0.3 ml/min. After injecting each concentration of Hg⁺² ion, the change in resonance angle ($\Delta\theta$) and the FWHM of the SPR curve were recorded, as reported in Figure 5.15. After, the chip surface was rinsed with deionized water, and subsequently a new concentration of the analyte was injected in the system. In Figure 5.15, the angle shift $\Delta\theta$ represents the difference between the resonance angle with deionized water (the reference) and that of the Hg⁺² at particular concentration. The sensors performance was described in terms of sensitivity and

limit of detection. The sensor sensitivity to analyte concentration is defined as $S_c = \Delta\theta/\Delta c$ (deg./ppm) [24] where Δc is the change in Hg^{+2} concentration and $\Delta\theta$ is the corresponding angle shift. The limit of detection (LOD) concentration is calculated using the equation [26, 130]:

$$LoD = 3SD/S_c \text{ (ppm} \times \text{deg./deg.)}, \quad (5.2)$$

where SD is the standard deviation of the blank signal. In SPR based sensor the SD can be measured from the change in the reflectivity (δR_{HM}) signals versus time around the half maximum (HM) of the SPR curve as shown in figure 5.14 (a). The $SD = \delta R_{HM}$ is related to a certain value of change in the incident angle ($\Delta\theta_{HM}$), as represented in Figure 5.14 (b). The estimated value of $\Delta\theta_{HM}$ is finally used to evaluate the LoD.

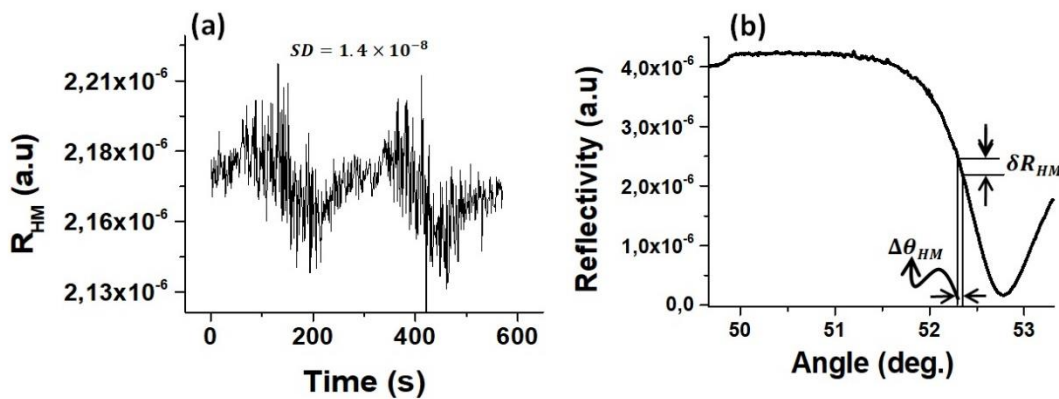


Figure 5.14: (a) Reflectivity at half maximum of SPR curve versus time graph at wavelength of $\lambda= 783\text{nm}$. (b) The corresponding SPR reflectivity curve of the Au thin film (49 nm) in deionized water.

Figure 5.15 (a) illustrates the change in resonance angle as a function of Hg^{+2} concentration for the Au/SLG, Au/SiO₂/SLG and bare Au sensors. The Au/SLG sensor revealed a larger SPR shift and a rapid response within few second for the lowest concentration 0.01ppm of Hg^{+2} ion.

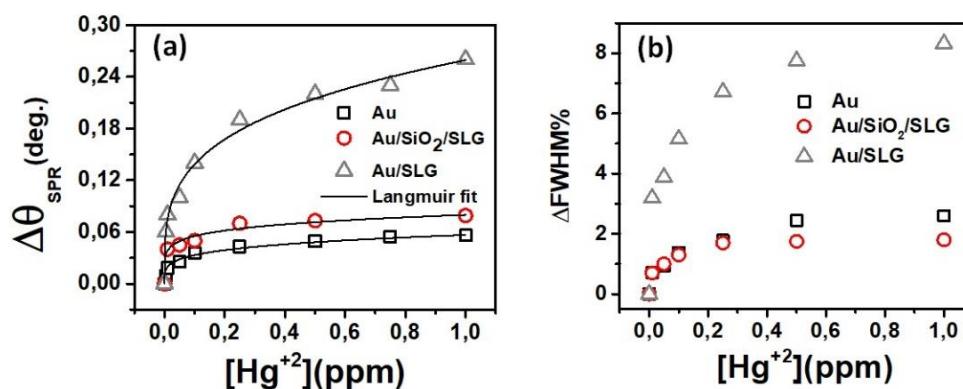


Figure 5.15: Experimental (a) SPR angle shift and (b) FWHM variation as a function of different concentration of Hg^{+2} ions using the low-damping SPR sensors in the bare Au, Au/SiO₂/SLG and Au/SLG architectures. The solid lines show the Langmuir fit on each experimental data.

Table 5.4 shows the experimentally estimated value of sensitivity and LoD in deg./ppm and Molarity (M) respectively. The highest sensitivity was found in the case of Au/SLG sensor as compared to that of Au/SiO₂/SLG and bare Au sensors. The sensitivity and LoD were calculated at the lower concentration of Hg^{+2} .

Table 5.4: Experimentally calculated values of sensitivity and LoD. The SD and $\Delta\theta_{HM}$ were measured from figure 5.14.

Sensors	S_c (deg./ppm)	SD	$\Delta\theta_{HM}$	LoD (M) $=3\Delta\theta_{HM}/S_c$
Au	1.8	1.4×10^{-8}	0.00158	1.31×10^{-8}
Au/SLG	12	1.4×10^{-8}	0.00158	1.98×10^{-9}
Au/SiO ₂ /SLG	8	1.4×10^{-8}	0.00158	2.97×10^{-9}

The LoD for Hg^{+2} using the Au/SLG interface was estimated to be 1.98×10^{-9} M. As far as our knowledge, this is the first demonstration of the real time SPR optical detection of Hg^{+2} ion based on unmodified graphene, which shows higher detection sensitivity than the previously reported functionalized graphene methods (Table 5.5). The lower LoD of the Au/SLG and Au/SiO₂/SLG interfaces indicated that the surface of SLG is more effective to adsorb the Hg^{+2} ions, confirming experimentally the theoretical prediction about the binding interaction of Hg^{+2} with infinite graphene [87].

Table 5.5: Comparison of some of the reported graphene-based sensors for Hg^{+2} ions detection.

Detection Method	Sensor	LoD (M)	Detection range (M)	Ref
Field effect transistor	rGO/TGA/AuNps	2.5×10^{-8}	2.5×10^{-8} to 1.42×10^{-5}	[132]
Field effect transistor	Graphene/1-octadecanethiol	5×10^{-8}	NA	[133]
Colorimetric	Ag@GO	33×10^{-8}	10-200 μM	[134]
UV-vis spectrometer	AgNPs/rGO	2×10^{-8}	0.1-5 μM	[135]
SPR Spectroscopy	Au/SLG	1.97×10^{-9}	0.05 -5 μM	This work
SPR Spectroscopy	Au/SiO ₂ /SLG	2.97×10^{-9}	0.05 -5 μM	This work
SPR Spectroscopy	Au	1.31×10^{-8}	0.05 -5 μM	This work

In order to understand the role of charge transfer on the enhancement of detection sensitivity, we deposited a dielectric layer of SiO₂ between graphene and gold thin film to possible stop the charge redistribution at graphene-metal interface and compared its sensing ability with that of Au/SLG. In Figure 5.15(a), the open circle shows the change in resonance angle for different Hg^{+2} concentration, where it is apparent that the SPR response is weaker after the insertion of SiO₂ between graphene and gold. Based on this observation, we conclude that the charge redistribution at graphene-metal interface play a significant role and can opens up the possibility for lowering the limit of detection down to 10^{-9} M without any complicated functionalization of graphene surface.

Nevertheless, the enhancement in the sensitivity of the Au/SLG interface seems to depend on the particular analyte under observation, and is bigger in the case of Hg^{+2} if compared to the sensing of glycerin (Section 4.3). On these bases, we make two hypotheses: 1) the Au/SLG interface has a better affinity to Hg^{2+} than the SLG interface alone; 2) Hg is present at the Au/SLG interface in both ionic and neutral form during the propagation of the plasma wave, supporting the wave with its electrons, increasing the density of the free charges and the sensitivity of the sensor. In the latter case, Hg^{+2} would undergo a fast two-electron redox reaction, which can be described by the equilibrium reaction



The divalent ions act as receptor, which always extracts electrons from graphene resulting in the increase in the hole concentration, which not only modifies the electronic properties of graphene but also change the optical properties.

Therefore, this plasmon induced charge transfer mechanism might be responsible for an apparent higher binding affinity of charged Hg^{+2} towards Au/SLG interface.

5.3.1. Adsorption isotherm model

To further understand the adsorption of Hg^{+2} on the bare gold and graphene surface, we studied the adsorption isotherms by monitoring the change in resonance angle and using Langmuir isotherm equation mathematically expressed as follows [108, 135]:

$$\Delta\theta = \frac{\Delta\theta_{\max}KC}{1 + KC} \quad (5.4)$$

Here $\Delta\theta$ is the SPR shift; $\Delta\theta_{\max}$ is the maximum SPR angle shift at saturation of Hg^{+2} adsorption; C is the Hg^{+2} concentration, and K is the affinity constant. The solid line in Fig 5.15(a) shows the fit of Langmuir equation to the experimental data obtained from the bare gold thin film (rectangle), Au/SLG (triangles) and Au/SiO₂/SLG (circles). The corresponding parameters for the adsorption isotherm model are listed in Table 5.6.

Table 5.6: The Langmuir parameters obtained from the fitting of different sensors used for the detection of Hg^{+2} .

Adsorbate	Adsorbent sensors	Langmuir parameters		
		$\Delta\theta_{\max}$	$K (\text{M}^{-1})$	R^2
Hg^{+2}	Au	0.033	1.1×10^4	0.974
	Au/SiO ₂ /SLG	0.054	1.5×10^4	0.975
	Au/SLG	0.142	4.6×10^4	0.984

These results indicate that the Langmuir isotherm model fit well on the experimental data obtained from Au/SLG sensor ($R^2 = 0.984$), with slightly higher binding affinity constant of $4.6 \times 10^4 \text{ M}^{-1}$ as compared to the Au/SiO₂/SLG sensor ($1.5 \times 10^4 \text{ M}^{-1}$). The higher affinity constant of the Au/SLG sensor toward Hg^{+2} ions support our conclusion of the enhancement of LoD, which is in part due to charge

transfer from graphene to gold in the absence of SiO₂. Thus, it can be concluded that the charge transfer mechanism in our graphene based SPR sensors provided a reliable enhancement of LoD, so that the presence of Hg⁺² ions as a target analyte can be detected with higher binding affinity as confirmed by Langmuir isotherm model.

5.3.2. Full Width Half Maximum (FWHM)

The FWHM of the SPR curve is the angular width of the SPR spectra at half value of the maximum reflectance. The change in FWHM determined from the SPR angular curves of Au/SLG, Au/SiO₂/SLG and for bare gold sensor as a function of Hg⁺² ion concentration is presented in Fig. 5.15 (b). Comparison reveals a drastic broadening of Au/SLG sensor toward 0.01ppm Hg⁺², while a comparatively a lower broadening is observed for the Au/SiO₂/SLG and bare gold sensors at the same lower concentration of Hg⁺². To the best of our knowledge, this trend of higher Δ FWHM values enabled by the Au/SLG sensor for Hg⁺² is observed for the first time and has a limited literature studies available for direct comparison. However, the possible reason for the broadening of SPR curves can be understood by considering two factors, that is by correlating the variation of the plasma frequency of the gold thin film with the propagation length of surface plasmon and the surface plasmon scattering produced by the adsorption of Hg⁺² ion [25].

To check the Hg⁺² ion presence on the graphene surface, we performed the X-ray photoelectron spectroscopy measurement. The results of XPS data is still under analysis.

5.4. Hybrid Au/SLG interfaces for Pb⁺² optical sensing

The sensing performance of hybrid Au/SLG interfaces is also evaluated for the detection of different concentration of Pb⁺² ions ranging from 0.01ppm to 1ppm. Figure 5.16 (a) shows shift of SPR angle of the bare Au, Au/SiO₂/SLG and Au/SLG sensors upon the adsorption of Pb⁺² ion concentrations. The results indicate that both the hybrid Au/SLG sensors are able to detect low traces of Pb⁺² ions with considerable shift in the SPR angle and reaching a saturation values at higher

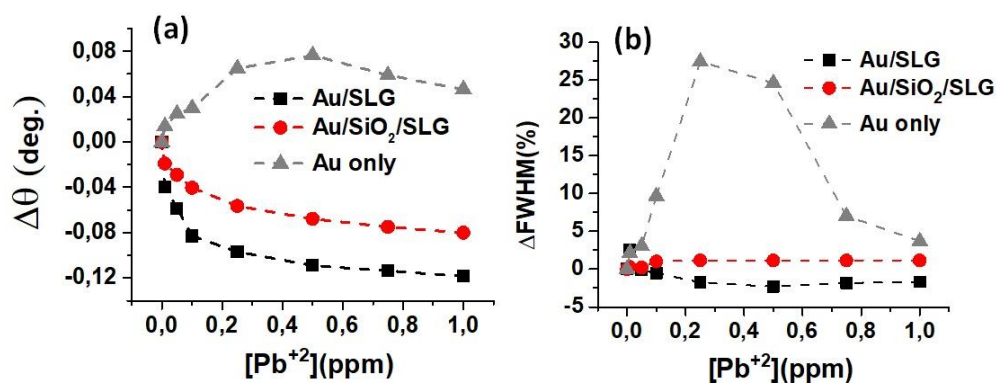


Figure 5.16: (a) The SPR angle shift as a function of different concentration of Pb^{+2} ions for bare Au and hybrid Au/SLG sensors. (b) The corresponding change in the FWHM with different concentration of Pb^{+2} ions.

concentrations. The experimentally measured performance parameters such as the sensitivity and LoD are listed in Table 5.7. We noticed that the SPR sensitivity is higher for the Au/SLG sensor than the Au/SiO₂/SLG, which could be due to enhancement of the plasma frequency arises from the direct charge transfer from SLG to Au thin as explained earlier [28].

Table 5.7: Experimentally calculated values of sensitivity and LoD.

The SD and $\Delta\theta_{HM}$ were measured from figure 5.14.

Sensors	(S_c) (deg./ppm)	SD	$\Delta\theta_{HM}$	LoD (M) $=3 \Delta\theta_{HM}/S_c $
Au	1.3	1.4×10^{-8}	0.00158	1.76×10^{-8}
Au/SLG	4	1.4×10^{-8}	0.00158	5.73×10^{-9}
Au/SiO ₂ /SLG	1.4	1.4×10^{-8}	0.00158	1.63×10^{-8}

It can also be seen that the SPR angle of Au/SLG and Au/SiO₂/SLG sensors upon the Pb^{+2} ions move towards smaller values, which presents a negative shift with respect to the SPR angle in the deionized water. It is well known that most SPR sensors exhibit a positive shift of the SPR angle due to increase in refractive index of the sensing layer during the analyte-ligand interaction. However, in literature there exist some experimental results which show negative shift behavior [136, 137]. Such an uncommon SPR response might arise due to decrease in the refractive index and/or the thickness of the sensing layers, that could be explained

as follow. At top most interface the Pb^{+2} ions act as electrons accepters, which can accept electrons from graphene and reduce to neutral ions on the SLG sensing surface. This suggest Pb-C bonding during the interaction between p_z orbital of C atoms and valence orbital of metal adsorbates [139]. On other hand at Au/SLG interface there is an electron transfer from graphene to thin gold film. Therefore, these redistributions of charges might form the whole structures as a hybrid metamaterial with unknown optical properties. Nevertheless, stronger arguments are needed to better understand the way in which the optical properties of this new hybrid structure changes. To get this fundamental knowledge we started collaboration with Prof. Ivan Shtepliuk at Department of Physics Linkoping University Sweden, which is performing DFT calculations in order to quantitatively understand both the electron transfer and binding energy of the Pb^{+2} ions on the Au and Au/SLG sensing platforms.

6 Ellipsometric Application of SPR spectroscopy

Another important application of SPR spectroscopy is the ellipsometric characterization of thin layer deposited over the Au sensor using different methods. In this chapter we will focused on different SPR based characterization techniques to investigate the optical properties of metal NPs, organic thin film and graphene. In the first part of the chapter, we employed a new method called the SPR two-color nanosizer for the determination of surface density and the mean statistical size of the citrate stabilized AuNPs in an effective composite layer. We will briefly discuss the modeling theory based on Maxwell's Garnett approximation, the accuracy evaluations and the limit of applicability of SPR two-color nanosizer. In the second part of the chapter, we introduced the two-film thickness method and the dual mode analysis based on DLWGs structure for the simultaneous determination of refractive index and thickness of organic luminescent materials. Finally, the mixed dual mode and two wavelengths method will be used to investigate the anisotropy of graphene.

6.1. SPR two-color nanosizer

Recently the use of AuNPs in the SPR spectroscopy have gain a considerable interest due to its high chemical stability and the enhancement of the resolution of optical biosensors using the metal nanoparticle-amplified SPR spectroscopy (PA-SPR) configuration [40, 139]. The knowledge about both the surface density (σ) and dimension of the nanoparticles to calculate the mass resolution of the sensor [40] or SERS gain [85], respectively are fundamental in PA-SPR spectroscopy and in surface enhanced Raman scattering (SERS) spectroscopy based on bidimensional arrays of AuNPs. SPR spectroscopy studies on self-assembled monolayers (SAM) of AuNPs in the Kretschmann configuration show that the dielectric constant of the Au/water composite film can be measured once that σ and the size of the AuNPs are determined by complementary techniques [67,139]. Depending on the dimension of the AuNPs and excitation wavelength, when σ is high, or the SiO₂,

interlayer thickness is below 5 nm, inter AuNPs dipole-dipole interactions and dipole interaction between the Au thin film and the AuNPs have to be considered. In this case, numerical or semianalytical optical models taking into account the optical anisotropy of the AuNPs have to be used for the accurate determination of σ [31, 140].

In the present section we show how SPR spectroscopy can be used for the development of a two-color SPR nanosizer, able to measure both the statistical mean radius $\langle r \rangle$ and the surface density σ of citrate stabilized AuNPs deposited over SiO₂ surfaces. These performances are possible when the optical density $\tau(\lambda, \sigma)$ of the SAM of AuNPs is negligible at both the excitation wavelengths. The latter condition is realized by minimizing the surface density σ of the bidimensional array of AuNPs and the overlap between the single nanoparticle extinction cross-section and the frequency of the laser source used to excite the SPPs. The value of measured by SPR spectroscopy is compared with the results obtained by traditional techniques such as AFM, TEM and DLS. The accuracy of the optical method is evaluated taking in consideration different experimental parameters, such as the uncertainty in the experimental values of the thickness and complex dielectric constant of the thin films composing the SPR sensing platforms, the nanoparticle surface density σ , and the experimental polydispersity of the colloidal solution of AuNPs. Finally, we present a detailed discussion about the limits of the applicability of the presented method to gold nanoparticles of different sizes.

6.1.1. Experimental method

Figure 6.1 represents the two-color SPR nanosizer in the Kretschmann configuration, with double laser sources at the wavelengths of 633 nm and 783 nm. The fabrication of SPR sensors chip used in this work is explained in section 3.1. The external SiO₂ thin film was functionalized with a self-assembled monolayer of 3- Aminopropyltriethoxysilane (APTS) [67], which acts as a Coulombic ligand for negative charged citrate stabilized AuNPs. The AuNPs were synthesized in this work using the chemical procedure described in [142] adapted to obtain statistical mean diameter of about 15 nm. A continuous flux pump attached to the fluidic cell used to inject the AuNPs at rate 0.3 mL/min (see section 3.4).

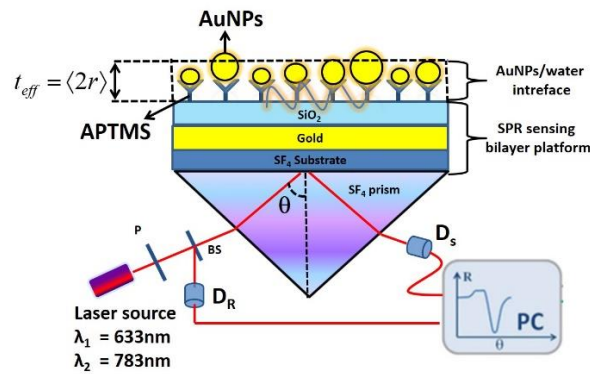


Figure 6.1: Two-color SPR nanosizer in the Kretschmann configuration. The thickness of the nanocomposite layer t_{eff} is considered equal to the statistical mean diameter of the AuNPs [143].

The application of the two-color SPR nanosizer to citrate stabilized AuNPs of unknown dimension involves the following main experimental procedure:

- 1) Consideration of the spectral overlap between the extinction cross-section of the AuNPs and the wavelength λ_1 and λ_2 of the excitation laser sources.
- 2) Accurate measurement of the dielectric constant and thickness of the gold and SiO_2 thin films constituting the SPR sensing platform, at both wavelengths λ_1 and λ_2 .
- 3) Deposition of SAM of AuNPs with sufficiently low optical density τ .
- 4) Analysis of the experimental data applying the two-color SPR method supported by MG theory in the low surface density approximation.

The theoretical model and the working principle have been already discussed in section 2.9. In the following section, we will investigate the main results obtained from the application of two-color SPR nanosizer.

6.1.2. Results and discussion

6.1.2.1. Comparative measurements

Figures 6.2(a) and (b) show the typical TEM and AFM images used for the comparative analysis of the dimension of the AuNPs respectively. In the inset of the figures, represent the corresponding experimental statistical size distributions. This size distribution is modelled using a normalized lognormal function as discussed in section 2.8. The same approach has been applied for the determination

of statistical mean size $\langle r \rangle$ and standard deviation δ using the statistical size distribution obtained by DLS. In Table 6.1, the values of the $\langle r \rangle$ and δ of the size distribution of the AuNPs are listed.

Table 6.1: Mean value $\langle r \rangle$ and standard deviation δ of the statistical distribution of radius of the citrate stabilized AuNPs measured using different experimental techniques.

Techniques	DLS	TEM	AFM
Radius ($\langle r \rangle$)	8.8 nm	7.4 nm	7.3 nm
Standard deviation (δ)	2.7 nm	1.5 nm	1.2 nm

Figure 6.2(c) represents the experimental extinction spectra of the colloidal dispersion of AuNPs, together with the theoretical fit of Mie [76], obtained using the TEM statistical distribution shown in Fig. 6.2(a). The overlap between the experimental and theoretical extinction spectra is excellent, confirming that the TEM size distribution and the value of TEM $\langle r \rangle$ of Table 6.1 are reliable, so that will be considered as our reference data in further discussion. The two vertical lines show the excitation wavelengths used in our experimental configuration. Moreover, the lines corresponding to λ_1 and λ_2 are considerably far from the LSPR band of the gold colloids, so that the single isolated AuNPs can be reasonably considered as transparent.

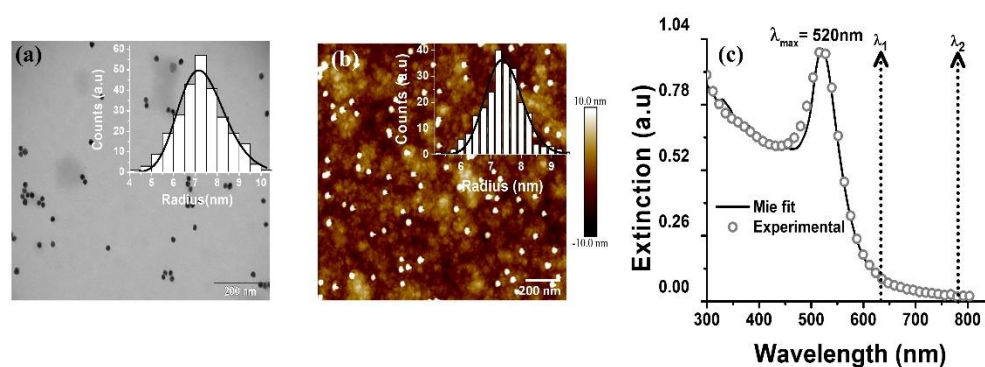


Figure 6.2: (a) TEM image of the AuNPs and (b) AFM image on $1 \mu\text{m} \times 1 \mu\text{m}$ region. The inset of the images show the statistical AuNPs size distribution obtained using (a) TEM and (b) AFM microscopy over a set of 400 data points. (c) Comparison between the experimental (open grey circles) and theoretical (continuous black line) extinction spectra of the colloidal dispersion of AuNPs in water [143].

6.1.2.2. Two-color SPR spectroscopy

Before the deposition of the SAM of AuNPs, the Au/SiO₂ bilayer constituting the optical sensing platform is characterized by two-color SPR spectroscopy as discussed in 2.6.2, in order to retrieve the values of both the refractive index and the thickness of gold and SiO₂ thin film at both laser radiation wavelengths. In Table 6.2 we summarize the results obtained at the excitation wavelengths of $\lambda_1 = 633$ nm and $\lambda_2 = 783$ nm.

Table 6.2: Experimental values of the optical parameters of the SPR sensing platform obtained using section 2.6.2. The refractive index of water and SF4 were taken from [144].

λ (nm)	SF4	Gold		SiO ₂		water
	ϵ_r	t(nm)	$\epsilon = \epsilon_r + i\epsilon_i$	t(nm)	ϵ_r	ϵ_r
633	3.06	49.8	-11.91+i1.51	29.12	2.15	1.77
783	3.02	49.8	-23.48+i1.79	29.12	2.13	1.76

Figure 6.3(a) represents the experimental SPR reflectivity curves of the Au/SiO₂ sensing platforms in water at the excitation wavelengths λ_1 and λ_2 , before and after the deposition of the SAM of AuNPs. Therein, for each wavelength λ we indicate the shift in the angle of resonance SPR $\Delta\theta_\lambda$ in the SPR curves upon the deposition of the Au/water composite thin film. As explained in [16,17,18], to each SPR $\Delta\theta_\lambda$ it is associated a continuous line in the plane ϵ_{eff} vs $\langle r \rangle = t_{eff}/2$, composed by the couples of values of the dielectric constant and thickness of the thin film under investigation which induce the angle shift observed experimentally.

For calculation of the lines in the plane ϵ_{eff} vs $\langle r \rangle = t_{eff}/2$ associated to the experimental SPR spectra, we used Winspall free software based on the classical transfer matrix method [104], which calculates the reflectivity curves of planar multilayer systems. In the program, we fix the values of the parameters of the Au/SiO₂ bilayer as listed in Table 6.2, and vary the values of ϵ_{eff} and t_{eff} of the Au/water composite thin film to match the experimental angle of resonance shift SPR $\Delta\theta_\lambda$. The results are shown in Fig. 6.3(b), where the filled black and grey points represent the solutions relative to the wavelengths λ_1 and λ_2 , respectively.

The intersection point of the curves highlighted in the figure represents the final measured value of both t_{eff} and ε_{eff} , obtained by shifting the curve associated to λ_2 using the parameter, $Q_{\lambda_1, \lambda_2} = 1.266$ calculated from Equation. (2.88). The value of the mean radius of the AuNPs estimated by SPR spectroscopy is $\langle r \rangle_{SPR} = 7.1nm$, which matches with an accuracy better than 0.5 nm with the results obtained by TEM and AFM analysis reported in Table 6.1, considered as reference results.

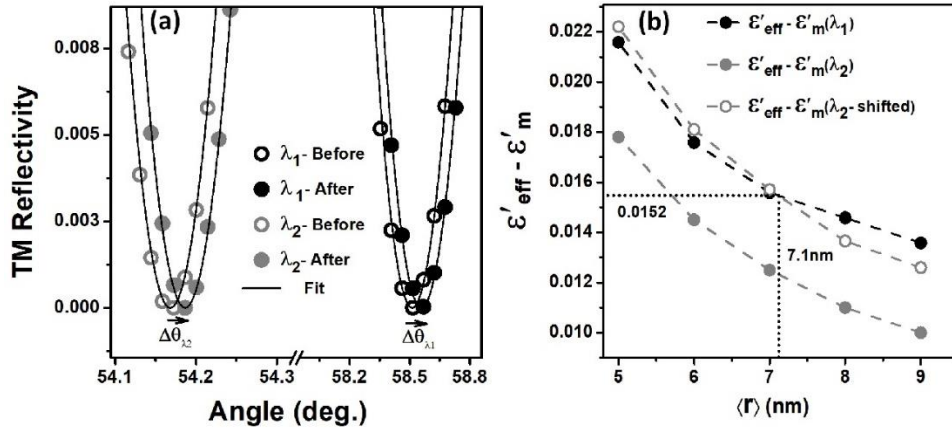


Figure 6.3: (a) Experimental SPR minimum angle profiles at λ_1 (black) and λ_2 (grey) before (open circles) and after (fill circles) the AuNPs. The observed SPR angle shift are $\Delta\theta_{\lambda_1} = 0.0471^\circ$ and $\Delta\theta_{\lambda_2} = 0.0186^\circ$. (b) Curves of the possible values in the plane ε_{eff} Vs $t_{eff}/2$ at the wavelengths λ_1 and λ_2 . The intersection point of the curves represents the real value, obtained by shifting the curves using the parameter $Q_{\lambda_1, \lambda_2} = 1.266$ calculated from Equation (2.88) [143].

From Figure 6.3(b), the calculate average radius $\langle r \rangle_{SPR} = 7.1nm$ and the value of the effective dielectric constant $\varepsilon'_{eff} - \varepsilon'_m = 0.0152$ is further put into equation (2.79) to find the value of filling fraction f using the following relation [143]:

$$f = \frac{(\varepsilon'_{eff} - \varepsilon'_m) (\varepsilon_i^2 + \varepsilon_r^2 + 4(\varepsilon_r - \varepsilon'_m))}{3 (\varepsilon_i^2 - 2\varepsilon_m'^2 + \varepsilon_r(\varepsilon_r + \varepsilon'_m))} \quad (6.1)$$

From Equation (6.1) we obtain $f = 0.0031$ and $\sigma_{SPR} = 27 NP/\mu m^2$, in good accordance with the average surface density of about $25 NP/\mu m^2$ as determined afterwards by AFM control measurements executed over the same sample.

6.1.2.3. Accuracy evaluation

The main source of experimental error in the determination of the optical constants and thickness of the composite AuNP/water thin film is ϵ_r , the real part of the dielectric constant of the gold thin film supporting the plasma. The accuracy $\delta\epsilon_r$ is about 0.5%, which propagates, and influences the determination of the crossing point of the curves of the possible values in the plane ϵ_{eff} vs $\langle r \rangle = t_{eff}/2$ at the wavelengths λ_1 and λ_2 (Figure 6.3(b)). To determine the value of $\Delta r_{experimental}$ we found the new intersection point in the plane at the wavelengths λ_1 and λ_2 by changing the value of the dielectric constant of the gold thin film supporting the plasma wave by $\delta\epsilon_r = \pm 0.5\%$. The new curves in the ϵ_{eff} vs $\langle r \rangle = t_{eff}/2$ plane is represented in Figure 6.4. From the results shown in the latter, we conclude that the experimental accuracy in the determination of the main radius by SPR spectroscopy is ± 0.5 nm, corresponding to $\Delta r_{experimental} \approx 7\%$.

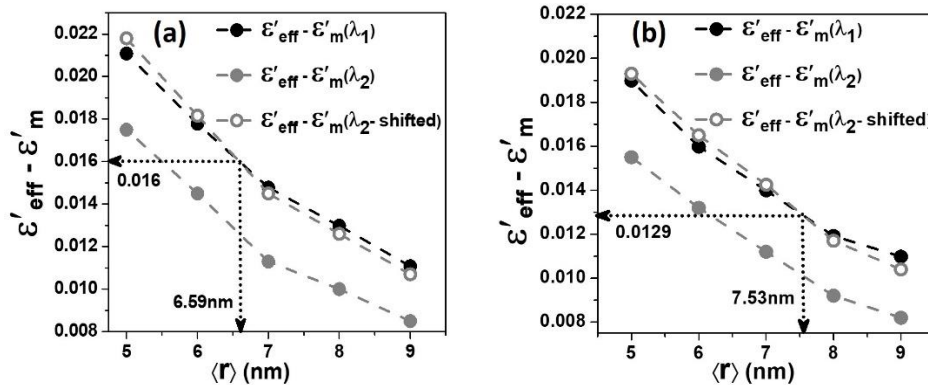


Figure 6.4: Curves in the plane ϵ_{eff} Vs $\langle r \rangle = t_{eff}/2$ corresponding to a variation $\delta\epsilon_r$ of the dielectric constant of the thin layer of gold supporting the plasma wave. (a) + 0.5%, (b) - 0.5%. The experimental accuracy in the determination of the main radius by SPR spectroscopy is ± 0.5 nm, corresponding to $\Delta r_{experimental} \approx 7\%$.) [143].

Apart from this the polydispersivity of the colloidal solution of AuNPs and nanoparticle surface density in the composite thin film are the other factors that have further influence in the accuracy of the result. To determine the dependence of the accuracy of the measurement of the mean size of the AuNPs on the surface density σ , we first used the Winspall to calculate the theoretical value of the shift in SPR angle $\Delta\theta_\lambda$ associated to the deposition of an array of spherical, identical

and perfectly monodispersed AuNPs with the radius equal to $\text{TEM} = 7.4$ nm. The calculus was repeated by fixing the values of the parameters of the Au/SiO₂ bilayer as listed in Table 6.2, and considering increasing values of σ up to about 150 NP/ μm^2 . For each value of surface density, we calculated the solution lines in the plane ϵ_{eff} Vs $\langle r \rangle$, and found the final value SPR by shifting the curve associated to λ_2 , accordingly to Equation. (2.81). Figure 6.5(a) shows the theoretical percentage deviation $\Delta r_{\text{density}}$ between $\langle r \rangle_{\text{TEM}}$ considered as the reference value, and $\langle r \rangle_{\text{SPR}}$ obtained by the theoretical application of the two-color method in the low surface density approximation. The results demonstrate that the accuracy scales almost linearly with σ , rising up to 10% for densities higher than ~ 100 NP/ μm^2 , but being as small as 2% when working with NPs surface densities $\sigma \leq 20$ NP/ μm^2 ($f \leq 2.5 \times 10^{-3}$), a condition which we demonstrated experimentally.

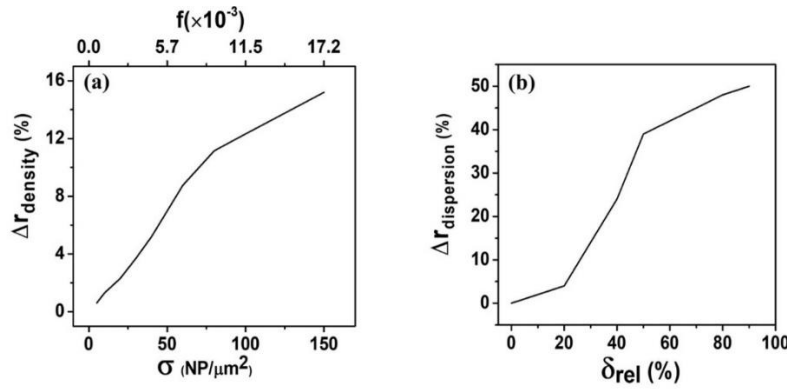


Figure 6.5: (a) Percentage deviation $\Delta r_{\text{density}}$ between the value $\langle r \rangle_{\text{TEM}}$ and the value of the average radius $\langle r \rangle_{\text{SPR}}$ obtained by the application of the two-color method depending on σ . (b) Percentage deviation $\Delta r_{\text{dispersion}}$ between $\langle r \rangle_{\text{log-normal}}$ and $\langle r \rangle_{\text{SPR}}$ obtained by the application of the two-color method depending on the relative radius standard deviation $\delta_{\text{rel}} = (\delta_{\text{log-normal}} / \langle r \rangle_{\text{log-normal}})$ [143].

When the colloidal dispersion of AuNPs is not perfectly monodispersed, then the real metal volume factor of the AuNPs array is different from the one calculated using the approximate expression $= 2\pi \langle r \rangle^2 \sigma / 3$, and depends on the size distribution parameter δ . To understand the effect of the polydispersity on the SPR spectra, we define a relative radius standard deviation $\delta_{\text{rel}} = \delta / \langle r \rangle$, and consider trials colloidal dispersions of AuNPs characterized by a normalized lognormal statistical distribution $n(r)$ with increasing δ_{rel} ranging between 0% and 90%. Considering for example the distribution obtained by the TEM measurements, we

have $\langle r \rangle_{\text{TEM}} = 7.4\text{nm}$ and $\delta_{\text{TEM}} = 1.5\text{nm}$, corresponding to a relative standard deviation $\delta_{\text{rel}} = 20\%$.

We evaluate theoretically the effect that the statistical size dispersion of the AuNPs has on the SPR curves defining a statistical metal volume filling fraction f_{stat} as discussed in section 2.8. When considering f_{stat} instead of f , the theoretical angle shift $\Delta\theta_{\lambda}^{\text{SPR}}$ upon interaction between the SiO_2 surface and the AuNPs is different from the angle shift obtained considering the array distribution of nanoparticles with the same surface density σ but constituted by identical AuNPs with radius equal to $\langle r \rangle_{\text{log-normal}}$, which is the statistical main radius calculated from the trial log-normal distribution $n(r)$. For each value of δ_{rel} , we used our code to calculate $\Delta\theta_{\lambda}^{\text{SPR}}$ stat and the corresponding solution lines in the plane ϵ_{eff} Vs $\langle r \rangle$, and found the final value $\langle r \rangle_{\text{SPR}}$ by shifting the curve associated to λ_2 accordingly to Equation. (2.88). The results are summarized in Fig. 6.5(b), where we represent the theoretical percentage deviation $\Delta r_{\text{dispersion}} = 100(\langle r \rangle_{\text{SPR}} - \langle r \rangle_{\text{log-normal}})/\langle r \rangle_{\text{log-normal}}$ depending on the parameter δ_{rel} . In the latter expression, $\langle r \rangle_{\text{log-normal}}$ is the reference value of the main radius, and $\langle r \rangle_{\text{SPR}}$ is the value of the main radius obtained by the application of the two-color method in the approximation of monodispersed colloidal solutions.

One can see that when the value of δ_{rel} is between 0% and 20%, $\Delta r_{\text{dispersion}}$ is lower than 4%. We conclude that two-color SPR spectroscopy can be used in a very low surface density regime ($f \leq 4 \cdot 10^{-3}$, $\sigma \leq 20 \text{ NP}/\mu\text{m}^2$) for the determination of the average dimension of spherical AuNPs with a mean diameter of the order of 15 nm with an accuracy $\Delta r = (\Delta r_{\text{dispersion}} + \Delta r_{\text{density}} + \Delta r_{\text{experimental}})$ better than $\sim 10\%$, when considering monodispersed nanoparticles (i.e $\delta_{\text{rel}} = 0$). In the same surface density conditions, when δ_{rel} of the size distribution of the colloidal AuNPs is lower than 20%, the average radius of the NPs can be measured with a relative accuracy Δr better than $\sim 15\%$. The presented theoretical calculations, show that the influence of the experimental parameters (surface density, polydispersivity, $\delta\epsilon_r$) on the accuracy of the method cannot be ruled out, and validate the optical method when the effective accuracy in the discrimination of AuNPs of different sizes can be maintained in the order of ~ 10 to 15%.

6.1.2.4. Limits of applicability of two-color SPR nanosizer

At the base of the reliability of the presented optical method is the validity of the Maxwell's Garnett (MG) theory. The hardest restriction in the use of the effective medium theories is related to the dimension of the nanoparticles included in the transparent dielectric matrix, since the scattering cross-section of the nanoparticles is neglected in the formulation of the effective dielectric constant ϵ_{eff} of the composite thin film [78, 144]. When the exact shape and spectral position of the maximum of the absorption cross-section of the composite thin film is desired, MG theory can be used for AuNPs with a mean diameter up to ~ 10 nm, while modified generalized Maxwell-Garnett Mie (MGM) theory can be used with reliable predictions up to nanoparticles diameters of ~ 40 nm [146]. In any case, when the scattering process of the isolated single AuNP is not negligible in the expression of the extinction crosssection σ_{ext} , all the effective medium theories lose their physical meaning, as pointed out in [147].

The solution that we propose in the present research to overcome the limits of effective medium theory in the prediction of the extinction properties of composite thin films, is to consider samples with negligible optical density, so that $\epsilon''_{\text{eff}} \approx f \approx 0$. The latter condition can be reached by probing the composite thin film with an excitation wavelength as far as possible from the LSPR resonances of the arrays of nanoparticles, and by the deposition of SAM of AuNPs with low surface density σ .

The optical density $\tau(\lambda, \sigma)$ SAM for a SAM of monodispersed AuNPs with surface density σ and thickness (i.e diameter) $2r$ can be simply written as [79]:

$$\tau(\lambda, \sigma, r) = \sigma_{\text{ext}}(\lambda) \frac{N}{V} \log(e) \cdot 2r = \log(e) \sigma \cdot \sigma_{\text{ext}}(\lambda). \quad (6.2)$$

where λ is the excitation wavelength, σ_{ext} is the extinction cross-section of the isolated AuNP, and N is the total number of nanoparticles contained in the volume $V = 2rA$. The optical densities of the composite monolayer calculated by Eq. (6.2) at the experimental surface density of $27 \text{ NP}/\mu\text{m}^2$ are $\tau_{\lambda_1} \approx 2.0 \times 10^{-4}$ and $\tau_{\lambda_2} \approx 3.5 \times 10^{-5}$. In these conditions, both the absorption and the scattering by the composite thin film are negligible ($\epsilon''_{\text{eff}} \approx 0$). Hence, the MG theory is used only to predict the effect that nanosized inclusions have on dispersion properties of the real part of

effective dielectric constant of the thin film, using the expression of ϵ_{eff} at the first order in f like in Equation (2.88).

Equation (6.2) gives important information about the procedure to be followed to deposit SAM of AuNPs with the same optical density using nanoparticles of different radius r . Considering the scaling relation between σ and σ_{ext} , when the dimension of the AuNPs increases we can maintain a low value of τ by decreasing the surface density σ . The scaling between $\sigma(r)$ and the dimension of the monodispersed AuNPs is shown in Fig. 6.6(a), where the reference experimental value τ_{λ_1} was considered. The scaling is shown for mean radius ranging from 7 to 30 nm, and the extinction cross-section $\sigma_{\text{ext}}(633 \text{ nm}, r)$ of the single nanoparticle was calculated applying the Mie theory with both dipole and quadrupole oscillations. In the same graph, for each value of nanoparticle surface density and radius, is represented the corresponding mass surface density of gold, calculated as $\sigma_{\text{mass}}(r) = \sigma(r)\rho_{\text{Au}}r^3$, where $\rho_{\text{Au}} = 19.32 \text{ g/cm}^3$ is the bulk density of gold.

In Fig. 6.6(b) are represented, for both wavelength λ_1 and λ_2 , the theoretical shift of the SPR angle $\Delta\theta(r, \sigma(r))$ associated to the deposition of a SAM of AuNPs with the calculated mass surface density $\sigma_{\text{mass}}(r)$, where the effective dielectric constant of the composite layer has been calculated by the use of Eq. (2.81). In Fig. 6.6(b) the horizontal dashed red-line, line is set in correspondence of $\Delta\theta_{\text{SPR}} = 0.01^\circ$, corresponding to a conservative value of the angular resolution of traditional or commercial SPR spectrometer, in terms of minimal observable angular shift [23].

As evident in Figure 6.6(a), to maintain a reference value of optical density of the SAM of $\tau_{\lambda_1} \approx 2.0 \times 10^{-4}$ for AuNPs up to diameters of the order of 60 nm, it is necessary to deposit SAM with a surface density of the order of $0.1 \text{ NP}/\mu\text{m}^2$. In this way, with the increasing of the linear dimension, the mass of gold deposited in form of nanoparticles on the SiO_2 surface decreases, ultimately approaching the range of $10^{-18} \text{ ng}/\mu\text{m}^2$. A similar trend is observed in the theoretical angle shift $\Delta\theta_{\text{SPR}}$ after the deposition of the SAMs of AuNPs, reported in Fig. 6.6(b). In the low surface density approximation, when the refractive index of the composite layer can be approximated as purely real, the surface mass density and the SPR angular shift are linearly proportional one with each other, and the two-color nanosizer can be considered as an accurate nanobalance, with a maximum response for SAM of

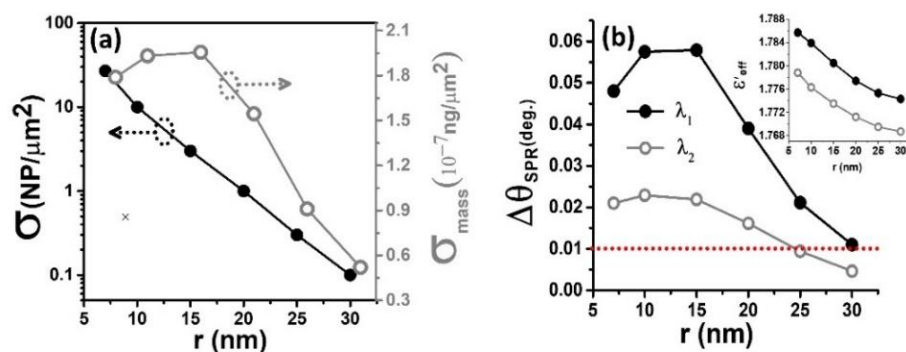


Figure 6.6: Theoretical behavior of SAM of monodisperse AuNPs with same optical density $\tau \approx \tau_{\lambda_1}$. (a) Surface density $\sigma(r)$ (black points, left Y-axes) and mass surface density of gold $\sigma_{\text{mass}(r)}$ expressed in $\text{ng}/\mu\text{m}^2$ (grey circles, right Y-axes) in function of the radius r of the AuNPs. (b) Shift of the angle of resonance $\Delta\theta(r)$ at both the excitation wavelengths λ_1 (black points) and λ_2 (grey circles) after the deposition of the associated mass surface density of gold $\sigma_{\text{mass}(r)}$. The dashed horizontal red-line is set in correspondence of $\Delta\theta_{\text{SPR}} = 0.01^\circ$ [143].

AuNPs with a mean radius of the order of 15 nm, corresponding to a maximum mass surface density of gold of about $2 \times 10^{-17} \text{ ng}/\mu\text{m}^2$. The smallest angle shifts $\Delta\theta_{\text{SPR}}$, observed at the wavelength of 783 nm for nanoparticles with a radius of 30 nm, is of the order of 0.005° degrees, corresponding to the double of the angular resolution of our experimental set-up, in terms of minimal observable angular shift.

6.2. Ellipsometric characterization of luminescent organic thin films by DLWGs

In this section, we report the employment of multimodal SPR spectroscopy for the simultaneous determination of thickness and dielectric constant of organic luminescent thin film Alq_3 and $\text{Eu}(\text{dbm}_3\text{phen})$ deposited on the DLWGs structure. Alq_3 is among the most stable and commonly used electron transport material in Organic Light Emitting Diodes (OLEDs) and organic photovoltaic cells (OPV) [148] due to strong luminescence, high electric conductance and low cost. In spite of its advance, applications in OLEDs based devices, the knowledge and understanding of the optical properties of Alq_3 is still limited.

In this work, a monomodal experimental approach based on two-film thickness (TFT) method is used to deduce the refractive index and thickness of

encapsulated thin film of Alq_3 . The resultant optical parameters are used as a reference in this work. The optical constants of both stable encapsulated Alq_3 and $\text{Eu}(\text{dbm}_3\text{phen})$ thin films are also determined using the dual mode of DLWGs at two wavelength 633nm and 783nm. Finally, the encapsulated sample are irradiated with UV radiation to observe simultaneously the induced modification on both thickness and refractive index of the thin film, by using the dual mode analysis.

6.2.1.

Characterization of Alq_3 using two film thickness method

In this method the two different nominal thickness $t_1 = 16\text{nm}$, and $t_2 = 32\text{nm}$ of Alq_3 were thermally deposited over 49nm thin Au film and the sample were encapsulated inside a nitrogen environment as explained in experimental section 3.1.4. Prior to the thermal deposition of Alq_3 , the bare gold thin film was characterized with Winspall free software by using the best fitting on the experimental reflectivity curve at SPR excitation wavelength of 633nm and 783nm. Table 6. Summarize the optical parameters obtained after fitting.

Table 6.3: Thickness and dielectric constant of Au thin before the deposition of Alq_3 .

λ (nm)	layer	t (nm)	ϵ_r	ϵ_i
633	BK7	0	2.29	0
	Au	49.91	-10.79	1.52
	Air	0	1	0
783	BK7	0	2.29	0
	Au	49.91	-21.42	1.79
	Air	0	1	0

Figure 6.7(a) show the experimental and theoretical monomodal SPR curve of the TFT samples. Following, the procedure of TFT method as explained in section 2.6.3, we can find the intersection point in the plane ($\epsilon_{\text{Alq}_3}, t_{\text{Alq}_3}$) which corresponding to the actual value of the thickness and dielectric constant of Alq_3 as shown in Figure 6.7(b).

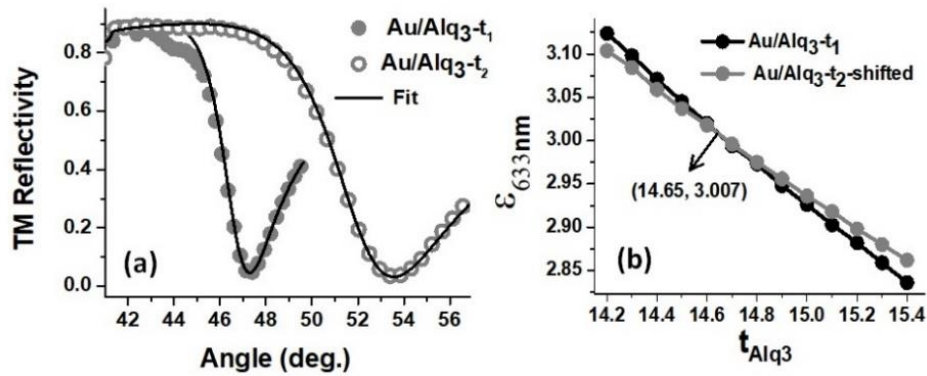


Figure 6.7: (a) Theoretical and experimental monomodal SPR curves of TFT method at wavelength of 633nm. The gray closed and open circles corresponds to the experimental SPR curve of nominal thickness of $t_1 = 16\text{nm}$ and $t_2 = 32\text{nm}$ respectively. (b) The set of possible values of ϵ_{Alq_3} and t_{Alq_3} of Alq₃ collected over the TFT sample. With the knowing values of the ratio between the thickness t_1 and t_2 , the intersection point gives the actual value of the Organic thin film.

In this case, the value of the thickness and dielectric constant of Alq₃ at wavelength of 633nm obtained from the intersection point $(\epsilon_{\text{Alq}_3}, t_{\text{Alq}_3})_{633\text{nm}} = (14.65, 3.01)$. We also performed measurement on the same sample and position at wavelength of 783nm. Figure 6.8 show the SPR experimental curve collected on the two different thickness t_1 and t_2 . Using the value of the thickness of Alq₃ i.e. 14.65nm, calculated at wavelength of 633nm we can obtained the best theoretical curve over the experimental with a dielectric constant of Alq₃ equal to 2.808.

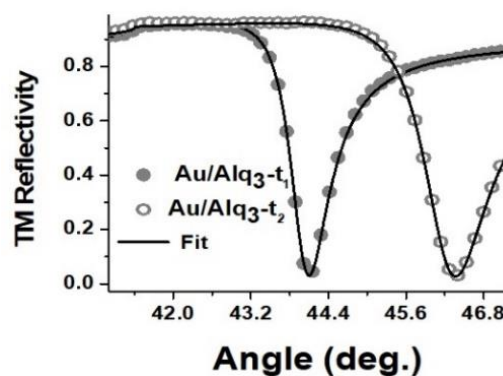


Figure 6.8: Theoretical and experimental monomodal SPR curves at wavelength of 783nm.

It should be noted that the position of the intersection point is highly depends on the dielectric constant and the thickness of the Au thin film and on the precise determination of the actual ratio of thickness t_1 and t_2 of the organic deposition [34].

The resultant value of the real part of the refractive index of Alq₃ obtained at the wavelength of 633nm and 783nm are coherent with the value reported in literature by using different characterization techniques [34, 71], [148]. The obtained value of refractive index at 633nm and 783nm in this work is compared with the reported ones in literature in table 6.4.

Table 6.4: Comparison of the real part of refractive index of Alq₃ calculated at 633nm and 783nm using in this work and other characterization techniques.

λ (nm)	n_{Alq_3}	Technique
633	1.73	Spectrophotometric [117]
	1.72	Spectroscopic ellipsometry[71]
	1.74	In this work (TFT)
	1.75	In this work (dual mode analysis)
783	1.68	In this work (TFT)
	1.70	In this work (dual mode analysis)

6.2.2.

Dual mode analysis for characterization of Alq₃ and Eu(dbm)₃phen

The basic procedure of dual mode analysis of DLWGs is discuss in section 6.2.2. In this method the two independent modes (TM₀ and TM₁) of DLWG structure has been utilized for the simultaneously determination of the refractive index and thickness of the encapsulated thin film of organic materials. Before the deposition of organic thin film, the optical parameters of Au and SiO₂ are determine by the best fitting of theoretical curve on the experimental SPR curve at two different wavelength 633nm and 783nm. The calculated values are listed in table 6.5. The Figure 6.9(a) represent the experimental and theoretical TM SPR reflectivity curves, where we can see two waveguide modes (TM₀ and TM₁) at $\lambda_1=633$ nm and only one TM mode at 783nm.

Table 6.5: The thickness and dielectric constant of Au and SiO₂ obtained using Winspall free software.

λ (nm)	layer	t (nm)	ϵ_r	ϵ_i
633	Au	46.79	-11.54	1.467
	SiO ₂	591.7	2.052	0
	Air	0	1	0
783	Au	46.79	-21.46	1.66
	SiO ₂	591.7	2.045	0
	Air	0	1	0

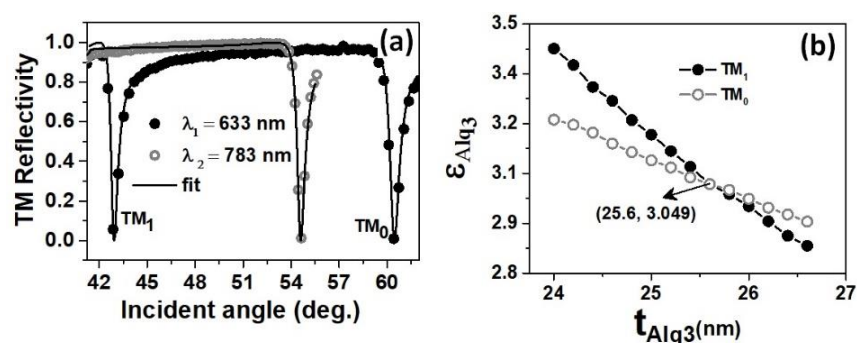


Figure 6.9: (a) Theoretical and experimental SPR curves of dual mode method. The closed and open circles correspond to the experimental SPR curve of at wavelength of 633nm and 783nm respectively. (b) The set of possible values of ϵ_{Alq_3} and t_{Alq_3} of Alq₃ collected over the sample at the wavelength of 633 nm. The intersection point gives the actual value of the organic thin film.

The measurement was performed without any modification in the encapsulated thin organic film. The resonance angle of TM₀ and TM₁ mode of the multimodal SPR curve is associated to a set of possible values of dielectric constant and thickness of Alq₃. These set of values are plotted in a $(\epsilon_{Alq_3}, t_{Alq_3})$ plan, yielding an intersection point that is the actual values of the thickness and refractive index Alq₃ as shown in the Figure 6.9(b). In this case, the intersection point corresponds to $(\epsilon_{Alq_3}, t_{Alq_3})_{633nm} = (25.6, 3.049)$. The refractive index at a wavelength of 783nm can be calculated by taking $t_{Alq_3} = 25.6$ fixed and varying

the refractive index until a best fitting is obtained between experimental and theoretical curve. The value of index of refraction of Alq_3 at two wavelengths is consistence with our reference value calculated in previous section and with other techniques as listed in table 6.4.

Following the same procedure, we can also determine simultaneously the thickness and dielectric constant of $\text{Eu}(\text{dbm})_3\text{phen}$ as shown in the Figure 6.10. The nominal thickness of $\text{Eu}(\text{dbm})_3\text{phen}$ was 26nm. In this case, the obtained values of the refractive index at 633nm and 783nm are 1.55 and 1.52 respectively, which are coherent with the literature [149, 150]. All these literature data about the index of refraction are based on theoretical models and as for our knowledge this is the first experimental attempt to deduce the refractive index of $\text{Eu}(\text{dbm})_3\text{phen}$.

Table 6.6: The thickness and dielectric constants of Au and SiO_2 determine by Winspall at two wavelengths before the deposition of organic materials

λ (nm)	Layer	t (nm)	ϵ_r	ϵ_i
633	Au	49.76	-11.18	1.59
	SiO_2	538.55	2.11	0
	Air	0	1	0
783	Au	46.79	-22.84	1.91
	SiO_2	538.55	2.09	0
	Air	0	1	0

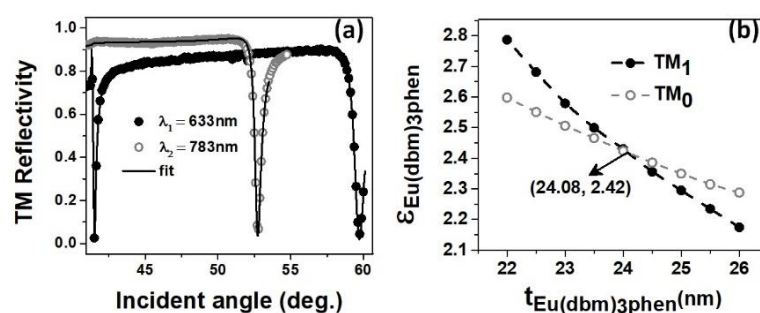


Figure 6.10: (a) Theoretical and experimental SPR curves of dual mode method for $\text{Eu}(\text{dbm})_3\text{phen}$ characterization. The closed and open circles correspond to the experimental SPR curve of at wavelength of 633nm and 783nm respectively. (b) The set of possible values of $\epsilon_{\text{Eu}(\text{dbm})_3\text{phen}}$ and $t_{\text{Eu}(\text{dbm})_3\text{phen}}$ Of $\text{Eu}(\text{dbm})_3\text{phen}$ collected over the sample near to the resonance of each mode.

Moreover, the study of the dual mode analysis is extended to understand the simultaneously effect on both thickness and refractive index of organic thin film after a control dose of UVA irradiation. For this particular study we thermally deposited a thin film of $\text{Eu}(\text{dbm})_3\text{phen}$ over the DLWGs, irradiated with an energy dose of 60 J/cm^2 and recorded the TM modes in resonance condition, both before and after UVA radiation. All the experimental setup and parameters are the same as discussed in section 5.1. The optical parameters of Au and SiO_2 were calculated before the UVA treatment using Winspall free software. The thickness and the dielectric constant of organic thin film were calculated by the dual mode analysis method before and after the irradiation. Table 6.7 reports the list of the thickness and dielectric constant of each layer before and after the irradiation.

Figure 6.11(a) show the experimental dual mode SPR curve before and after UVA irradiation at a wavelength of 633nm . A significant SPR angle shift of in TM_0 ($\Delta\theta_{\text{TM}_0} = 0.019^\circ$) and TM_1 ($\Delta\theta_{\text{TM}_1} = 0.013^\circ$) has been observed after the irradiation. Figure 6.11(b) represents the application of dual mode for the determination of change in the thickness and refractive index of $\text{Eu}(\text{dbm})_3\text{phen}$ before and after the UVA irradiation. We observed a change in the refractive index of about $\Delta n_{633\text{nm}} = 0.0183$, and no changes in the thickness of the organic luminescent thin films.

Table 6.7: The calculated optical parameters of each layer in the $\text{BK7}/\text{Au}/\text{SiO}_2/\text{Eu}(\text{dbm})_3\text{phen}$ structure before and after irradiation with UVA light.

	layer	$\lambda = 633\text{nm}$		
		t(nm)	ϵ_r	ϵ_i
Before UVA	BK7	0	2.29	0
	Au	51.2	-9.82	1.53
	SiO_2	634.9	2.06	0

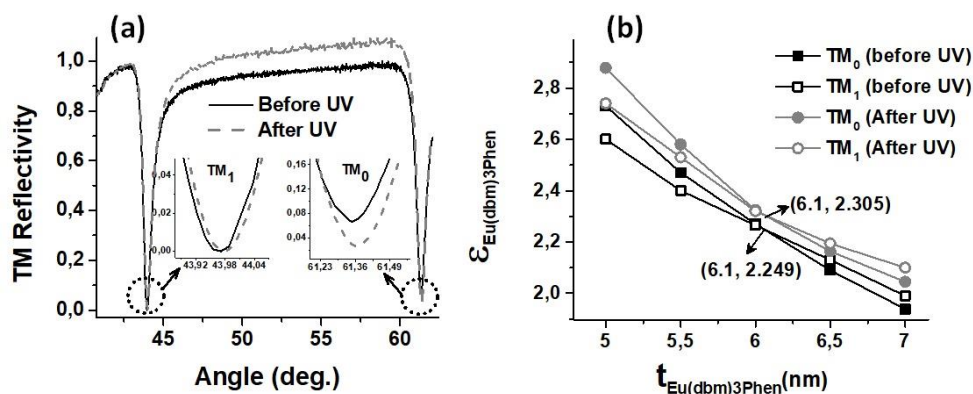


Figure 6.11: (a) The experimental SPR curves of the DLWGs structure with $\text{Eu}(\text{dbm})_3\text{phen}$ as organic thin film, before and after UVA radiation at wavelength of 633nm. The inset show the observable shift in the resonance angles after the organic thin film modification. (b) Application of dual mode analysis method before and after UVA treatment.

6.3.

Investigation of the anisotropy of SLG by DLWGs

In the first part of this section, we will characterize the SLG by using the monomodal SPR and Raman spectroscopy. We will discuss the limitation of using the monomodal SPR method for the determination of refractive index and thickness of CVD grown graphene. In the second part of this section, we present a multimodal technique based on the mixed dual mode and two wavelengths method for the characterization of anisotropy of graphene, as possible solution to the limitation of monomodal SPR spectroscopy.

6.3.1.

SPR and Raman spectroscopy on Au/SLG

The quality of the CVD grown graphene on Cu foil before and after transfer on metal thin surfaces were examined by Raman spectroscopy. Figure 6.13 (a) shows the Raman spectra of as grown graphene on copper (black line) as well as of transfer printed graphene on gold (red line) and silver (blue) thin films. The G and 2D band Raman peaks of graphene grown on copper are located at wavenumber of about 1575 cm^{-1} and 2709 cm^{-1} respectively, furthermore the absence of D-peak confirms high quality graphene without any defects. The I_{2D}/I_G intensity ratio is approximately 4.5 and the FWHM is 33 cm^{-1} indicating the growth of a monolayer

graphene. The position of the G and 2D Raman peaks of printed graphene on gold and silver are at $\sim 1575/\sim 2678$ cm^{-1} and $\sim 1577/\sim 2695$ cm^{-1} respectively. We calculated the intensity ratio I_{2D}/I_G and the full width half maximum (FWHM) of 2D band of graphene on Au chip surface as 2.3 and 43 cm^{-1} respectively, while in the case of graphene on silver the I_{2D}/I_G and FWHM were 2.4 and 36 cm^{-1} . These Raman features of graphene on gold and silver guarantee high quality monolayer graphene. It is note that we observed a weak D-peak at 1336 cm^{-1} for graphene on silver, which can be attributed to the defects present in the graphene after wet transfer process.

After transfer of graphene layer, we characterized graphene on Au by using SPR spectroscopy. Figure 6.13 (b) displays the SPR angular reflectivity spectrum with and without graphene on gold thin film in air at excitation wavelength of 783 nm. The resonance angle of the bare gold locates at 42.68° and shifts to 42.96° in the presence of graphene printed gold surface. The values of refractive index (n, k) and thickness of each layer used to make a theoretical fit over the experimental points are summarized in the inset table as shown in figure 6.13(b). The obtained thickness and the real and imaginary parts of the graphene over gold surface are in

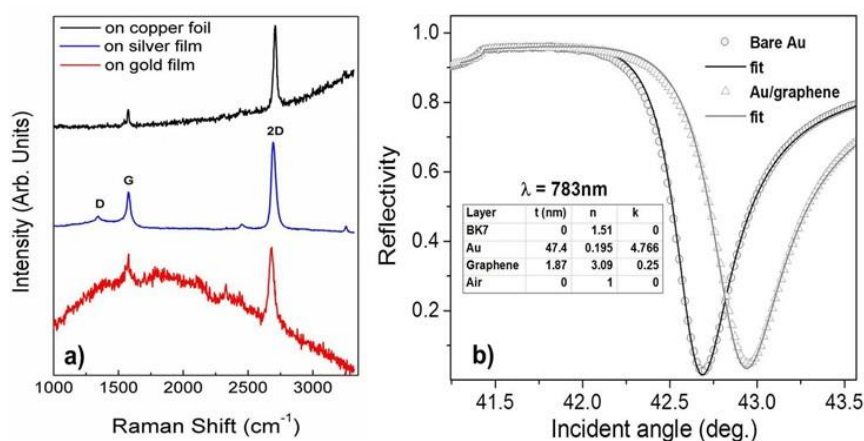


Figure 6.12: (a) Raman spectra of graphene on copper (black) and after transfer on gold (red) and silver (blue) thin films via PU route [92]. (b) SPR curve of bare gold and typical graphene protected gold device. The inset shows the values of the thickness and optical constants of gold and graphene used for the calculus of the theoretical fit [100].

good agreement with literature at the wavelength of 783nm. In addition, we noticed that the thickness (1.87 nm) of graphene on gold surface is larger than the single graphene-graphene thickness in graphite (i.e. 0.34 nm), due to the presence of the possible gap between the graphene and the sensor surface [39] and the change in the complex dielectric constant of the graphene caused by the charge transfer between gold and graphene [28].

6.3.2. Anisotropy characteristics of graphene by DLWGs

In previous section, we observed that when the monomodal SPR measurement is performed on the Au/SLG hybrid interface, the values of refractive index (3.09) and the thickness (1.87nm) of SLG could be obtained for 783nm. In this process, we first measured the refractive index of the Au thin film ϵ_{Au} , previously to the deposition of graphene. After the SLG transfer, we repeated the SPR measurement on the Au/SLG interface, and used the Winspall software in order to make the theoretical fit on the experimental curves, and obtain the values of the thickness and dielectric constant of SLG (t_{SLG} , ϵ_{SLG}).

These values are slightly larger than the one reported in the literature [38, 39], which could be due to two main possible reasons. The first, is the interaction of SLG with the Au thin film, in which the electrons are transferred to Au [28], and produce modification in the dielectric constant of both gold layer and SLG. Hence, in the absence of a dielectric spacer between Au and SLG, the Au/SLG bilayer, should be modeled as a new effective layer, with the thickness of the Au thin film and an effective dielectric constant.

The discrepancy between the theoretical values reported in literature for t_{SLG} and ϵ_{SLG} , and the experimental ones obtained by the use of monomodal Au/SLG interfaces, could also arise from the anisotropy of graphene. In fact, in SPR measurement the penetration direction of SPP field is perpendicular to the Au substrate, while in the spectroscopic ellipsometry, the light passes through sample both in perpendicular and parallel direction and thus give perpendicular mixed value of the complex RI [152].

Furthermore, the possible gap between SLG and Au, is another factor which complicates the measurement of the thickness of SLG using a single layer transfer,

so that a multiple transfer of different SLGs is needed in order to retrieve the exact value of the gap [39].

To overcome the limitations described above, we propose an alternative technique based on the DLWGs structure in which the mixed two wavelengths and dual (excitation of both TM and TE polarization modes) mode analysis methods are used to determine the thickness and complex refractive index of CVD grown graphene. The advantage of DLWGs is not only the excitation of TM and TE mode to probe the anisotropy of SLG, but also the suppression of the electron transfer mechanism between the Au thin film and the SLG, due the presence of a thick SiO₂ dielectric layer.

In particular, we propose the following strategy:

- 1) Measurement of the parameters of the DLWGs (dielectric constants and thickness of Au and SiO₂ thin films at λ_1 and λ_2)
- 2) Transfer of the first SLG. Measurement of the SPR curve of DLWG/SLG in both TE and TM polarizations at λ_1 and λ_2 , followed by a changing the refractive index of the external medium (water, ethanol).
- 3) Transfer of second SLG. Measurement of the SPR curve in both TE and TM polarizations at λ_1 and λ_2 in water.

The step 3 is after repeated other two times, until we have four layers of SLG over the DLWGs. After that, we will apply the procedure reported in [39] and will retrieve the values of t_{SLG} and ε_{SLG} in both TM and TE polarization.

We successfully completed the first part of this project, and transferred four layers (1L, 2L, 3L and 4L) over the Au thin film. The quality of each transferred graphene layer was characterized by Raman spectroscopy (data analysis in progress). After, each transfer the SPR reflectivity spectra with TM and TE mode was collected by using two different wavelengths. The SPR measurements were performed in water, due to the higher stability of DLWGs in water as studied in section 4.2.4. Figure 6.14 (a-b) show the experimental SPR TM reflectivity curves of DLWGs without graphene and with four-layer graphene repeatedly transfer over the DLWGs at $\lambda_1 = 633nm$ and $\lambda_2 = 783n$.

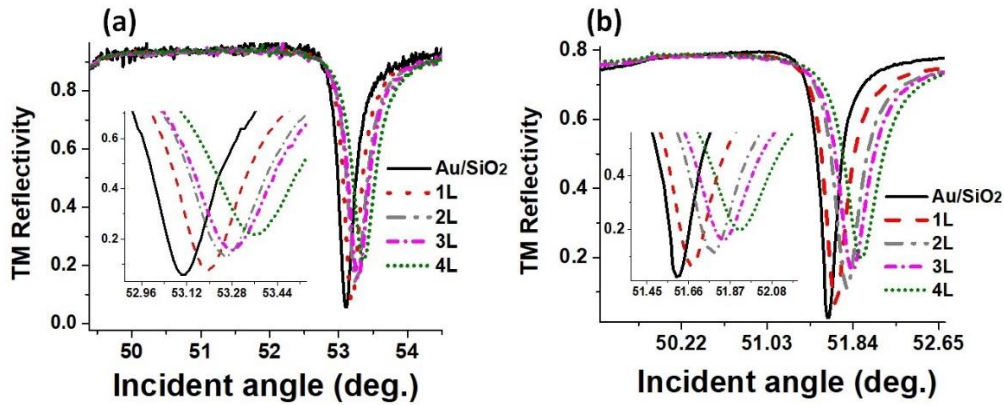


Figure 6.13: The experimental SPR curves collected on DLWGs structure for TM polarization mode with and without graphene layers at (a) $\lambda_1 = 633\text{nm}$ and (b) $\lambda_2 = 783\text{nm}$.

We also performed similar measurements on the same DLWGs with TE polarization mode. Figure 6.15 display the experimental SPR reflectivity curve of DLWGs for TE polarization mode with and without the graphene layer at two different wavelengths. The work is in progress and we are analyzing the data.

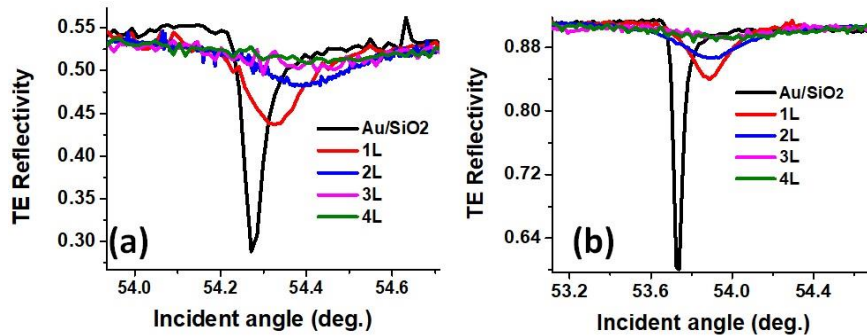


Figure 6.14: The experimental SPR curves collected on DLWGs structure for TE polarization mode with and without graphene layers at (a) $\lambda_1 = 633\text{nm}$ and (b) $\lambda_2 = 783\text{nm}$.

7 Conclusions and perspectives

7.1. Conclusions

- **Fabrication of stable and sensitive SPR low damping platform**

In the first part of the thesis, we analyzed the stability of the SPR response in air and water of plasmonic devices established by gold and silver thin films. The stability measurements were carried out on unprotected samples, samples with typical OLED encapsulation, and devices protected by a single layer of graphene. Instead of using metallic adhesion layer like chromium or titanium, we choose MPTS as a molecular low damping adhesion layer between metal and glass substrate to minimize or avoid the degradation processes, broadening and angular shift of the SPR curve. In order to interpret the role of the SiO₂/MPTS/Metal and Metal/air interfaces in the degradation process, the average roughness of the gold and silver thin film has been tested by AFM microscopy along 24 and 6 hours respectively. From the experimental results performed in air, it was concluded that the main source of the degradation of the plasmonics properties is the gradual delamination of the thin metal film deposited on the glass. The degradation arises either due to the oxidation of –SH group which may lead to the formation of disulfides bridge (RS-SR), or due to the water humidity, which promotes the break of siloxane (Si-O-Si) groups. These undesired reactions might form defects into the metal/SiO₂ interface and inducing a partial delamination. Moreover, it was found that the graphene protected Au and Ag thin films shows stability similar to the samples protected by OLED encapsulation technique. Specifically, for Au/SLG and Ag/SLG a shift in the resonance angle of about 0.005⁰ was observed along 4 hours, which is comparable to the zero-angle indetermination in the SPR spectroscopy. The aim of this study was to put a limit useful for accurate characterization of the dielectric thin film by SPR spectroscopy.

In the case of stability in water, we have experimentally investigated the influence of MPTS and Cr as adhesion layers while graphene as protecting layer on

the stability and sensitivity of SPR sensors by using angle interrogation mode of SPR spectroscopy for 24 hours at excitation wavelength of 783nm. We found that the stability could be enhanced by either using MPTS as adhesion layer or taking the protection of graphene. For MPTS/Au/H₂O and MPTS/Au/SLG/ H₂O samples, the FWHM of the SPR curves is measured to be significantly reduced about 5% and 0.5% up to 5 hours respectively. The AFM has been used to monitor the morphology and the phase of the 49nm thin gold and silver film with MPTS as adhesion layer before and after immersion in DI water along 44 h. In case of gold a reduction in the roughness from 1.94nm to 1.38nm has been measured, which revealed a smooth gold surface and hence a suppression of the broadening of the SPR curves as observed experimentally. In addition, the bare silver thin film with MPTS and Cr adhesion layer showed a poor chemical stability in aqueous conditions either due to the solubilization of preexisting Ag₂O in water as silver hydroxide, or dissolution of metallic Ag by the absorption of ambient CO₂, which activates the release of Ag⁺ ions with the formation of CO₃⁻²(carbonate). The presence of Ag⁺ ion in DI water was confirmed by the inductively coupled plasma mass spectrometry (ICPMS) measurement, and the trace amount of carbon was investigated by XPS measurement.

We finally verified that the transfer of SLG on the external surface of the SPR sensors also enhanced the bulk refractive index (RI) sensitivity, due to the transfer of electron from SLG to gold to adjust the Fermi level of graphene due to high work function of gold.

We definitively succeeded in the main objective to define the fabrication parameters, in terms of geometry and materials constituting the multilayer devices, in order to obtain high sensitivity, low damping, and high stable SPR sensing platforms.

- **Optical Sensing**

- **UVA dosimeter**

We succeeded in proving the principle of work of an SPR based UVA dosimeter. This goal was reached investigating the degradation processes of luminescent organic thin films by the use of AFM, photoluminescence and SPR spectroscopy with single mode sensing platforms. The plasmonic sensors are operated both in air and nitrogen environments, where they are irradiated with

controlled doses of UVA radiation. SPR measurements reveal a strict correlation between the refractive index increase and quenching of the photoluminescence of the organic thin films. The results are promising for the development of compact plasmonic UVA dosimeters in the surface plasmon coupled emission configuration (SPCE) with lanthanide β -diketonate complex materials.

- **SPR nanocounter**

The response of the resonance wave mode of the DLWGs to a bidimensional array of citrate stabilized AuNPs was studied experimentally for the correct counting of NPs for the particle-amplified surface plasmon resonance (PA-SPR) spectroscopy. The nanocomposite layer constituted by AuNPs was characterized by the Maxwell's Garnett theory and the Fresnel reflection coefficient under the assumption that dipolar interaction between the metal NPs and the metal substrate are negligible and that the composite layer is a homogenous planar layer. On the bases of this hypothesis, we experimentally demonstrated the use TM1 resonance mode of SPR DLWGs for the accurate counting of AuNPs (nominal diameter was 14.6 nm) in the range between 20 and 200 NP/ μm^2 . A good agreement been found between AFM and SPR based results in NPs counting. The results are promising to open a new way to accomplish a quantitative measurement of the acceptance of NPs by lipidic or artificial cellular membranes using PA-SPR spectroscopy.

- **Hybrid Au/SLG interfaces for Hg⁺² and Pb⁺² ions sensing**

The work on the optical sensing of Hg⁺² using Au/SLG interface is in progress and we can draw at the moment only partial conclusions based on both our experimental results and the literature review.

We have verified that the enhancement of sensitivity during the sensing of Hg⁺² is higher than the case of glycerine sensing using the same Au/SLG device. This can be explained by two reasons [87]: (i) a plasmon induced charge transfer mechanism from SLG to Hg⁺² may be responsible for the apparent higher binding affinity of charged Hg⁺² towards Au/SLG interface, with possible reduction reactions to form a neutral Hg⁰, (ii) a high density thin film of Hg⁺² is forming on the Au/SLG interface, due to the particular affinity of binding site of this hybrid metal-2D material structure. Moreover, we also demonstrated the higher binding affinity constant of Hg⁺² on Au/SLG interface by using a Langmuir Isotherm model.

This better ability is attributed specifically to the Au/SLG interface. This is because the bottom Au layer may change the preferential binding site of Hg ions over the graphene, changing the electronic structure of SLG.

In this study, the SPR based response for the optical detection of Pb^{+2} was compared for bare Au and hybrid Au/SLG sensors. The SPR responses of the Au/SLG sensor had greater sensitivity and lowest LoD than Au/SiO₂/SLG and bare Au surfaces.

- **Ellipsometric characterization**

- **Two color SPR nanosizer**

Another important objective of this work, was the application of SPR spectroscopy in the Kretschmann configuration for the accurate characterization of nanomaterials. We demonstrate both theoretically and experimentally the principle of work of a two-color SPR nanosizer applied to a nanocomposite film of water and AuNPs. The limitation of the MG theory in the prediction of the extinction properties of composite thin films is overcome when the optical density of the Au/water composite film is negligible, which allow the effective medium theory to reliably predict the dispersion properties of the effective refractive index of the composite thin film, that can be approximated as purely real. This is demonstrated experimentally through the determination of the statistical mean size of a colloidal solution of polydisperse citrate stabilized AuNPs with a nominal diameter of ~15 nm. The experimental performances are comparable to expensive techniques such as AFM microscopy, DLS or TEM. For the bigger sized AuNPs, the theoretical calculations show that the application of the two-color SPR nanosizer is only limited by the angular resolution of the SPR sensing platform. Once the control of the optical density τ of the composite thin film is obtained by proper choice of the excitation laser wavelengths and the deposition of SAM of AuNPs with progressively lower mass surface density (i.e. $\Delta\theta_{\text{SPR}}$). Since commercial or traditional SPR spectrometers with angular interrogation in the Kretschmann configuration are characterized by a typical angular resolution better than $\sim 0.01^\circ$, our theoretical results suggest that a standard configuration of a two-color SPR nanosizer in the visible range may be suited for characterization of AuNPs up to diameters of the order of ~50 nm.

- **Characterization of organic luminescent materials**

The dual mode of DLWGs have been used for the first time to simultaneously measure the thickness and refractive index of a thin film of Alq₃ and Eu(dbm₃Phen) at the wavelength of 633 nm and 783 nm. The results were consistent with the TFT method [34]. The encapsulated sample of Eu(dbm₃Phen) was irradiated with the control dose of UVA radiation, which induced modification in term of change its thickness and refractive index. In order to determine this modification, we successfully applied the dual mode analysis. We observed a negative change in the refractive index of Eu(dbm₃Phen), and an increase in the thickness. As for we know this would be the first observation of this phenomenon, so that further measurements have to be repeated in order to confirm this uncommon result.

- **Investigation of anisotropy of SLG by DLWGs**

The work about the characterization of anisotropic properties of SLG is in progress. We proposed an alternative technique to explore the anisotropy of graphene, which is based on the mixed two mode and two-wavelength approach. The CVD graphene has been transferring on the Au SPR sensor and the transfer process was repeated four times, and therefore the sample studied in this work were four layers CVD graphene over the Au SPR sensor. We complete the first initial fabrication part and successfully transferred four layers of graphene over the DLWGs. The SPR reflectivity curves are collected after each transfer process for TM and TE polarization at both wavelength 633nm and 783nm. We are analyzing the experimental data.

The aim of the study is to overcome the two main limitations in the determination of thickness and refractive index of graphene using SPR spectroscopy. The first limit is related to the differentiation of TM and TE polarization mode, since all the works in literature are using the TM mode for the thickness-refractive index determination of SLG by SPR spectroscopy [39], and therefore polarization different from that used in more typical approaches such as spectroscopic ellipsometry [39]. As graphene is a geometrical anisotropic material, we suppose that its complex refractive is a component of both the planar and perpendicular [39]. Taking the advantages of dual mode of DLWGs, we aim to characterize the graphene to determine not only the complex RI but also the

thickness simultaneously. A limitation in this sense, is given by the indetermination of the thickness of the first layer (1L) of graphene, that maybe due to the electron transfer from graphene to the Au thin film, or the presence of a gap between the two material [28].

7.2. Perspective and future work

To draw conclusions on a small part of the presented experimental work, we still need to perform further investigation, both from experimental and computational point of view. In the following, we make a list of the activities are needed to conclude our investigation.

Sensing by Au/SLG interfaces

- I. To verify the reusability of the Hg^{2+} and Pb^{+2} ions sensor.
- II. To calculate the theoretical affinity of Hg^{2+} and Pb^{+2} ions for the Au/SLG interface (by external collaborations).

Probing the SLG anisotropy

- III. Manipulate and analyze the experimental data obtained during the SPR ellipsometric characterization of SLG by two-color approach on DLWGs.

8 Productions

8.1.

List of publications

- Q. Zaman, J. Souza, O. Pandoli, K. Q. Costa, V. Dimitriev, D. Fulvio, M. Cremona, R. Q. Aucelio, G. Fontes, And T. Del Rosso. *Two-color surface plasmon resonance nanosizer for gold nanoparticles*. **Optics Express**, v. 27, n. 3, p. 3200-3216, 2019.
- T. Del Rosso, Q. Zaman, E.C. Romani, O. Pandoli, R.Q. Aucelio, L.Melo de Lima , M. Cremona , V. Dmitriev, K. Queiroz da Costa, F. Lazaro Freire Jr, M.E.H.Maia da Costa. *Enhanced stability of plasmonic metal thin films by CVD grown graphene transfer*. **Thin Solid Films**, v. 644, p. 65-70, 2017.
- T. Del Rosso, Q. Zaman, M. Cremona, O. Pandoli, A. R. J. Barreto. *SPR sensors for monitoring the degradation processes of Eu (dbm) 3 (phen) and Alq3 thin films under atmospheric and UVA exposure*. **Applied Surface Science**, v. 442, p. 759-766, 2018.
- J. S. Costa, Q. Zaman, K. Q da Costa, V. Dmitriev, O. Pandoli, G. Fontes, & T. Del Rosso. *Limits of the Effective Medium Theory in Particle Amplified Surface Plasmon Resonance Spectroscopy Biosensors*. **Sensors**, v. 19, n. 3, p. 584, 2019.
- T. Del Rosso, S. R. W.Louro, F. L. Deepak, E. C. Romani, Q. Zaman, Tahir, O. Pandoli, M. Cremona, F. L. Freire Junior, P. A. A. De Beule, T. De St. Pierre, R. Q.Aucelio, G. Mariotto, S. Gemini Piperni, A. R. Ribeiro, S. M. Landi, A. Magalhães. *Biocompatible Au@ Carbynoid/Pluronic-F127 nanocomposites synthesized by pulsed laser ablation assisted CO2 recycling*. **Applied Surface Science**, v. 441, p. 347-355, 2018.

8.2. Conferences

The obtained research results have been presented on the following scientific conferences:

- Quaid Zaman, E. C. Romani, F. L. Freire Jr., Omar Pandoli , Ricardo Queiroz Aucelio , Marco Cremona , Tommaso Del Rosso .*Enhanced Stability of Metal Depositions Supporting Plasma Waves by Graphene Transfer*. Graphene 2017 (Barcelona-Spain), March **2017**. Poster.
- Quaid Zaman, E. C. Romani, F. L. Freire Jr., Omar Pandoli , Ricardo Queiroz Aucelio , Marco Cremona , Tommaso Del Rosso .*Enhanced Stability of Metal Depositions Supporting Plasma Waves by Graphene Transfer*. Brazilian Physical Society Meeting XL ENFMC (Búzios, R. J Brazil) March **2017**. Oral.
- Q. Zaman, O. Pandoli, M. Cremona, R.Q. Aucelio, T. Del Rosso. *All optical characterization of gold nanoparticles by two colour SPR spectroscopy*. Autumn Meeting of the Brazilian Physical Society (Foz do Iguaçu, Brazil). May **2018**. Oral.
- Quaid Zaman, A.R. Jardim Barreto, Omar Pandoli , Marco Cremona Tommaso Del Rosso. *SPR sensors for the monitoring of the degradation process of $\text{Eu}(\text{dbm})_3(\text{phen})$ and Alq_3 thin films under atmospheric and UVA exposure*. Autumn Meeting of the Brazilian Physical Society (Foz do Iguaçu, Brazil). May **2018**. Poster.
- Quaid Zaman, Omar Pandoli, Ricardo Queiroz Aucelio, Marco Cremona, Tommaso Del Rosso. *Complete characterization of citrate stabilized gold nanoparticles by two-color surface plasmon resonance spectroscopy*. XVI Brazilian MRS meeting (Gramado, Brazil) September **2017**. Poster.
- Q. Zaman, A. N. Barbosa, O. Pandoli, R Q Aucelio, C. Toloza, M. Cremona, F. Lazaro Freir Jr , T. Del Rosso. *Improved performance of hybrid metal-graphene SPR sensors with low-damping metal-dielectric interface*. Nanophotonics and Micro/Nano Optics International Conference (RomeItaly) October 2018. Poster

Appendix A

Matlab Codes developed

A.1

Calculation of the dielectric function of small NPs

In this appendix we developed a code based on the MATLAB for the determination of the sized dependent complex refractive index of the small metal NPs using the mean free path limitation [45]. We used the modified bulk refractive index data sheet of Johnson and Christy [50].

```

%% clear all;

file_data = load ('Modified_J_C_n_k.txt');
Wavelength = file_data(:,1); %% wavelength in nm%%
n1 = file_data(:,2); %% real part of refractive index%%
k1 = file_data(:,3); %% Imaginary part of refractive index%%
Wavelength_um = file_data(:,4);

%% Dielectric function of bound electrons
e_real = n1.^2-k1.^2; % Real part of dielectric function%
e_imag = 2.*n1.*k1; % Imaginary part of dielectric function%
e_bulk = e_real+1i.*e_imag; % Bulk dielectric constant%
w_p = 1.3E16; %% Plasma frequency%
Gama_bulk = 1.64E14; %% Damping constant%
c_s = 3E17; %%Speed of light %
w = 2.*pi.*c_s./Wavelength; %Angular frequency%
e_free = 1- w_p.^2./(w.^2+1i.*w.*Gama_bulk); %Dielectric constant
of free electrons%
e_bound = e_bulk -e_free; %%Dielectric constant of bound
electrons%
e_bound_imag = imag(e_bound); %imaginary part of bound
electrons%%

%% Average Radius
r1 = 2 %% Radius of the particle%
v_f = 14.1E14; %% Fermi velocity of electron%
c = 1; %% Proportionality constant%

```

```

Gamma_r1 = Gama_bulk + (c.*v_f./r1); %Damping constant of small
particles%
e1_size_imag
=e_bound_imag+(Gamma_r1.*w_p.^2)./(w.*(w.^2+Gamma_r1.^2));
n1_size = sqrt (0.5.*(sqrt (e_real.^2+e1_size_imag.^2)+ e_real));
k1_size = sqrt(0.5.*(sqrt(e_real.^2+e1_size_imag.^2)- e_real));

%% Plot of n1_size
plot(Wavelength,n1_size,'-r');
hold on; box on; grid on;
title('Au nanoparticles with different size');
xlabel('Wavelength (nm)');
ylabel('n-size');
xlim([350 1000]);
legend('n1_size');

%% Plot of K1 size
plot(Wavelength,k1_size,'-r');
hold on; box on; grid on;
title('Au nanoparticles with different size');
xlabel('Wavelength (nm)');
ylabel('k-size');
xlim([350 1000]);
legend('k1size');

```

A.2

Application of Mie Theory for the calculation of the mass concentration of metal NPs with statistical size distribution

The code developed in this Appendix is to calculate the Mie extinction efficiency and the mass concentration of colloidal suspension of small statistical sized metal NPs under the mean free path limitation. This code gives the fitting analysis between the experimental UV-Vis spectra and the Mie theory by considering the Lognormal distribution function to determine the statistical size of NPs from the TEM image.

```

%% Initialization
clear all;

%% Declaration of ranges, constants and Lognormal function
file_data = load('Modified_J_C_n_k.txt'); %optical constant of
AuNPs (Johnson and christy data)

```

```

exp_meas = load('experimental_ph7.txt'); %Uv-vis spectra of AuNPs
file_liquid = 'N_H2O.txt';
lambda = 0.25:0.001:0.8; %wavelength domain (um)
d_0 = 1e4; %Cuvete length um
E = 1; %Maximum experimental value of extinction spectrum
dp = 19.32; %Density of NP (g/cm^3)
lambda_max = 0.518e-6; %SPR resonance wavelength (um)
y0 = 0; %LogNorm constant
xc = 3.217; %14.32; %LogNorm constant
w_omega = 0.307; %0.143; %LogNorm constant
A = 302;%271;%151; %LogNorm constant
n_fitted = @(r) y0 + (A./(sqrt(2*pi).* r.*1e3 .* w_omega)).*exp(-
(log(r.*1e3/xc).^2)/(2*(w_omega).^2)); % Log Normal function
radius_min = 1/1e3; %Minimum radius um
radius_max = 30/1e3; %Maxium radius
radius_interval = 0.1/1e3;
radius_vec = (radius_min:radius_interval:radius_max):%radius in um
n_int = integral(n_fitted, radius_min, radius_max); %Calculate
numerical integral

%% Dielectric function of bound electrons

Wavelength = file_data(:,1); % wavelength in nm
n_ref_index = file_data(:,2); % real part of
refractive index
k_ref_index = file_data(:,3); % Imaginary part of
refractive index
Wavelength_um = file_data(:,4);
e_real = n_ref_index.^2-k_ref_index.^2; % Real part of
dielectric function
e_Imag = 2.*n_ref_index.*k_ref_index; % Imaginary part of
dielectric function
e_bulk = e_real+1i.*e_Imag ; % Bulk dielectric
constant
w_p = 1.3E16; % Plasma frequency
Gama_bulk = 1.64E14; % Damping constant
c_s = 3E17; %Speed of light
w = 2.*pi.*c_s./Wavelength ; %Angular frequency
e_free = 1- w_p.^2./(w.^2+1i.*w.*Gama_bulk);% Dielectric constant
of free electrons

```

```

e_bound = e_bulk - e_free; % Dielectric constant
of bound electrons
e_bound_imag = imag(e_bound); %imaginary part of bound
electrons
v_f = 14.1E14; % Fermi velocity of electron
c = 1; % Proportionality constant
%%
colors = 'rgbkcrgbkcrgbkc';
figure;
hold on; box on; grid on;

for l = 1:length(radius_vec)
    %% Particle properties

    a = radius_vec(l);
    Gamma_a = Gama_bulk + (c.*v_f ./ (a*1e3)); % Damping constant
of small particles%
    wp_w = w_p.^2 ./ (w.^2 + Gamma_a.^2);
    e_size_imag
=e_bound_imag + (Gamma_a.*w_p.^2) ./ (w.*(w.^2 + Gamma_a.^2));
    n_size = sqrt(0.5.*(sqrt(e_real.^2 + e_size_imag.^2) + e_real));
    k_size = sqrt(0.5.*(sqrt(e_real.^2 + e_size_imag.^2) - e_real));

    N_Au.wavelength = Wavelength_um;
    N_Au.N = n_size - li*k_size;
    N_Au.eps = N_Au.N.^2;
    N_Au = INL_MD_Interpolate(N_Au, lambda);
    N_liquid = INL_MD_Load(file_liquid);
    N_liquid = INL_MD_Interpolate(N_liquid, lambda);

    n = size(lambda, 2);

    for k = 1:n
        [a_n, b_n, x] =
INL_MS_SolidSphere(lambda(k), a, N_liquid.N(k), N_Au.N(k));
        n_norm(l) = n_fitted(a) / n_int;
        Q_ext_ss(k, l) =
INL_MS_ExtinctionEfficiency(a_n, b_n, x);
        sigma_ext_pesad(k, l) = a ^ 2 * Q_ext_ss(k, l) *
n_norm(l) * radius_interval; %R^2*Q*n*dr

```

```

end
end

%% Show the graphs
espec_ext = -sum(sigma_ext_pesad');
[peak, locs] = findpeaks(espec_ext); %Find peaks in results
N_particles = (2.303 * E / (d_0 * pi * peak(end))) * 1e12;%NP
Density per cm^3
n_mass = @(r) ( n_fitted(r) / n_int ) .* r.^3;
Concentration = (N_particles * 4/3 * pi * dp
*integral(n_mass,radius_min,radius_max)) * 1e-12 %Concentration in
(g/cm^3)

%% plot results
title('Au nanoparticles');
xlabel('Wavelength (nm)');
ylabel('Extinsion (a.u.)');
xlim([300 800]);
ylim([0 1.25]);
espec_ext= espec_ext/peak(end);%Normalize results by the last peak
plot(lambda*1000,espec_ext,'-b','LineWidth',3);
plot(exp_meas(:,1),exp_meas(:,2),'g','LineWidth',3);
hold off;
legend('Solid sphere logNorm','Experimental curve');

```

A.3 XPS spectra of silver thin film

X-ray photoelectron spectroscopy (XPS) gives a sensitive measure of the chemical state in the near surface region of materials. XPS has been employed on a 49nm thin silver film before and after immersion in DI water for 24 hours to measure the possible oxidation of Ag. The results are still under discussion.

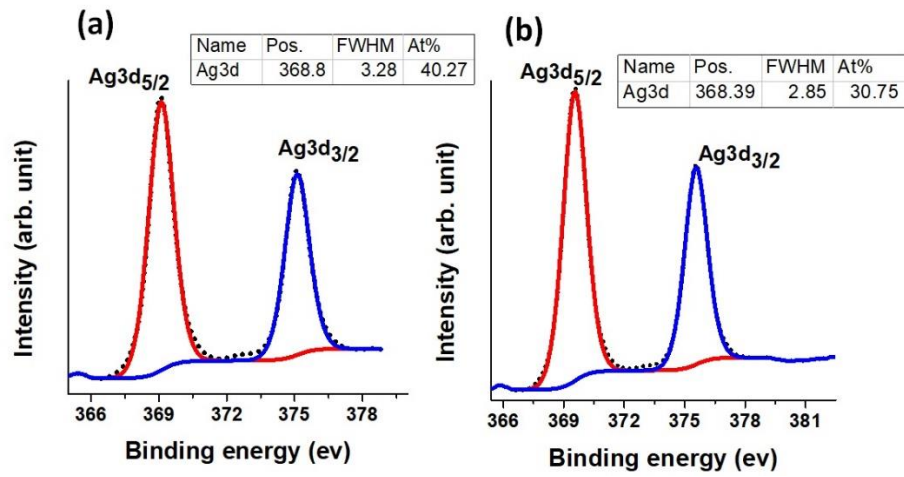


Figure A.2: XPS spectrum of the Ag3d_{3/2} and Ag3d_{5/2} of 49nm thin silver thin film (a) before and (b) after immersion in water.

9 Bibliography

- [1] R. Feynman, “There is plenty of room at the bottom,” *Caltech Eng. Sci.*, vol. 23, no. 5, pp. 22–36, 1960.
- [2] R. M. Bakker *et al.*, “Enhanced localized fluorescence in plasmonic nanoantennae,” *Appl. Phys. Lett.*, vol. 92, no. 4, p. 043101, Jan. 2008.
- [3] G. Binnig, H. Rohrer, C. Gerber, and E. Weibel, “Surface Studies by Scanning Tunneling Microscopy,” *Phys. Rev. Lett.*, vol. 49, no. 1, pp. 57–61, Jul. 1982.
- [4] C. J. Sjö Dahl, “[Disposables in today’s dental practice. Presentation of a new disposable syringe for rubber and hydrocolloid impressions].,” *Sver. Tandlakarforb. Tidn.*, vol. 60, no. 24, pp. 1115–9, Dec. 1968.
- [5] E. Ozbay, “Plasmonics: Merging photonics and electronics at nanoscale dimensions,” *Science (80-.)*, vol. 311, no. 5758, pp. 189–193, 2006.
- [6] J. A. Schuller, E. S. Barnard, W. Cai, Y. C. Jun, J. S. White, and M. L. Brongersma, “Plasmonics for extreme light concentration and manipulation,” *Nat. Mater.*, vol. 9, no. 3, pp. 193–204, Mar. 2010.
- [7] D. J. de Aberasturi, A. B. Serrano-Montes, and L. M. Liz-Marzán, “Modern Applications of Plasmonic Nanoparticles: From Energy to Health,” *Adv. Opt. Mater.*, vol. 3, no. 5, pp. 602–617, May 2015.
- [8] J. A. Webb and R. Bardhan, “Emerging advances in nanomedicine with engineered gold nanostructures,” *Nanoscale*, vol. 6, no. 5, p. 2502, 2014.
- [9] M. Xiao, R. Jiang, F. Wang, C. Fang, J. Wang, and J. C. Yu, “Plasmon-enhanced chemical reactions,” *J. Mater. Chem. A*, vol. 1, no. 19, p. 5790, 2013.
- [10] M. Harder, Y. Gui, and C.-M. Hu, “Electrical Detection of Magnetization Dynamics via Spin Rectification Effects,” *Energy Environ. Sci.*, vol. 5, no. 1, pp. 5133–5146, May 2016.
- [11] Y. H. Jang, Y. J. Jang, S. Kim, L. N. Quan, K. Chung, and D. H. Kim, “Plasmonic Solar Cells: From Rational Design to Mechanism Overview,” *Chem. Rev.*, vol. 116, no. 24, pp. 14982–15034, Dec. 2016.

- [12] A. G. Curto, G. Volpe, T. H. Taminiau, M. P. Kreuzer, R. Quidant, and N. F. van Hulst, “Unidirectional Emission of a Quantum Dot Coupled to a Nanoantenna,” *Science* (80-.), vol. 329, no. 5994, pp. 930–933, Aug. 2010.
- [13] L. Vinet and A. Zhedanov, “A ‘missing’ family of classical orthogonal polynomials,” *Adv. Mater.*, vol. 24, no. 21, pp. 2890–2895, Nov. 2010.
- [14] O. Tokel, F. Inci, and U. Demirci, “Advances in Plasmonic Technologies for Point of Care Applications,” *Chem. Rev.*, vol. 114, no. 11, pp. 5728–5752, Jun. 2014.
- [15] R. W. Wood, “On a Remarkable Case of Uneven Distribution of Light in a Diffraction Grating Spectrum,” *Proc. Phys. Soc. London*, vol. 18, no. 1, pp. 269–275, Jun. 1902.
- [16] L. Rayleigh, “On the Dynamical Theory of Gratings,” *Proc. R. Soc. A Math. Phys. Eng. Sci.*, vol. 79, no. 532, pp. 399–416, Aug. 1907.
- [17] U. Fano, “The Theory of Anomalous Diffraction Gratings and of Quasi-Stationary Waves on Metallic Surfaces (Sommerfeld’s Waves),” *J. Opt. Soc. Am.*, vol. 31, no. 3, p. 213, Mar. 1941.
- [18] R. H. Ritchie, “Plasma Losses by Fast Electrons in Thin Films,” *Phys. Rev.*, vol. 106, no. 5, pp. 874–881, Jun. 1957.
- [19] E. Sugawara and H. Nikaido, “Properties of AdeABC and AdeIJK Efflux Systems of *Acinetobacter baumannii* Compared with Those of the AcrAB-TolC System of *Escherichia coli*,” *Antimicrob. Agents Chemother.*, vol. 58, no. 12, pp. 7250–7257, Dec. 2014.
- [20] A. Otto, “Excitation of nonradiative surface plasma waves in silver by the method of frustrated total reflection,” *Zeitschrift für Phys. A Hadron. Nucl.*, vol. 216, no. 4, pp. 398–410, Aug. 1968.
- [21] I. Pockrand, J. D. Swalen, J. G. Gordon, and M. R. Philpott, “Surface plasmon spectroscopy of organic monolayer assemblies,” *Surf. Sci.*, vol. 74, no. 1, pp. 237–244, May 1978.
- [22] M. Piliarik, L. Párová, and J. Homola, “High-throughput SPR sensor for food safety,” *Biosens. Bioelectron.*, vol. 24, no. 5, pp. 1399–1404, Jan. 2009.
- [23] B. Liedberg, C. Nylander, and I. Lundström, “Biosensing with surface plasmon resonance — how it all started,” *Biosens. Bioelectron.*, vol. 10, no. 8, pp. i–ix, Jan. 1995.
- [24] J. Homola, “Surface Plasmon Resonance Sensors for Detection of Chemical

- and Biological Species,” *Chem. Rev.*, vol. 108, no. 2, pp. 462–493, Feb. 2008.
- [25] H. Raether, *Surface Plasmons on Smooth and Rough Surfaces and on Gratings*, vol. 111. Berlin, Heidelberg: Springer Berlin Heidelberg, 1988.
- [26] I. Poizot-Martin, C. Aquilina, R. Bouabdallah, M. C. Alessi, J. Sayag, and J. A. Gastaut, “[Acrosyndrome disclosing protein S deficiency in human immunodeficiency virus infection],” *Ann. Med. Interne (Paris)*, vol. 143, no. 2, pp. 109–12, 1992.
- [27] M. Piliarik and J. Homola, “Surface plasmon resonance (SPR) sensors: approaching their limits?,” *Opt. Express*, vol. 17, no. 19, p. 16505, Sep. 2009.
- [28] K. Chung *et al.*, “Enhancing the Performance of Surface Plasmon Resonance Biosensor via Modulation of Electron Density at the Graphene-Gold Interface,” *Adv. Mater. Interfaces*, vol. 5, no. 19, p. 1800433, Oct. 2018.
- [29] S. Zeng *et al.*, “Graphene-Gold Metasurface Architectures for Ultrasensitive Plasmonic Biosensing,” *Adv. Mater.*, vol. 27, no. 40, pp. 6163–6169, Oct. 2015.
- [30] L. A. Lyon, M. D. Musick, and M. J. Natan, “Colloidal Au-Enhanced Surface Plasmon Resonance Immunosensing,” *Anal. Chem.*, vol. 70, no. 24, pp. 5177–5183, Dec. 1998.
- [31] J. Costa *et al.*, “Limits of the Effective Medium Theory in Particle Amplified Surface Plasmon Resonance Spectroscopy Biosensors,” *Sensors*, vol. 19, no. 3, p. 584, 2019.
- [32] K. A. Peterlinz and R. Georgiadis, “Two-color approach for determination of thickness and dielectric constant of thin films using surface plasmon resonance spectroscopy,” *Opt. Commun.*, vol. 130, no. 4–6, pp. 260–266, Oct. 1996.
- [33] H. E. de Bruijn, B. S. F. Altenburg, R. P. H. Kooyman, and J. Greve, “Determination of thickness and dielectric constant of thin transparent dielectric layers using surface plasmon resonance,” *Opt. Commun.*, vol. 82, no. 5–6, pp. 425–432, May 1991.
- [34] T. Del Rosso, J. E. H. Sánchez, R. D. S. Carvalho, O. Pandoli, and M. Cremona, “Accurate and simultaneous measurement of thickness and refractive index of thermally evaporated thin organic films by surface plasmon resonance spectroscopy,” *Opt. Express*, vol. 22, no. 16, p. 18914,

- Aug. 2014.
- [35] H. E. de Bruijn, B. S. F. Altenburg, R. P. H. Kooyman, and J. Greve, “Determination of thickness and dielectric constant of thin transparent dielectric layers using surface plasmon resonance,” *Opt. Commun.*, vol. 82, no. 5–6, pp. 425–432, May 1991.
- [36] H. Fujiwara, *Spectroscopic Ellipsometry*. Chichester, UK: John Wiley & Sons, Ltd, 2007.
- [37] A. M. Kostruba and O. G. Vlokh, “Accuracy of traditional ellipsometry and complex ellipsometry-transmission photometry techniques for absorptive-film/transparent-substrate systems,” in *Polarimetry and Ellipsometry*, 1997, pp. 266–271.
- [38] S. Cheon, K. D. Kihm, H. G. Kim, G. Lim, J. S. Park, and J. S. Lee, “How to Reliably Determine the Complex Refractive Index (RI) of Graphene by Using Two Independent Measurement Constraints,” *Sci. Rep.*, vol. 4, no. 1, p. 6364, May 2015.
- [39] H. Jussila, H. Yang, N. Granqvist, and Z. Sun, “Surface plasmon resonance for characterization of large-area atomic-layer graphene film,” *Optica*, vol. 3, no. 2, p. 151, Feb. 2016.
- [40] T. Špringer, M. L. Ermini, B. Špačková, J. Jabloňkú, and J. Homola, “Enhancing Sensitivity of Surface Plasmon Resonance Biosensors by Functionalized Gold Nanoparticles: Size Matters,” *Anal. Chem.*, vol. 86, no. 20, pp. 10350–10356, Oct. 2014.
- [41] X. Li, K. Tamada, A. Baba, W. Knoll, and M. Hara, “Estimation of Dielectric Function of Biotin-Capped Gold Nanoparticles via Signal Enhancement on Surface Plasmon Resonance,” *J. Phys. Chem. B*, vol. 110, no. 32, pp. 15755–15762, Aug. 2006.
- [42] M.-C. Daniel and D. Astruc, “Gold Nanoparticles: Assembly, Supramolecular Chemistry, Quantum-Size-Related Properties, and Applications toward Biology, Catalysis, and Nanotechnology,” *Chem. Rev.*, 2004.
- [43] P. Eaton *et al.*, “A direct comparison of experimental methods to measure dimensions of synthetic nanoparticles,” *Ultramicroscopy*, vol. 182, pp. 179–190, Nov. 2017.
- [44] J. R. Miranda-Andrades *et al.*, “Speciation and ultra trace determination of

- mercury in produced waters from offshore drilling operations using portable instrumentation and matrix-matching calibration,” *Microchem. J.*, vol. 146, pp. 1072–1082, May 2019.
- [45] L. B. Scaffardi, N. Pellegrini, O. de Sanctis, and J. O. Tocho, “Sizing gold nanoparticles by optical extinction spectroscopy,” *Nanotechnology*, vol. 16, no. 1, pp. 158–163, Jan. 2005.
- [46] T. Del Rosso, Q. Zaman, M. Cremona, O. Pandoli, and A. R. J. Barreto, “SPR sensors for monitoring the degradation processes of Eu(dbm)₃(phen) and Alq₃ thin films under atmospheric and UVA exposure,” *Appl. Surf. Sci.*, vol. 442, pp. 759–766, 2018.
- [47] S. A. Maier, *Plasmonics: Fundamentals and Applications*. New York, NY: Springer US, 2007.
- [48] Weiner J. and Nunes F., *Light-Matter Interaction: Physics and Engineering at the Nanoscale*, 1st ed. Oxford University Press, 2013.
- [49] Y. Li, *Plasmonic Optics: Theory and Applications*. SPIE, 2017.
- [50] P. B. Johnson and R. W. Christy, “Optical Constants of the Noble Metals,” *Phys. Rev. B*, vol. 6, no. 12, pp. 4370–4379, Dec. 1972.
- [51] R. G. W. Brown, “Absorption and Scattering of Light by Small Particles,” *Opt. Acta Int. J. Opt.*, vol. 31, no. 1, pp. 3–3, Jan. 1984.
- [52] J. Zhang, L. Zhang, and W. Xu, “Surface plasmon polaritons: physics and applications,” *J. Phys. D. Appl. Phys.*, vol. 45, no. 11, p. 113001, Mar. 2012.
- [53] L. Novotny and B. Hecht, *Principles of Nano-Optics*. Cambridge: Cambridge University Press, 2012.
- [54] Y. Yamamoto and T. Kimura, “Coherent optical fiber transmission systems,” *IEEE J. Quantum Electron.*, vol. 17, no. 6, pp. 919–935, Jun. 1981.
- [55] E. Kretschmann, “Die Bestimmung optischer Konstanten von Metallen durch Anregung von Oberflächenplasmaschwingungen,” *Zeitschrift für Phys. A Hadron. Nucl.*, vol. 241, no. 4, pp. 313–324, Aug. 1971.
- [56] J. Worm Winspal, “3.02 <http://www.mpip-mainz.mpg.de/groups/knoll/software>.”
- [57] J. Homola, “Present and future of surface plasmon resonance biosensors,” *Anal. Bioanal. Chem.*, vol. 377, no. 3, pp. 528–539, Oct. 2003.
- [58] K. Matsubara, S. Kawata, and S. Minami, “Optical chemical sensor based on surface plasmon measurement,” *Appl. Opt.*, vol. 27, no. 6, p. 1160, Mar.

- 1988.
- [59] J.-F. Masson, “Surface Plasmon Resonance Clinical Biosensors for Medical Diagnostics,” *ACS Sensors*, vol. 2, no. 1, pp. 16–30, Jan. 2017.
- [60] J.-P. Renaud *et al.*, “Biophysics in drug discovery: impact, challenges and opportunities,” *Nat. Rev. Drug Discov.*, vol. 15, no. 10, pp. 679–698, Oct. 2016.
- [61] G. Hu *et al.*, “High-precision measurement of optical constants of ultra-thin coating using surface plasmon resonance spectroscopic ellipsometry in Otto-Bliokh configuration,” *Opt. Express*, vol. 25, no. 12, p. 13425, Jun. 2017.
- [62] J. Homola, I. Koudela, and S. S. Yee, “Surface plasmon resonance sensors based on diffraction gratings and prism couplers: sensitivity comparison,” *Sensors Actuators B Chem.*, vol. 54, no. 1–2, pp. 16–24, Jan. 1999.
- [63] X. Fan, I. M. White, S. I. Shopova, H. Zhu, J. D. Suter, and Y. Sun, “Sensitive optical biosensors for unlabeled targets: A review,” *Anal. Chim. Acta*, vol. 620, no. 1–2, pp. 8–26, Jul. 2008.
- [64] Z. Salamon, H. A. Macleod, and G. Tollin, “Coupled plasmon-waveguide resonators: a new spectroscopic tool for probing proteolipid film structure and properties,” *Biophys. J.*, vol. 73, no. 5, pp. 2791–2797, Nov. 1997.
- [65] S. Mahajna, M. Neumann, O. Eyal, and A. Shalabney, “Plasmon-Waveguide Resonances with Enhanced Figure of Merit and Their Potential for Anisotropic Biosensing in the Near Infrared Region,” *J. Sensors*, vol. 2016, pp. 1–6, 2016.
- [66] F. Bahrami, J. S. Aitchison, and M. Mojahedi, “A highly optimized plasmon waveguide resonance biosensor,” in *2012 IEEE Photonics Conference, IPC 2012*, 2012.
- [67] M. S. Golden, A. C. Bjonnes, and R. M. Georgiadis, “Distance- and Wavelength-Dependent Dielectric Function of Au Nanoparticles by Angle-Resolved Surface Plasmon Resonance Imaging,” *J. Phys. Chem. C*, vol. 114, no. 19, pp. 8837–8843, May 2010.
- [68] H. E. de Bruijn, R. P. H. Kooyman, and J. Greve, “Determination of dielectric permittivity and thickness of a metal layer from a surface plasmon resonance experiment,” *Appl. Opt.*, vol. 29, no. 13, p. 1974, May 1990.
- [69] M. O. Vassell, “Structure of optical guided modes in planar multilayers of optically anisotropic materials,” *J. Opt. Soc. Am.*, vol. 64, no. 2, p. 166, Feb.

- 1974.
- [70] I. Pockrand, "Surface plasma oscillations at silver surfaces with thin transparent and absorbing coatings," *Surf. Sci.*, vol. 72, no. 3, pp. 577–588, Apr. 1978.
- [71] S. Kumar, V. K. Shukla, and A. Tripathi, "Ellipsometric investigations on the light induced effects on tris(8-hydroxyquinoline) aluminum (Alq3)," *Thin Solid Films*, vol. 477, no. 1–2, pp. 240–243, Apr. 2005.
- [72] J. Matsuoka, N. Kitamura, S. Fujinaga, T. Kitaoka, and H. Yamashita, "Temperature dependence of refractive index of SiO₂ glass," *J. Non. Cryst. Solids*, vol. 135, no. 1, pp. 86–89, Oct. 1991.
- [73] T. Del Rosso, W. Margulis, J. Fontana, and I. C. S. Carvalho, "Plasmonics for the Characterization of Metal Organic Films and Nanoparticles," in *Metal Nanostructures for Photonics*, Elsevier, 2019, pp. 223–259.
- [74] J. W. Weber, V. E. Calado, and M. C. M. van de Sanden, "Optical constants of graphene measured by spectroscopic ellipsometry," *Appl. Phys. Lett.*, vol. 97, no. 9, p. 091904, Aug. 2010.
- [75] M. Bruna and S. Borini, "Optical constants of graphene layers in the visible range," *Appl. Phys. Lett.*, vol. 94, no. 3, p. 031901, Jan. 2009.
- [76] E. Hutter and J. H. Fendler, "Exploitation of Localized Surface Plasmon Resonance," *Adv. Mater.*, vol. 16, no. 19, pp. 1685–1706, Oct. 2004.
- [77] J. A. Creighton and D. G. Eadon, "Ultraviolet–visible absorption spectra of the colloidal metallic elements," *J. Chem. Soc., Faraday Trans.*, vol. 87, no. 24, pp. 3881–3891, 1991.
- [78] M. A. Garcia, "Surface plasmons in metallic nanoparticles: fundamentals and applications," *J. Phys. D. Appl. Phys.*, vol. 44, no. 28, p. 283001, Jul. 2011.
- [79] Michael Quinten, "Optical Properties of Nanoparticle Systems: Mie and beyond - Quinten - Wiley Online Library," *Wiley-VCH Verlag GmbH & Co. KGaA, Weinheim*, 2011. .
- [80] T. Del Rosso *et al.*, "Biocompatible Au@Carbynoid/Pluronic-F127 nanocomposites synthesized by pulsed laser ablation assisted CO₂recycling," *Appl. Surf. Sci.*, vol. 441, pp. 347–355, 2018.
- [81] J. C. M. Garnett, "Colours in Metal Glasses and in Metallic Films," *Philos. Trans. R. Soc. A Math. Phys. Eng. Sci.*, vol. 203, no. 359–371, pp. 385–420,

- Jan. 1904.
- [82] L. He, E. A. Smith, M. J. Natan, and C. D. Keating, “The Distance-Dependence of Colloidal Au-Amplified Surface Plasmon Resonance,” *J. Phys. Chem. B*, vol. 108, no. 30, pp. 10973–10980, Jul. 2004.
- [83] L. He *et al.*, “Colloidal Au-Enhanced Surface Plasmon Resonance for Ultrasensitive Detection of DNA Hybridization,” *J. Am. Chem. Soc.*, vol. 122, no. 38, pp. 9071–9077, Sep. 2000.
- [84] L. Huang *et al.*, “Prostate-specific antigen immunosensing based on mixed self-assembled monolayers, camel antibodies and colloidal gold enhanced sandwich assays,” *Biosens. Bioelectron.*, vol. 21, no. 3, pp. 483–490, Sep. 2005.
- [85] A. Shiohara, Y. Wang, and L. M. Liz-Marzán, “Recent approaches toward creation of hot spots for SERS detection,” *J. Photochem. Photobiol. C Photochem. Rev.*, vol. 21, pp. 2–25, Dec. 2014.
- [86] G. Giovannetti, P. A. Khomyakov, G. Brocks, V. M. Karpan, J. van den Brink, and P. J. Kelly, “Doping Graphene with Metal Contacts,” *Phys. Rev. Lett.*, vol. 101, no. 2, p. 026803, Jul. 2008.
- [87] I. Shteplyuk, N. M. Caffrey, T. Iakimov, V. Khranovskyy, I. A. Abrikosov, and R. Yakimova, “On the interaction of toxic Heavy Metals (Cd, Hg, Pb) with graphene quantum dots and infinite graphene,” *Sci. Rep.*, vol. 7, no. 1, p. 3934, Dec. 2017.
- [88] I. Piwoński, J. Grobelny, M. Cichomski, G. Celichowski, and J. Rogowski, “Investigation of 3-mercaptopropyltrimethoxysilane self-assembled monolayers on Au(111) surface,” *Appl. Surf. Sci.*, vol. 242, no. 1–2, pp. 147–153, Mar. 2005.
- [89] T. G. Habteyes *et al.*, “Metallic Adhesion Layer Induced Plasmon Damping and Molecular Linker as a Nondamping Alternative,” *ACS Nano*, vol. 6, no. 6, pp. 5702–5709, Jun. 2012.
- [90] A. K. Mahapatro, A. Scott, A. Manning, and D. B. Janes, “Gold surface with sub-nm roughness realized by evaporation on a molecular adhesion monolayer,” *Appl. Phys. Lett.*, vol. 88, no. 15, p. 151917, Apr. 2006.
- [91] D. M. Mattox, “Arc Vapor Deposition,” in *Handbook of Physical Vapor Deposition (PVD) Processing*, Elsevier, 1998, pp. 406–425.
- [92] C. Vilani, E. C. Romani, D. G. Larrudé, G. M. Barbosa, and F. L. Freire,

- “Direct transfer of graphene films for polyurethane substrate,” *Appl. Surf. Sci.*, vol. 356, pp. 1300–1305, Nov. 2015.
- [93] F. Jenkins and H. White, *Fundamentals of optics*. New York: McGraw Hills, 2001.
- [94] R. C. Thompson, “Optical Waves in Layered Media,” *J. Mod. Opt.*, vol. 37, no. 1, pp. 147–148, Jan. 1990.
- [95] S. H. Choi and K. M. Byun, “Investigation on an application of silver substrates for sensitive surface plasmon resonance imaging detection,” *J. Opt. Soc. Am. A*, vol. 27, no. 10, p. 2229, Oct. 2010.
- [96] B. A. Sexton, B. N. Feltis, and T. J. Davis, “Characterisation of gold surface plasmon resonance sensor substrates,” *Sensors Actuators A Phys.*, vol. 141, no. 2, pp. 471–475, Feb. 2008.
- [97] S. A. N.H. Salah, D. Jenkins, L. Panina, R. Handy, G. Pan, “Self-sensing surface plasmon resonance for the detection of metallic nanoparticles,” *Smart Nanosyst. Eng. Med*, vol. 2, pp. 10–22, 2013.
- [98] Y. Zhao *et al.*, “Highly impermeable and transparent graphene as an ultra-thin protection barrier for Ag thin films,” *J. Mater. Chem. C*, vol. 1, no. 32, p. 4956, 2013.
- [99] J. C. Reed, H. Zhu, A. Y. Zhu, C. Li, and E. Cubukcu, “Graphene-Enabled Silver Nanoantenna Sensors,” *Nano Lett.*, vol. 12, no. 8, pp. 4090–4094, Aug. 2012.
- [100] T. Del Rosso *et al.*, “Enhanced stability of plasmonic metal thin films by CVD grown graphene transfer,” *Thin Solid Films*, vol. 644, pp. 65–70, Dec. 2017.
- [101] A. Schaub, P. Slepíčka, I. Kašpárková, P. Malinský, A. Macková, and V. Švorčík, “Gold nanolayer and nanocluster coatings induced by heat treatment and evaporation technique,” *Nanoscale Res. Lett.*, vol. 8, no. 1, p. 249, 2013.
- [102] C. Lee, C. S. Robertson, A. H. Nguyen, M. Kahraman, and S. Wachsmann-Hogiu, “Thickness of a metallic film, in addition to its roughness, plays a significant role in SERS activity,” *Sci. Rep.*, vol. 5, no. 1, p. 11644, Dec. 2015.
- [103] P. Pallavicini, G. Dacarro, M. Galli, and M. Patrini, “Spectroscopic evaluation of surface functionalization efficiency in the preparation of

- mercaptopropyltrimethoxysilane self-assembled monolayers on glass,” *J. Colloid Interface Sci.*, vol. 332, no. 2, pp. 432–438, Apr. 2009.
- [104] L. M. Walpita, “Solutions for planar optical waveguide equations by selecting zero elements in a characteristic matrix,” *J. Opt. Soc. Am. A*, vol. 2, no. 4, p. 595, Apr. 1985.
- [105] M. Todeschini, A. Bastos da Silva Fanta, F. Jensen, J. B. Wagner, and A. Han, “Influence of Ti and Cr Adhesion Layers on Ultrathin Au Films,” *ACS Appl. Mater. Interfaces*, vol. 9, no. 42, pp. 37374–37385, Oct. 2017.
- [106] H. Shen, N. Guillot, J. Rouxel, M. Lamy de la Chapelle, and T. Toury, “Optimized plasmonic nanostructures for improved sensing activities,” *Opt. Express*, vol. 20, no. 19, p. 21278, Sep. 2012.
- [107] H. L. Johnston, F. Cuta, and A. B. Garrett, “The Solubility of Silver Oxide in Water, in Alkali and in Alkaline Salt Solutions. The Amphoteric Character of Silver Hydroxide,” *J. Am. Chem. Soc.*, vol. 55, no. 6, pp. 2311–2325, Jun. 1933.
- [108] K. Fujiwara, G. A. Sotiriou, and S. E. Pratsinis, “Enhanced Ag + Ion Release from Aqueous Nanosilver Suspensions by Absorption of Ambient CO₂,” *Langmuir*, vol. 31, no. 19, pp. 5284–5290, May 2015.
- [109] E. S. Forzani, H. Zhang, W. Chen, and N. Tao, “Detection of Heavy Metal Ions in Drinking Water Using a High-Resolution Differential Surface Plasmon Resonance Sensor,” *Environ. Sci. Technol.*, vol. 39, no. 5, pp. 1257–1262, Mar. 2005.
- [110] S. Scholz, D. Kondakov, B. Lüsse, and K. Leo, “Degradation Mechanisms and Reactions in Organic Light-Emitting Devices,” *Chem. Rev.*, vol. 115, no. 16, pp. 8449–8503, Aug. 2015.
- [111] D. Y. Kondakov, W. C. Lenhart, and W. F. Nichols, “Operational degradation of organic light-emitting diodes: Mechanism and identification of chemical products,” *J. Appl. Phys.*, vol. 101, no. 2, p. 024512, Jan. 2007.
- [112] X. Zhou *et al.*, “Real-Time Observation of Temperature Rise and Thermal Breakdown Processes in Organic LEDs Using an IR Imaging and Analysis System,” *Adv. Mater.*, vol. 12, no. 4, pp. 265–269, Feb. 2000.
- [113] S. C. Xia, R. C. Kwong, V. I. Adamovich, M. S. Weaver, and J. J. Brown, “OLED Device Operational Lifetime: Insights and Challenges,” in *2007 IEEE International Reliability Physics Symposium Proceedings. 45th*

- Annual*, 2007, pp. 253–257.
- [114] M. Cölle and W. Brütting, “Thermal, structural and photophysical properties of the organic semiconductor Alq₃,” *Phys. status solidi*, vol. 201, no. 6, pp. 1095–1115, May 2004.
- [115] H. Aziz *et al.*, “Humidity-induced crystallization of tris (8-hydroxyquinoline) aluminum layers in organic light-emitting devices,” *Appl. Phys. Lett.*, vol. 72, no. 7, pp. 756–758, Feb. 1998.
- [116] W. R. Brito *et al.*, “Spectroscopic evidence of photodegradation by ultraviolet exposure of tris(8-hydroxyquinoline) aluminum (Alq₃) thin films,” *J. Braz. Chem. Soc.*, vol. 21, no. 12, pp. 2367–2372, Dec. 2010.
- [117] A. . Djurišić *et al.*, “Spectroscopic ellipsometry of the optical functions of tris (8-hydroxyquinoline) aluminum (Alq₃),” *Thin Solid Films*, vol. 416, no. 1–2, pp. 233–241, Sep. 2002.
- [118] E. S. Andreiadis, N. Gauthier, D. Imbert, R. Demadrille, J. Pécaut, and M. Mazzanti, “Lanthanide Complexes Based on β -Diketonates and a Tetradentate Chromophore Highly Luminescent as Powders and in Polymers,” *Inorg. Chem.*, vol. 52, no. 24, pp. 14382–14390, Dec. 2013.
- [119] C. Himcinschi *et al.*, “Spectroscopic ellipsometric characterization of organic films obtained via organic vapor phase deposition,” *Appl. Phys. A*, vol. 80, no. 3, pp. 551–555, Feb. 2005.
- [120] S. Biju, D. B. A. Raj, M. L. P. Reddy, and B. M. Kariuki, “Synthesis, Crystal Structure, and Luminescent Properties of Novel Eu 3+ Heterocyclic β -Diketonate Complexes with Bidentate Nitrogen Donors,” *Inorg. Chem.*, vol. 45, no. 26, pp. 10651–10660, Dec. 2006.
- [121] F. Papadimitrakopoulos, Xian-Man Zhang, and K. A. Higginson, “Chemical and morphological stability of aluminum tris(8-hydroxyquinoline) (Alq/sub 3/): effects in light-emitting devices,” *IEEE J. Sel. Top. Quantum Electron.*, vol. 4, no. 1, pp. 49–57, 1998.
- [122] V. K. Shukla and S. Kumar, “Investigations of environmental induced effects on AlQ 3 thin films by AFM phase imaging,” *Appl. Surf. Sci.*, vol. 253, no. 16, pp. 6848–6853, Jun. 2007.
- [123] W. R. Brito, W. G. Quirino, C. Legnani, C. R. Ponciano, M. Cremona, and M. L. M. Rocco, “Ultraviolet photodegradation of tris(8-hydroxyquinolate) aluminum (Alq₃) thin films studied by electron and laser

- stimulated desorption,” *Opt. Mater. (Amst.)*, vol. 35, no. 1, pp. 29–32, Nov. 2012.
- [124] T. Pagnot, P. Audebert, and G. Tribillon, “Photostability study of europium dibenzolymethide embedded in polystyrene thin films with high concentration,” *Chem. Phys. Lett.*, vol. 322, no. 6, pp. 572–578, Jun. 2000.
- [125] W. Quirino, R. Reyes, C. Legnani, P. C. Nóbrega, P. A. Santa-Cruz, and M. Cremona, “Eu- β -diketonate complex OLED as UV portable dosimeter,” *Synth. Met.*, vol. 161, no. 11–12, pp. 964–968, Jun. 2011.
- [126] A. Mills and P. Grosshans, “UV dosimeter based on dichloroindophenol and tin(IV) oxide,” *Analyst*, vol. 134, no. 5, p. 845, 2009.
- [127] Z.-D. Zhang *et al.*, “Selective Solar-Blind UV Monitoring Based on Organic Field-Effect Transistor Nonvolatile Memories,” *Adv. Electron. Mater.*, vol. 3, no. 8, p. 1700052, Aug. 2017.
- [128] “Comsol Multiphysics Modeling Software. Available online: <https://www.comsol.com> (accessed on 2 November 2018).”
- [129] T. C. Choy, *Effective Medium Theory: Principles and Applications*, 2nd ed. Oxford University Press: Oxford, UK, 2016.
- [130] P. Holmes, K. A. F. James, and L. S. Levy, “Is low-level environmental mercury exposure of concern to human health?,” *Sci. Total Environ.*, vol. 408, no. 2, pp. 171–182, Dec. 2009.
- [131] P. M. Lee, Z. Chen, L. Li, and E. Liu, “Reduced graphene oxide decorated with tin nanoparticles through electrodeposition for simultaneous determination of trace heavy metals,” *Electrochim. Acta*, vol. 174, pp. 207–214, Aug. 2015.
- [132] K. Chen *et al.*, “Hg(II) Ion Detection Using Thermally Reduced Graphene Oxide Decorated with Functionalized Gold Nanoparticles,” *Anal. Chem.*, vol. 84, no. 9, pp. 4057–4062, May 2012.
- [133] T. Zhang *et al.*, “Self-Assembled 1-Octadecanethiol Monolayers on Graphene for Mercury Detection,” *Nano Lett.*, vol. 10, no. 11, pp. 4738–4741, Nov. 2010.
- [134] K. Zangeneh Kamali *et al.*, “Amalgamation based optical and colorimetric sensing of mercury(II) ions with silver@graphene oxide nanocomposite materials,” *Microchim. Acta*, vol. 183, no. 1, pp. 369–377, Jan. 2016.
- [135] A. M. Golsheikh, N. M. Huang, H. N. Lim, and R. Zakaria, “One-pot

- sonochemical synthesis of reduced graphene oxide uniformly decorated with ultrafine silver nanoparticles for non-enzymatic detection of H₂O₂ and optical detection of mercury ions,” *RSC Adv.*, vol. 4, no. 69, pp. 36401–36411, 2014.
- [136] N. H. Kamaruddin, A. A. A. Bakar, N. N. Mobarak, M. S. Dzulkefly Zan, and N. Arsad, “Binding affinity of a highly sensitive Au/Ag/Au/Chitosan-graphene oxide sensor based on direct detection of Pb²⁺ and Hg²⁺ ions,” *Sensors (Switzerland)*, vol. 17, p. 2277, 2017.
- [137] N. F. Lokman *et al.*, “Highly sensitive SPR response of Au/chitosan/graphene oxide nanostructured thin films toward Pb (II) ions,” *Sensors Actuators B Chem.*, vol. 195, pp. 459–466, May 2014.
- [138] Y. W. Fen, W. M. M. Yunus, and N. A. Yusof, “Surface plasmon resonance optical sensor for detection of Pb²⁺ based on immobilized p-tert-butylcalix[4]arene-tetrakis in chitosan thin film as an active layer,” *Sensors Actuators B Chem.*, vol. 171–172, pp. 287–293, Aug. 2012.
- [139] M. F. Santangelo, I. Shteplyuk, D. Filippini, I. G. Ivanov, R. Yakimova, and J. Eriksson, “Real-time sensing of lead with epitaxial graphene-integrated microfluidic devices,” *Sensors Actuators, B Chem.*, 2019.
- [140] Y. Uchiho, M. Shimojo, K. Furuya, and K. Kajikawa, “Optical Response of Gold-Nanoparticle-Amplified Surface Plasmon Resonance Spectroscopy,” *J. Phys. Chem. C*, vol. 114, no. 11, pp. 4816–4824, Mar. 2010.
- [141] K. Q. da Costa, J. S. Costa, V. Dmitriev, T. Del Rosso, O. Pandoli, and R. Q. Aucelio, “Analysis of surface plasmon resonance sensor coupled to periodic array of gold nanoparticles,” in *2015 SBMO/IEEE MTT-S International Microwave and Optoelectronics Conference (IMOC)*, 2015, pp. 1–5.
- [142] J. Turkevich, P. C. Stevenson, and J. Hillier, “A study of the nucleation and growth processes in the synthesis of colloidal gold,” *Discuss. Faraday Soc.*, vol. 11, p. 55, 1951.
- [143] Q. Zaman *et al.*, “Two-color surface plasmon resonance nanosizer for gold nanoparticles,” *Opt. Express*, vol. 27, no. 3, p. 3200, 2019.
- [144] M. Polyanskiy, “Refractive index database.,” *RefractiveIndex.INFO*. 2008.
- [145] M. A. García, J. Llopis, and S. E. Paje, “A simple model for evaluating the optical absorption spectrum from small Au-colloids in sol-gel films,” *Chem. Phys. Lett.*, vol. 315, no. 5–6, pp. 313–320, Dec. 1999.

- [146] Y. Battie, A. Resano-Garcia, N. Chaoui, Y. Zhang, and A. En Naciri, "Extended Maxwell-Garnett-Mie formulation applied to size dispersion of metallic nanoparticles embedded in host liquid matrix," *J. Chem. Phys.*, vol. 140, no. 4, p. 044705, Jan. 2014.
- [147] R. Ruppin, "Evaluation of extended Maxwell-Garnett theories," *Opt. Commun.*, vol. 182, no. 4–6, pp. 273–279, Aug. 2000.
- [148] P. E. Burrows and S. R. Forrest, "Electroluminescence from trap-limited current transport in vacuum deposited organic light emitting devices," *Appl. Phys. Lett.*, vol. 64, no. 17, pp. 2285–2287, Apr. 1994.
- [149] A. B. Djurišić *et al.*, "Optical functions of tris (8-hydroxyquinoline) aluminum (Alq 3) by spectroscopic ellipsometry," *Appl. Phys. A Mater. Sci. Process.*, vol. 76, no. 2, pp. 219–223, Feb. 2003.
- [150] C. C. L. Pereira, S. Dias, I. Coutinho, J. P. Leal, L. C. Branco, and C. A. T. Laia, "Europium(III) Tetrakis(β -diketonate) Complex as an Ionic Liquid: A Calorimetric and Spectroscopic Study," *Inorg. Chem.*, vol. 52, no. 7, pp. 3755–3764, Apr. 2013.
- [151] H. Tian, R. Tang, and M. Zhao, "Synthesis, Characterization, and Photophysical Properties of Dinuclear Eu(III) and Tb (III) Complexes Based on β -diketonate with Triphenylamine and Pyridine Moieties," *ECS J. Solid State Sci. Technol.*, vol. 2, no. 3, pp. R33–R38, Dec. 2013.
- [152] V. G. Kravets *et al.*, "Spectroscopic ellipsometry of graphene and an exciton-shifted van Hove peak in absorption," *Phys. Rev. B*, vol. 81, no. 15, p. 155413, Apr. 2010.